THE UNIVERSITY OF TULSA

THE GRADUATE SCHOOL

A TWO-PHASE TRANSIENT WELLBORE MODEL FOR SIMULATION OF

PRESSURE DATA.

by

Faustino Alonso Fuentes-Nucamendi

A dissertation submitted in partial fulfillment of

the requirements for the degree of Doctor of Philosophy

in the Discipline of Petroleum Engineering

The Graduate School

The University of Tulsa

1996

THE UNIVERSITY OF TULSA

THE GRADUATE SCHOOL

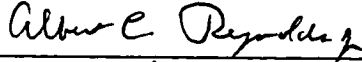A TWO-PHASE TRANSIENT WELLBORE MODEL FOR SIMULATION OF

PRESSURE DATA.

by

Faustino Alonso Fuentes-Nucamendi

A DISSERTATION

APPROVED FOR THE DISCIPLINE OF

PETROLEUM ENGINEERING

By Dissertation Committee

_____, Chairperson

_____

_____

_____

ii

ABSTRACT

Faustino A. Fuentes-Nucamendi (Doctor of Philosophy in Petroleum Engineering)

A Two-Phase Transient Wellbore Model for Simulation of Pressure Data.

(268 pp. - Chapter V)

Directed by Professor Albert C. Reynolds

(231 Words)

This work describes the development of a mechanistic model to predict the effect that transient two-phase gas-oil flow in the wellbore has on pressure drawdown and buildup behavior. A one-dimensional drift-flux model is used to derive the partial differential equations governing the two-phase flow in the wellbore. The black-oil approach, which accounts for a variable bubble-point pressure, is used to account for the effect of interphase mass transfer. After obtaining the pertinent finite-difference equations, solutions are computed by a sequential, iterative calculation procedure. We present the development of a wellbore simulator that implements the proposed model and the finite-difference solution procedure.

A procedure was developed to couple the wellbore model with a two-phase flow reservoir simulator in order to allow two-phase flow in both the wellbore and the reservoir. The coupled model should prove useful for the design of well tests and

allows one to understand the physics of complex wellbore phenomena including phase redistribution.

In addition, a subplex method was implemented to calculate the bottom-hole pressures and flow rates from wellhead conditions. The procedure uses a time-dependent linear temperature gradient in the wellbore to reduce computational time. Except at early shut-in times, the method yields reasonable estimates of bottom-hole pressure during buildup tests, but is not sufficiently accurate to be used with confidence to predict bottomhole pressures during drawdown tests.

ACKNOWLEDGMENTS

My deepest appreciation and gratitude are expressed to Dr. Albert C. Reynolds, Jr. for his advice, encouragement, and guidance throughout this study. Dr. Reynolds was responsible for bringing me to Tulsa. His enthusiasm and unconditional support during hard times will never be forgotten; I hope that I can reciprocate his courtesy some day. My heartfelt thanks and appreciation are also due to Dr. Ovadia Shoham and Dr. Leslie G. Thompson for their continuous encouragement, friendship and extraordinary support during my studies and the course of this work. To Dr. Shoham, I wish to express my greatest gratitude for enlightening me in the field of two-phase flow modeling and transient two-phase flow modeling. Dr. Thompson, I thank for giving me a superb boost in the numerical reservoir simulation and well testing areas. I take this opportunity to thank Dr. Siamack Shirazi for his suggestions, reviewing this work and being on my committee.

I am extremely grateful for the financial support provided by the convenium U.N.A.M./PEMEX, through which I could pursue an advanced degree in engineering. I gratefully acknowledge the financial support from TUPREP (Tulsa University Petroleum Reservoir Exploitation Projects) for this study. My utmost appreciation to Dr. Heber Cinco Ley and Dr. Fernando Samaniego for their friendship and unconditional support.

I wish to thank Dr. Randalhl D. Roadifer for providing me the RDRBOS (r-z)

v

reservoir simulator and Dr. Thomas H. Rowan for providing me with the subplex method program, used in this study.

I would like to thank my fellow graduate students for their support and encouragement.

I gratefully thank and dedicate this work to my wife, Magaly, whose love, encouragement, understanding, and personal sacrifices made this dream possible. This work is also dedicated to my parents Dr. Luis A. Fuentes and Miriam Nucamendi de Fuentes and mama Benny Navarro for their unconditional support and love.

My deepest gratitude to the Great White Brotherhood, for their eternal support and guidance; I am that I am.

TABLE OF CONTENTS

ix

Appendices

LIST OF TABLES

LIST OF FIGURES

xii

xiii

xiv

CHAPTER I

INTRODUCTION.

Pressure transient testing has been used in the petroleum industry to evaluate reservoir characteristics for many years. It is well-known that there are several factors that can influence the pressure response, such as skin, wellbore storage, phase redistribution, partial penetration, etc.

Numerous analytical well testing solutions exits which treat the wellbore storage coefficient as constant. These solutions are used worldwide and accepted in the industry today, even though it is well recognized that in practice the wellbore storage may be variable. Somewhat surprisingly, there are few papers related to effect of wellbore phase segregation, a variable wellbore storage and a complete well dynamics influence. It is well-known, however, that when wellbore phase segregation occurs during a pressure buildup test, the buildup data may exhibit a characteristic pressure hump. The main objective of the present study is to develop a mechanistic model to predict the effect that transient two-phase gas-oil flow in the wellbore has on the behavior of pressure drawdown and buildup data. In this study, a one-dimensional drift-flux model is used to derive partial differential equations governing the phase segregation process. The black-oil approach, which accounts for a variable bubble-point pressure, is used to account for the effect of interphase mass transfer. After obtaining the corresponding finite-difference equations, solutions are computed with

1

a sequential, iterative calculation procedure.

A computer simulator has been developed to implement the proposed model and the finite-difference solution procedure. For the purpose of verification, the simulator was first used to generate pressure responses from a buildup test in a well where single phase flow exits in the wellbore before shut-in. The analysis of generated pressure buildup data was carried out by type-curve matching with the classical wellbore storage and skin type curves and also by using Horner analysis. These studies yield correct values of permeability, skin factor, initial reservoir pressure and also the wellbore storage coefficient.

After verification, the simulator was applied to simulate the phase redistribution process occurring in the wellbore during pressure buildup tests in wells shut-in at the surface. This study presents two cases: a buildup test in a naturally flowing well and a buildup test in a gas-lift well. The investigation confirms that the wellbore storage coefficient can either increase or decrease, as reported in the literature. The variation in the wellbore storage coefficient is affected by both phase segregation and gas compression. If the magnitude of afterflow is small after the end of wellbore phase segregation, then phase segregation will be the dominating factor, and pressure buildup data will show an increasing wellbore storage coefficient. On the other hand, if the afterflow is still large after gas and liquid have completely segregated in the wellbore, the gas column will be compressed due to afterflow and the pressure buildup data will show a decreasing wellbore storage coefficient.

These cases were used to consider numerical accuracy and stability of the model, and to investigate the validity of the Fair[1] and Hegeman[2] models for wellbore

phase redistribution. Additionally, an isothermal and a non-isothermal transient process of wellbore phase segregation were simulated to investigate its effect on pressure response.

Finally, several simulations were done and synthetic wellhead and bottomhole data were recorded. The wellhead data were used to invert the wellhead pressure and rate response to bottomhole conditions. The data obtained from the inverse problem solution was compared with the recorded bottomhole data, in order to verify the feasibility of using it as a method to verify actually recorded bottomhole data or as an alternative method to produce bottomhole data that can be analyzed with normal method using only the wellhead pressure and rate responses.

1.1 Background.

All pressure transient tests are the same in a sense that we attempt to obtain reservoir flow properties by monitoring and analyzing output signals (pressure or flow rate) generated by a reservoir as it responds to input signals (changes in flow rate or pressure). Although pressure is easily measured down-hole, the measurement and control of flow rates are usually done at the wellhead, not at bottomhole.

Considering a drawdown test, if a constant wellhead rate is maintained, the bottomhole does not respond immediately to the pressure/rate condition imposed at surface, i.e., the sandface rate is initially zero and continuously increases as the bottomhole the pressure/rate condition responds to the surface conditions, reaching a maximum value equal to the surface rate as steady-steady conditions are reached. This process is called unloading[3,4], and its time length is strongly dependent on the

well producing conditions, reservoir fluid PVT properties and wellbore characteristics.

On the other hand, during a buildup test, a no-flow wellhead rate is established at the beginning of the test, and, as in the drawdown test, the bottomhole does not react instantaneously to the new pressure/rate condition imposed at surface. In this case, the sandface rate continuously decreases from the maximum value reached at the end of the production period to a minimum value of zero, or, may even becomes negative: i.e., backflow could occur. This process is called afterflow and could include a certain period of backflow.

In pressure transient analysis, the period where the surface and sandface rates are different is referred as the wellbore storage period. In order to model the influence of wellbore effects on the bottomhole pressure, the wellbore storage coefficient was introduced[3,4,5]. Treating the wellbore storage coefficient as a constant may be adequate for tests in wells operated under single phase flow conditions, but it is not valid under multiphase flow conditions; i.e., when oil and gas flow simultaneously in the wellbore, a variable wellbore storage coefficient will be obtained. To develop better well test analysis techniques, a better understanding of the physics of multiphase flow in the wellbore is essential.

Complicated phenomena occur when gas and oil flow simultaneously in the wellbore. One anomalous behavior which occurs in pressure buildup tests is the "pressure hump", which is characterized by the fact that the bottomhole pressure builds up to a maximum and then falls off[6].

The first study that reported problems associated with wellbore phase redistribution was presented by Stegemeier and Matthews[6] in the late 1950's. They

conducted simple bubble-rise laboratory tests as well as field tests, to confirm the influence of phase segregation on the pressure response during a buildup test. It was found that in many cases, this pressure hump behavior was due to the segregation of gas and liquid after the well was shut-in at the wellhead[6,7]. Pitzer et al.[7] showed that the magnitude of the wellbore phase redistribution effects depends on producing well characteristics, i.e., the producing gas-oil ratio and stabilized rate of flow in the well. Due to the effect of phase redistribution, the Horner semilog straight line is often delayed or completely suppressed and standard semilog analysis cannot be used. Analysis techniques for the pressure buildup response were not presented in either of these works[6,7].

The work by Fair[1] is the first attempt to correct wellbore effects caused by phase redistribution in pressure buildup tests. In Fair's model, phase redistribution was treated as a wellbore storage effect and incorporated into the inner boundary condition for the diffusivity equation. Based on limited experimental data, it was assumed that the phase redistribution pressure function has an exponential form. New analytical solutions were then obtained and new type curves were developed for the analysis of field data. Fair's analytical solution shows that, at early times, a well experiencing phase segregation in the wellbore will act like a well with constant storage, but with an apparent storage coefficient, C_{aD}. Then, a transition period will follow during which the wellbore storage coefficient can increase, decrease or even become negative. However, at late times, the well will again act like a well with constant storage, with storage coefficient equal to C_D. Since $C_D > C_{aD}$, Fair's model has been referred to as an increasing wellbore storage model.

Later on, Hegeman et al.[2] reported that in some cases, field data indicated that the exponential function used by Fair does not always give a good representation of the phase redistribution pressure change. Hegeman et al. modified and extended the technique of Fair by using an error function to represent the phase redistribution pressure function. The Hegeman et al. model apparently was motivated entirely by a desire to obtain a model which predicted a behavior closer to field buildup data, especially when the field data exhibits a decreasing wellbore storage coefficient. In order to match some field data, however, Hegeman et al. assigned negative values to the phase redistribution pressure change parameter which means that phase redistribution causes bottomhole pressure to increase more slowly. This appears to be unreasonable from a physical point of view. The Hegeman et al. model leads to a decreasing wellbore storage coefficient. Like Fair's model, the work of Hegeman et al. shows that, at early times, a well will exhibit a constant wellbore storage coefficient, C_{aD}, while at late times, the well will exhibit a constant wellbore storage coefficient, C_D. Since $C_D < C_{aD}$, the model by Hegeman et al. has been referred to as a decreasing storage model.

In 1986, Thompson et al.[8] showed that there exist three different types of pressure responses when phase redistribution occurs and presented conditions under which each of the three types of pressure responses exists. It was also shown that the analysis using Fair's type curves could lead to multiple solutions. They presented correlations to predict the beginning of the semilog straight line for the three types of pressure response when phase redistribution exists.

The Fair and Hegeman et al. models can be used to prepare type curves.

However. as pointed out by Fair (also see Ref. 8), type curve matching can lead to multiple solutions. In Ref. 9, we also encountered nonuniqueness problems when we used nonlinear regression to match synthetic well-test pressure data generated from our phase segregation simulator with the analytical solutions of Fair and Hegeman et al. Rushing et al.[10] proposed an automatic history matching technique to analyze pressure buildup data influenced by wellbore phase redistribution. This automated type-curve analysis method uses a Gauss-Newton least squares procedure.

Fair's results[1] (also see Thompson et al.[8]) indicate that phase redistribution effects may not be severe enough to be easily detected on a log-log plot of buildup pressure change versus shut-in time; however, as shown in Refs. 11 and 12, pressure derivative plots can be used to detect the presence of phase segregation and locate the beginning of the Horner semilog straight line. However, it was found that the derivative of a pressure buildup response influenced by wellbore phase segregation is quite similar to the derivative of the pressure buildup response obtained from a dual porosity reservoir. They discussed methods to distinguish the two types of responses from each other.

The important influence that phase segregation can have on pressure buildup data, and the lack of a model which incorporated the true physical process of phase segregation, motivated the present work, as well as that of previous researchers[13,14], to consider the development of a wellbore model to capture the essential physics of transient two-phase flow in the wellbore. The simulators developed in Ref. 13 as well as in Ref. 14 used classical multiphase flow methods for the wellbore. Those methods were developed for steady-state flow, and therefore are clearly inappropriate

for applications that involves transient flow.

Winterfeld[13] developed a two-fluid wellbore model and coupled it with a (r-z) reservoir simulator. His model allows three phase flow, but assumes isothermal flow in both the wellbore and the reservoir. He used semi-empirical correlations for the viscous forces between phases at phase interfaces. Newton iteration was used to solve the combined equation reservoir/wellbore equations. Winterfield showed that his model predicts a pressure hump when phase segregation causes a sufficiently large pressure increase.

Following the same basic approach of Winterfeld[13], Almehaideb et al.[14] developed a numerical model which couples a wellbore model with a black-oil reservoir simulator. Instead of writing continuity equations for each phase with an interphase mass transfer term as done by Winterfield for the wellbore equations, they perform a mass balance on the oil, gas and water components using the standard black-oil approach. Although, their basic model is a two-fluid model, they also implemented an alternate procedure which incorporates the mixture momentum equation instead of the individual phase momentum equations. They claim, however that the mixture momentum equation can not be used for countercurrent two-phase flow, i.e., can not be used to simulate pressure buildup when phase segregation occurs. Their discussion of pressure buildup is confined to one example. In their example, the two-fluid model shows a pressure hump, whereas the solution obtained with the model incorporating the mixture momentum equation does not show this anomaly (see Fig. 10 of Ref. 14). However, unlike the behavior of Fair's model[1] and Winterfield's numerical results, the "pressure hump" exhibited is not smooth.

More recently, Hasan and Kabir[15] presented a mechanistic approach to model wellbore phase segregation. As noted in a later paper[16] by the same authors, their coupling of the wellbore and reservoir flow, which uses a different form of Duhamel's principle than used in this work and previous reports presented by the author[9,17] and Xiao et al.[19], appears to yield a less robust scheme that the procedure presented here. Stability problems encountered by Hasan and Kabir wellbore/reservoir coupling forced them to switch to an exponential form of the sandface flowrate at low rates.

In Ref. 16, Hasan and Kabir presented a mechanistic model to predict the pressure increase due to a single bubble migrating upward through the liquid column during a pressure buildup test, and presented approximate analytical solutions for this pressure change during early shut-in times. Quite interestingly, their analytical solutions have the same exponential form as the empirical one used by Fair[1].

To the best of our knowledge, no existing simulator has been able to generate results which confirm the conjectured equations given by Fair[1] and Hegeman et al.[2] for the phase redistribution pressure rise.

1.2 Outline.

The main objective of this work is to develop computer simulators coupling wellbore multiphase flow with reservoir flow and investigate the effect of wellbore multiphase flow on pressure buildup data.

In Chapter II, we present the main features of the transient wellbore model. Using basic principles and considering local and instantaneous formulations, the equations that govern the wellbore fluid dynamics are derived. The model is based on the

drift flux model formulation and all the equations required to compute the physical properties and a variable bubble-point pressure are based on a black-oil model formulation. These equations are derived and explained in detail in Chapter II. Governing equations for the wellbore model that include fully transient mass and momentum equations are described and detailed methodology to compute the heat transfer in flowing wells is presented. These equations allow us to compute the pressure, concentration, velocity and temperature profile in a wellbore during drawdown and buildup tests. The drift-flux model closure relationship formulation is presented. The initial and boundary conditions are established. Methodology to couple the wellbore model with the reservoir through a convolution integral (Duhamel's principle) or through a numerical (r-z) reservoir simulator is presented.

Chapter III focuses on a detailed description of how the system of nonlinear partial differential equations governing the phase segregation process in the wellbore is solved numerically using finite difference methods. The wellbore is divided into uniform control volumes and the finite difference equations are derived with a system of staggered grids. A multistep implicit formulation has been selected to enhance stability. The method consists of a basic step to solve for pressures, a stabilizing step to solve for mixture velocities and a final step to estimate oil concentrations. Detailed discussion of the calculation procedures for the drawdown and the buildup periods is presented at the end of Chapter III.

In Chapter IV, pressures responses generated with the simulator for several drawdown and buildup tests are presented and discussed. As part of the model validation three cases are presented: the first case consists of a drawdown and buildup

test in a naturally flowing well where single-phase oil flows in the wellbore. The second case is a buildup test in a naturally flowing well but two phases develop in the wellbore during production. The last case represents a pressure buildup test conducted in a gas-lift well producing only single phase oil from the reservoir.

In the second part of the chapter, we analyze several buildup pressure responses obtained from our model. The wellbore model was derived from basic principles, so it is appropriate to consider whether buildup data obtained from it can be analyzed using the Fair[1] and Hegeman[2] models. The TUPREP nonlinear regression package based on least absolute value is used. Additionally, an isothermal and non-isothermal transient process of wellbore segregation is simulated and the influence of temperature in the buildup pressure response is analyzed.

In the last part of chapter IV, synthetic wellhead and bottomhole data are presented for several cases. The wellhead data are used to invert the wellhead pressure and rate response to bottomhole conditions. The data obtained from the inverse problem solution are compared with the recorded bottomhole data, in order to verify the feasibility of using it as a practical method to replace bottomhole measurements.

Finally, Chapter V summarizes the results and conclusions of the present work, and suggests areas where additional investigation is needed.

CHAPTER II

DRIFT FLUX MODEL

Investigation of transient gas-liquid two-phase flow in pipes has been pursued by the following three general approaches[20,21]: the homogeneous model, the separated or two-fluid model and the drift-flux model[22,23,24,25]. Our formulation is based on the drift-flux model. The procedure uses a black-oil formulation with variable bubble-point to model the two-phase flow of oil and gas. For the reservoir, both single-phase flow of oil and two-phase flow of oil and gas are considered. In the case of single-phase flow, we can rigorously couple the reservoir and wellbore through a convolution integral (Duhamel's principle) or through a numerical reservoir simulator. In the case of two-phase flow, a numerical reservoir simulator is used. Additionally, we allow the injection of gas at the bottomhole. This option allows us not only to simulate gas-lift, but also to approximate the effect of both gas and oil flowing into the well at the sandface provided that the flowing gas-oil ratio is specified.

2.1   General PVT Properties and Multiphase Flow Variables Definitions.

Here, a general two-component, two phase black-oil model will be described. The reader well note that the formulation is quite similar to a standard one used in reservoir simulation[26]. Throughout our formulation, oil-field units are used and the standard conditions assumed are given by $p_{sc} = 14.7$ [psia] and $T_{sc} = 60$ [$^{\circ}F$].

12

Throughout this study, the subscript sc is used to denote standard conditions. The black-oil wellbore model has the following characteristics :

- Two component system:

  - $\hat{o}$ =oil component.

  - $\hat{g}$ =gas component.

- Two-phase system:

  - l =liquid phase=oil phase.

  - g =gas phase.

By use the following notation:

$$V_m = \text{volume of phase } m \text{ at some pressure } (p)$$

$$\text{and temperature} (T), \tag{2.1}$$

$$V_{\hat{cs},m} = \text{volume of component } \hat{c} \text{ at standard conditions} \tag{2.2}$$

$$\text{that is obtained from phase } m.$$

$$m_{cm} = \rho_{\hat{cs}} V_{\hat{cs},m} = \text{mass of component } \hat{c} \text{ in the volume } V_{\hat{cs},m}. \tag{2.3}$$

The formation volume factor of the oil phase is defined by

$$B_o = \frac{V_o}{V_{\hat{os},o}}, \tag{2.4}$$

that is, the ratio of the volume of oil plus its dissolved gas at reservoir conditions to the volume of the oil component at the standard conditions in $[RB/STB]$. In a similar way, the formation volume factor of the gas is

$$B_g = \frac{V_g}{V_{\widehat{gs},g}}.$$
(2.5)

i.e., as the ratio of the volume of free gas (only gas component) at reservoir conditions to the resulting volume of the gas obtained at standard conditions in $[ft^3/scf]$.

In general, the solubility ratio of component $\widehat{c}$ in phase m defined as

$$R_{s,cm} = \frac{V_{\widehat{cs},m}}{V_{\widehat{ms},m}}.$$
(2.6)

Thus, the solubility of the gas component in the oil phase is given by

$$R_{s,go} = \frac{V_{\widehat{gs},o}}{V_{\widehat{os},o}},$$
(2.7)

which is, the volume of gas at standard conditions dissolved at a given pressure and temperature in a unit volume of stock-tank oil in $[scf/STB]$.

The phase density of the gas phase is defined as ratio of mass of oil and gas components in the gas phase to the volume of that phase at specified conditions and is given by

$$\rho_g = \frac{m_{og} + m_{gg}}{V_g}.$$
(2.8)

where o, g are the components present in the gas phase, g, and m_{og} and m_{gg} are defined as $m_{og} = \rho_{\widehat{os}}V_{\widehat{os},g}$ and $m_{gg} = \rho_{\widehat{gs}}V_{\widehat{gs},g}$ respectively, where $\rho_{\widehat{os}}$ and $\rho_{\widehat{gs}}$ are the densities of component $\widehat{o}$ and $\widehat{g}$ at standard conditions. Considering the two-

components (o, g) and using the definitions of formation volume factor and solubility ratio, we have

$$\rho_g = \frac{1}{B_g} \left(\rho_{\widehat{gs}} + \frac{R_{s,og}\rho_{\widehat{os}}}{5.615} \right),$$ (2.9)

and for the liquid (oil) phase the density is defined as

$$\rho_l = \frac{1}{B_o} \left(\rho_{\widehat{os}} + \frac{R_{s,go}\rho_{\widehat{gs}}}{5.615} \right).$$ (2.10)

In our work, we assume that the oil component is not allowed to vaporize into the gas phase $(R_{s,og} = 0)$. Then, letting $R_s = R_{s,go}$, $\rho_{gs} = \rho_{\widehat{gs}}$ and $\rho_{os} = \rho_{\widehat{os}}$, the gas phase density and liquid (oil) phase density, respectively, are given in units of lbm/ft^3 by

$$\rho_g = \frac{\rho_{gs}}{5.615 B_g},$$ (2.11)

and

$$\rho_l = \frac{R_s \rho_{gs}}{5.615 B_o} + \frac{\rho_{os}}{B_o},$$ (2.12)

where we now assume B_g represents the gas formation volume factor in $[RB/scf]$, B_o represents the oil formation volume factor in $[RB/STB]$ and R_s represents the dissolved or solution gas-oil ratio in $[scf/STB]$. The 5.615 factor in Eq. 2.11 convert B_g from $[RB/scf]$ to $[ft^3/scf]$. The 5.615 factor in Eq. 2.12 convert R_s from $[scf/STB]$ to $[STB/STB]$.

From Eq. 2.12 the partial densities of the gas and oil components in the liquid phase, denoted, respectively, by ρ_{gl} and ρ_{ol}, are given by

$$\rho_{gl} = \frac{R_s \rho_{gs}}{5.615 B_o},$$ (2.13)

$$\rho_{ol} = \frac{\rho_{os}}{B_o}, \tag{2.14}$$

By using Eq. 2.13 and 2.14, we can rewrite Eq. 2.12 as

$$\rho_l = \rho_{gl} + \rho_{ol}. \tag{2.15}$$

The mass fraction of component $\hat{c}$ in phase m is defined as

$$
\begin{aligned}
C_{cm} &= \frac{m_{cm}}{m_m}, \\
&= \frac{\rho_{\hat{cs}} V_{\hat{cs},m}}{\rho_m V_m} = \frac{\rho_{\hat{cs}}}{\rho_m} \frac{V_{\hat{ms},m}}{V_m} \frac{V_{\hat{cs},m}}{V_{\hat{ms},m}},
\end{aligned} \tag{2.16}
$$

by using formation volume factor and solubility ratio definitions, Eq. 2.16 yields

$$C_{cm} = \frac{\rho_{\hat{cs}} R_{s,cm}}{\rho_m B_m}. \tag{2.17}$$

Considering Eq. 2.17, the mass fraction of the gas component in the liquid (oil) phase and the mass fraction of the oil component in the liquid phase, respectively, are given by

$$C_{gl} = \frac{\rho_{gs} R_s}{5.615 \, B_o \rho_l}, \tag{2.18}$$

$$C_{ol} = \frac{\rho_{os}}{B_o \rho_l}. \tag{2.19}$$

where

$$C_{gl} + C_{ol} = 1. \tag{2.20}$$

By considering the mass fraction definitions, we can rewrite Eqs. 2.13 and 2.14 as

$$\rho_{gl} = C_{gl} \rho_l, \tag{2.21}$$

and

$$\rho_{ol} = C_{ol}\rho_l.$$ (2.22)

By combining Eqs. 2.18 and 2.19, we can calculate the solution gas-oil ratio as

$$R_s = \left(\frac{C_{gl}}{C_{ol}}\right)\left(\frac{5.615\rho_{os}}{\rho_{gs}}\right).$$ (2.23)

If we denote E_g and E_l as the gas void fraction and liquid holdup, respectively, we have

$$E_g + E_l = 1,$$ (2.24)

The gas-liquid two-phase mixture density is defined as

$$\rho_m = E_g\rho_g + E_l\rho_l.$$ (2.25)

Defining the mass concentration of oil and gas components in the two-phase system by C_l and C_g, respectively, and considering material balance, we obtain

$$C_g = \frac{E_l\rho_{gl} + E_g\rho_g}{\rho_m}.$$ (2.26)

$$C_l = \frac{E_l\rho_{ol}}{\rho_m},$$ (2.27)

where

$$C_l + C_g = 1.$$ (2.28)

The total gas-oil ratio in a two-phase system, R, is defined as the ratio of the volume of the total gas component in $[scf]$, to the volume of the total oil component in $[STB]$. By considering the definitions of C_l and C_g, we have

$$R = \left(\frac{C_g}{C_l}\right)\left(\frac{5.615\rho_{os}}{\rho_{gs}}\right).$$ (2.29)

Values of R from Eq. 2.29 are used to compute the bubble-point pressure at each location along the wellbore. Using Eqs. 2.11 to 2.14, 2.23, 2.26 and 2.27 it can be shown that Eq. 2.29 is equivalent to

$$R = R_s + \left(\frac{B_o}{B_g}\right)\left(\frac{1 - E_l}{E_l}\right). \tag{2.30}$$

We can rearrange the preceding equation to compute liquid holdup as

$$E_l = \frac{B_o}{B_o + B_g(R - R_s)}. \tag{2.31}$$

In the multiphase flow literature, superficial gas velocity, v_{sg}, and superficial liquid velocity, v_{sl}, are defined respectively as

$$v_{sg} = \frac{q_g}{A}, \tag{2.32}$$

and

$$v_{sl} = \frac{q_l}{A}, \tag{2.33}$$

where q_g and q_l are the gas and liquid phase volumetric flow rates in $[ft^3/sec]$ and A is the pipe cross sectional area in $[ft^2]$. Correspondingly, the gas and liquid phase true velocities are defined as

$$v_g = \frac{q_g}{AE_g}, \tag{2.34}$$

and

$$v_l = \frac{q_l}{AE_l}, \tag{2.35}$$

where AE_g and AE_l represent the pipe cross sectional area occupied by the gas and liquid phase, respectively. From Eqs. 2.32 through 2.35, we obtain relationships between the superficial velocity and the true velocity as follows:

$$v_{sg} = E_g v_g. \tag{2.36}$$

and

$$v_{sl} = E_l v_l. \tag{2.37}$$

The relative velocity between gas and liquid phase is defined as

$$v_r = v_g - v_l. \tag{2.38}$$

In case of the drift-flux model, the two-phase mixture velocity is defined as the density-averaged superficial velocity, i.e.,

$$v_m = \frac{v_{sg}\rho_g + v_{sl}\rho_l}{\rho_m}. \tag{2.39}$$

Note that we have $v_m = v_g$ when $E_g = 1$. Similarly, we have $v_m = v_l$ when $E_l = 1$. From Eq. 2.25 and Eqs. 2.36 through 2.39, one can easily derive the following relationships between the true velocity and the mixture velocity:

$$v_g = v_m + \frac{E_l\rho_l v_r}{\rho_m}, \tag{2.40}$$

and

$$v_l = v_m - \frac{E_g\rho_g v_r}{\rho_m}, \tag{2.41}$$

Eqs. 2.40 and 2.41 indicate that the flow of each individual phase is a result of relative fluid motion superposed on the mixture velocity. Because of these relationships, the drift-flux model is also referred to as the diffusion model.

2.2 Governing Equations.

Gas-liquid two-phase flow is considered in the wellbore. Because the anomalous pressure buildup behavior is believed to be caused by phase redistribution in the

wellbore, we focus our effort on the analysis of wellbore two-phase flow. The superposition principle can be used to relate the bottomhole pressure with the sandface flow rate, provided that the bottomhole pressure at the instant of shut-in is higher than the initial bubble-point pressure. A reservoir simulator is coupled with the wellbore model so that either single-phase oil flow or two-phase flow in the reservoir can be considered. As discussed later, the reservoir model essentially provides a boundary condition for the wellbore flow. This study is concentrated on the investigation of wellbore transient two-phase flow during pressure drawdown and buildup tests.

Throughout this study, the z-coordinate lies along the wellbore which is assumed to be vertical. In relation to the z-coordinate the upward direction is positive.

2.2.1 Material Balance Equations.

A standard volume balance for the oil and gas components, respectively, can be written as:

$$\frac{\partial}{\partial t}\left[E_l \rho_{ol}\right] + \frac{\partial}{\partial z}\left[E_l \rho_{ol} v_l\right] = 0.$$ (2.42)

and

$$\frac{\partial}{\partial t}\left[E_g \rho_g + E_l \rho_{gl}\right] + \frac{\partial}{\partial z}\left[E_g \rho_g v_g + E_l \rho_{gl} v_l\right] = 0.$$ (2.43)

Substituting Eqs. 2.11, 2.13, 2.14, 2.36, 2.37 in Eqs. 2.42 and 2.43, we have

$$\frac{\partial}{\partial t}\left[\frac{E_l}{B_o}\rho_{os}\right] + \frac{\partial}{\partial z}\left[\frac{v_{sl}}{B_o}\rho_{os}\right] = 0,$$ (2.44)

and

$$\frac{\partial}{\partial t}\left[\frac{E_g}{B_g}\rho_{gs} + \frac{E_l R_s}{B_o}\rho_{gs}\right] + \frac{\partial}{\partial z}\left[\frac{v_{sg}}{B_g}\rho_{gs} + \frac{v_{sl}R_s}{B_o}\rho_{gs}\right] = 0. \tag{2.45}$$

By substituting Eq. 2.14 in Eq. 2.44, we find that

$$\frac{\partial}{\partial t}\left[E_l\rho_{ol}\right] + \frac{\partial}{\partial z}\left[v_{sl}\rho_{ol}\right] = 0. \tag{2.46}$$

Similarly, using Eqs. 2.11 and 2.13 in Eq. 2.45, yields

$$\frac{\partial}{\partial t}\left[E_g\rho_g + E_l\rho_{gl}\right] + \frac{\partial}{\partial z}\left[v_{sg}\rho_g + v_{sl}\rho_{gl}\right] = 0. \tag{2.47}$$

If we consider our drift-flux model formulation, we can rewrite the oil and gas component mass balance equations in terms of v_m and v_r. By using Eqs. 2.36, 2.37, 2.40 and 2.41 in Eqs. 2.46 and 2.47, respectively, we find

$$\frac{\partial}{\partial t}\left[E_l\rho_{ol}\right] + \frac{\partial}{\partial z}\left[E_l\rho_{ol}v_m\right] = \frac{\partial}{\partial z}\left[\frac{\rho_{ol}E_l\rho_g E_g v_r}{\rho_m}\right], \tag{2.48}$$

and

$$\frac{\partial}{\partial t}\left[E_g\rho_g + E_l\rho_{gl}\right] + \frac{\partial}{\partial z}\left[(E_g\rho_g + E_l\rho_{gl})v_m\right] = -\frac{\partial}{\partial z}\left[\frac{\rho_{ol}E_l\rho_g E_g v_r}{\rho_m}\right]. \tag{2.49}$$

By using Eqs. 2.26 and 2.27, Eqs. 2.48 and 2.49 can be written in terms of component concentrations as follows:

$$\frac{\partial}{\partial t}\left[C_l\rho_m\right] + \frac{\partial}{\partial z}\left[C_l\rho_m v_m\right] = \frac{\partial D_r}{\partial z}. \tag{2.50}$$

and

$$\frac{\partial}{\partial t}\left[C_g\rho_m\right] + \frac{\partial}{\partial z}\left[C_g\rho_m v_m\right] = -\frac{\partial D_r}{\partial z}. \tag{2.51}$$

where the parameter D_r represents diffusion caused by relative motion and is defined by

$$D_r = C_l\rho_g E_g v_r. \tag{2.52}$$

Summation of Eqs. 2.50 and 2.51 results in the following overall mass balance equation for the flow system:

$$\frac{\partial}{\partial t}[\rho_m] + \frac{\partial}{\partial z}[\rho_m v_m] = 0. \tag{2.53}$$

Eqs. 2.50, 2.51 and 2.53 are the three basic mass balance equations. In principle, any two of these equations can be used. In this study, we choose to use Eqs. 2.50 and 2.53, i.e., the oil component mass balance equation and the overall mass balance equation.

2.2.2 Momentum Equation.

Phase segregation after the well is shut-in is a slow and gravity dominated process. Here, however, we consider a full momentum equation. For vertical flow, the gas and liquid momentum equations in any consistent set of units, respectively, are given by Eq. A.56 (see Appendix A) as follows

$$\frac{\partial}{\partial t}[E_g \rho_g v_g] + \frac{\partial}{\partial z}\left[E_g \rho_g v_g^2\right] + \Gamma_{gl} v_{gi} = -E_g \frac{\partial}{\partial z}[p_g] + (p_{gi} - p_g)\frac{\partial}{\partial z}[E_g]$$
$$-E_g \rho_g g - \tau_{gw}\frac{S_g^w}{A} + \tau_{gi}\frac{S_g^i}{A}, \tag{2.54}$$

$$\frac{\partial}{\partial t}[E_l \rho_l v_l] + \frac{\partial}{\partial z}\left[E_l \rho_l v_l^2\right] + \Gamma_{lg} v_{li} = -E_l \frac{\partial}{\partial z}[p_l] + (p_{li} - p_l)\frac{\partial}{\partial z}[E_l]$$
$$-E_l \rho_l g - \tau_{lw}\frac{S_g^w}{A} - \tau_{li}\frac{S_l^i}{A}. \tag{2.55}$$

where Γ_{lg} and Γ_{gl} are the mass sources of the phases generated per unit volume of the pipe. v_{li} and v_{gi} are the phase velocities at the gas liquid interface. p_{li} and p_{gi} are the phase pressures at the gas liquid interface and τ_{li} and τ_{gi} are the interfacial shear forces.

Since $\Gamma_{lg} = -\Gamma_{gl}$, summing the two momentum equations, Eqs. 2.54 and 2.55, we obtain the following combined momentum equation for the gas-liquid mixture:

$$\frac{\partial}{\partial t}\left[E_g\rho_g v_g + E_l\rho_l v_l\right] + \frac{\partial}{\partial z}\left[E_g\rho_g v_g^2 + E_l\rho_l v_l^2\right] + \Gamma_{gl}\left(v_{gi} - v_{li}\right) =$$

$$-E_g\frac{\partial}{\partial z}\left[p_g\right] - E_l\frac{\partial}{\partial z}\left[p_l\right] + \left(p_{gi} - p_{li}\right)\frac{\partial}{\partial z}\left[E_g\right]$$

$$+ \left(p_l - p_g\right)\frac{\partial}{\partial z}\left[E_g\right] - \left[E_g\rho_g + E_g\rho_g\right]g$$

$$- \left[\tau_{lw}\frac{S_l^w}{A} + \tau_{gw}\frac{S_g^w}{A}\right] + \left[\tau_{gi}\frac{S_g^i}{A} - \tau_{li}\frac{S_l^i}{A}\right]. \tag{2.56}$$

From Yadigaraglu[27] the following interfacial transfer condition holds:

$$\tau_{gi}\frac{S_g^i}{A} - \tau_{li}\frac{S_l^i}{A} - \Gamma_{ml}\left[v_{gi} - v_{li}\right] + \left(p_{gi} - p_{li}\right)\frac{\partial}{\partial z}\left[E_g\right] = -2\sigma H\frac{\partial}{\partial z}\left[E_g\right], \tag{2.57}$$

where σ is the surface tension and H is the mean curvature of the interface.

In the drift flux model, we apply the two-phase mixture momentum equation and a constitutive relation for the relative velocity. In order to simplify our mixture momentum, the following assumptions for the conditions at the interface are applied:

a) the gas and liquid phase pressures are equal. i.e., $p_{gi} \approx p_{li}$,

b) the surface tension can be neglected.

Using Eqs. 2.39, 2.40, 2.41 and 2.53, and considering the preceding assumptions, it can be shown that mixture momentum equation converted to field units is equivalent to

$$\frac{\rho_m}{144g_c}\frac{\partial}{\partial t}\left[v_m\right] + \frac{\rho_m v_m}{144g_c}\frac{\partial}{\partial z}\left[v_m\right] + \frac{\partial}{\partial z}\left[\frac{(1-E_l)\rho_g E_l\rho_l v_r^2}{144g_c\rho_m}\right] + \frac{\partial p}{\partial z} + \frac{\rho_m g}{144g_c} + \tau_w = 0. \tag{2.58}$$

where $\tau_w = \left(\tau_{wl}S_l^w\right)/A + \left(\tau_{wg}S_g^w\right)/A$, represents the pressure losses due to wall shear stress. Allison et al.[28] used the Lockhart-Martinelli[29] method to develop correlations

for the two-phase friction factors which depend on the flow regimes. However, their correlations are reasonably well approximated by the Colebrook-White[30] correlation based on mixture properties. In our case, we are using a drift-flux model which considers slippage but assumes that the fluids are well-mixed, (i.e., a homogeneous model) in the part of the wellbore where two phases coexist, thus we consider it appropriate to base our correlation for the pressure losses due to shear stress on the mixture density and velocity.

Under the preceding assumption, τ_w is given by

$$\tau_w = \frac{f_m \rho_m |v_m| v_m}{(144 g_c) 2d}.$$ (2.59)

where f_m is defined from the Colebrook-White correlation:

$$\frac{1}{\sqrt{f_m}} = 1.74 - 2 \log \left[\frac{2\epsilon}{d} - \frac{18.7}{R_{em} \sqrt{f_m}} \right].$$ (2.60)

Eq. 2.60 is nonlinear, but can be solved easily by Newton's method using as the initial guess the explicit expression given by Zigrang and Sylvester[31]:

$$\frac{1}{\sqrt{f_m}} = -2 \log \left[\frac{\epsilon/d}{3.7} - \frac{5.02}{R_{em}} \log \left(\frac{\epsilon/d}{3.7} + \frac{13.0}{R_{em}} \right) \right].$$ (2.61)

In Eqs. 2.60 and 2.61, R_{em} is the Reynolds number, which, in field units, is given by

$$R_{em} = \frac{1488 \rho_m v_m d}{\mu_m}.$$ (2.62)

In Eqs. 2.60, 2.61 and 2.62, the mixture density is defined by Eq. 2.25 and the mixture viscosity is calculated from

$$\mu_m = \mu_l E_l + \mu_g (1 - E_l).$$ (2.63)

Eqs. 2.50, 2.53 and 2.58 are the three fundamental equations describing transient flow of a gas-liquid mixture in the wellbore. The three primary dependent variables are the oil component concentration, C_l, the mixture velocity, v_m, and the pressure, p. Once the concentration distribution is determined, the total gas-oil ratio, R, can be calculated from Eq. 2.29. Consequently, with known values of R and the pressure distribution, liquid holdup can be obtained through Eq. 2.31.

2.2.3 Energy Equation and Heat Transfer in Wells.

As the reservoir fluids flow through the wellbore, they lose heat to the surrounding rock. In this work, we consider convective heat loss between the flowing fluids and the pipe wall, conductive heat losses through the pipes walls (tubing and casing) and through any insulation or coating material and convective heat losses between the fluid in the annular space and the tubing and casing walls. Additionally, heat losses due to radiation can be considered and may be important for steam injection or geothermal wells.

Fourier's law for radial heat flow by conduction is given by

$$q = -k_h \, A \frac{\partial T}{\partial r} = -2\pi \, r \, \Delta z \, k_h \frac{\partial T}{\partial r}, \qquad (2.64)$$

Integrating Eq. 2.64 from r_i to r_{i+1} and rearranging the resulting equation gives

$$q = 2\,\pi\,k_h\,\Delta z\,\frac{(T_i - T_{i+1})}{\ln\,(r_{i+1}/r_i)}. \qquad (2.65)$$

where k_h is the thermal conductivity of the medium in $[BTU/hr - ft -^\circ F]$. q is the rate of heat flow in $[BTU/hr]$, T is the temperature in $[^\circ F]$. Δz is the gridblock size in $[ft]$.

Eq. 2.65 can be applied to predict the heat loss through the tubing, the casing, the pipe insulation and the cement. For example, when computing the heat loss through the tubing with Eq. 2.65, r_i and r_{i+1}, respectively, represent the inner and outer radii of the tubing and T_i and T_{i+1}, respectively, represent the temperature at the inner and outer surfaces of the tubing. When introducing temperature effects into our wellbore simulator, Δz will be the gridspacing in the z direction and Eq. 2.64 will be applied on each gridblock.

For heat convection, Newton's law of cooling is given by

$$q = h_f A \Delta T, \quad \tag{2.66}$$

where h_f is the convective heat transfer coefficient in $[BTU/hr - ft^2 -^\circ F]$. In the case of radial heat flux, Eq. 2.66 becomes

$$q = 2\pi r_i \, h_f \, \Delta z \, (T_i - T_{i+1}). \tag{2.67}$$

We apply Eq. 2.67 in each z-direction gridblock to predict the rate of convective heat flow between the fluid in the tubing and the tubing wall; in this case, r_i will be the inner radius of the tubing, so

$$q = 2\pi r_{ti} \, h_f \, \Delta z \, (T_f - T_{ti}). \tag{2.68}$$

When Eq. 2.67 is used to predict the heat loss due to convection in the annulus, we have

$$q = 2\pi r_{to} \, h_{ann} \, \Delta z \, (T_{to} - T_{ci}). \tag{2.69}$$

or in case of an insulated tubing,

$$q = 2\pi r_{ins} \, h_{ann} \, \Delta z \, (T_{ins} - T_{ci}). \tag{2.70}$$

where h_{ann} is the convective heat transfer coefficient of the annulus fluid in $[BTU/hr - ft^2 -° F]$, r_{ti} is tubing internal radius in $[ft]$, r_{to} is the tubing external radius in $[ft]$, r_{ins} is outer radius of the insulation in $[ft]$.

In the case of radiation heat losses, we can write our heat loss equation as

$$q = 2\pi r_i \, h_r \, \Delta z \, (T_i - T_{i+1}),$$ (2.71)

where h_r is the radiation heat transfer coefficient in $[BTU/hr - ft^2 -° F]$. Conduction, natural convection and radiation are important heat transfer mechanisms for the annulus. In practice, a heat transfer coefficient h_{ann} can be used to consider the combined effect of conduction and natural convection. The radiation heat losses are important when the annulus is filled with gas but will not be considered here. Applying Eq. 2.71 for our annulus space gives:

$$q = 2\pi \, r_{ins} \, h_r \, \Delta z \, (T_{ins} - T_{ci}).$$ (2.72)

Combining Eq. 2.70 and 2.72 gives

$$q = 2\pi \, r_{ins} \, (h_{ann} + h_r) \, \Delta z \, (T_{ins} - T_{ci}).$$ (2.73)

We assume the well configuration as shown in Fig. 2.1 and assume steady-state heat flow, i.e., at each z location and at each time, the heat flow is constant for $0 < r < r_w$, where r_w is the outer radius of the cement. Then, since we have steady-state heat flow across the tubing, annulus, casing, etc., we can write:

$$
\begin{aligned}
q &= \frac{(T_f - T_{ti})}{1/(2\pi\, r_{ti} h_f\, \Delta z)} = \frac{(T_{ti} - T_{to})}{\ln(r_{to}/r_{ti})/(2\pi\, k_s \Delta z)} = \frac{(T_{to} - T_{ins})}{\ln(r_{ins}/r_{ti})/(2\pi\, k_{ins}\Delta z)} \\
&= \frac{(T_{ins} - T_{ci})}{1/[2\pi\, r_{ins}\, \Delta z(\,h_{ann} + h_r\,)]} = \frac{(T_{ci} - T_{co})}{\ln(r_{co}/r_{ci})/(2\pi\, k_s\Delta z)} \\
&= \frac{(T_{co} - T_w)}{\ln(r_w/r_{co})/(2\pi\, k_{cem}\Delta z)},
\end{aligned}
$$ (2.74)
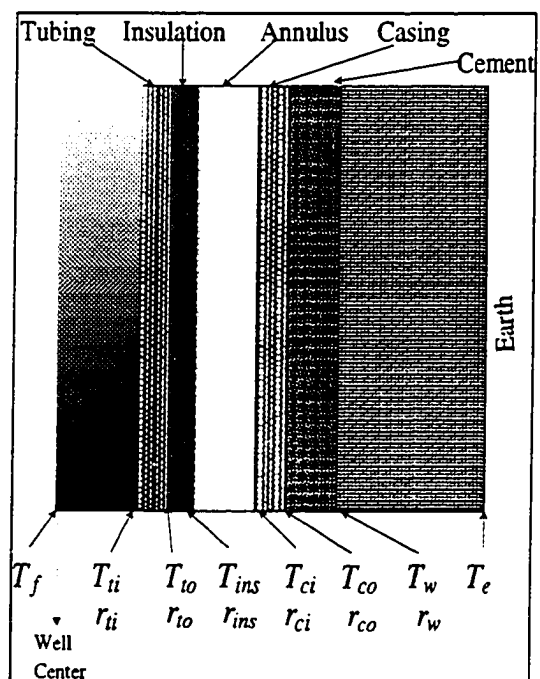
Figure 2.1: Typical Well Configuration

which can be rearranged to obtain

$$T_f - T_w = \frac{q}{2\pi \Delta z} \left[\frac{1}{r_{ti} h_f} + \frac{\ln(r_{to}/r_{ti})}{k_s} + \frac{\ln(r_{ins}/r_{ti})}{k_{ins}} + \frac{1}{r_{ins}(h_{ann} + h_r)} \right.$$
$$\left. + \frac{\ln(r_{co}/r_{ci})}{k_s} + \frac{\ln(r_w/r_{co})}{k_{cem}} \right] . \tag{2.75}$$

In Eq. 2.75, k_s is the thermal conductivity of the steel, k_{cem} is the thermal conductivity of the cement, and k_{ins} is the thermal conductivity of the insulation.

If we define a overall heat transfer coefficient as

$$U_o^{-1} = \frac{1}{r_{ti} h_f} + \frac{\ln(r_{to}/r_{ti})}{k_s} + \frac{\ln(r_{ins}/r_{ti})}{k_{ins}} + \frac{1}{r_{ins}(h_{ann} + h_r)} + \frac{\ln(r_{co}/r_{ci})}{k_s} + \frac{\ln(r_w/r_{co})}{k_{cem}},$$
$$\tag{2.76}$$

with units $[BTU/hr - ft -^\circ F]$, Eq. 2.75 can be rewritten as

$$q = 2\pi U_o \Delta z (T_f - T_w) . \tag{2.77}$$

2.2.3.a   Formation Temperature.

Assuming heat flow is only in the radial direction, an energy balance on the formation gives

$$\frac{1}{r} \frac{\partial}{\partial r} \left(r \frac{\partial T}{\partial r} \right) = \frac{c_{pe} \rho_e}{k_e} \frac{\partial T}{\partial t} = \frac{1}{\alpha_e} \frac{\partial T}{\partial t}, \tag{2.78}$$

where c_{pe} is the earth's heat capacity, ρ_e is the earth's density, k_e is the earth's thermal conductivity and α_e is the earth's thermal diffusivity, i.e., $\alpha_e = k_e/(c_{pe} \rho_e)$. To complete the specification of our initial-boundary-value problem (IBVP), we define the following conditions:

Initial Condition:

$$T(r, t = 0) = T_e. \tag{2.79}$$

Inner Boundary Condition:

$$q = -2\pi r_w \, k_e \Delta z \left(\frac{\partial T}{\partial r}\right)_{r_w}.$$

(2.80)

Outer Boundary Condition:

$$\lim_{r \to \infty} T(r,t) = T_e.$$

(2.81)

In order to generalize our solution, we recast our IBVP (Eq. 2.78-2.81) in terms of the following dimensionless variables:

Dimensionless radius, r_D:

$$r_D = \frac{r}{r_w},$$

(2.82)

Dimensionless time, t_D :

$$t_D = \frac{\alpha_e t}{r_w^2},$$

(2.83)

Dimensionless temperature drop, T_D :

$$T_D = \frac{(T - T_e)}{\dfrac{q}{2\pi k_e \Delta z}}.$$

(2.84)

Using the above dimensionless variables, we have our dimensionless IBVP as

$$\frac{1}{r_D}\frac{\partial}{\partial r_D}\left(r_D \frac{\partial T_D}{\partial r_D}\right) = \frac{\partial T_D}{\partial t_D}.$$

(2.85)

$$T_D(r_D, 0) = 0.$$

(2.86)

$$r_D \frac{\partial T_D}{\partial r_D}\Big|_{r_D=1} = -1,$$

(2.87)

and

$$\lim_{r_D \to \infty} T_D\left(r_D, t_D\right) = 0. \tag{2.88}$$

The IBVP has the following Laplace space solution

$$\overline{T}_D = \frac{K_o\left(r_D\sqrt{u}\right)}{u^{3/2}K_1\left(r_D\sqrt{u}\right)}, \tag{2.89}$$

where $\overline{T}_D$ is the Laplace transform of T_D with respect to t_D and u is the Laplace variable.

Evaluating Eq. 2.89 at $r_D = 1$, we obtain our wellbore solution as

$$\overline{T}_{wD} = \frac{K_o\left(\sqrt{u}\right)}{u^{3/2}K_1\left(\sqrt{u}\right)}. \tag{2.90}$$

At long times, $(t_D > 25)$, the dimensionless wellbore temperature drop can be closely approximated by a semilog equation, i.e.,

$$T_{wD} = \frac{1}{2}\left[\ln t_D + 0.80907\right]. \tag{2.91}$$

This approximation for $t_D > 25$ was proposed by Ramey[32], who used a line source solution for T_D.

Following Ramey's work, we let $f(t) = T_{wD}$. Then rearranging Eq. 2.84, we find

$$q = 2\pi k_e \Delta z \frac{\left(T_w - T_e\right)}{f\left(t\right)}. \tag{2.92}$$

2.2.3.b Coupling Wellbore and Reservoir Heat Transfer Solutions.

By equating Eq. 2.77 with Eq. 2.92, and simplifying we find

$$q = 2\pi U_o k_e \Delta z \frac{\left(T_f - T_e\right)}{\left(U_o f\left(t\right) + k_e\right)}. \tag{2.93}$$

We define the final combined heat transfer coefficient U as

$$U \cong \frac{1}{r_{to}} \left[\frac{1}{U_o} + \frac{f(t)}{k_e} \right]^{-1},$$ (2.94)

with field units $[BTU/hr -^\circ F]$. With this notation, Eq. 2.93 can be written as

$$q = 2\pi r_{to} U \, \Delta z \, (T_f - T_e) = U \, A_{po} \, (T_f - T_e),$$ (2.95)

where $A_{po} = 2\pi r_{to} \Delta z$. or equivalently,

$$\hat{q} = U \, (T_f - T_e).$$ (2.96)

where $\hat{q} = q/2\pi r_{to}\Delta z$ is the heat flux, i.e., heat flow per unit area, $[BTU/hr - ft^2]$.

2.2.3.c A Unified Model for Predicting Flowing Temperature Distribution in the Wellbore.

In this section we use the approach of Alves et al.[33] to predict the fluid temperature distribution in the wellbore under steady-state conditions.

The steady-state continuity, momentum, and energy balances, in the wellbore can be written as

$$\frac{d}{dz} (\rho v) = 0,$$ (2.97)

$$\frac{d}{dz} \left(\rho v^2 \right) = -\frac{dp}{dz} - \rho g \sin \theta - \frac{\tau \pi d}{A_p},$$ (2.98)

$$\frac{d}{dz} \left[\rho \left(e + \frac{1}{2} v^2 \right) \right] = -\frac{d}{dz} (pv) - \rho v g \sin \theta - \frac{\hat{q} \pi d}{A_p},$$ (2.99)

respectively. In Eq. 2.99. e is internal energy per unit of mass, v is the fluid velocity. p is pressure, τ is the shear stress at the pipe wall. ρ is the fluid density and θ is the

inclination angle with respect to the horizontal plane. Note that $\hat{q}$ is the heat flux from the fluid to the earth as defined by Eq. 2.96.

Using the continuity equation, Eq. 2.97, we can write Eqs. 2.98 and 2.99, respectively as

$$\frac{dp}{dz} = -\rho v \frac{dv}{dz} - \rho g \sin\theta - \frac{\tau \pi d}{A_p},$$

(2.100)

and

$$\rho v \frac{d}{dz}\left(e + \frac{1}{2}v^2\right) = -\rho v v \frac{dv}{dz} - \rho v g \sin\theta - \frac{\hat{q}\pi d}{A_p},$$

(2.101)

Eq. 2.101 is equivalent to

$$\frac{dh}{dz} = -v\frac{dv}{dz} - g\sin\theta - \frac{\hat{q}\pi d}{W}.$$

(2.102)

Combining Eqs. 2.102 and 2.96 yields

$$\frac{dh}{dz} = -v\frac{dv}{dz} - g\sin\theta - \frac{U\pi d}{W}(T - T_e).$$

(2.103)

By using thermodynamics definitions, we can write the wellbore enthalpy gradient as

$$\frac{dh}{dz} = c_p\frac{dT}{dz} - \eta\, c_p\frac{dp}{dz}.$$

(2.104)

where h is enthalpy, c_p is the heat capacity at constant pressure, and η is the Joule-Thompson coefficient.

Combining Eqs. 2.103 and 2.104, we find that

$$\frac{dT}{dz} + \frac{U\pi d}{W c_p}T = \frac{U\pi d}{W c_p}T_e + \frac{1}{c_p}\left(\eta\, c_p\frac{dp}{dz} - g\sin\theta - v\frac{dv}{dz}\right).$$

(2.105)

where W is the mass flow rate. Ramey[32] defined the relaxation distance, A, as

$$A = \frac{W\, c_p}{U \pi d}.$$ (2.106)

Defining a dimensionless parameter, Φ, as

$$\Phi = \left(\rho\eta\, c_p \frac{dp}{dz} - \rho g \sin\theta - \rho v \frac{dv}{dz} \right) \Big/ \frac{dp}{dz}.$$ (2.107)

and using Eq. 2.106, we can rewrite Eq. 2.105 as

$$\frac{dT}{dz} + \frac{1}{A}T = \frac{1}{A}T_e + \frac{1}{c_p\,\rho}\frac{dp}{dz}\Phi.$$ (2.108)

We assume that the surrounding temperature is a linear function of depth

$$T_e = T_{ei} - g_e\, L \sin\theta.$$ (2.109)

where g_e is the geothermal gradient in $[^\circ F/100\,ft]$, θ is the inclination angle with respect to horizontal, and L is depth in the z-direction in $[100\,ft]$.

By substituting Eq. 2.109 into Eq. 2.108, we find

$$\frac{dT}{dz} + \frac{1}{A}T = \frac{1}{A}T_{ei} - \frac{1}{A}\,L\sin\theta + \frac{1}{c_p\rho}\frac{dp}{dz}\Phi.$$ (2.110)

Eq. 2.110 can be solved for a given pipe segment to obtain

$$T_f = (T_{ei} - g_e L \sin\theta) + (T_{bh} - T_{ei})\exp(-L/A)$$ (2.111)

$$+ g_e\, A \sin\theta\,[1 - \exp(-L/A)] + \frac{1}{\rho\, c_p}\frac{dp}{dz}\Phi A\,[1 - \exp(-L/A)].$$

As discussed in Ref. 33, for an ideal gas, $\eta = 0$. Neglecting the acceleration term Eq. 2.111 becomes identical to Ramey's expression for ideal gas. For an incompressible liquid, $\eta = -1/\rho\, c_p$ and if the frictional losses are not considered, Eq. 2.111 becomes Ramey's expression for an incompressible liquid.

From thermodynamics definitions and considering two-phase flow of a real gas and an incompressible liquid, the mixture heat capacity is defined as

$$\bar{c}_p = \frac{W_g\, c_{pg} + W_l\, c_{pl}}{W}.$$
(2.112)

where $\bar{c}_p$ is the two-phase heat capacity at constant pressure in $[BTU/lbm -^\circ F]$, c_{pg} is the gas phase heat capacity at constant pressure in $[BTU/lbm -^\circ F]$, c_{pl} is the liquid phase heat capacity at constant pressure in $[BTU/lbm -^\circ F]$, W is total mass flow rate in $[lb_m/sec]$, W_g is gas mass flow rate in $[lb_m/sec]$ and W_l is liquid mass flow rate in $[lb_m/sec]$.

The average Joule-Thomson coefficient in field units $[^\circ F - ft^3/BTU]$ is given by

$$\bar{\eta} = -\frac{1}{\bar{c}_p W} \left\{ \frac{W_g}{\rho_g} \left[-\frac{T_f}{Z} \left(\frac{\partial Z}{\partial T_f} \right)_p \right] + \frac{W_l}{\rho_l} \right\}.$$
(2.113)

where Z is the gas compressibility factor.

It can be shown that Eq. 2.111 for two-phase flow, converted to field units, is equivalent to

$$T_f = (T_{ei} - g_e L \sin \theta) + (T_{bh} - T_{ei}) \exp(-L/A)$$

$$+ g_e A \sin \theta \left[1 - \exp(-L/A) \right] + \frac{144}{\rho_m \bar{c}_p} \frac{dp}{dz} \frac{\Phi A}{J} \left[1 - \exp(-L/A) \right].$$
(2.114)

where J is equal to $778.2\,(ft - lb_f/BTU)$ and T_f is temperature of the flowing fluids.

The relaxation distance A in field units is equal to

$$A = \left(\frac{3600}{2\pi} \right) W \bar{c}_p \left(\frac{1}{U_o} + \frac{f(t)}{k_e} \right) = \frac{3600\, W\, \bar{c}_p}{\pi\, d\, U}.$$
(2.115)

where A is in $[ft]$, W is in $[lbm/\sec]$, $\bar{c}_p$ is in $[BTU/lbm -^\circ F]$, U is in $[BTU/hr - ft^2 -^\circ F]$, and k_e is in $[BTU/hr - ft -^\circ F]$.

It is important to note that the total solution expressed by Eq. 2.114 reduces to single-phase solution so it can be safely applied to our process of phase segregation. The total solution that this equation represents consist of three main parts: an overall heat transfer computation for the flowing fluids, a heat flux computation through all the well components (pipes, insulation, annular fluids, cement, etc.) and a transient heat conduction to the earth. This overall combination of solutions is able to give us a well defined rate normalized approximation of the wellbore heat losses. Eq. 2.114 is applied for each gridblock in the wellbore at each time step of the simulation process.

2.2.3.d Estimating Convective Heat Transfer Coefficient (h_f).

Turbulent Flow. Correlating equations that reproduce experimentally or analytically obtained estimates of the heat transfer coefficient and the Nusselt number have been used in the oil industry for several years. The Nusselt number, N_{nu}, is defined as the ratio of the convective conductance h_f to the pure molecular thermal conductance k/d, i.e.,

$$N_{nu} = \frac{h_f}{k_f/d}. \tag{2.116}$$

The Prandtl number, N_{pr}, is defined as the ratio of momentum diffusivity to thermal diffusivity of the fluid

$$N_{pr} = \frac{\nu}{\alpha} = 2.492 \frac{\mu_f c_p}{k_f}. \tag{2.117}$$

where μ_f is the fluid viscosity in $[cp]$.

In Ref. 34, the expression developed by Sleicher and Rouse[35] is recommended for the Nusselt number provided the pipe is smooth, $10^4 < N_{re} < 10^6$, $0.1 < N_{pr} <$

10^5. The relevant expression is

$$N_{nu} = 5 + 0.015 N_{re}^a N_{pr}^b, \qquad (2.118)$$

where

$$a = 0.88 - \frac{0.24}{4 + N_{pr}}. \qquad (2.119)$$

and

$$b = \frac{1}{3} + 0.5 \exp\left(-0.6\, N_{pr}\right), \qquad (2.120)$$

This correlation is useful for both liquids and gases (see Ref. 34).

The effect of the pipe roughness on the heat-transfer coefficient is usually less than its effect on the friction factor in case the of head losses (pressure losses). The Reynolds analogy, which suggests that the heat transfer coefficient, h, is proportional to friction factor, f, is predicated on shear providing flow resistance, but this is not the case when roughness elements protrude above the laminar sublayer. Under this circumstance, the departure from Reynolds' analogy can be expressed by defining an effectiveness parameter $\tilde{\xi}$ as[36]

$$\tilde{\xi} = \frac{(N_{nu}/f_r)_r}{(N_{nu}/f_s)_s} = \log_{10}\left[\frac{N_{pr}^{0.33}}{\varphi_{re}^{0.243}}\right] - 0.32 \times 10^{-3}\varphi_{re}\,\log_{10}\left(N_{pr}\right) + 1.25, \qquad (2.121)$$

where

$$\varphi_{re} = N_{re}\left(\frac{\epsilon}{d}\right)\left(\frac{f_r}{8}\right)^{1/2}. \qquad (2.122)$$

f_s is the friction factor for smooth pipes, f_r is the friction factor for rough pipes. ϵ is the pipe roughness in $[ft]$, d is the pipe diameter in $[ft]$.

Laminar Flow. A satisfactory expression for heat transfer rates in laminar flow is given by an empirical modification of the Graetz problem[37], developed by Sieder and

Tate[38] including the correction proposed by Sellars et al.[39] for the constant heat flux case. The Nusselt number is given by.

$$N_{nu} = 2.232\, N_{re}^{1/3}\, N_{pr}^{1/3}(L/d)^{-1/3}, \tag{2.123}$$

where L is the pipe length in $[ft]$. Another expression that produces reasonable results was proposed by Hausen[10] and is given by

$$N_{nu} = 4.392 + \frac{0.0894\, \Psi^3}{1 + 0.04\Psi^2}, \tag{2.124}$$

where $\Psi = N_{re}^{1/3}\, N_{pr}^{1/3}(L/d)^{-1/3}$. To avoid numerical oscillations, it is assumed that laminar flow exists for $N_{re} < 2000$, turbulent flow for $N_{re} > 2500$, and transition flow between $2000 < N_{re} < 2500$. The Nusselt number in the transition zone is calculated by linear interpolation between the values obtained from Eqs. 2.118 and 2.124.

The value of the convection coefficient (h_f) is obtained from the Nusselt number definition as

$$h_a = \frac{k_f\, N_{nu}}{d_{ti}}, \tag{2.125}$$

with units $[Btu/hr - ft^2 -^\circ F]$; here d_{ti} is the pipe diameter in $[ft]$.

According to Ref. 41 the correlations defined by Eqs. 2.118 and 2.124 give reasonable results for gases and liquids. This being the case, we apply to the two-phase flow, by using mixture properties to compute the Reynolds, Prandtl and Nusselt numbers[33].

2.2.3.e Estimating Natural Convection (h_{ann}).

The literature indicated that the estimation of the natural convection coefficients is difficult. Dropkin and Sommerscales[42,43] performed vertical plates studies to estimate the annular heat transfer coefficient for natural convection (h_{ann}). By assuming that for vertical concentric cylinders the effect of curvature can be neglected, we can write

$$N_{nu} = 0.049 \, (N_{gr}N_{pr})^{1/3} \, N_{pr}^{0.074},$$
(2.126)

where N_{gr} is the Grashof number, defined in field units as

$$N_{gr} = 8913.0704 \times 10^3 \, (d_{ci} - d_{ins})^3 \, \frac{\rho_{ann}^2 \, \beta \, (T_{ins} - T_{ci})}{\mu_{ann}^2}.$$
(2.127)

In Eq. 2.127, ρ_{ann} is the density of the annular space fluid in $[lb_m/ft^3]$, μ_{ann} is the viscosity of the annular space fluid in $[cp]$, and β is the thermal volumetric expansion coefficient of the annular space fluid in $[1/°F]$. The Prandtl number is calculated as

$$N_{pr} = 2.492 \frac{c_{pann} \, \mu_{ann}}{k_{ann}}.$$
(2.128)

Eq. 2.127 is valid for $5 \times 10^4 < N_{gr}N_{pr} < 7.17 \times 10^8$, and was developed for liquids, but also gives satisfactory results for gases[42,43]. Another correlation was proposed by Evans and Stefany in Ref. 45 for a cylindrical annulus formed by two long vertical concentric cylinders. i.e..

$$N_{nu} = \left[\, 1, \quad 0.603 \, C_1 \frac{(N_{gr}N_{pr})^{1/4} \ln(d_{ci}/d_{ins})}{\left[(e/d_{ins})^{3/5} + (e/d_{ci})^{3/5}\right]^{5/4}} \, \right]_{max},$$
(2.129)

where $e = (d_{ci}/d_{inst})/2$, and C_1 is obtained by using the following equation:

$$C_1 = \exp[\quad -0.63412 + 0.09606 \times \ln{(N_{pr})}$$

$$-0.013472 \times \ln{(N_{pr})}^2 + 0.00063 \times \log{(N_{pr})}^3]. \qquad (2.130)$$

In our model, we use Eq. 2.129 since this correlation was developed for an annulus between to two cylindrical pipes.

From the definition of Nusselt number, the heat transfer coefficient can be computed as

$$h_{ann} = \frac{2\,k_{ann}\,N_{nu}}{d_{ins}\ln\left(\dfrac{d_{ci}}{d_{ins}}\right)}, \qquad (2.131)$$

with units $[Btu/hr - ft^2 - ^\circ F]$. It is important to note that for Grashof numbers below 2000, the heat transfer is essentially all conduction, so that $N_{nu} = 1$, and for this region we have

$$h_{ann} = \frac{2\,k_{ann}}{d_{ins}\ln\left(\dfrac{d_{ci}}{d_{ins}}\right)}. \qquad (2.132)$$

Correlations for liquids that also give reasonable results for gases[12, 13] are applied to two-phase flow by using mixture properties to compute the Reynolds. Prandtl. Nusselt and Grashof numbers[33].

2.2.3.f   Procedure for Calculating Fluid Temperature.

The following procedure is applied for each wellbore gridblock to compute the temperature profile. This procedure can be considered as one additional step in our

multistep numerical solution procedure that is described in the next chapter.

1. By assuming that conduction is the dominant heat transfer mechanism in the annulus space, we estimate U_{to} with the following equation:

$$U_{to} = \frac{1}{r_{to}} \left[\frac{\ln(r_{to}/r_{ti})}{k_s} + \frac{\ln(r_{ci}/r_{to})}{k_{ann}} + \frac{\ln(r_{co}/r_{ci})}{k_s} + \frac{\ln(r_w/r_{co})}{k_{cem}} \right]^{-1}. \quad (2.133)$$

2. Calculate t_D and compute the dimensionless time function, $f(t) = T_{wD}$ using Eq. 2.90, i.e.,

$$\overline{T}_{wD} = \frac{K_o(\sqrt{u})}{u^{3/2}K_1(\sqrt{u})}. \quad (2.90)$$

3. Compute Φ, $\overline{c}_p$, $\overline{\eta}$, A using Eqs. 2.107, 2.112, 2.113 and 2.115 respectively, i.e.,

$$\Phi = \left(\rho_m \overline{\eta}\, \overline{c}_p \frac{dp}{dz} - \rho_m g \sin\theta - \rho_m v_m \frac{dv_w}{dz} \right) \bigg/ \frac{dp}{dz}, \quad (2.107)$$

$$\overline{c}_p = \frac{W_g\, c_{pg} + W_l\, c_{pl}}{W}, \quad (2.112)$$

$$\overline{\eta} = -\frac{1}{\overline{c}_p W} \left\{ \frac{W_g}{\rho_g} \left[-\frac{T_f}{Z} \left(\frac{\partial Z}{\partial T_f} \right)_p \right] + \frac{W_l}{\rho_l} \right\}. \quad (2.113)$$

$$A = \left(\frac{3600}{2\pi} \right) W \overline{c}_p \left(\frac{1}{U_{to}} + \frac{f(t)}{k_e} \right). \quad (2.115)$$

4. Estimate a value of T_f, using Eq. 2.114, i.e..

$$T_f = (T_{ei} - g_e L \sin\theta) + (T_{bh} - T_{ei}) \exp(-L/A)$$

$$+ g_e A \sin\theta\, [1 - \exp(-L/A)] + \frac{144}{\rho_m \overline{c}_p} \frac{dp}{dz} \frac{\Phi A}{J} [1 - \exp(-L/A)]. \quad (2.114)$$

5. Calculate the cement-formation interface temperature as

$$T_w = \frac{r_{to} U_{to}\, f(t)\, T_f + k_e T_e}{r_{to}\, U_{to}\, f(t) + k_e}. \quad (2.134)$$

6. Calculate the heat transfer as

$$q = 2\pi r_{to} U_{to} \Delta z \left[T_f - T_w \right].$$ (2.135)

7. Compute the casing temperature with the following equation:

$$T_{ci} = T_w + \left(\frac{\ln\left(r_w/r_{co}\right)}{k_{cem}} + \frac{\ln\left(r_{co}/r_{ci}\right)}{k_s} \right) r_{to} U_{to} \left(T_f - T_w \right).$$ (2.136)

8. Calculate the outside tubing temperature,

$$T_{to} = T_f - \frac{q}{2\pi \Delta z} \left(\frac{1}{r_{ti} h_f} + \frac{\ln\left(r_{to}/r_{ti}\right)}{k_s} \right).$$ (2.137)

9. Calculate the annulus Nusselt number and convective heat transfer coefficient h_{ann} using Eqs. 2.126 or 2.129 and 2.131 respectively, i.e.,

$$N_{nu} = 0.049 \left(N_{gr} N_{pr} \right)^{1/3} N_{pr}^{0.074},$$ (2.126)

$$N_{nu} = \left[1, \ 0.603 \, C_1 \frac{\left(N_{gr} N_{pr} \right)^{1/4} \ln\left(d_{ci}/d_{ins} \right)}{\left[\left(e/d_{ins} \right)^{3/5} + \left(e/d_{ci} \right)^{3/5} \right]^{5/4}} \right]_{max},$$ (2.129)

$$h_{ann} = \frac{2 \, k_{ann} \, N_{nu}}{d_{ins} \ln\left(\dfrac{d_{ci}}{d_{ins}} \right)}.$$ (2.131)

10. Recompute the overall heat transfer coefficient, U_{to}.

$$U_{toc} = \frac{1}{r_{to}} \left[\frac{1}{r_{ti} h_f} + \frac{\ln\left(r_{to}/r_{ti}\right)}{k_s} + \frac{1}{r_{to} h_{ann}} + \frac{\ln\left(r_{co}/r_{ci}\right)}{k_s} + \frac{\ln\left(r_w/r_{co}\right)}{k_{cem}} \right]^{-1}.$$ (2.138)

11. Compare the estimated value of U_{to} computed in step 1 with the value computed in step 10. If $|U_{toc} - U_{to}| > \epsilon$, let $U_{to} = U_{toc}$ and go back to step 2.

2.2.4 Closure Relationship.

A relationship for the relative velocity, v_r, is necessary to close the model formulation. It is known that v_r is a flow pattern dependent variable. During the buildup period, since the effect of phase segregation is maximized for bubbly and slug flows[7], it is possible to restrict the model to handle bubbly and slug flow regimes only but in a more general case, the following flow regimes relations are used.

2.2.4.a Bubbly Flow Regime.

The relative velocity of a gas bubble in liquid for turbulent flow regime is obtained by balancing the drag force with the pressure and gravity force. The following well known Harmathy equation (see Ref. 20) is used:

$$v_r = \frac{0.79}{E_l} \left[\frac{\sigma(\rho_l - \rho_g)}{\rho_l^2} \right]^{1/4} , \qquad (2.139)$$

where σ is the gas-liquid surface tension. Note that all variables in Eq. 2.139 are in oil field units.

2.2.4.b Slug Flow Regime.

The relative velocity in oil field units is given by the well known Niklin et al. equation (see Refs. 20 and 47),

$$v_r = \frac{0.61}{E_l} \left[\frac{d(\rho_l - \rho_g)}{\rho_l} \right]^{1/2} , \qquad (2.140)$$

where d is the diameter of the tubing string in $[ft]$.

2.2.4.c Churn-Turbulent Flow Regime.

Due to high flux in this flow regime, the effects of distribution of velocity and momentum are dominant in comparison to other effects. Thus,

$$v_r = \frac{1}{0.3048} \left[\frac{v_m}{(1 - E_g C_o)/(C_o - 1) + E_g \rho_g / \rho_l} \right], \qquad (2.141)$$

where $C_o = 1.1$ as suggested by Hsu[48].

2.2.4.d Annular Flow Regime.

In annular flow, the constitutive equation for the relative velocity between the phases can be obtained by taking the interfacial momentum transfer and the flow structure into account[21]. Neglecting the effects of gravity, the relative velocity for cocurrent and turbulent flow is given by

$$v_r = \frac{1}{0.3048} \left[\frac{v_m}{\left[(76 - 75E_g)\rho_g / \rho_l \sqrt{E_g} \right]^{1/2} + E_g \rho_g / \rho_m} \right]. \qquad (2.142)$$

In cases where only bubbly and slug flow are considered. the change of flow pattern from bubbly flow to slug flow occurs when the gas void fraction is around 0.20. To avoid numerical oscillation[49], it is assumed that bubbly flow exists for $E_g \leq 0.15$, slug flow exists for $E_g \geq 0.25$ and for $0.15 < E_g < 0.25$, the flow is in the transition zone. The relative velocity in the transition zone is calculated by linear interpolation between values obtained from Eqs. 2.139 and 2.140.

In a general case, a continuous relation for the relative velocities for all the flow regimes is a requirement in order to avoid numerical oscillations. Hsu[48] developed an empirical flow pattern map for vertical flow that allows the identification of the

different flow regimes, creates a smooth transition between the different flow regimes, and enables us to compute the relative velocity in the different transition zones by using linear interpolation. The flow pattern map is presented in Fig. 2.2.

The following procedure is applied for each wellbore gridblock to determine the flow pattern:

1. Calculate the total mass flux in $[kg/m^2 - sec]$, i.e.,

$$G = 4.8825 \, \rho_m \, v_m \qquad (2.143)$$

where ρ_m is the mixture density in $[lb_m/ft^3]$ and v_m is the mixture velocity in $[ft/sec]$.

2. Calculate the gas void fraction using Eq. 2.31, i.e.,

$$E_l = \frac{B_o}{B_o + B_g(R - R_s)}. \qquad (2.31)$$

3. Determine the correspondent flow pattern using Fig. 2.2. Note the flow pattern can be different in each wellbore gridblock.

2.2.5 Initial and Boundary Conditions.

2.2.5.a Drawdown Period.

It is assumed that initially the well is under static condition, i.e., no flow conditions, so that the bottomhole pressure is equal to the average reservoir pressure and the pressure at each well gridblock from bottomhole to wellhead is computed based on the density of the well fluids, i.e.,
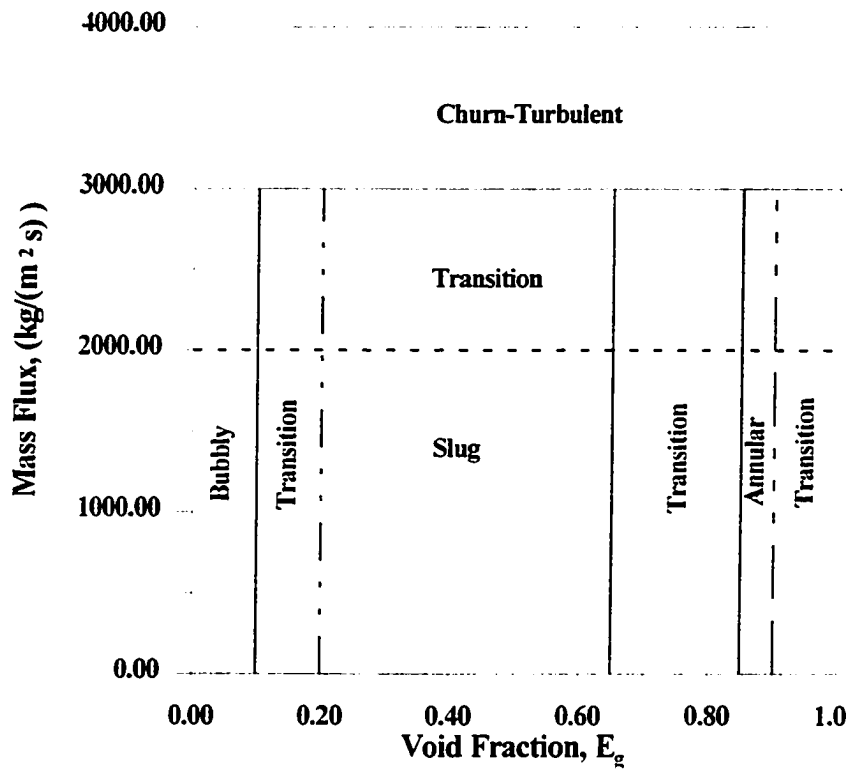
Figure 2.2: Flow Pattern Map for Vertical Flow

$$\frac{\partial p}{\partial z} = -\frac{\rho_m g}{144 \, g_c}.$$ (2.144)

Note that in Eq. 2.144, we assume that the upward direction is the positive z-direction.

The wellbore is connected with the reservoir at the bottomhole. When using an analytical solution, the dimensionless pressure solution at the sandface for the constant sandface rate production problem with no skin effect, i.e., $s = 0$, is denoted as p_{cD}. Since we assume radial flow, values of p_{cD} can be obtained by numerical inversion of the following Laplace space solution:

$$\overline{p}_{cD} = \frac{K_o(\sqrt{u})}{u^{3/2} K_1(\sqrt{u})}.$$ (2.145)

For $t_D > 25$, a semi-log approximation can be used to evaluate p_{cD}, i.e.,

$$p_{cD} = \frac{1}{2} \left[\ln t_D + 0.80907 \right].$$ (2.146)

The dimensionless wellbore pressure for the constant sandface rate production problem with an infinitesimally thin skin is

$$p_{wcD} = \frac{kh[p_i - p_{wf}]}{141.2 \, q\mu} = \frac{1}{2} \left[\ln t_D + 0.80907 \right] + s.$$ (2.147)

from which the bottomhole flowing pressure, p_{wf}, can be easily computed.

In case of using the RDRBOS[50] two-dimensional $(r-z)$ reservoir simulator (see Figs. 2.3 and 2.4), the simulator is run under a total rate inner boundary condition. The production rate can be computed by using the Darcy's Law at the wellbore for the required phase, so that the production at a total volumetric reservoir flow rate in $[RB/D]$ can be calculated as
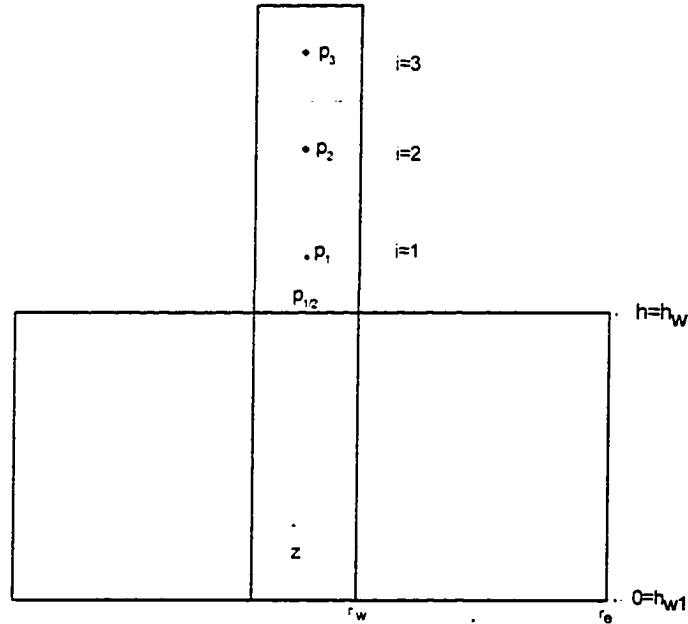
Figure 2.3: Reservoir and Wellbore Scheme for a Full Penetration Well

$$q_t = 2\pi(1.127 \times 10^{-3})r_w \int_{h_{w1}}^{h_{w2}} k_h \left(\frac{k_{ro}}{\mu_o}\frac{\partial p_o}{\partial r} + \frac{k_{rg}}{\mu_g}\frac{\partial p_g}{\partial r} + \frac{k_{rw}}{\mu_w}\frac{\partial p_w}{\partial r} \right)_{r_w} dz, \qquad (2.148)$$

where the perforated interval corresponds to $h_{w1} \leq z \leq h_{w2}$. Under this condition the reservoir simulator solves for the corresponding bottomhole flowing pressure.

$p_{wf} = p_{wb}$, at the wellbore reference block. In our case, the top perforated gridblock is selected as the reference block; this selection is imposed by the lower-boundary condition of the wellbore simulator that requires the bottomhole pressure exactly at the lower-boundary. This means, $p_{\frac{1}{2}} = p_{wf}$, where $p_{\frac{1}{2}}$ corresponds to the wellbore simulator lower boundary pressure and p_{wf} corresponds to the bottomhole flowing pressure computed by the reservoir simulator (see Figs. 2.3 and 2.4).
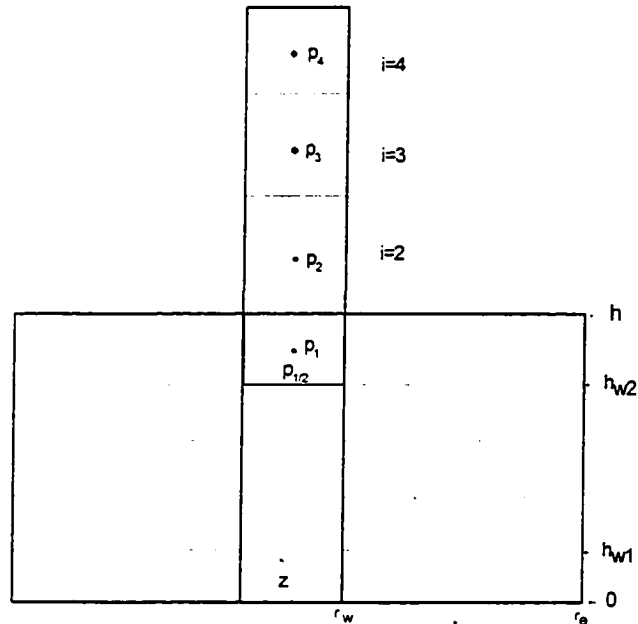
Figure 2.4: Reservoir and Wellbore Scheme for a Partial Penetration Well.

For a full detailed description of the implementation of the initial and boundary conditions for the reservoir simulator RDRBOS, the reader is referred to Ref. 50.

At each time, the wellbore simulator imposes a constant rate lower boundary condition as the inner boundary condition for the (r-z) simulator, obtaining the corresponding flowing wellbore pressure. A iterative procedure is required to guarantee that the mass-conservation as well as the upper and lower boundary conditions are satisfied in the wellbore and that the inner boundary condition for the (r-z) simulator is also satisfied. A detailed calculation algorithm is described in the next chapter.

2.2.5.b Buildup Period.

If a buildup test is simulated without the explicit simulation of the transient drawdown period, it is assumed that the well produces at a constant rate for a sufficiently long period of time so that steady-state flow is established in the wellbore prior to the instant of shut-in. With a known sandface production rate and producing time, the spatial distributions of the mixture velocity, oil concentration, and pressure are calculated at the instant of shut-in from a steady-state model. But if the transient drawdown simulation has been done, the spatial distribution of the mixture velocity, oil concentration and pressure that we have at the instant of shut-in are used as the initial conditions for the buildup period simulation.

We assume that wellhead shut-in occurs instantaneously, and so, the boundary condition at the wellhead during the pressure buildup period is

$$[v_m]_{wh} = 0, \quad [v_r]_{wh} = 0, \quad \Delta t > 0, \tag{2.149}$$

where Δt is the shut-in time.

The wellbore is connected with the reservoir at the bottomhole. Immediately after shut-in, fluids may continue to flow into the wellbore, i.e., afterflow occurs. At late times, fluids may even be injected back into the reservoir due to wellbore phase segregation.

In the case where the bottomhole pressure remains above bubble point pressure, we use an analytical solution to relate sandface flow rate and bottomhole pressure. The boundary condition at bottomhole for the wellbore flow is obtained by

applying Duhamel's principle, i.e.,

$$p_{wsD} = \int_0^{t_{pD}+\Delta t_D} q_D(\tau)p'_{cD}(t_{pD} + \Delta t_D - \tau)d\tau + sq_D(t_{pD} + \Delta t_D), \qquad (2.150)$$

where t_p is the producing time and t_{pD} is the dimensionless producing time.

In Eq. 2.150, p_{wsD} is the dimensionless buildup bottomhole pressure defined as

$$p_{wsD} = \frac{kh(p_i - p_{ws})}{141.2q\mu}, \qquad (2.151)$$

where q is the sandface production rate in $[RB/D]$ at the instant of shut-in. The dimensionless flow rate, q_D, is defined as

$$q_D(\tau) = \frac{q_{sf}(\tau)}{q}. \qquad (2.152)$$

For $0 < \tau \le t_p$, $q_{sf} = q$ and $q_D(\tau) = 1$, i.e., when considering the single-phase reservoir flow case, we assume that the drawdown solution is equivalent to the one obtained for production at a constant sandface rate. The dimensionless time, t_D, is defined as

$$t_D = \frac{2.637 \times 10^{-4}kt}{\phi c_t \mu r_w^2}. \qquad (2.153)$$

where t is in hours. In Eq. 2.150, t_{pD} is the dimensionless producing time, obtained by replacing t with producing time t_p in Eq. 2.153, and Δt_D in Eq. 2.150 is the dimensionless shut-in time, obtained by replacing t with Δt in Eq. 2.153. In Eq. 2.150, p_{cD} is the dimensionless pressure solution at the sandface for the constant sandface rate production problem with no skin effect, i.e., $s = 0$. Since we assume radial flow, values of p_{cD} can be obtained by numerical inversion of the following

Laplace space solution:

$$\bar{p}_{cD} = \frac{K_o(\sqrt{u})}{u^{3/2} K_1(\sqrt{u})}.$$ (2.154)

For $t_D > 25$, the semi-log approximation can be used to evaluate p_{cD}, i.e.,

$$p_{cD} = \frac{1}{2}\left[\ln t_D + 0.80907\right].$$ (2.155)

The dimensionless wellbore pressure for the constant sandface rate production problem with an infinitesimally thin skin is

$$p_{wcD} = \frac{kh[p_i - p_{wf}]}{141.2\,q\mu} = \frac{1}{2}\left[\ln t_D + 0.80907\right] + s.$$ (2.156)

Eq. 2.150, which relates sandface flow rate with bottomhole pressure, is the bottomhole boundary condition for the wellbore two-phase flow system. For a given time and flow rate, Eq. 2.150 is numerically integrated to give the bottomhole shut-in pressure, p_{ws}.

When using the two-dimensional $(r - z)$ reservoir simulator, the simulator is run at each buildup period simulation timestep under total rate inner boundary conditions. i.e.,

$$q_t = 2\pi(1.127 \times 10^{-3})r_w \int\limits_{h_{w1}}^{h_{w2}} k_h \left(\frac{k_{ro}}{\mu_o}\frac{\partial p_o}{\partial r} + \frac{k_{rg}}{\mu_g}\frac{\partial p_g}{\partial r} + \frac{k_{rw}}{\mu_w}\frac{\partial p_w}{\partial r}\right)_{r_w} dz.$$ (2.157)

where the perforated interval corresponds to $h_{w1} \le z \le h_{w2}$. Under this condition the reservoir simulator computes the corresponding bottomhole pressure. This interaction between the wellbore simulator and the wellbore simulator allows us to simulate a process of afterflow during the buildup period.

CHAPTER III

NUMERICAL SOLUTION METHOD

The system of nonlinear partial differential equations governing the phase segregation process in the wellbore is solved numerically using a finite difference method. The wellbore is divided into uniform control volumes, as shown in Fig. 3.1. In the wellbore, flow occurs in the z direction only. Finite difference equations are derived with a system of staggered grids where dependent variables are defined at different positions in each control volume[51]. Specifically, we define oil concentration and all physical properties at the center of each control volume while the mixture velocity is defined at the control volume boundaries or faces. Thus, our finite difference solution directly yields oil concentration at the center of each gridblock and mixture velocity at the boundary of each gridblock, i.e., at the gridblock interfaces.

In this chapter, we present the finite difference equation systems used to solve for mixture velocity, pressure and the mass concentration of the oil component. The formulation is applied during the drawdown and buildup periods. Additionally during a drawdown period, we sometimes use the so-called "steady-state" formulation, for cases where the bottomhole pressure remains above the bubble point pressure so that the reservoir flow equation can be solved analytically. This procedure is applicable where the total sandface rate is constant and the drawdown period is long enough so that the sandface flow rate become equal to the surface rate. For a detailed discussion

53

N+1/2

N

N-1/2

i+1/2

i

i-1/2

2

3/2

1

1/2
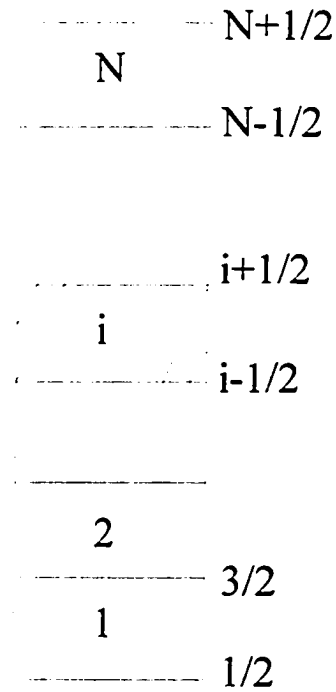
Figure 3.1: Control Volumes and Staggered Grids.

of the steady-state wellbore model, the reader is referred to Refs. 9,17-19.

3.1 Overall Mass Balance Equation.

Finite difference equations are obtained by integrating the corresponding partial differential equations over each of the control volumes. Integrating the overall mass balance equation, Eq. 2.53, over the ith control volume, we obtain

$$\frac{(\rho_m)_i^{n+1} - (\rho_m)_i^n}{\Delta t} + \frac{(\rho_m v_m)_{i+\frac{1}{2}}^{n+1} - (\rho_m v_m)_{i-\frac{1}{2}}^{n+1}}{\Delta z} = 0, \tag{3.1}$$

for $i = 1, 2, ..., N$. (N is the total number of cells in the calculation domain: see Fig. 3.1. Rearranging Eq. 3.1, we obtain

$$\left[\frac{(\rho_m)_{i+\frac{1}{2}}^{n+1}}{\Delta z}\right](v_m)_{i+\frac{1}{2}}^{n+1} = \left[\frac{(\rho_m)_{i-\frac{1}{2}}^{n+1}}{\Delta z}\right](v_m)_{i-\frac{1}{2}}^{n+1} - \frac{(\rho_m)_i^{n+1} - (\rho_m)_i^n}{\Delta t}, \tag{3.2}$$

for $i = 1, 2, ..., N$.

Summation of Eq. 3.2 over all i and rearranging the resulting equation gives

$$(v_m)_{\frac{1}{2}}^{n+1} = (\frac{\Delta z}{\Delta t})\frac{\sum_{i=1}^{N}[(\rho_m)_i^{n+1} - (\rho_m)_i^n]}{(\rho_m)_{\frac{1}{2}}^{n+1}} + \frac{(\rho_m)_{n+\frac{1}{2}}^{n+1}}{(\rho_m)_{\frac{1}{2}}^{n+1}}(v_m)_{N+\frac{1}{2}}^{n+1}. \tag{3.3}$$

Note that Eq. 3.3 is the wellbore mass conservation equation. During the buildup period, the boundary condition at the top of the well is a no-flow boundary condition, i.e., $v_{m,N+\frac{1}{2}} = 0$ (Eq. 2.149) and Eq. 3.3 reduces to

$$(v_m)_{\frac{1}{2}}^{n+1} = (\frac{\Delta z}{\Delta t})\frac{\sum_{i=1}^{N}[(\rho_m)_i^{n+1} - (\rho_m)_i^n]}{(\rho_m)_{\frac{1}{2}}^{n+1}}. \tag{3.4}$$

In Eqs. 3.1 through 3.4, values of mixture densities at the control volume faces are required. An upstream weighting technique is used to evaluate these variables. For example, for $(\rho_m)_{i+\frac{1}{2}}$, we have

$$(\rho_m)_{i+\frac{1}{2}} = \left[\frac{1+\beta_{i+\frac{1}{2}}}{2}\right](\rho_m)_i + \left[\frac{1-\beta_{i+\frac{1}{2}}}{2}\right](\rho_m)_{i+1}. \tag{3.5}$$

where the coefficient for the upstream weighting is defined as

$$\beta_{i+\frac{1}{2}} = SGN(v_{m,i+\frac{1}{2}}^{n+1}) = \begin{cases} +1 & v_{m,i+\frac{1}{2}}^{n+1} \geq 0 \\ -1 & v_{m,i+\frac{1}{2}}^{n+1} < 0, \end{cases} \tag{3.6}$$

Once the sandface velocity, $(v_m)_{\frac{1}{2}}^{n+1}$, satisfying both the bottomhole boundary conditions and the wellbore mass conservation equation (Eqs. 3.3 or 3.4) is obtained,

Eq. 3.2 can be applied recursively to compute velocity from the bottomhole to the wellhead. Further details of this computational procedure are given later.

3.1.1 Oil Component Concentration Equation.

To derive the finite difference equation for the oil component concentration, it is necessary to write the finite difference overall mass balance equation in a different form. Applying the concept of upstream weighting, we have

$$(\rho_m v_m)_{i+\frac{1}{2}}^{n+1} = (\rho_m)_i^{n+1} max\left[(v_m)_{i+\frac{1}{2}}^{n+1}, 0\right] - (\rho_m)_{i+1}^{n+1} max\left[-(v_m)_{i+\frac{1}{2}}^{n+1}, 0\right]. \qquad (3.7)$$

Substituting equations for $(\rho_m v_m)_{i+\frac{1}{2}}^{n+1}$ and $(\rho_m v_m)_{i-\frac{1}{2}}^{n+1}$ into Eq. 3.1 and multiplying both sides of the resulting equation by $(C_l)_i^{n+1}$, we obtain

$$\frac{(C_l)_i^{n+1}(\rho_m)_i^{n+1} - (C_l)_i^{n+1}(\rho_m)_i^n}{\Delta t} + \frac{(C_l)_i^{n+1}(\rho_m)_i^{n+1} max\left[(v_m)_{i+\frac{1}{2}}^{n+1}, 0\right]}{\Delta z}$$

$$- \frac{(C_l)_i^{n+1}(\rho_m)_{i+1}^{n+1} max\left[-(v_m)_{i+\frac{1}{2}}^{n+1}, 0\right]}{\Delta z} - \frac{(C_l)_i^{n+1}(\rho_m)_{i-1}^{n+1} max\left[(v_m)_{i-\frac{1}{2}}^{n+1}, 0\right]}{\Delta z}$$

$$+ \frac{(C_l)_i^{n+1}(\rho_m)_i^{n+1} max\left[-(v_m)_{i-\frac{1}{2}}^{n+1}, 0\right]}{\Delta z} = 0. \qquad (3.8)$$

Integrating the oil component mass balance, Eq. 2.50, over the ith control volume and using upstream weighting, we obtain

$$\frac{(C_l\rho_m)_i^{n+1} - (C_l\rho_m)_i^n}{\Delta t} + \frac{(C_l\rho_m)_i^{n+1} max\left[(v_m)_{i-\frac{1}{2}}^{n+1}, 0\right]}{\Delta z}$$

$$- \frac{(C_l\rho_m)_{i+1}^{n+1} max\left[-(v_m)_{i-\frac{1}{2}}^{n+1}, 0\right]}{\Delta z} - \frac{(C_l\rho_m)_{i-1}^{n+1} max\left[(v_m)_{i-\frac{1}{2}}^{n+1}, 0\right]}{\Delta z}$$

$$+ \frac{(C_l\rho_m)_i^{n+1} max\left[-(v_m)_{i-\frac{1}{2}}^{n+1}, 0\right]}{\Delta z} = \frac{(D_r)_{i+\frac{1}{2}}^{n+1} - (D_r)_{i-\frac{1}{2}}^{n+1}}{\Delta z}. \qquad (3.9)$$

Subtracting Eq. 3.8 from Eq. 3.9 and rearranging yields

$$-a(C_l)_{i-1}^{n+1} + b(C_l)_i^{n+1} - c(C_l)_{i+1}^{n+1} = d,$$ (3.10a)

where

$$a = \frac{(\rho_m)_{i-1}^{n+1}}{\Delta z} max \left[(v_m)_{i-\frac{1}{2}}^{n+1}, 0 \right],$$ (3.10b)

$$b = \frac{(\rho_m)_i^n}{\Delta t} + \frac{(\rho_m)_{i-1}^{n+1}}{\Delta z} max \left[(v_m)_{i-\frac{1}{2}}^{n+1}, 0 \right] + \frac{(\rho_m)_{i+1}^{n+1}}{\Delta z} max \left[-(v_m)_{i+\frac{1}{2}}^{n+1}, 0 \right],$$ (3.10c)

$$c = \frac{(\rho_m)_{i+1}^{n+1}}{\Delta z} max \left[-(v_m)_{i+\frac{1}{2}}^{n+1}, 0 \right],$$ (3.10d)

and

$$d = \frac{(D_r)_{i+\frac{1}{2}}^{n+1} - (D_r)_{i-\frac{1}{2}}^{n+1}}{\Delta z} + \frac{(C_l \rho_m)_i^n}{\Delta t},$$ (3.10e)

for $i = 1, 2, ..., N$. Note that if we write Eq. 3.10a, for all control volumes, in a matrix form, the coefficient matrix will be a tridiagonal matrix. Solution of the system of nonlinear algebraic equations will yield the oil component concentration distribution along the wellbore.

For the evaluation of diffusion terms at the control volume boundaries in Eq. 3.10e, Alhanati[52] suggested that for numerical stability reasons that we should chose the minimum value in the two adjacent cells, i.e., for $(D_r)_{i+\frac{1}{2}}$, we have

$$(D_r)_{i+\frac{1}{2}} = min \left[(D_r)_i, (D_r)_{i+1} \right].$$ (3.11)

Note that during the buildup period, from the boundary condition at the wellhead, we should have $(D_r)_{N+\frac{1}{2}} = 0$. On the other hand, in case of using a reservoir analytical solution, since we consider single phase liquid flow at bottomhole, we should also have $(D_r)_{\frac{1}{2}} = 0$.

Overrelaxation can be used to accelerate convergence and underrelaxation can be used to slow down the changes in a variable at each iteration. Without relaxation, the new value for the oil component concentration from Eq. 3.10a is

$$(C_l)_i^{n+1} = \frac{\left[a(C_l)_{i-1}^{n+1} + c(C_l)_{i+1}^{n+1} \right] + d}{b}. \tag{3.12}$$

Considering relaxation, the new value will be computed as

$$(C_l)_i^{n+1} = \Theta \left[\frac{\left[a(C_l)_{i-1}^{n+1} + c(C_l)_{i+1}^{n+1} \right] + d}{b} \right] + (1 - \Theta)(C_l^*)_i^{n+1}, \tag{3.13}$$

where Θ is the relaxation factor and $(C_l^*)_i^{n+1}$ is the previous iteration value. Eq. 3.13 can be rearranged to give

$$-a(C_l)_{i-1}^{n+1} + \hat{b}(C_l)_i^{n+1} - c(C_l)_{i+1}^{n+1} = \hat{d}. \tag{3.14a}$$

where

$$\hat{b} = \left(\frac{b}{\Theta} \right), \tag{3.14b}$$

and

$$\hat{d} = d + (1 - \Theta) \left(\frac{b}{\Theta} \right) (C_l^*)_i^{n+1}. \tag{3.14c}$$

Eq. 3.14a indicates that relaxation can be achieved by slightly modifying the original finite difference equation, Eq. 3.10a. Overrelaxation corresponds to using $1 < \Theta < 2$, underrelaxation is obtained when $0 < \Theta < 1$, and no relaxation corresponds to $\Theta = 1$. As in Refs. 9, 17 and 19, our code includes the option of using relaxation, however with our formulation, we found relaxation is not needed.

It should be pointed out that there is no guarantee that C_l obtained from Eq. 3.14a always remain in the interval $[0,1]$. If solution of Eq. 3.14a returns any values of C_l outside this range, the iteration process will no longer maintain the continuity of each individual fluid[53]. Carver[53] suggested that since 3.14a is an expression of mass balance, it is not sufficient merely to solve Eq. 3.14a, and then set $(C_l)_i^{n+1} = 1$ if we obtain $(C_l)_i^{n+1} > 1$ and set $(C_l)_i^{n+1} = 0$ if we obtain $(C_l)_i^{n+1} < 1$. This type of modification will degrade the mass balance because the remaining variables will not be adjusted appropriately. Alhanati[52] and Carver[53] proposed modifications to Eq. 3.14a so that C_l obtained always stays in the desired interval. As discussed in Refs. 9, 17 and 19, the main modification is done by splitting the positive and negative components of $\widehat{d}$. First, we rewrite Eq. 3.14a as

$$\widehat{b}(C_l)_i^{n+1} = \left[a(C_l)_{i-1}^{n+1} + c(C_l)_{i+1}^{n+1}\right] + \widehat{d_1} - \widehat{d_2}, \qquad (3.15)$$

where $\widehat{d_1}$ and $\widehat{d_2}$ are the positive and negative components of $\widehat{d}$, respectively, ($\widehat{d} = \widehat{d_1} - \widehat{d_2}$, $\widehat{d_1} \geq 0$, $\widehat{d_2} > 0$). Since all coefficients in Eq. 3.15 are non-negative, $(C_l)_i^{n+1}$ can not become negative unless $\widehat{d_1} < \widehat{d_2}$. Under this condition, Eq. 3.14a is modified to

$$-a(C_l)_{i-1}^{n+1} + \tilde{b}(C_l)_i^{n+1} - c(C_l)_{i+1}^{n+1} = \hat{d}_1, \qquad (3.16a)$$

where

$$\tilde{b} = \left[\hat{b} + \frac{\hat{d}_2}{(C_l^*)_i^{n+1}} \right]. \qquad (3.16b)$$

Eq. 3.16a indicates that by modifying the coefficients of Eq. 3.14a, the computed concentration is ensured to retain a positive sign, providing the previous iteration value is positive. On the other hand, if $\hat{d}_1 > \hat{d}_2$ in Eq. 3.15, the solution of Eq. 3.15 will be guaranteed to give positive values for all positions. However, under this condition, it is at least possible to obtain a value of oil component concentration greater than one. To keep the oil component concentration below one is the same as keeping the gas component concentration above zero. Therefore, we transform Eq. 3.15 to

$$\hat{b}\left[1 - (C_l)_i^{n+1}\right] = \left[a\left[1 - (C_l)_{i-1}^{n+1}\right] + c\left[1 - (C_l)_{i+1}^{n+1}\right]\right]$$
$$+ \left[\hat{b} + \hat{d}_2\right] - \left[a + c + \hat{d}_1.\right]. \qquad (3.17)$$

The strategy to keep $[1 - (C_l)_i^{n+1}]$ positive is the same as the strategy to keep $(C_l)_i^{n+1}$ positive. Therefore, proceeding as before, we eventually obtain the following modification of Eq. 3.17:

$$-a(C_l)_{i-1}^{n+1} + \bar{b}(C_l)_i^{n+1} - c(C_l)_{i-1}^{n+1} = \bar{d}, \qquad (3.18a)$$

where

$$\overline{b} = \left[\hat{b} + \frac{a + c + \hat{d}_1}{1 - (C_1^*)^{n+1}} \right], \tag{3.18b}$$

and

$$\overline{d} = \frac{(a + c + \hat{d}_2)(C_1^*)^{n+1} + \hat{d}}{1 - (C_1^*)^{n+1}}. \tag{3.18c}$$

The implementation of the previous formulations with or without relaxation and the use of the procedures to keep the oil component concentration within the correct range is simple, because the modifications require only easy transformations of the original system of equations.

3.2 Mixture Momentum Equation.

A multistep numerical procedure has been selected for stability-enhancing reasons. In this approach the mixture momentum equation is solved by a two-step method that consists of a basic step for pressures and a stabilizing step for mixture velocities. In the final step, we obtain the oil concentration from the continuity equation. Here, we discuss the finite difference form for the mixture momentum equations.

To construct a finite-difference approximation for the mixture momentum. we consider Eq. 2.58 at the point $z_{i+1/2}$. From a physical viewpoint, the finite difference approximation for the partial differential equation, Eq. 2.58. at this point may be constructed as a momentum balance on the control volume lying between z_i and z_{i+1} (see Fig. 3.1) which is referred to as the $(i + 1/2)^{th}$ control volume for the momentum equation. Integrating, Eq. 2.58, over the $(i + 1/2)^{th}$ control volume

$$\frac{\overline{\rho}_{m_{i+1/2}}^{n+1}}{144 g_c \Delta t} \left[v_{m_{i+1/2}}^{n+1} - v_{m_{i+1/2}}^{n} \right] + \frac{p_{i+1}^{n+1} - p_i^{n+1}}{\Delta z} + \tau_{w_{i+1/2}}^{n+1} = \quad (3.19a)$$

$$-\frac{\overline{\rho}_{m_{i+1/2}}^{n+1} g}{144 g_c} - \frac{\overline{\rho}_{m_{i+1/2}}^{n+1} v_{m_{i+1/2}}^{n+1}}{144 g_c \Delta z} \left[v_{m_{i+1}}^{n+1} - v_{m_i}^{n+1} \right]$$

$$-\frac{1}{144 g_c \Delta z} \left[\left(\rho_f v_r^2 \right)_{i+1}^{n+1} - \left(\rho_f v_r^2 \right)_{i}^{n+1} \right],$$

for $i = 1, 2, \ldots, N$, where

$$\tau_{w_{i+1/2}}^{n+1} = \left. \left| \frac{f_m \rho_m |v_m|}{144 g_c (2d)} \right|_{i+1/2}^{n} v_{m_{i+1/2}}^{n+1}, \quad (3.19b)$$

$$\overline{\rho}_{m_{i+1/2}}^{n+1} = \frac{\rho_{m_{i+1}}^{n+1} + \rho_{m_i}^{n+1}}{2}, \quad (3.19c)$$

and

$$\rho_{f_i}^{n+1} = \left[\frac{(1 - E_l)\rho_g E_l \rho_l}{\rho_m} \right]_i^{n+1}. \quad (3.19d)$$

Using Eq. 3.19b in Eq. 3.19a and rearranging, we have

$$-\left(\frac{1}{\Delta z} \right) p_i^{n+1} + \left[\frac{\overline{\rho}_{m_{i+1/2}}^{n+1}}{\Delta t} + \left(\frac{f_m \rho_m |v_m|}{2d} \right)_{i+1/2}^{n} \right] \frac{v_{m_{i+1/2}}^{n+1}}{144 g_c} + \left(\frac{1}{\Delta z} \right) p_{i+1}^{n+1} =$$

$$-\frac{\overline{\rho}_{m_{i+1/2}}^{n+1} g}{144 g_c} + \frac{\overline{\rho}_{m_{i+1/2}}^{n+1} v_{m_{i+1/2}}^{n}}{144 g_c \Delta t} - \frac{\overline{\rho}_{m_{i+1/2}}^{n+1} v_{m_{i+1/2}}^{n+1}}{144 g_c \Delta z} \left[v_{m_{i+1}}^{n+1} - v_{m_i}^{n+1} \right]$$

$$-\frac{1}{144 g_c \Delta z} \left[\left(\rho_f v_r^2 \right)_{i+1}^{n+1} - \left(\rho_f v_r^2 \right)_{i}^{n+1} \right]. \quad (3.20)$$

In Eq. 3.20, we apply the following upstream weighting schemes:

$$\left(\rho_f v_r^2 \right)_i = \begin{cases} \rho_{f,} \overline{v}_{r,i} v_{r,i-1/2}, & \overline{v}_{r,i} \geq 0 \\ \\ \rho_{f,} \overline{v}_{r,i} v_{r,i+1/2}, & \overline{v}_{r,i} < 0, \end{cases} \quad (3.21a)$$

$$v_{m,i+1/2}\left[v_{m_{i+1}} - v_{m_i}\right] = v_{m_{i+1/2}} \begin{cases} \left(v_{m,i+1/2} - v_{m,i-1/2}\right), & v_{m,i+1/2} \geq 0 \\ \\ \left(v_{m,i+3/2} - v_{m,i+1/2}\right), & v_{m,i+1/2} < 0, \end{cases}$$ (3.21b)

where

$$\bar{v}_{r_i} = \frac{v_{r_{i-1/2}} + v_{r_{i+1/2}}}{2}.$$ (3.21c)

Following the suggestion of Mahaffy[54], additional robustness is obtained using the following form of the friction term :

$$\bar{\rho}^n_{m_{i+1/2}}\left(\frac{f_m}{2d}\right)^n_{i+1/2}|v^n_{m_{i+1/2}}|v^{n+1}_{m_{i+1/2}} = \bar{\rho}^n_{m_{i+1/2}}\left(\frac{f_m}{2d}\right)^n_{i+1/2}|v^n_{m_{i+1/2}}|\left[2v^{n+1}_{m_{i+1/2}} - v^n_{m_{i+1/2}}\right].$$

(3.22)

Applying Eq. 3.22 in Eq. 3.20, the mixture momentum equation becomes

$$-\left(\frac{1}{\Delta z}\right)p^{n+1}_i + \left[\frac{\bar{\rho}^{n+1}_{m_{i+1/2}}}{\Delta t} + 2\left(\frac{f_m}{2d}\right)^n_{i+1/2}\bar{\rho}^n_{m_{i+1/2}}|v^n_{m_{i+1/2}}|\right]\frac{v^{n+1}_{m_{i+1/2}}}{144g_c} + \left(\frac{1}{\Delta z}\right)p^{n+1}_{i+1} =$$

$$-\frac{\bar{\rho}^{n+1}_{m_{i+1/2}}g}{144g_c} + \left[\frac{\bar{\rho}^{n+1}_{m_{i+1/2}}}{\Delta t} + \left(\frac{f_m}{2d}\right)^n_{i+1/2}\bar{\rho}^n_{m_{i+1/2}}|v^n_{m_{i+1/2}}|\right]\frac{v^n_{m_{i+1/2}}}{144g_c}$$

$$-\frac{\bar{\rho}^{n+1}_{m_{i+1/2}}v^{n+1}_{m_{i+1/2}}}{144g_c\Delta z}\left[v^{n+1}_{m_{i+1}} - v^{n+1}_{m_i}\right] - \frac{1}{144g_c\Delta z}\left[\left(\rho_f v^2_r\right)^{n+1}_{i+1} - \left(\rho_f v^2_r\right)^{n+1}_i\right].$$ (3.23)

or equivalently,

$$-\left(\frac{1}{\Delta z}\right)p^{n+1}_i + \left[\frac{\bar{\rho}^{n+1}_{m_{i+1/2}}}{\Delta t} + 2\left(\frac{f_m}{2d}\right)^n_{i+1/2}\bar{\rho}^n_{m_{i+1/2}}|v^n_{m_{i+1/2}}|\right]\frac{v^{n+1}_{m_{i+1/2}}}{144g_c} + \left(\frac{1}{\Delta z}\right)p^{n+1}_{i+1} = M_i.$$

(3.24)

where

$$M_i = -\frac{\overline{\rho}_{m_{i+1/2}}^{n+1} g}{144 g_c} + \left[\frac{\overline{\rho}_{m_{i+1/2}}^{n+1}}{\Delta t} + \left(\frac{f_m}{2d}\right)_{i+1/2}^{n} \overline{\rho}_{m_{i+1/2}}^{n} |v_{m_{i+1/2}}^{n}|\right] \frac{v_{m_{i+1/2}}^{n}}{144 g_c}$$

$$-\frac{\overline{\rho}_{m_{i+1/2}}^{n+1} v_{m_{i+1/2}}^{n+1}}{144 g_c \Delta z} \left[v_{m_{i+1}}^{n+1} - v_{m_i}^{n+1}\right] \tag{3.25}$$

$$-\frac{1}{144 g_c \Delta z} \left[\left(\rho_f v_r^2\right)_{i+1}^{n+1} - \left(\rho_f v_r^2\right)_{i}^{n+1}\right].$$

If we consider Eq. 3.24 for node $(i-1)$, we have

$$-\left(\frac{1}{\Delta z}\right) p_{i-1}^{n+1} + \left[\frac{\overline{\rho}_{m_{i-1/2}}^{n+1}}{\Delta t} + 2\left(\frac{f_m}{2d}\right)_{i-1/2}^{n} \overline{\rho}_{m_{i-1/2}}^{n} |v_{m_{i-1/2}}^{n}|\right] \frac{v_{m_{i-1/2}}^{n+1}}{144 g_c} + \left(\frac{1}{\Delta z}\right) p_i^{n+1} = M_{i-1}. \tag{3.26}$$

Subtracting Eq. 3.26 from Eq. 3.24 gives

$$+\left(\frac{\Delta t}{\Delta z}\right) p_{i-1}^{n+1} - \left(\frac{2\Delta t}{\Delta z}\right) p_i^{n+1} + \left(\frac{\Delta t}{\Delta z}\right) p_{i+1}^{n+1}$$

$$+\left[\overline{\rho}_{m_{i+1/2}}^{n+1} v_{m_{i+1/2}}^{n+1} - \overline{\rho}_{m_{i-1/2}}^{n+1} v_{m_{i-1/2}}^{n+1}\right]\left(\frac{1}{144 g_c}\right) =$$

$$\Delta t\left[M_i - M_{i-1}\right]$$

$$-\left(\frac{2\Delta t}{144 g_c}\right)\left[\left(\frac{f_m}{2d}\right)_{i+1/2}^{n} \overline{\rho}_{m_{i+1/2}}^{n} |v_{m_{i+1/2}}^{n}| v_{m_{i+1/2}}^{n+1}\right]$$

$$+\left(\frac{2\Delta t}{144 g_c}\right)\left[\left(\frac{f_m}{2d}\right)_{i-1/2}^{n} \overline{\rho}_{m_{i-1/2}}^{n} |v_{m_{i-1/2}}^{n}| v_{m_{i-1/2}}^{n+1}\right]. \tag{3.27}$$

Recall that our finite difference form of the mixture continuity equation is

given by

$$\frac{1}{\Delta t}\left[\rho_{m_i}^{n+1} - \rho_{m_i}^{n}\right] + \frac{1}{\Delta z}\left[\rho_{m_{i+1/2}}^{n+1} v_{m_{i+1/2}}^{n+1} - \rho_{m_{i-1/2}}^{n+1} v_{m_{i-1/2}}^{n+1}\right] = 0. \tag{3.28}$$

Letting Δ_t denote the time difference operator, we have $\Delta_t \rho_i = \rho_{m_i}^{n+1} - \rho_{m_i}^{n}$. It is well

known that

$$\Delta_t(ab) = a^{n+1}\Delta_t(b) + b^n \Delta_t(a), \tag{3.29}$$

Applying Eq. 3.29 to the definition of ρ_m given by Eq. 2.25, we obtain

$$\rho_{m_i}^{n+1} - \rho_{m_i}^n = \Delta_t \rho_m = \rho_{g_i}^{n+1} \Delta_t E_{g_i} + \rho_{l_i}^{n+1} \Delta_t E_{l_i} + E_{g_i}^n \Delta_t \rho_{g_i} + E_{l_i}^n \Delta_t \rho_{l_i}. \qquad (3.30)$$

Using

$$E_l + E_g = 1, \qquad (3.31a)$$

$$\Delta_t E_{l_i} = -\Delta_t E_{g_i}. \qquad (3.31b)$$

and the approximations

$$\Delta_t \rho_{l_i} \approx \left(\frac{d\rho_{l_i}}{dp_i} \right) \Delta_t p_i, \qquad (3.31c)$$

and

$$\Delta_t \rho_{g_i} \approx \left(\frac{d\rho_{g_i}}{dp_i} \right) \Delta_t p_i, \qquad (3.31d)$$

Eq. 3.30 simplifies to

$$\Delta_t \rho_{m_i} = \left[\rho_{g_i}^{n+1} - \rho_{l_i}^{n+1} \right] \Delta_t E_{g_i} + \left[E_{g_i}^n \frac{d\rho_{g_i}}{dp} + (1 - E_{g_i})^n \frac{d\rho_{l_i}}{dp} \right] \Delta_t p_i. \qquad (3.32)$$

Since the equations we need to solve are nonlinear, we use an iterative method. In this procedure, the superscript $(n + 1, k)$ or (k) always denotes the value of the variable at the old iterative at time t^{n+1} and $(n + 1)$ by itself denotes the value at the new $(k + 1)$ iteration step.

By using Eq. 3.32, we can rewrite Eq. 3.28 as

$$\rho_{m_{i+1/2}}^{n+1} v_{m_{i+1/2}}^{n+1} - \rho_{m_{i-1/2}}^{n+1} v_{m_{i-1/2}}^{n+1} + \frac{\Delta z}{\Delta t} \vartheta_{m_i} p_i^{n+1} = C_i. \qquad (3.33)$$

where

$$C_i = \frac{\Delta z}{\Delta t}\left[\vartheta_{m_i} p_i^n - \left(\rho_{g_i}^k - \rho_{l_i}^k\right)\left(E_{g_i}^k - E_{g_i}^n\right)\right],\tag{3.34}$$

and

$$\vartheta_{m_i} = E_{g_i}^n \frac{d\rho_{g_i}}{dp} + (1 - E_{g_i})^n \frac{d\rho_{l_i}}{dp}.\tag{3.35}$$

In solving Eq. 3.34 iteratively, we use the approximations

$$\frac{d\rho_{g_i}}{dp} = \frac{\rho_{g_i}^k - \rho_{g_i}^n}{p_i^k - p_i^n},\tag{3.36a}$$

and

$$\frac{d\rho_{l_i}}{dp} = \frac{\rho_{l_i}^k - \rho_{l_i}^n}{p_i^k - p_i^n}.\tag{3.36b}$$

Note that at the first iteration when $\rho_{l_i}^k = \rho_{l_i}^n$, $\rho_{g_i}^n = \rho_{g_i}^n$ and $p_i^k = p_i^n$ the derivatives are computed numerically by adding a small Δp_i to the present value of p_i^k and computing the corresponding values of the fluid densities using the PVT property correlations or doing interpolation in the PVT properties table.

If we combine Eq. 3.27 and 3.33, we obtain our basic step equation for pressures

$$\left(\frac{\Delta t}{\Delta z}\right)p_{i-1}^{n+1} - \left[\frac{2\Delta t}{\Delta z} + \frac{\Delta z}{\Delta t}\frac{\vartheta_{m_i}}{144 g_c}\right]p_i^{n+1} + \left(\frac{\Delta t}{\Delta z}\right)p_{i+1}^{n+1} = \overline{M}_i - \overline{C}_i.\tag{3.37a}$$

where

$$\overline{M}_i = \Delta t\left[M_i - M_{i-1}\right]$$

$$- \left(\frac{2\Delta t}{144 g_c}\right)\left[\left(\frac{f_m}{2d}\right)_{i+1/2}^n \rho_{m_{i+1/2}}^n |v_{m_{i+1/2}}^n| v_{m_{i+1/2}}^k\right]$$

$$+ \left(\frac{2\Delta t}{144g_c}\right)\left[\left(\frac{f_m}{2d}\right)^n_{i-1/2}\rho^n_{m_{i-1/2}}|v^n_{m_{i-1/2}}|v^k_{m_{i-1/2}}\right]$$

$$- \left(\frac{1}{144g_c}\right)\left[\overline{\rho}^k_{m_{i+1/2}}v^k_{m_{i+1/2}} - \overline{\rho}^k_{m_{i-1/2}}v^k_{m_{i-1/2}}\right], \tag{3.38a}$$

and

$$\overline{C}_i = \frac{\Delta z}{\Delta t}\left[\vartheta_{m_i}p^n_i - \left(\rho^k_{g_i} - \rho^k_{l_i}\right)\left(E^k_{g_i} - E^n_{g_i}\right)\right]\left(\frac{1}{144g_c}\right)$$

$$- \left[\rho^k_{m_{i+1/2}}v^k_{m_{i+1/2}} - \rho^k_{m_{i-1/2}}v^k_{m_{i-1/2}}\right]\left(\frac{1}{144g_c}\right). \tag{3.38b}$$

The pressure profile is obtained by solving Eq. 3.37a. Note that the form is such that the associated matrix problem will be strictly diagonally dominant. Next, we introduce our stabilizing equation for the velocities. If we consider our mixture momentum equation as

$$\left[\frac{\overline{\rho}^{n+1}_{m_{i+1/2}}}{\Delta t} + 2\left(\frac{f_m}{2d}\right)^n_{i+1/2}\overline{\rho}^{n+1}_{m_{i+1/2}}|v^n_{m_{i+1/2}}|\right]\frac{v^{n+1}_{m_{i+1/2}}}{144g_c} =$$

$$- \left(\frac{1}{\Delta z}\right)\left[p^{n+1}_{i+1} - p^{n+1}_i\right]$$

$$+ \left[\frac{\overline{\rho}^{n+1}_{m_{i+1/2}}}{\Delta t} + \left(\frac{f_m}{2d}\right)^n_{i+1/2}\overline{\rho}^{n+1}_{m_{i+1/2}}|v^n_{m_{i+1/2}}|\right]\frac{v^n_{m_{i+1/2}}}{144g_c}$$

$$- \frac{\overline{\rho}^{n+1}_{m_{i+1/2}}g}{144g_c} - \frac{\overline{\rho}^{n+1}_{m_{i+1/2}}v^{n+1}_{m_{i+1/2}}}{144g_c\Delta z}\left[v^{n+1}_{m_{i+1}} - v^{n+1}_{m_i}\right]$$

$$- \frac{1}{144g_c\Delta z}\left[\left(\rho_f v^2_r\right)^{n+1}_{i+1} - \left(\rho_f v^2_r\right)^{n+1}_i\right]. \tag{3.39}$$

Again, following the suggestion of Mahaffy[54], additional robustness is obtained with the following approximation of $v\Delta_z v$ term

$$v_{m_{i+1/2}}^{n+1} \left[v_{m_{i+1}}^{n+1} - v_{m_i}^{n+1} \right] = 2 v_{m_{i+1/2}}^{n+1} \left[v_{m_{i+1}}^n - v_{m_i}^n \right] - v_{m_{i+1/2}}^n \left[v_{m_{i+1}}^{n+1} - v_{m_i}^{n+1} \right]. \tag{3.40}$$

Our upstream weighting scheme, Eq. 3.21b gives

$$v_{m_{i+1/2}}^{n+1} \left[v_{m_{i+1}}^{n+1} - v_{m_i}^{n+1} \right] = v_{m_{i+1/2}}^{n+1} \begin{cases} \left(v_{m_{i+1/2}}^{n+1} - v_{m_{i-1/2}}^{n+1} \right), & v_{m_{i+1/2}}^{n+1} \geq 0 \\[2mm] \left(v_{m_{i+3/2}}^{n+1} - v_{m_{i+1/2}}^{n+1} \right), & v_{m_{i+1/2}}^{n+1} < 0, \end{cases}$$

$$= v_{m_{i+1/2}}^{n+1} \left[\alpha_{i+1/2}^1 v_{m_{i+3/2}}^{n+1} + \alpha_{i+1/2}^0 v_{m_{i+1/2}}^{n+1} - \alpha_{i+1/2}^2 v_{m_{i-1/2}}^{n+1} \right] \tag{3.41a}$$

where

$$\alpha_{i+\frac{1}{2}}^0 = SGN \left(v_{m_{i+1/2}}^{n+1} \right) \begin{cases} +1 & v_{m_{i+1/2}}^{n+1} \geq 0 \\[2mm] -1 & v_{m_{i+1/2}}^{n+1} \geq 0, \end{cases} \tag{3.41b}$$

$$\alpha_{i+1/2}^1 = \frac{1 - \alpha_{i+1/2}^0}{2}, \tag{3.41c}$$

$$\alpha_{i+1/2}^2 = \frac{1 + \alpha_{i+1/2}^0}{2}. \tag{3.41d}$$

By using Eq. 3.41a in Eq. 3.40, our $r\Delta_z v$ term becomes

$$v_{m_{i+1/2}}^{n+1} \left[v_{m_{i+1}}^{n+1} - v_{m_i}^{n+1} \right] = \left[2(v_{m_{i+1}}^n - v_{m_i}^n) - \alpha_{i+1/2}^0 v_{m_{i+1/2}}^n \right] v_{m_{i+1/2}}^{n+1}$$

$$- \left(\alpha_{i+1/2}^1 v_{m_{i+1/2}}^n \right) v_{m_{i+3/2}}^{n+1} + \left(\alpha_{i+1/2}^2 v_{m_{i+1/2}}^n \right) v_{m_{i-1/2}}^{n+1}. \tag{3.42}$$

Applying Eq. 3.42 in Eq. 3.39 and we can write the stabilizing equation for velocities as

$$a_{i+1/2} v_{m_{i-1/2}}^{n+1} + b_{i+1/2} v_{m_{i+1/2}}^{n+1} + c_{i+1/2} v_{m_{i+3/2}}^{n+1} = r_i, \tag{3.43a}$$

where

$$a_{i+1/2} = + \frac{\alpha_{i+1/2}^2 v_{m_{i+1/2}}^n}{144 g_c \Delta z}, \tag{3.43b}$$

$$b_{i+1/2} = \left[\frac{1}{\Delta t} + 2\left(\frac{f_m}{2d}\right)^n_{i+1/2} |v^n_{m_{i+1/2}}|\right]\left(\frac{1}{144g_c}\right)$$

$$+ \left(\frac{1}{\Delta z}\right)\left[2\left(v^n_{m_{i+1}} - v^n_{m_i}\right) - \alpha^0_{i+1/2}v^n_{m_{i+1/2}}\right]\left(\frac{1}{144g_c}\right), \quad (3.43c)$$

$$c_{i+1/2} = -\frac{\alpha^1_{i+1/2}v^n_{m_{i+1/2}}}{144g_c\Delta z}, \quad (3.43d)$$

and

$$r_i = \frac{1}{\overline{\rho}^k_{m_{i+1/2}}\Delta z}[p^k_{i+1} - p^k_i] - g +$$

$$+ \left[\frac{1}{\Delta t} + \left(\frac{f_m}{2d}\right)^n_{i+1/2} |v^n_{m_{i+1/2}}|\right]\frac{v^n_{m_{i+1/2}}}{144g_c}$$

$$+ \frac{1}{144g_c\overline{\rho}^k_{m_{i+1/2}}\Delta z}\left[\left(\rho_f v_r^2\right)^k_{i+1} - \left(\rho_f v_r^2\right)^k_i\right]. \quad (3.44)$$

Another option for computing velocities without obtaining stability or convergence difficulties is to simply solve Eq. 3.1, i.e.,

$$\frac{(\rho_m)^{n+1}_i - (\rho_m)^n_i}{\Delta t} + \frac{(\rho_m v_m)^{n+1}_{i+\frac{1}{2}} - (\rho_m v_m)^{n+1}_{i-\frac{1}{2}}}{\Delta z} = 0, \quad (3.45)$$

for velocities from bottom to top once we have solved Eq. 3.43a for pressures. During the implementation of the computational code, we found practically no difference in the response found by using either Eq. 3.43a or 3.45. Since Eq. 3.45 requires less computational effort, we used it to compute velocities.

3.3 Calculation Algorithms.

3.3.1 Drawdown Period Calculation Procedure.

For the drawdown period, the model requires input data on reservoir/well parameters, simulator control data and fluid property data including ρ_{os} and ρ_{gs}, oil-

gas surface tension, and tabulated data for R_s, B_o and B_g as functions of pressure in the case of isothermal flow or as functions of pressure and temperature in the non-isothermal flow case, if this is the case, all the fluid properties are computed by using empirical correlations (see chapter 2 of Ref. 30).

Initially (at $t = 0$) we assume the well is closed so that a gravity equilibrium condition exists in the wellbore. Thus, the static wellbore pressure profile can be computed by only considering the gravity difference from the bottomhole pressure, p_{ws}, to the wellhead.

Once the pressure distribution in the wellbore is known, the calculation of variables during drawdown is based on the solution of a predictor equation for pressure, a stabilizer equation for velocities, a concentration-continuity equation and a simplified energy equation to compute the temperature profile. In the following, we present a detailed description of the procedure for calculating variables at a new timestep, where we assume that production is at specified oil rate at the wellhead, q_o, $[STBO/D]$.

3.3.1.a Calculation at a New Timestep.

During pressure drawdown, pressure, mixture velocity and oil component mass concentration distributions in the wellbore at a new timestep are determined using the following procedure:

In this procedure as in the rest of the calculation procedures, the superscript $(n + 1, k)$ or (k), always denotes the value of the variable at the old iterative time t^{n+1} and $(n + 1)$ denotes the value at the new $(k + 1)$ iteration step.

1. Guess values for $(C_l)_i^{n+1}$ for $i = 1, ..., N$, denoted $(C_l)_i^{k+1}$ to obtain an approximation for the new oil component mass concentration profile. This guess can be obtained by simply using the values at the old time step.

2. For the non-isothermal case, guess values for $(T_f)_i^{k+1}$. For the first timestep during the drawdown period, a linear temperature profile is used as the initial guess, i.e.,

$$(T_f)_i^{k+1} = T_{bh} - g_e(L_{bh} - z_i) \qquad (3.46)$$

where T_{bh} is the temperature at bottomhole in $[°F]$, g_e is the geothermal gradient in $[°F/100 \ ft]$ and L_{bh} is the depth of the well in the z-direction in $[100 \ ft]$, z_i is the depth in the z-direction of the wellbore gridblock i in $[100 \ ft]$. For the subsequent timesteps, $(T_f)_i^{k+1} = (T_f)_i^n$ is used as the initial guess. In case of isothermal computations, we set $(T_f)_i^{k+1} = (T_f)_{av}$.

3. Calculate the mixture sandface velocity, $(v_m)_{\frac{1}{2}}^{n+1}$, that satisfies both the bottomhole boundary condition and the wellbore mass conservation, by the following procedure:

   (a) Assume a sandface velocity and the total production rate, $(q_t)^{k+1}$. As initial guess the value at the old timestep is used.

   (b) Calculate the distribution of the total gas-oil ratio, R, and determine the distribution of the bubble-point pressure along the wellbore from linear interpolation with the physical properties table for the isothermal case or from the PVT correlation for R_s in case of non-isothermal computations.

(c) From the bottomhole boundary condition and using the total production rate $(q_t)^{k+1}$, calculate the bottomhole pressure, $p_{\frac{1}{2}}^{k+1} = p_{wf}^{n+1}$, obtained from the analytical solution or from the (r-z) reservoir simulator.

(d) Calculate the pressure profile using the predictor equation for pressures, Eq. 3.37a. In applying Eq. 3.37a all the physical properties are computed using interpolation with the physical properties table in the isothermal case or directly from PVT-correlations in the non-isothermal case.

(e) Once we compute p_i^{k+1}, calculate $(\rho_g)_i^{k+1}$ and $(\rho_l)_i^{k+1}$, from Eq. 2.11 and 2.12, i.e.,

$$(\rho_g)_i^{k+1} = \left(\frac{\rho_{gs}}{5.615 B_g}\right)_i^{k+1}, \tag{2.11}$$

and

$$(\rho_l)_i^{k+1} = \left(\frac{R_s \rho_{gs}}{5.615 B_o} + \frac{\rho_{os}}{B_o}\right)_i^{k+1}. \tag{2.12}$$

(f) Calculate $(E_l)_i^{k+1}$ and calculate $(\rho_m)_i^k$, from Eqs. 2.31 and 2.25 respectively, i.e.,

$$(E_l)_i^{k+1} = \left(\frac{B_o}{B_o + B_g(R - R_s)}\right)_i^{k+1}, \tag{2.31}$$

$$(\rho_m)_i^k = (\rho_g E_g + \rho_l E_l)_i^{k+1}. \tag{2.25}$$

(g) Using the stabilizer equation for velocities, Eq. 3.43a or 3.45 , calculate $v_{m_i}^{n+1,k+1}$.

(h) If $|p_i^{k+1} - p_i^k| > \epsilon$, let $p_i^k = p_i^{k+1}$, and go back to step 3c.

(i) Update the oil component mass concentration, Eq. 3.14a;

(j) Compute the new values of $(T_f)_i^{k+1}$, using the procedure to calculate temperature and overall heat transfer coefficient, described in section 2.2.3.

(k) Check convergence. If $|(C_l)_i^{k+1} - (C_l)_i^k| < \epsilon$ is not satisfied for any i ($i = 1, 2, ..., N$), replace $(C_l)_i^k$ by $(C_l)_i^{k+1}$ for $i = 1, 2, ..., N$ and go back to step 3.b.

(l) Calculate a new sandface velocity, $(v_m)_{\frac{1}{2}, mass\,balance}^{k+1}$, from Eq. 3.5.

(m) To accelerate convergence of the sandface velocity from Steps 3a to 3l, we use the secant method[55]. Let x_0 and x_1 represent two initial guesses of the sandface mixture velocity, and Δx_0 and Δx_1 denote the corresponding velocity differences between the guessed value and the one obtained from Step 3l. Based on the secant method, a new velocity should be determined as

$$(v_m)_{\frac{1}{2}}^{k+1} = x_2 = x_1 - \frac{\Delta x_1(x_1 - x_0)}{\Delta x_1 - \Delta x_0}. \qquad (3.47)$$

(n) A check of convergence is made, $|(v_m)_{\frac{1}{2}, mass\,balance}^{k+1} - (v_m)_{\frac{1}{2}}^{k+1}| < \epsilon$. If convergence is not achieved, set $\Delta x_o = \Delta x_1$,

$\Delta x_1 = \left[(v_m)_{\frac{1}{2}, mass\,balance}^{k+1} - (v_m)_{\frac{1}{2}}^{k+1}\right]$, $x_o = x_1$, $x_1 = (v_m)_{\frac{1}{2}}^{k+1}$ and $(v_m)_{\frac{1}{2}}^{k+1} = x_2$. Repeat steps 3b-3n until convergence.

4. Accept all the values of the variables at the iteration level $k + 1$ as the correct values of time level $n + 1$, i.e., $(p)_i^{n+1} = (p)_i^{k+1}$, etc.

5. Repeat steps 1-3 for all time steps.

3.3.1.b Calculation of Distributions of Dependent Variables Under Steady State Flow Conditions.

Under the assumption that steady-state conditions have been reached during the production period. from the production rate, q, and production time, t_p, the bottomhole pressure at the instant of shut-in, $p_{wf,s}$, is computed from the semilog approximation (Eq. 2.155) or is obtained from the reservoir simulator results.

When steady-state two-phase flow is assumed to exist in the wellbore before shut-in, once than the pressure is known at any wellbore gridblock position the following procedure can be used to compute the value of dependent variables at the gridblock.

Dependent Variables Computational Procedure for Steady State Two-Phase Flow.

i. From a known pressure, the PVT fluid properties, i.e., R_s, B_o, B_g, are computed from PVT fluid properties table interpolation or from PVT fluid properties correlations[30].

ii. Compute ρ_g and ρ_g using Eqs. 2.11 and 2.12, i.e.,

$$\rho_g = \frac{\rho_{gs}}{5.615\,B_g},$$

(2.11)

$$\rho_l = \frac{R_s \rho_{gs}}{5.615\,B_o} + \frac{\rho_{os}}{B_o}.$$

(2.12)

iii. From mass balance, calculate the in-situ gas and liquid phase volumetric flow

rate, q_g and q_l in $[ft^3/\sec.]$:

$$q_g = \frac{5.615\,[q_{gs} - q_{os}R_s]\,B_g}{86400}.$$ (3.48)

$$q_l = \frac{5.615\,q_{os}B_o}{86400}.$$ (3.49)

iv. Calculate the superficial gas and liquid velocities, v_{sg} and v_{sl} respectively, from

Eqs. 2.32 and 2.33,

$$v_{sg} = \frac{q_g}{A},$$ (2.32)

$$v_{sl} = \frac{q_l}{A}.$$ (2.33)

v. Compute the gas void fraction from Eq. 2.31, i.e.,

$$E_l = \frac{B_o}{B_o + B_g(R - R_s)}.$$ (2.31)

vi. Determine the existing flow pattern from Fig. 2.2.

vii. Calculate the relative velocity, v_r, according to the flow pattern Eqs. 2.139 to

2.141 and verify the value of E_l using the following equation:

$$\frac{v_{sg}}{1 - E_l} - \frac{v_{sl}}{E_l} = v_r.$$ (3.50)

viii. Finally compute the mixture properties, mixture density, ρ_m, and velocity, v_m.

using Eqs. 2.25 and 2.39, i.e.,

$$\rho_m = \rho_g E_g + \rho_l E_l,$$ (2.25)

$$v_m = \frac{v_{sg}\rho_g + v_{sl}\rho_l}{\rho_m}.$$ (2.39)

ix. Calculate the oil component concentration. C_l, and the in-situ total gas oil ration. R, i.e..

$$C_l = \frac{E_l \rho_{ol}}{\rho_m},$$ (3.51)

$$R = \left(\frac{C_g}{C_l}\right)\left(\frac{5.615\rho_{os}}{\rho_{gs}}\right).$$ (3.52)

x. Using the value of R the corresponding bubble-point pressure can be computed from R_s table interpolation or from R_s PVT-correlations.

Pressure and Dependent Variables Distribution - Calculation Procedure. The distribution of the dependent variables along the wellbore under steady-state two-phase flow conditions is determined according to the following procedure:

1. Considering the bottomhole pressure, $p_{\frac{1}{2}} = p_{wf,s}$, obtained from the analytical solution or from the (r-z) reservoir simulator, we compute $(v_m)_{\frac{1}{2}}$ with the procedure described in dependent variables computation procedure section.

2. Guess a value of $p^*_{1+\frac{1}{2}}$.

3. Compute $p_1 = \frac{1}{2}[p_{\frac{1}{2}} + p^*_{1+\frac{1}{2}}]$.

4. Using p_1 compute $(C_l)_1$ and $(\rho_m)_1$ and all the other variables as described previously in the dependent variables computation procedure section.

5. Calculate $p_{1+\frac{1}{2}}$ from a steady-state two-phase flow momentum equation.

6. if $\left|p_{1+\frac{1}{2}} + p_{1+\frac{1}{2}}^*\right| > \epsilon$, let $p_{1+\frac{1}{2}}^* = p_{1+\frac{1}{2}}$ and go back to step 3.

7. Once the procedure converges, compute $(v_m)_{1+\frac{1}{2}}$ using $p_{1+\frac{1}{2}}$ and the dependent variables computation procedure previously described.

8. Repeat step 2-7 for all the wellbore gridblocks, until the wellhead position is reached.

3.3.2   Buildup Period Calculation Procedure.

The model requires input data on reservoir/well parameters, simulator control data and fluid property data including ρ_{os} and ρ_{gs}, oil-gas surface tension, and tabulated data for R_s, B_o and B_g as functions of pressure in the case of isothermal flow or computed using PVT correlations for the non-isothermal flow case. For results presented here, R_s, B_o and B_g as functions of pressure and temperature are obtained from empirical correlations[30].

The model offers the option of assuming that steady-state flow exists in the wellbore prior to shut-in and that during the flow period, we produce the reservoir at a constant total sandface rate, q_t, [RB/D], or a transient flow simulation can be done during the drawdown period, assuming that we produce at a constant wellhead rate, q_o, [STBO/D].

In considering steady-state flow for the drawdown period, from the production rate, q_t, and producing time, t_p, we can calculate the bottomhole pressure at the instant of shut-in, $p_{wf,s}$, using the semilog approximation or using the RDRBOS (r-z) simulator. For steady-state flow, if the pressure at a given position is known, all other

variables can be calculated. But in case of simulating the complete drawdown period using our simulator. as described in previous section, the producing conditions that exists at the instant of the shut-in are used, that means, that the bottomhole pressure present at the instant of shut-in is set as the $p_{wf,s}$.

Once the distribution of variables at the instant of shut-in is known. the calculation of variables during buildup is based on the solution of a predictor equation for pressures, a stabilizer equation for velocities, a concentration-continuity equation and a simplified energy equation to compute the temperature profile as was previously described. In the following, we present a detailed description of the procedure for calculating variables at a new timestep.

3.3.2.a Calculation at a New Timestep.

During pressure buildup, pressure, mixture velocity and oil component mass concentration distributions in the wellbore at a new timestep are determined using the following procedure:

1. Guess values for $(C_l)_i^{n+1}$ for $i = 1, ..., N$. denoted $(C_l)_i^{k-1}$, to obtain an approximation for the new oil component mass concentration profile. This guess can be obtained either by extrapolation of values at the previous timesteps or by simply using the value at the old time step.

2. Guess values for $(T_f)_i^{k+1}$ for the non-isothermal case. For the first timestep during the build-up period, the temperature profile from the drawdown period is used as the initial guess, and for the subsequent timesteps, $(T_f)_i^{k+1} = (T_f)_i^n$ is

used as the initial guess. In case of isothermal computations, we set $(T_f)_i^{k+1} = (T_f)_{av}$.

3. Calculate the distribution of the total gas-oil ratio, R, and determine the distribution of the bubble-point pressure along the wellbore from linear interpolation with the physical properties table for the isothermal case or from the PVT correlation for R_s in case of non-isothermal computations.

4. Calculate the sandface velocity, $(v_m)_{\frac{1}{2}}^{n+1}$, that satisfies both the bottomhole boundary condition and the wellbore mass conservation, by the following procedure:

   (a) Assume a sandface velocity. This value can be obtained by simply using the value at the old timestep.

   (b) From the bottomhole boundary condition, calculate the bottomhole pressure, $p_{\frac{1}{2}}^{k+1} = p_{ws}^{n+1}$. obtained from the analytical solution or from the (r-z) reservoir simulator.

   (c) Calculate the pressure profile using the predictor equation for pressures, Eq. 3.37a. Note that all the physical properties are computed using interpolation with the physical properties table or directly from PVT-correlations.

   (d) Once we compute p^{k+1}, calculate $\rho_{l_i}^{k+1}$ and $\rho_{g_i}^{k+1}$,from Eq. 2.11 and 2.12, i.e.,

$$(\rho_g)_i^{k+1} = \left(\frac{\rho_{gs}}{5.615 B_g}\right)_i^{k+1},$$

(2.11)

and

$$(\rho_l)_i^{k+1} = \left(\frac{R_s \rho_{gs}}{5.615 B_o} + \frac{\rho_{os}}{B_o}\right)_i^{k+1}.$$

(2.12)

(e) Calculate $E_{l_i}^{k+1}$ and calculate $\rho_{m_i}^{k+1}$, from Eqs. 2.31 and 2.25 respectively, i.e.,

$$(E_l)_i^{k+1} = \left(\frac{B_o}{B_o + B_g(R - R_s)}\right)_i^{k+1},$$

(2.31)

$$(\rho_m)_i^k = (\rho_g E_g + \rho_l E_l)_i^{k+1}.$$

(2.25)

(f) Using the stabilizer equation for velocities, Eq. 3.43a or 3.45, calculate $v_{m_i}^{k+1}$.

(g) If $|p_i^{n+1,k} - p_i^{n+1,k+1}| > \epsilon$, let $p_i^{n+1,k} = p_i^{n+1,k+1}$, and go back to step 4c.

(h) Calculate a new sandface velocity, $(v_m)_{\frac{1}{2}, massbalance}^{k+1}$, from Eq. 3.4.

(i) To accelerate convergence on the sandface velocity from Steps 4a to 4h, we use the secant method[55]. Let x_0 and x_1 represent two initial guesses of the sandface velocity, and Δx_0 and Δx_1 denote the corresponding velocity differences between the guessed value and the one obtained from Steps 4h. Based on the secant method, a new velocity should be determined as

$$(v_m)_{\frac{1}{2}}^{k+1} = x_2 = x_1 - \frac{\Delta x_1 (x_1 - x_0)}{\Delta x_1 - \Delta x_0}.$$

(3.53)

(j) A check of convergence is made, $|(v_m)_{\frac{1}{2}, massbalance}^{k+1} - (v_m)_{\frac{1}{2}}^{k+1}| < \epsilon$. If convergence is not achieved, set $\Delta x_o = \Delta x_1$,

$$\Delta x_1 = \left[(v_m)^{k+1}_{\frac{1}{2},mass\,balance} - (v_m)^{k+1}_{\frac{1}{2}} \right], \quad x_o = x_1, \quad x_1 = (v_m)^{k+1}_{\frac{1}{2}}, \quad \text{and}$$

$(v_m)^{k+1}_{\frac{1}{2}} = x_2, \, \Delta x_o = \Delta x_1$. Repeat steps 4b-4j until convergence.

5. Update the oil component mass concentration using Eq. 3.45.

6. Compute the new values of $(T_f)^{k+1}_i$, using the procedure to calculate temperature and overall heat transfer coefficient, described in section 2.2.3.

7. Check convergence. If $|(C_l)^{k+1}_i - (C_l)^k_i| < \epsilon$ is not satisfied for any i ($i = 1, 2, ..., N$), replace $(C_l)^k_i$ by $(C_l)^{k+1}_i$ for $i = 1, 2, ..., N$ and go back to step 2.

8. Accept all the values of the variables at the iteration level $k + 1$ as the correct values at the time level $n + 1$, i.e., $(p)^{n+1}_i = (p)^{k+1}_i$, etc.

9. Repeat steps 1-8 for all time steps.

CHAPTER IV

ANALYSIS OF RESULTS.

In this chapter, pressure responses generated with the simulator for several pressure drawdown and buildup tests are presented and discussed. These cases were used to verify that the model gives physically meaningful results, to consider numerically accuracy and stability and to investigate the validity of the Fair[1] and Hegeman[2] models for wellbore phase redistribution. Cases A consider drawdown and buildup tests in a naturally flowing well where only single-phase oil flows in the wellbore prior to shut-in. Cases B are buildup tests in a naturally flowing well, but unlike Cases A, the bottomhole flowing pressures in Cases B are only slightly higher than the reservoir fluid initial bubble-point pressure and as a result, two-phase flow develops in the wellbore during production. Cases C represent pressure buildup tests conducted in a gas-lift well producing only single phase oil from the reservoir. Cases M represent pressure drawdown and buildup tests conducted in a naturally flowing well: in all these cases the RDRBOS two-dimensional (r-z) reservoir simulator is coupled to the wellbore model to numerically simulate the reservoir. This option allow us to simulate two-phase flow in both the wellbore and reservoir.

82

4.1 Model Validation.

4.1.1 Simulation of Single Phase Flow.

Here, we consider a pressure drawdown and buildup tests for wells having only single phase oil flow in both the wellbore and the reservoir. The wellbore storage is due to wellbore fluid compressibility. The drawdown data can be analyzed with the classical wellbore storage and skin type curves, to estimate values of skin factor, wellbore storage and formation flow capacity. The buildup data acquired in these tests can be analyzed with Horner analysis and type-curve matching with the wellbore storage and skin drawdown type curves to yield values of formation flow capacity, skin factor and wellbore storage coefficient. The reservoir was infinite-acting during the tests so that the Horner straight line should extrapolate to the initial reservoir pressure at infinite shut-in time.

Case A was designed as the way to verify our simulator under single phase liquid flow conditions in the wellbore. Table 4.1 presents a list of input parameters for Case A. A flow period of 50-hours followed by a 20-hours buildup test was considered. It is important to notice that for single-phase flow, there is no separation of gas and oil components; thus, the bubble-point pressure remains constant along the wellbore.

The log-log plots of drawdown and buildup data for Case A are shown in Fig. 4.1 and 4.2, respectively. At early time, pressure and pressure derivative data form a unit slope straight line, showing the effect of wellbore storage. As shown in Fig. 4.1 for the drawdown period and Fig. 4.2 for the buildup period, nonlinear regression with the classical wellbore storage and skin model yields parameters which
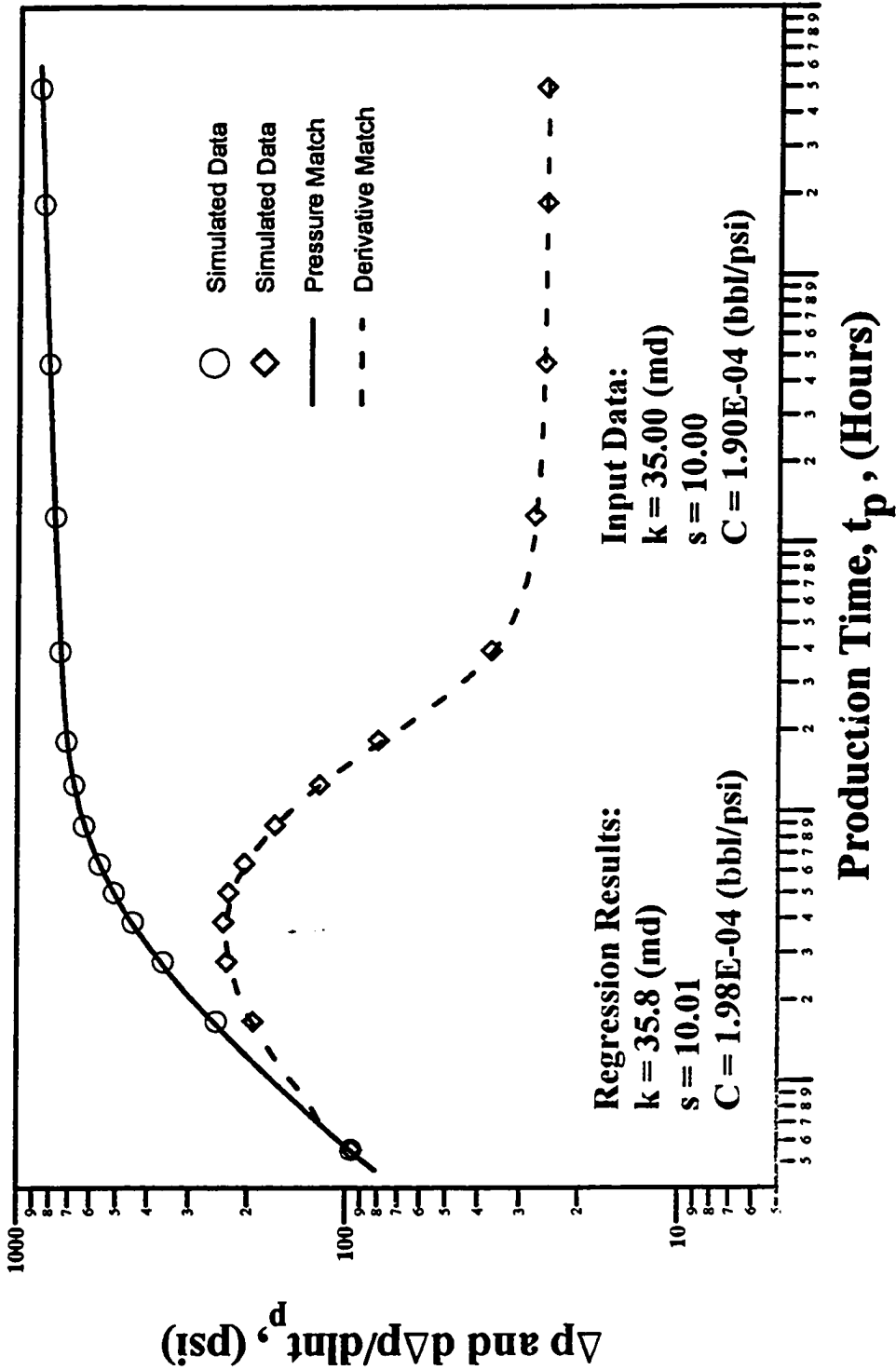
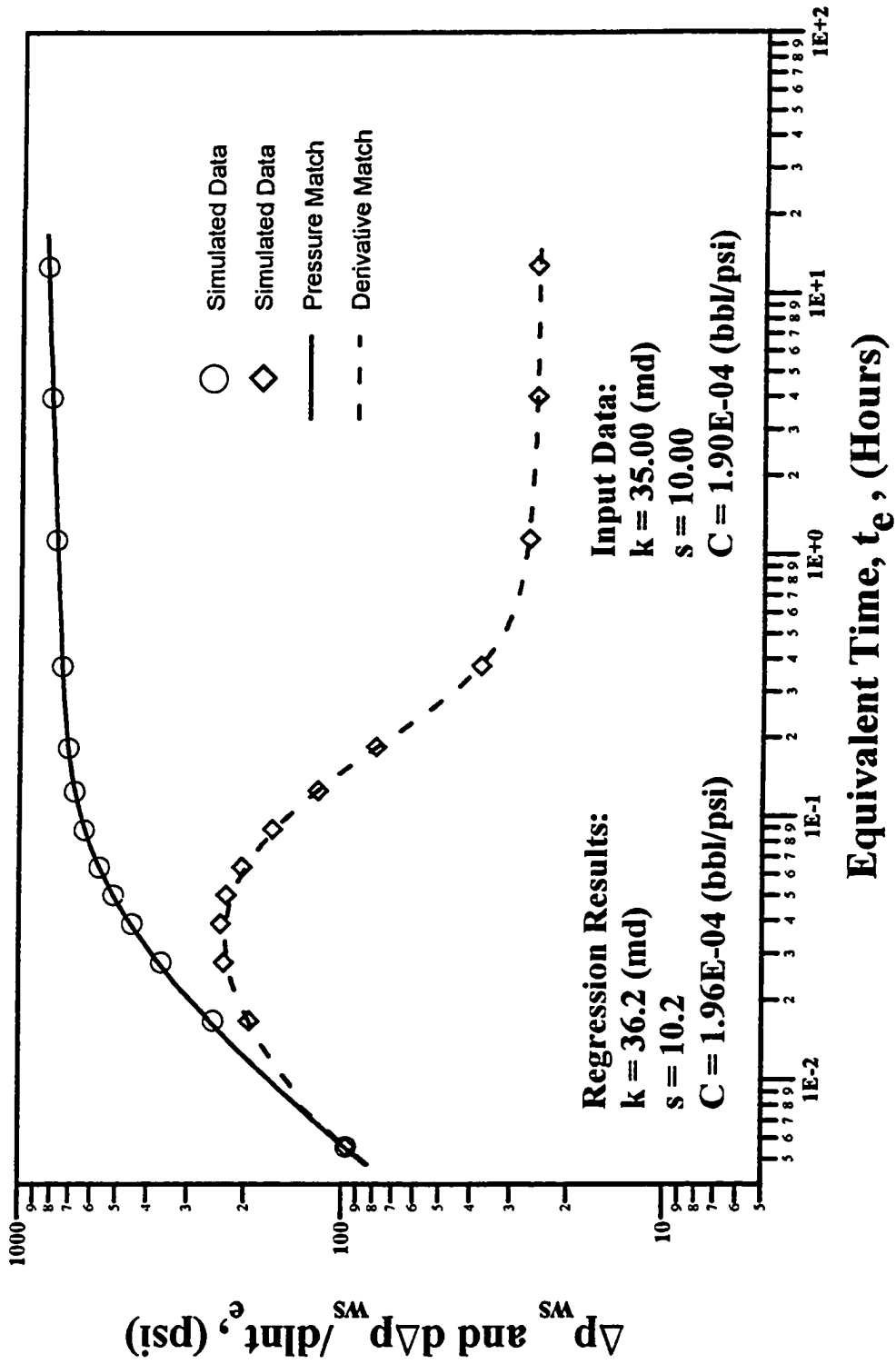**Fig. 4.1 - Type Curve Analysis for Case A, Single Phase Oil Well**

Fig. 4.2 - Type Curve Analysis for Case A, Single Phase Oil Well

Parameter	Value	Unit
Drawdown oil production rate	95.00	RB/D
Total production time	50.00	hours
Inital reservoir pressure	5215.00	psia
Initial bubble point pressure	214.70	psia
Oil compressibility (p>p_b)	1.0e-5	1/psia
Oil component API gravity at s.c.	45.00	API
Gas component specific gravity at s.c.	0.70	-
Oil-gas surface tension	4.50	dynes/cm
Wellbore pipe inside diameter	1.80	inch
Formation absolute permeability	35.00	md.
Formation thickness	15.00	ft.
Formation porosity	0.20	-
Wellbore radius	0.364	ft.
System isothermal compressibility	2e-5	1/psia
Average oil viscosity	2.00	cp.
Skin factor	10.00	-
Wellbore depth	6000.00	ft.
Spatial Increment	30.00	ft.
Buildup simulation time	20.00	hours

Table 4.1: Input Parameters for Case A

are in excellent agreement with their corresponding input values. The input value for the wellbore storage coefficient is calculated from the input fluid compressibility ($c_f = 1.0 \times 10^{-5}\,\text{psia}^{-1}$) and the wellbore volume. i.e., $C = c_f V_w = 1.90 \times 10^{-4}$ bbl/psia.

A Horner plot of pressure buildup data for case A is presented in Fig. 4.3. At early times, pressure data deviate from the semilog straight line: this deviation is due to wellbore storage effects. At late times, buildup data exhibit a semilog straight line; semilog analysis of these data yields estimates of flow capacity, skin factor and the initial reservoir pressure. As noted in Fig. 4.3, the parameters calculated from semilog analysis agree very well with their corresponding input values.

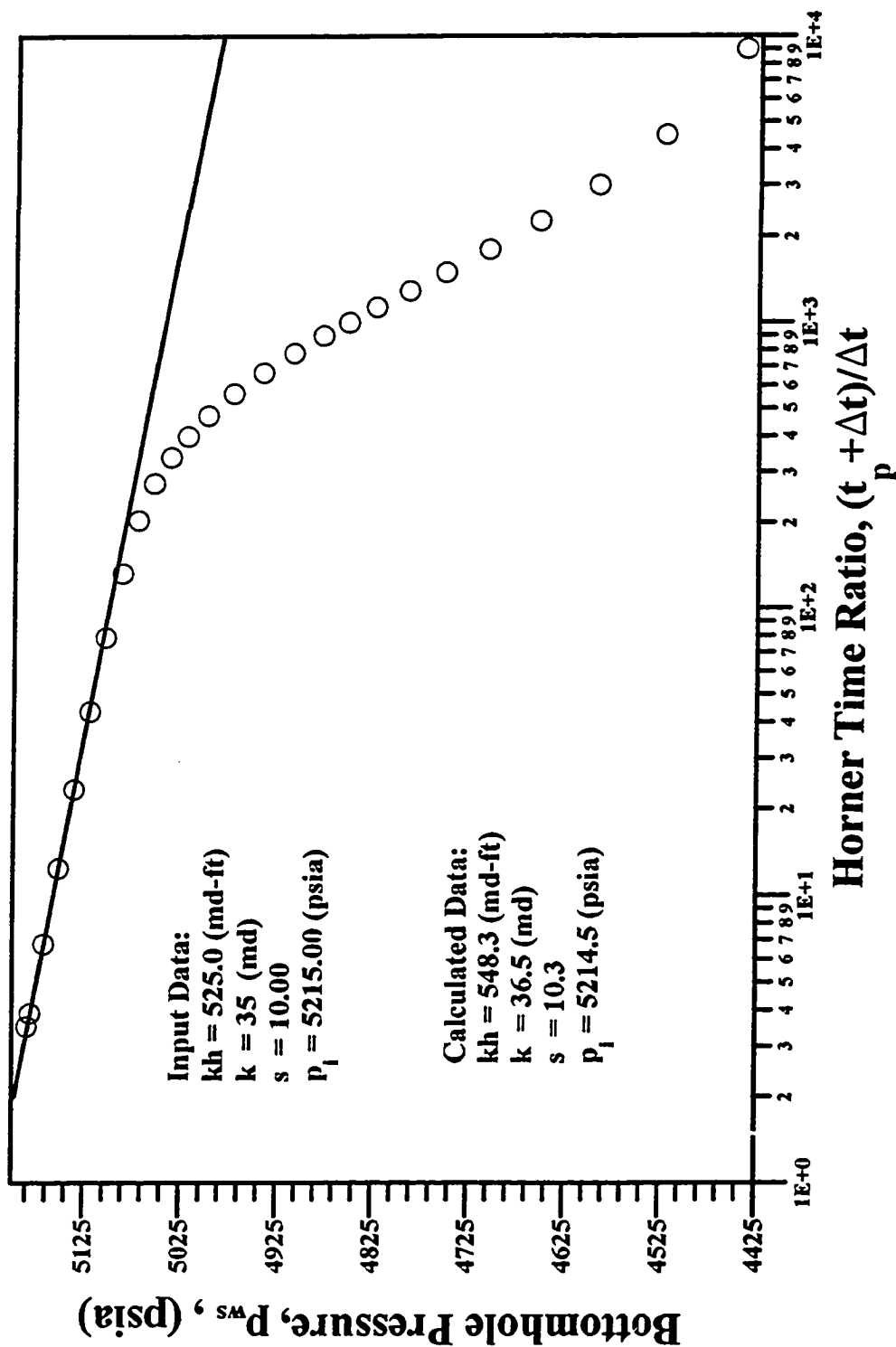A plot of the variation in sandface flow rate as a function of shut-in time is

Fig. 4.3 – Horner Plot of Pressure Buildup Data for Case A

Input Data:
kh = 525.0 (md-ft)
k = 35 (md)
s = 10.00
p_i = 5215.00 (psia)

Calculated Data:
kh = 548.3 (md-ft)
k = 36.5 (md)
s = 10.3
p_i = 5214.5 (psia)

shown in Fig. 4.4. It can be seen that the sandface rate undergoes a significant decline at early shut-in times, i.e., at the beginning of the test, and is approximately a straight line, indicating that rate decline is approximately of exponential form, as suggested by Van Everdingen and Hurst[3].

The bottomhole pressure and sandface flow rate generated with the simulator can be used to calculate the wellbore storage coefficient. The wellbore storage coefficient is defined as the change of total volume of wellbore fluids per unit change in bottomhole pressure:

$$C = \frac{\Delta V}{\Delta p},$$
(4.1)

where ΔV is the change in volume of fluid in the wellbore at wellbore conditions in [bbl], and Δp is the change in bottomhole pressure in [psia]. For pressure buildup tests, Eq. 4.1 can be written as

$$C = \frac{dV/dt}{dp_{ws}/dt} = \frac{q_{sf}/24}{dp_{ws}/dt}.$$
(4.2)

where q_{sf} is in [RB/D] and p_{ws}/dt is in [psia/hour].

For the drawdown period, part of the produced fluid comes from the expansion of the fluids in the wellbore, the wellbore storage is caused by fluid compressibility and can be computed from

$$C = c_f \, V_w$$
(4.3)

where c_f is the compressibility of the wellbore fluids in [psia^{-1}] and V_w is the wellbore volume in [bbl].
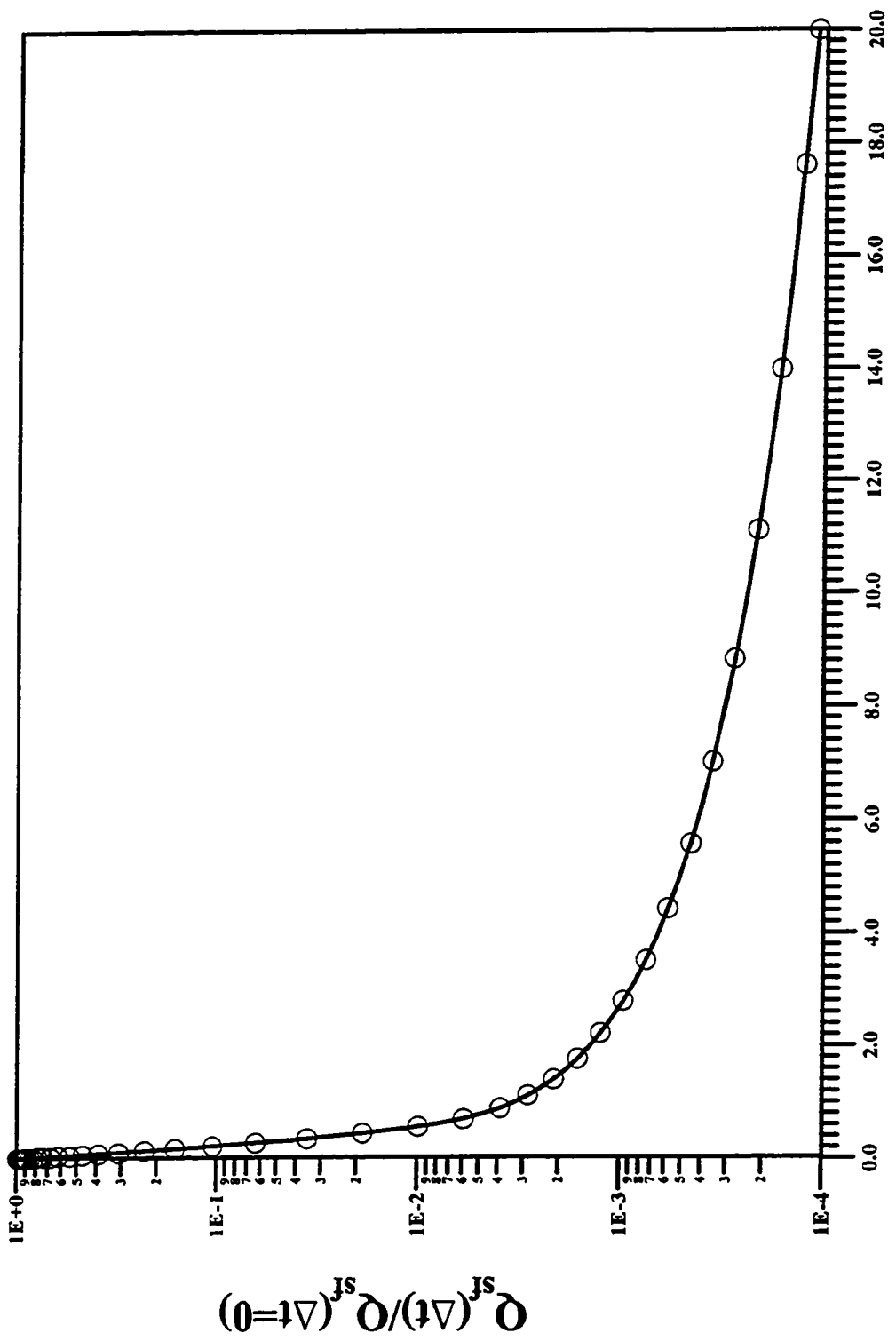
Fig. 4.4 – Normalized Sandface Flow Rate as a Function of Shut-in Time for Case A.

For the drawdown period, using the value of the oil compressibility and the volume of the wellbore, a wellbore storage coefficient of 1.90×10^{-4} bbl/psia is obtained. During the buildup test, applying bottomhole pressure and sandface flow rate data in Eq. 4.2, a constant wellbore storage coefficient of 1.85×10^{-4} bbl/psia is obtained for the entire duration of the test even though both p_{ws} and q_{sf} are varying. Note that this value differs slightly from 1.88×10^{-4} bbl/psia obtained from Eq. 4.3. The calculated value using nonlinear regression for C for the drawdown period is 1.94×10^{-4} bbl/psia and for the buildup period is 1.93×10^{-4} bbl/psia, these values are in excellent agreement with the input value which is computed from the input oil compressibility and the wellbore volume.

For the single-phase flow case, the results obtained and shown in Figs. 4.1-4.4 validate our model and solution algorithm, for the single-phase flow case.

4.1.2   Model Stability Verification.

In this section, pressure responses generated with our numerical simulator for two pressure buildup tests are presented and analyzed. Case B is a buildup test in a naturally flowing well, the bottomhole pressure in cases B is slightly higher than the reservoir fluid initial bubble-point and as a result, two-phase flow develops in the wellbore during production but single-phase flow exists in the reservoir. Case C represents a pressure buildup test conducted in a gas-lift well producing only single phase oil from the reservoir. Results from the new simulation are compared with results obtained from the explicit model of Ref. 19, using a finite grid and small time steps, $\Delta z = 30$ ft. and $\Delta t = 4$ sec. This small time step results are assumed to give

the correct solution.

4.1.2.a   Case B.

Case B is a pressure build-up test in a well that was flowed at a constant sandface rate for 120 hours prior to conducting a 20 hours pressure buildup test. The objective is to simulate the transient process of wellbore phase segregation and to examine its effect on pressure buildup data analysis. Input parameters of Case B are chosen such that bottomhole pressure is only a few psi higher than the initial reservoir bubble-point pressure, and consequently, only single-phase flow occurs in the reservoir, but two-phase flow develops in the wellbore. Table 4.2 gives a list of input parameters used in Case B and Table 4.3 tabulates B_o, R_s and B_g as functions of pressure (wellbore temperature is assumed to be 150°F).

Fig. 4.5 presents a log-log plot of buildup data generated for Case B using our previous explicit simulator[19] with several different values of the time step. Throughout the Courant number is defined by $v\,\Delta t/\Delta x$ where Δt is referred to the size of the time step (not shut-in time) used in the simulation. In computing the Courant number for the buildup period. we always set v equal to the bottomhole mixture velocity at the instant of shut-in. Toward the end of the buildup test, the derivative is still decreasing and fitting a semilog straight line through the last data points will yield a low estimate of kh. At early times, although wellbore segregation is taking place, the buildup data show the classical appearance of the wellbore storage and skin solution. In the transition region, the derivative data curve rises above the pressure data, indicating a decreasing wellbore storage[2] (see Fig. 4.6). The behavior of the buildup

Parameter	Value	Unit
Drawdown oil production rate	100.00	RB/D
Total production time	120.00	hours
Inital reservoir pressure	5215.00	psia
Initial bubble point pressure	2710.00	psia
Oil compressibility (p>p_b)	1.0e-5	1/psia
Oil component API gravity at s.c.	45.00	API
Gas component specific gravity at s.c.	0.70	-
Oil-gas surface tension	4.50	dynes/cm.
Wellbore pipe inside diameter	1.80	inch
Formation absolute permeability	25.00	md.
Formation thickness	10.00	ft.
Formation porosity	0.20	-
Wellbore radius	0.364	ft.
System isothermal compressibility	2e-5	1/psia
Average oil viscosity	2.00	cp.
Skin factor	15.00	-
Wellbore depth	9000.00	ft.
Spatial Increment	30.00	ft.
Buildup simulation time	20.00	hours

Table 4.2: Input Parameters for Case B

data is comparable to the behavior of field data reported by Hegeman et al.[2]

The wellbore storage coefficient calculated from Eq. 4.2 is presented in Fig. 4.6. As shown in Fig. 4.6, this well experiences an order of magnitude decrease in the wellbore storage coefficient during the 20-hour pressure buildup test. At early times, buildup data show a constant wellbore storage coefficient, the wellbore storage coefficient declines sharply around $\Delta t = 1.0$ hour which, as shown later, roughly corresponds to the time when the gas column begins to be compressed. At late times, the well again behaves like a well with a constant wellbore storage coefficient. Fig. 4.7 presents sandface flow rate as a function of shut-in time. Compared to Case A, the sandface flow rate for Case B decreases more slowly.

We expect that the explicit method will be stable as long as the time step is

p	B_o	R_s	B_g
(psia)	(RB/STB)	(scf/STB)	(RB/scf)
214.7	1.059474	45.256641	0.139674E-01
414.7	1.082794	100.044716	0.705830E-02
614.7	1.109518	160.754761	0.464529E-02
814.7	1.139001	225.723618	0.342061E-02
1014.7	1.170882	294.077362	0.268376E-02
1214.7	1.204915	365.266510	0.219513E-02
1414.7	1.240920	438.909729	0.185027E-02
1614.7	1.278753	514.725098	0.159619E-02
1814.7	1.318298	592.494812	0.140309E-02
2014.7	1.359457	672.044739	0.125281E-02
2214.7	1.402147	753.232605	0.113366E-02
2414.7	1.446294	835.939514	0.103775E-02
2614.7	1.491835	920.064026	0.959553E-03
2814.7	1.538714	1005.519287	0.895068E-03
3014.7	1.586879	1092.229370	0.841354E-03
3214.7	1.636284	1180.127563	0.796194E-03
3414.7	1.686889	1269.154541	0.757891E-03
3614.7	1.738654	1359.257568	0.725133E-03
3814.7	1.791545	1450.389038	0.696891E-03
4014.7	1.845530	1542.505493	0.672355E-03
4214.7	1.900579	1635.567871	0.650881E-03
4414.7	1.956664	1729.540405	0.631954E-03
4614.7	2.013758	1824.389648	0.615160E-03
4814.7	2.071839	1920.085938	0.600165E-03
5014.7	2.130883	2016.600464	0.586700E-03
5214.7	2.190870	2113.907959	0.574546E-03
5414.7	2.251778	2211.983643	0.563524E-03
5614.7	2.313589	2310.804688	0.553491E-03
5814.7	2.376285	2410.350342	0.544329E-03
6014.7	2.439848	2510.600098	0.535942E-03

Table 4.3: Physical Properties as Function of Pressure for Case B
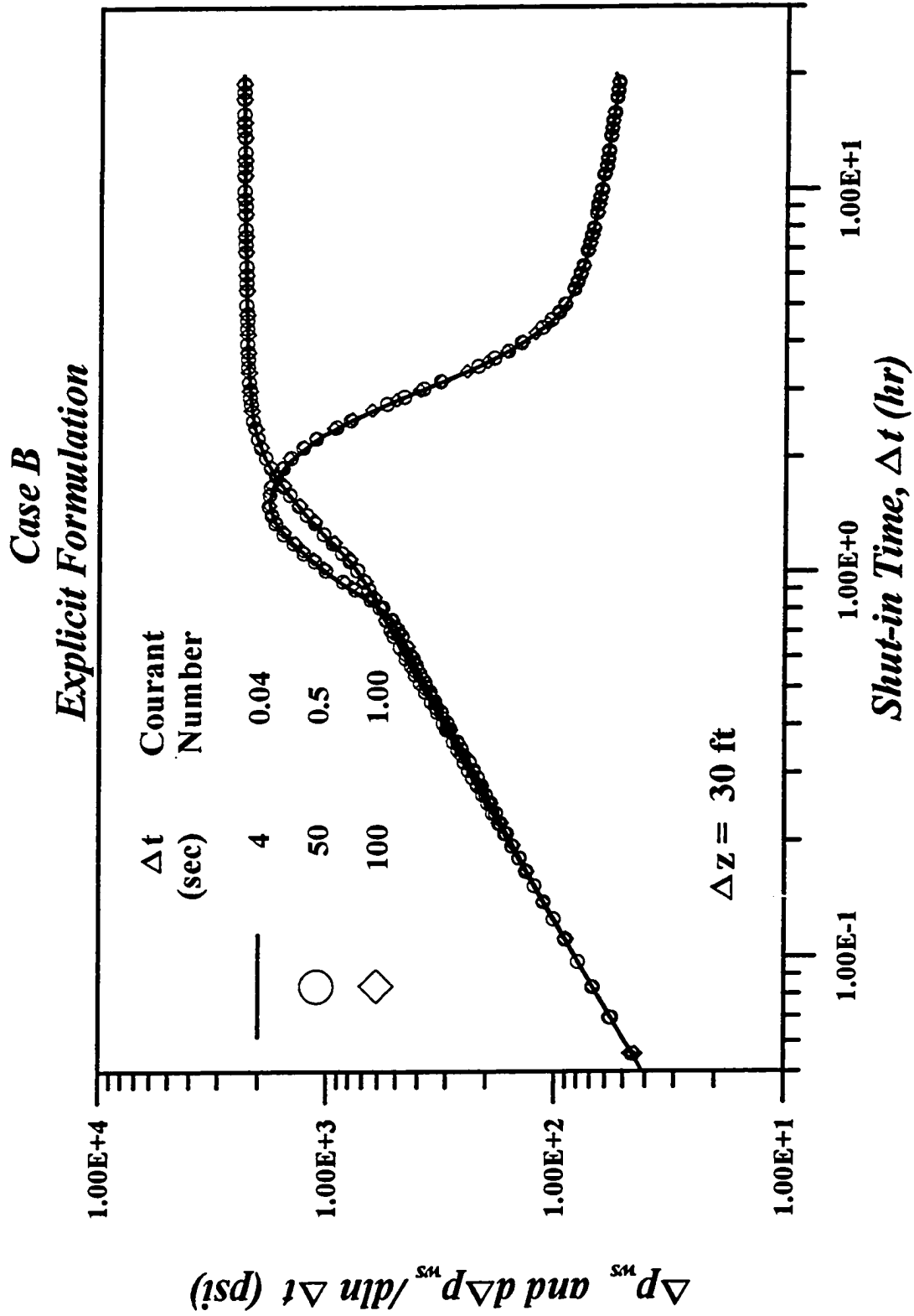
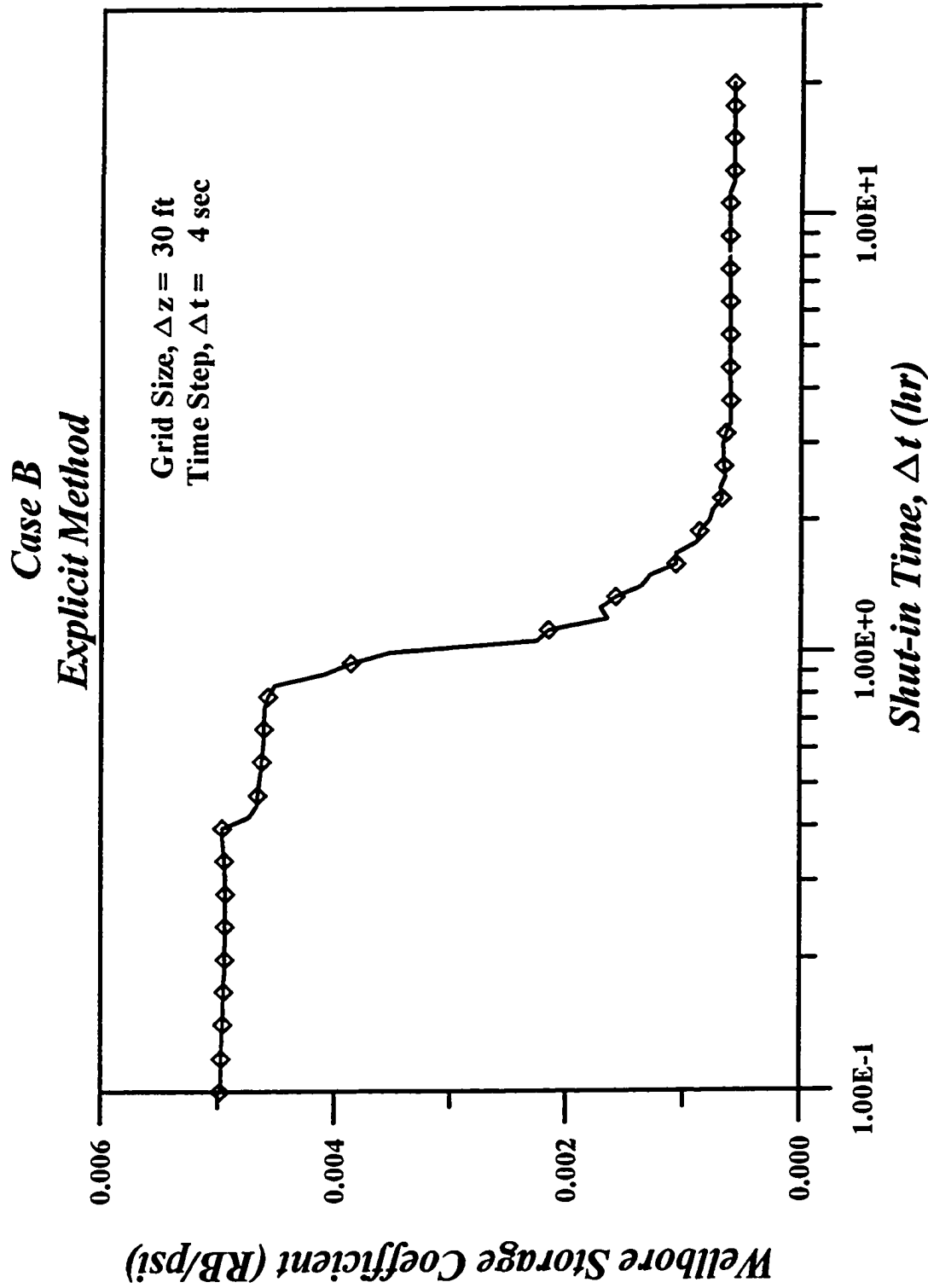Fig. 4.5 - Log-Log Plot of Pressure and Pressure Derivative for Case B.

95

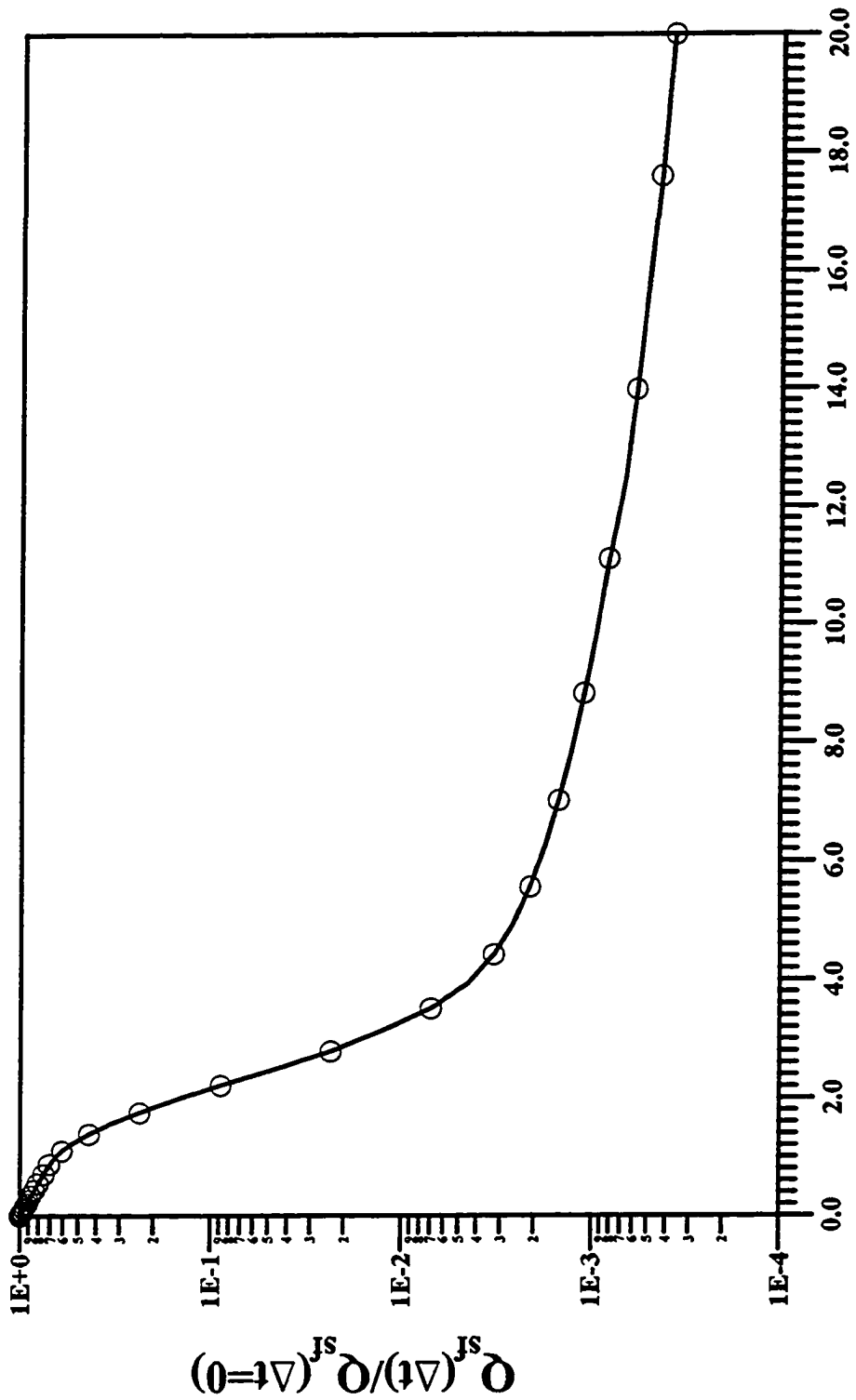Fig. 4.6 – Change in Wellbore Storage Coeffient for Case B.

Fig. 4.7 – Normalized Sandface Flow Rate as a Function of Shut-in Time for Case B

limited by the Courant number relation:

$$|\frac{\Delta t \, v_m}{\Delta x}| \leq 1. \tag{4.4}$$

In applying, Eq. 4.4, we use the maximum mixture velocity predicted by our numerical model.

In order to investigate the Courant number limitation, the explicit simulator was run with several time steps with a fixed number of wellbore gridblocks; specifically we use $\Delta z = 30$ ft. so the number of gridblocks is equal to 300. As Fig. 4.5 shows, the explicit simulator gives stable and consistent results as long as the Courant number limitation is satisfied, but when the time step was increased to a value above 100 seconds, so the Courant number is exceeded, the simulator fails to converge for the full range of relaxation factors ($0 < \theta < 2$). This means 15,000 iterations were tried without obtaining convergence. When, our new multistep simulator was run for the same conditions, we obtained the results presented in Fig. 4.8. At early times, both simulators are in excellent agreement; in the transition region the results from the new simulator are shifted a little to the right; see the derivative curve. This behavior for the cases when the Courant number is not violated (50, 100 sec.), may simply be due to the differences in the numerical schemes. For the cases when the Courant condition is violated, the behavior probably simply reflects a loss of accuracy for the large time steps used. However, the simulator shows a stable behavior even for the case where we violated the Courant stability condition by a factor of 10.

Both simulators show good agreement when the Courant number is not violated. On the other hand, there is a significant difference between simulator per-
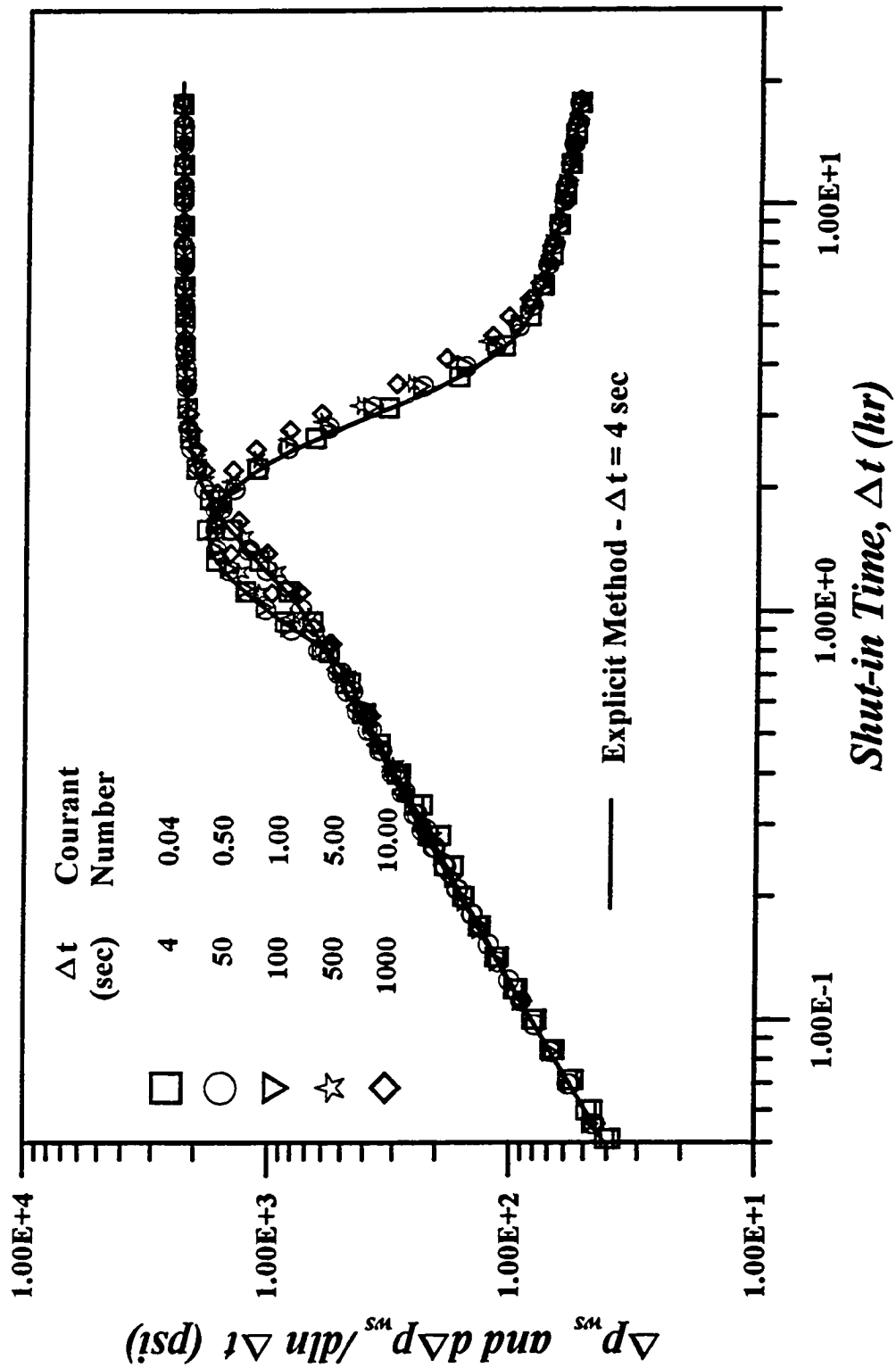
Fig. 4.8 – Log-Log Plot of Pressure and Pressure Derivative for Case B.

formance when we consider the computational execution time. Simulation using the explicit simulator for the case of $\Delta t = 100$ sec. and $\Delta z = 30$ ft., required 10 hours on a PC-Pentium 66 MHz in comparison with 45 minutes required for the new simulator.

Fig. 4.9 presents the wellbore storage coefficient computed for all the cases. All results are in excellent agreement except for the case with $\Delta t = 1000$ sec., which gives slightly different results than obtained in the other cases. Again, this difference can attributed to inaccuracy caused by the large time step size.

The distribution of the gas void fraction along the wellbore for several Δt values is shown in Fig. 4.10. The total wellbore depth is 9000, Fig. 4.10 only shows the top 1000 ft. The profile at $\Delta t = 1000$ sec. shows that a single phase gas zone has been formed in the top 350 ft. At $\Delta t = 4000$ sec., the two phases are almost completed segregated, the wellbore void fraction profile shows a single phase gas zone for the top 650 ft. After $\Delta t = 4000$ sec., the gas-oil interphase moves continuously upward compressing the gas column. Note that $\Delta t = 4000$ sec. corresponds to approximately the time at which the pressure/pressure derivative responses in Fig. 4.5 shows an anomalous behavior. This is a clear indication that the decreasing wellbore storage behavior of Case B is due to the compression of the gas column after wellbore phase segregation has ceased, i.e., after $\Delta t = 4000$ sec., the test behaves like a closed chamber test[56]. The results from the new simulator for different time steps are presented in the same figure. For a simulation time equal to 1000 seconds, the gas-oil interphase is shifted a little to the right of the explicit solution for time steps 100 and 500 seconds. This is due to a loss of accuracy loss caused by large times steps; at late times the agreement between both simulators is reasonable good.
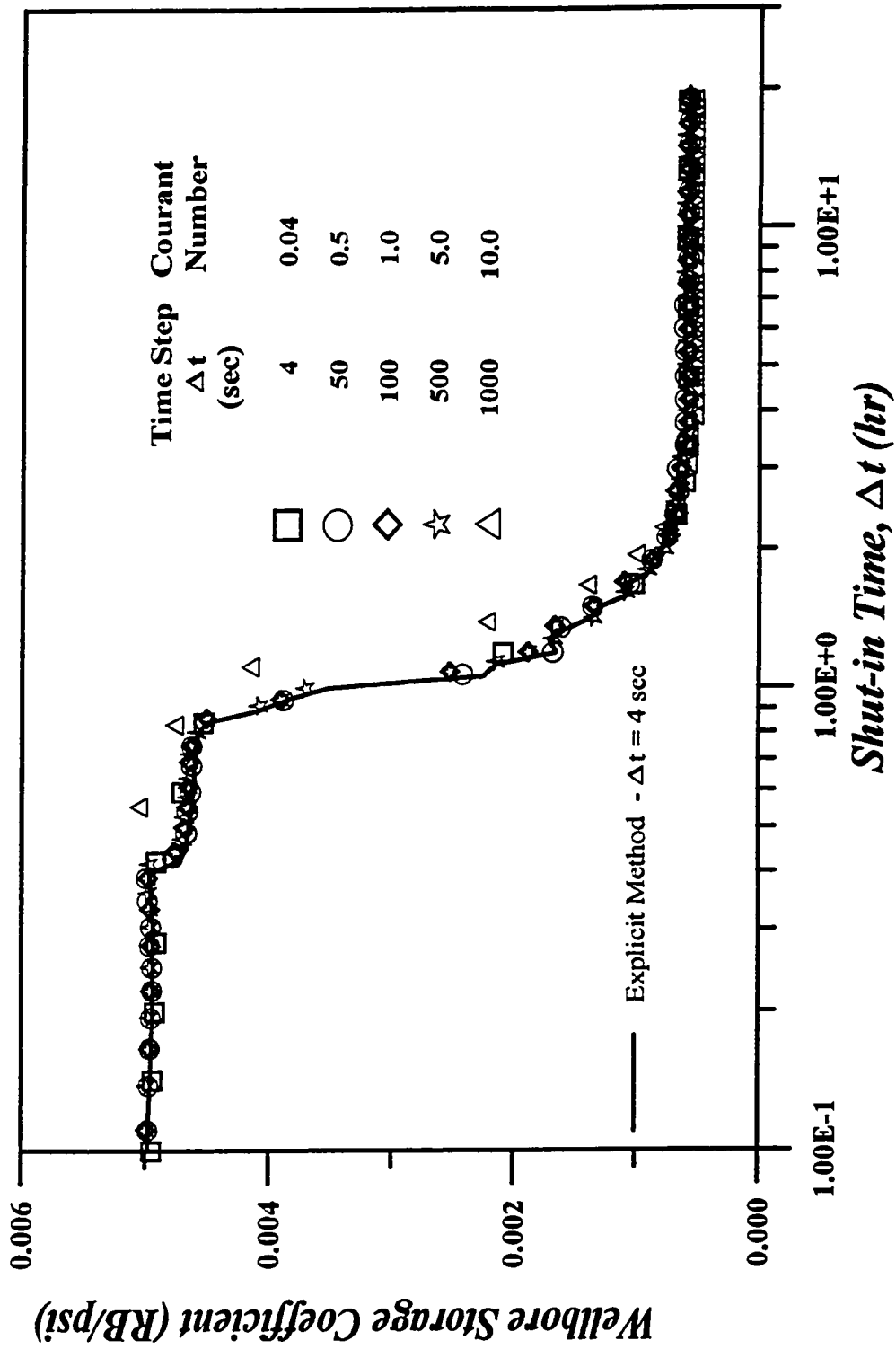
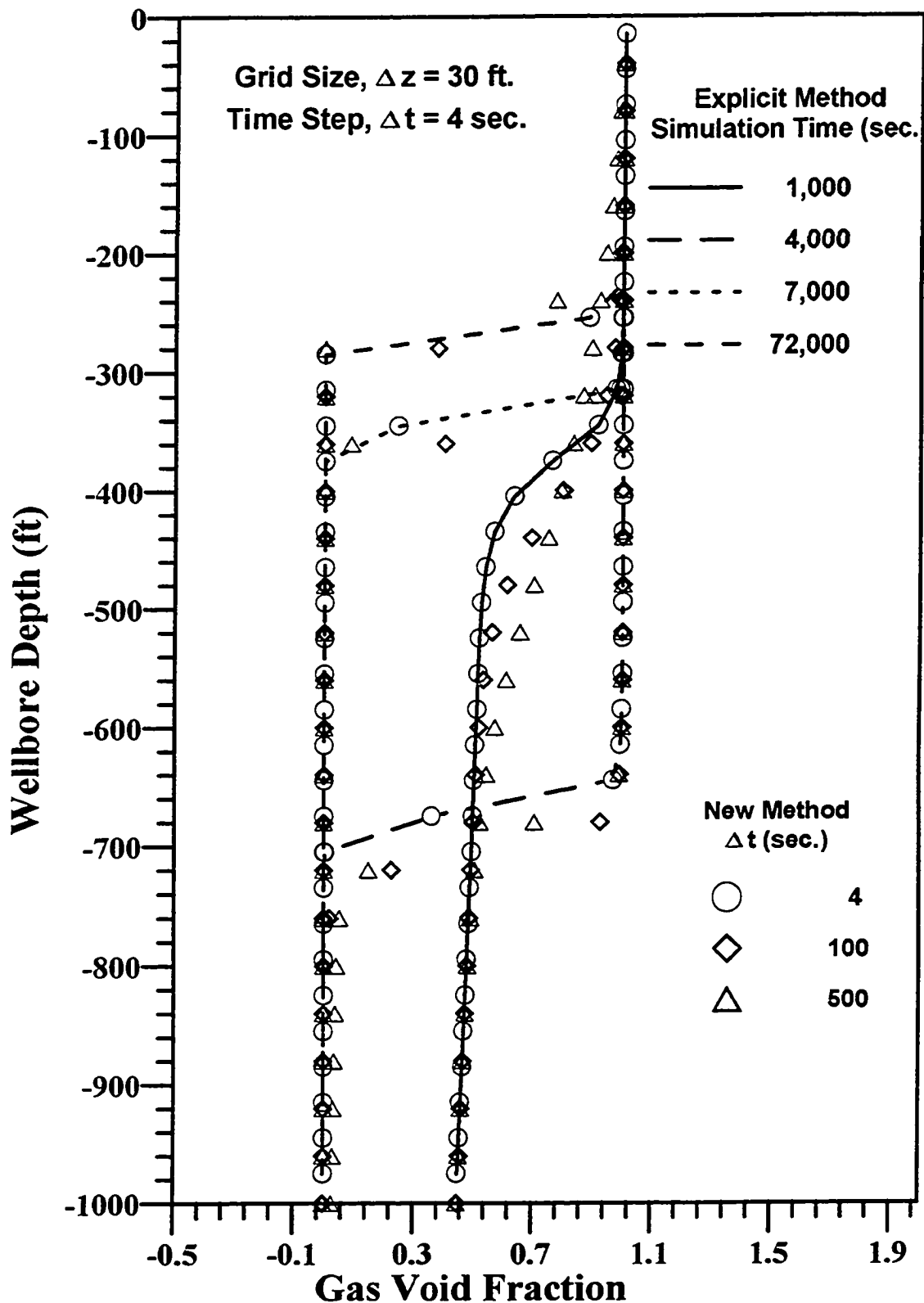Fig. 4.9 – Change in Wellbore Storage Coeffient for Case B.

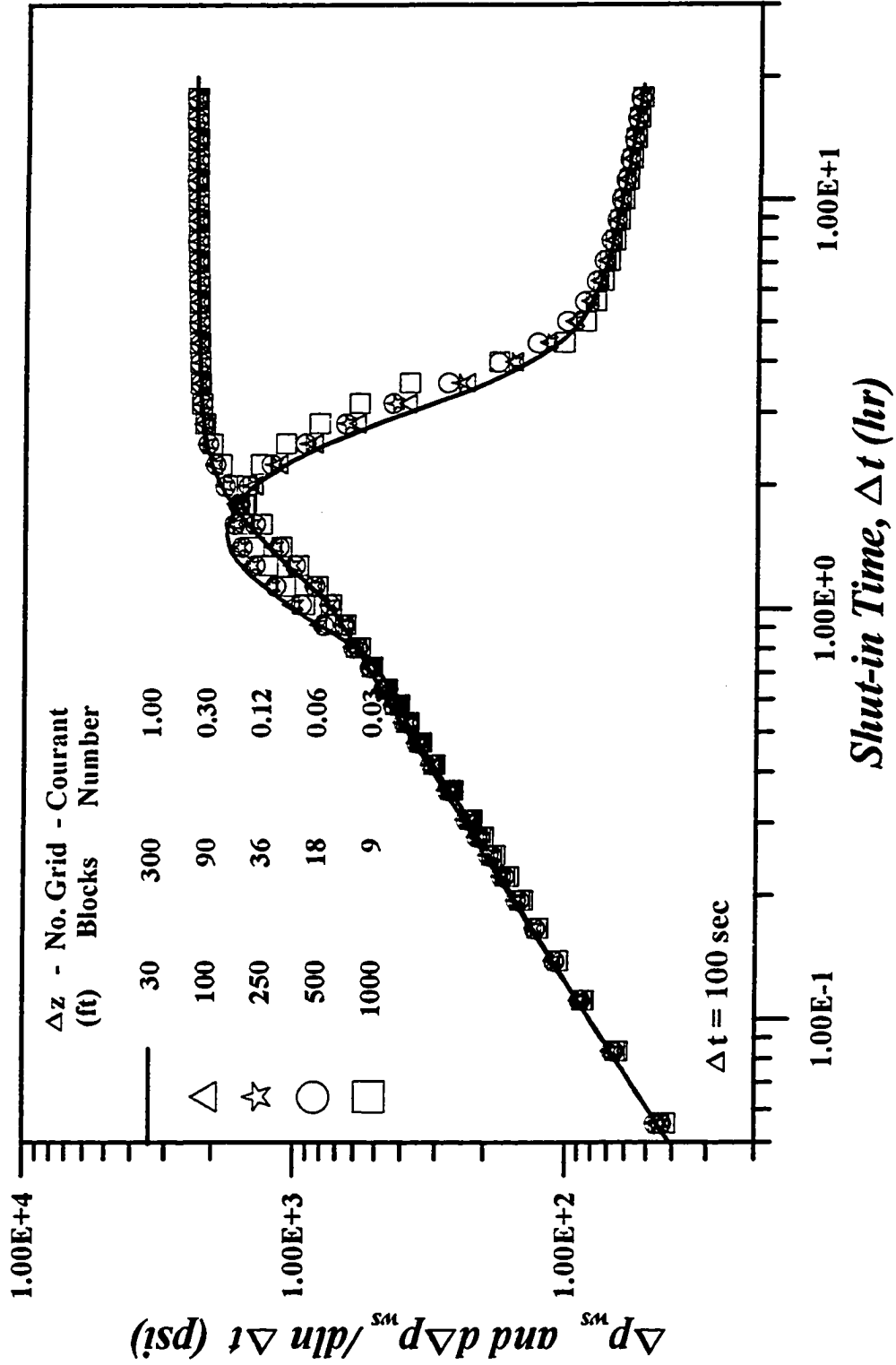**Fig. 4.10 - Gas void fraction distribution for Case B**

Fig. 4.11 - Log-Log Plot of Pressure and Pressure Derivative for Case B.

To investigate the stability and accuracy performance of the new simulator, the time step was fixed at 100 seconds and several cases were run with Δz varying from sizes 30 to 1000 feet. Fig. 4.11 presents the results, and as this figure shows, the simulation results agree very well at early and late times, but there is some difference during the transition period. Again the main difference appears when the computational time is considered; 45 minutes was required for the case $\Delta z = 30$ ft. as compared to 5 minutes for $\Delta z = 1000$ ft.

4.1.2.b Case C.

Case C shows that our simulator can also be used to simulate pressure buildup tests in gas-lift wells. Also, unlike Case B, for Case C, phase segregation produces a hump in the wellbore pressure. For Case C, the following assumptions were used: 1) the gas injection point was placed at the sandface; 2) no mass transfer occurs between the injected gas and reservoir fluids; 3) the produced oil is incompressible, i.e., $B_o = 1$, and does not contain solution gas, i.e., $R_s = 0$. All other parameters are listed in Table 4.4. Again we, considered a 120-hour flow period followed by a 20 hours buildup test.

By using the explicit simulator, a log-log plot of buildup data was generated (see Fig. 4.12). At early times, although wellbore segregation is taking place, the buildup data show the behavior of the classical wellbore storage and skin solution[57]. In the transition region, the derivative data curve shows a v-shape depression, giving some negative values. The behavior of the buildup data is comparable to the behavior of field data reported by Olarewaju[11]. At late times, the derivative curve is constant,
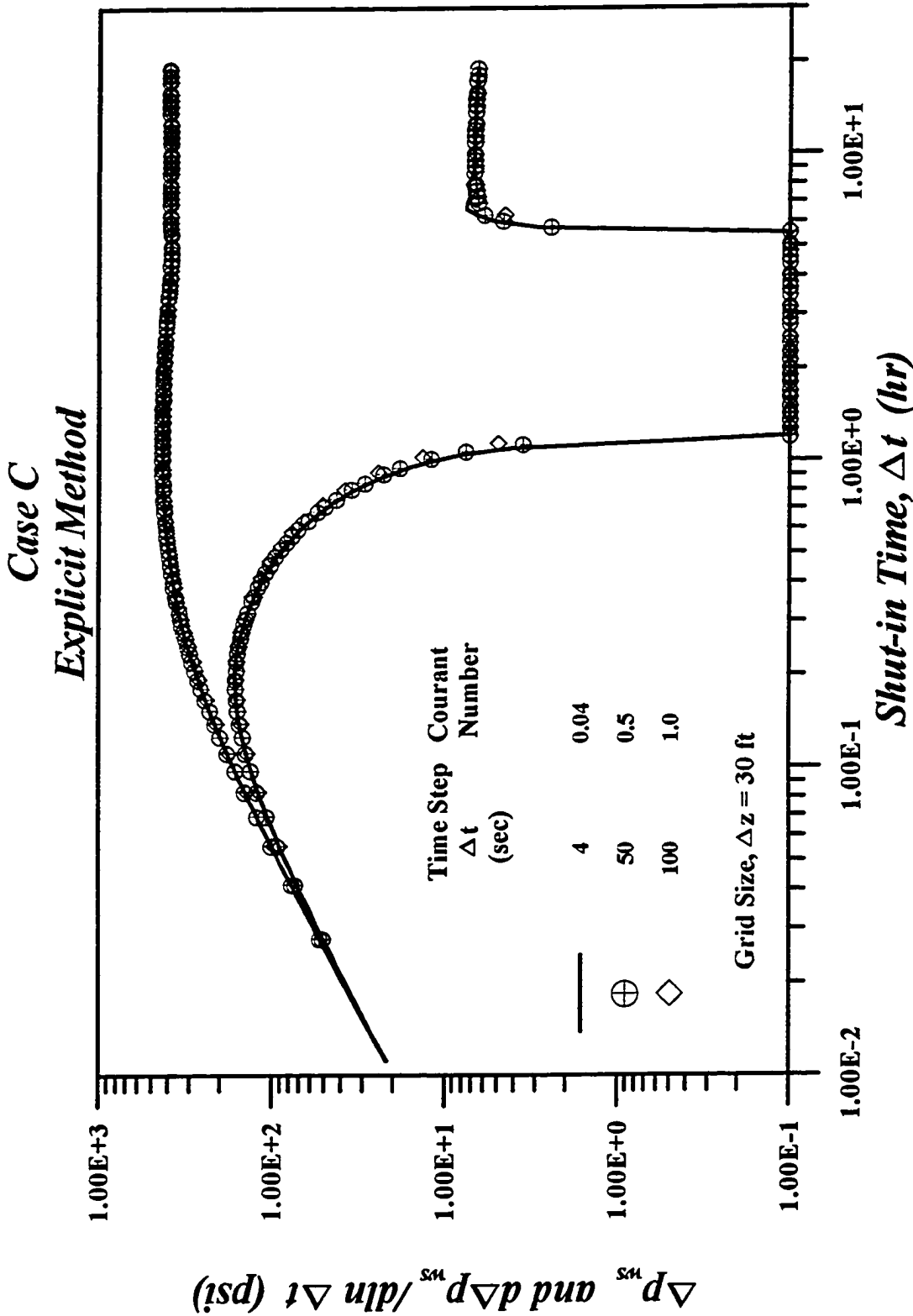
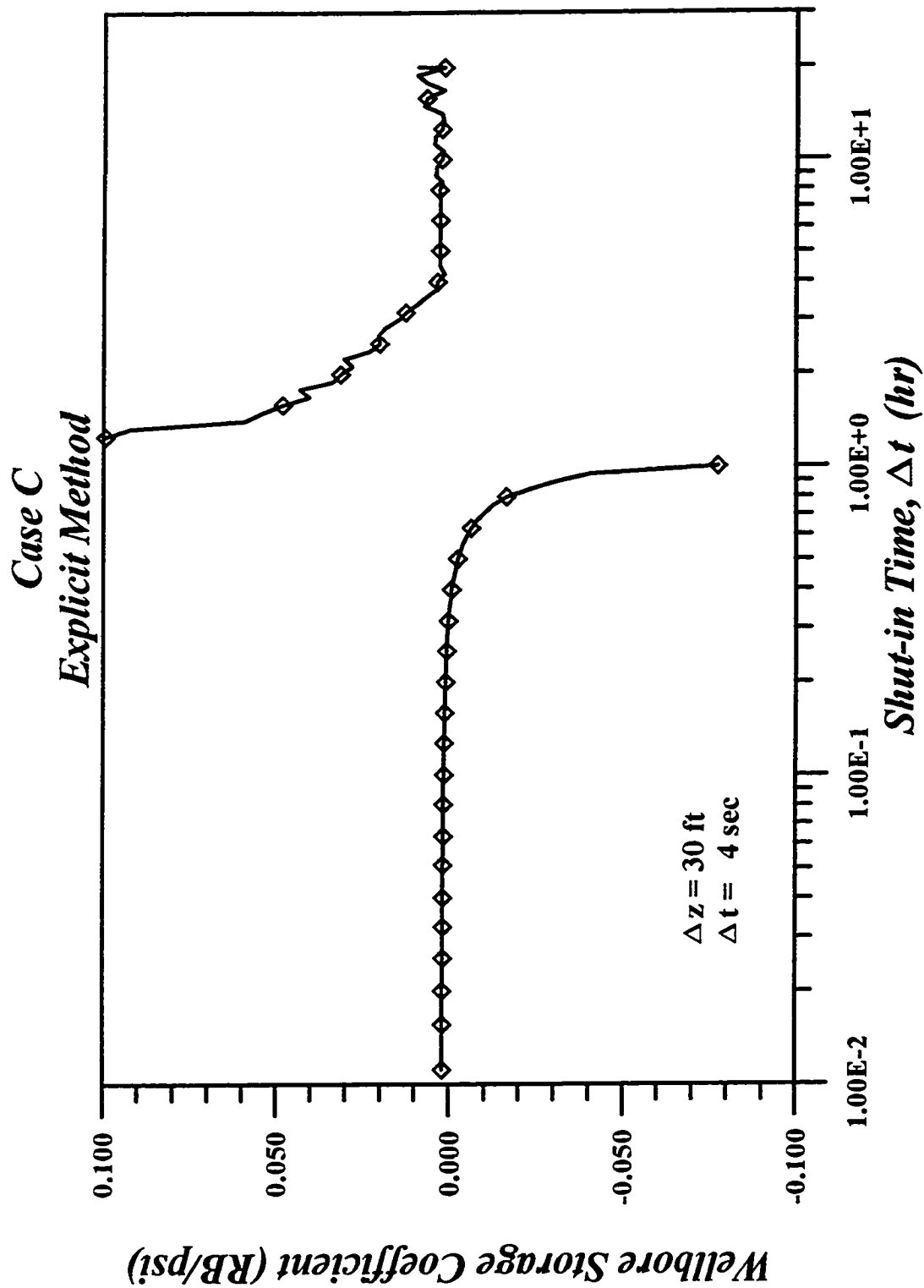Fig. 4.12 – Log-Log Plot of Pressure and Pressure Derivative for Case C.

Fig. 4.13 - Change in Wellbore Storage Coeffient for Case C.

Parameter	Value	Unit
Drawdown oil production rate	100.00	RB/D
Gas Injection Rate	200000.00	scf/D
Total production time	120.00	hours
Inital reservoir pressure	5215.00	psia
Oil compressibility (p>p_b)	0.0	1/psia
Oil component API gravity at s.c.	45.00	API
Gas component specific gravity at s.c.	0.9665	-
Oil-gas surface tension	4.50	dynes/cm.
Wellbore pipe inside diameter	1.80	inch
Formation absolute permeability	25.00	md.
Formation thickness	75.00	ft.
Formation porosity	0.20	-
Wellbore radius	0.364	ft.
System isothermal compressibility	2e-5	1/psia
Average oil viscosity	2.00	cp.
Skin factor	12.00	-
Wellbore depth	9000.00	ft.
Spatial Increment	30.00	ft.
Buildup simulation time	20.00	hours

Table 4.4: Input Parameters for Case C

which indicates that wellbore storage effects have becomes negligible and pressure data during this time period will fall on the semilog straight line. The change in the wellbore storage coefficient computed from Eq. 4.2 is presented in Fig. 4.13. At early times, buildup data show a constant wellbore storage coefficient. Then, a transition period follows during which the wellbore storage coefficient decreases and even becomes negative, indicating a reversal in the direction of flow. Once the wellbore pressure passes the maximum hump point, the wellbore storage coefficient becomes a large positive number, but as the test continues, the wellbore storage coefficient decreases. At late times, the well again acts like a well with constant storage. The wellbore storage coefficient at late times is approximately 40% larger than the wellbore storage coefficient at early times.

As in Case B, for the explicit method, the time step is limited by the Courant number relation. The explicit simulator was run with several time steps with a fixed number of wellbore gridblocks, i.e. for $\Delta z = 30$ ft. The explicit simulator gives stable and consistent results as long as the Courant number limitation is satisfied, but as in Case B, when the time step was increased to a value above 100 seconds, the simulator fails to converge for the full range of relaxation factors $(0 < \theta < 2)$; this means 15,000 iterations were tried without obtaining convergence. The results are presented in Fig. 4.12.

Fig. 4.14 presents the results that were obtained from the new simulator for Case C. At early and late times, results from both simulators are in excellent agreement, but similar to Case B results, in the transition region, the results for the pressure derivative curve are somewhat different especially when the Courant number is exceeded. The variation of the wellbore storage coefficient for all the cases is presented in Fig. 4.15. Again results for $\Delta t > 100$ sec. are somewhat different than results obtained from the other cases at intermediate times.

The computational execution time required is quite different for the two simulators. For the case of $\Delta t = 100$ sec. and $\Delta z = 30$ ft.: the explicit simulator required 12 hours to run on a PC-Pentium 66 MHz in comparison with 60 minutes required for the new simulator.

The distributions of the gas void fraction along the wellbore for certain shut-in times Δt values are presented in Fig. 4.16. As shown, as the buildup test progresses, the single gas phase zone grows. Results not shown indicate that from $\Delta t = 18,000$ seconds to the end of the buildup test, the gas-oil contact remains almost unchanged.
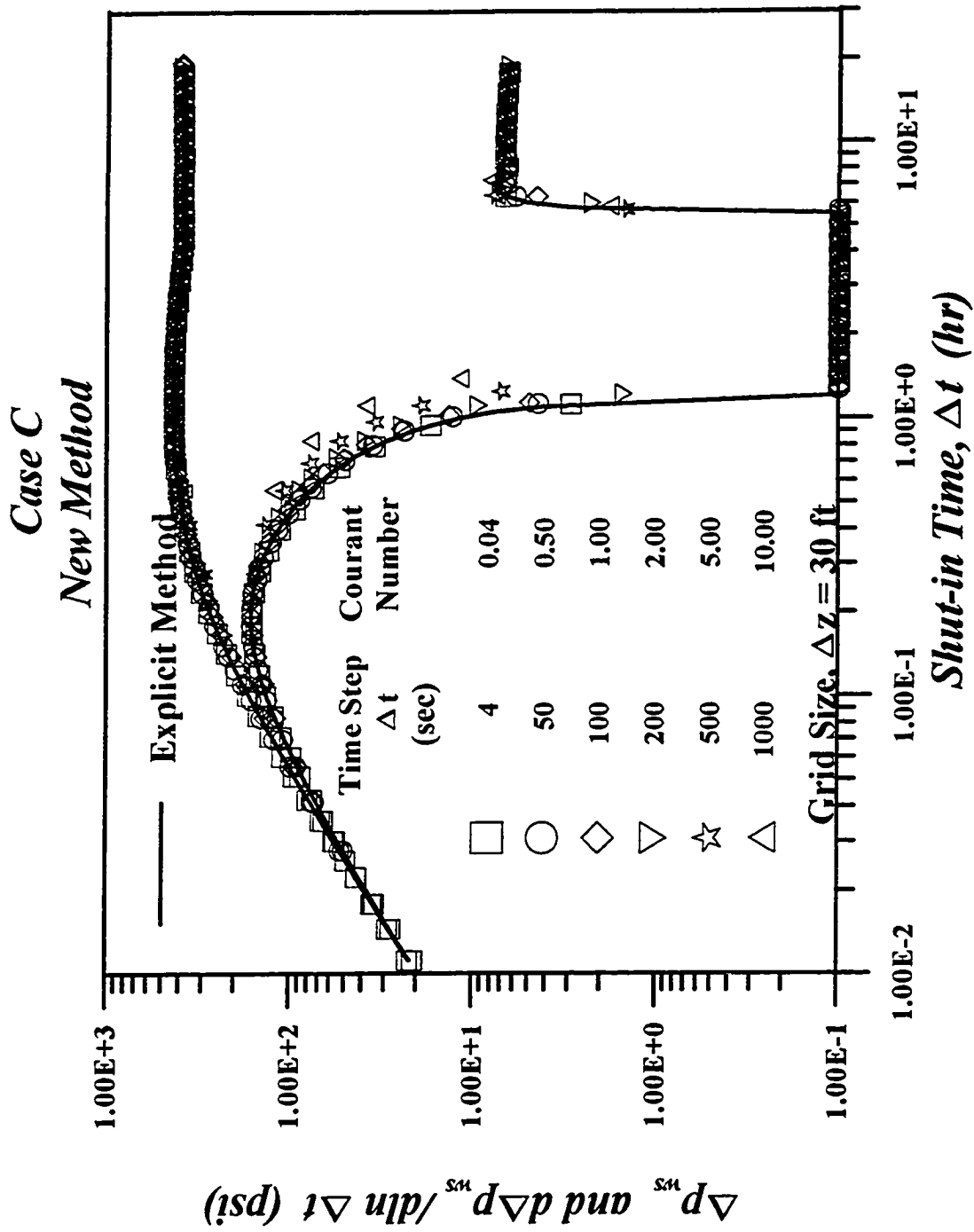
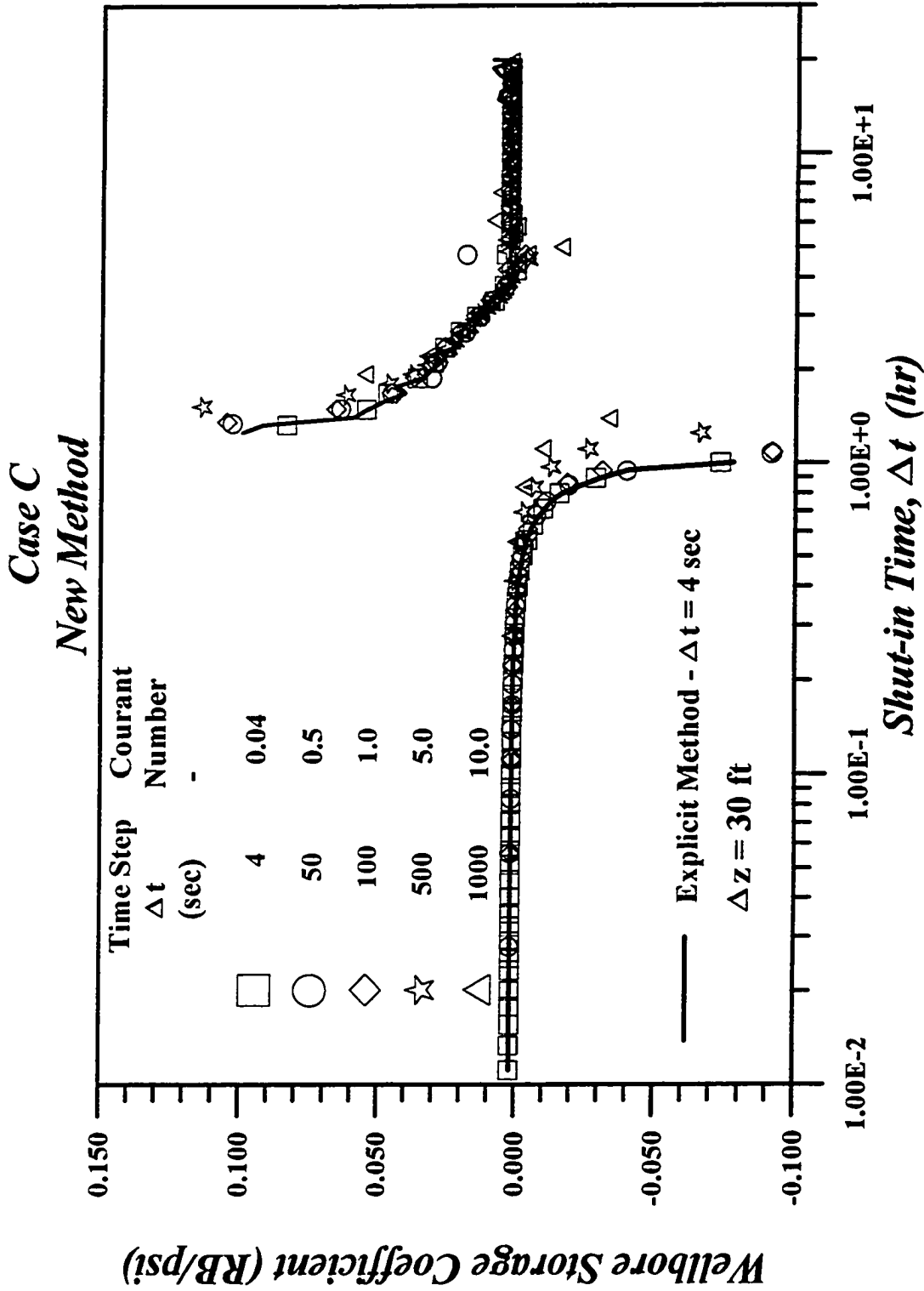Fig. 4.14 – Log-Log Plot of Pressure and Pressure Derivative for Case C.

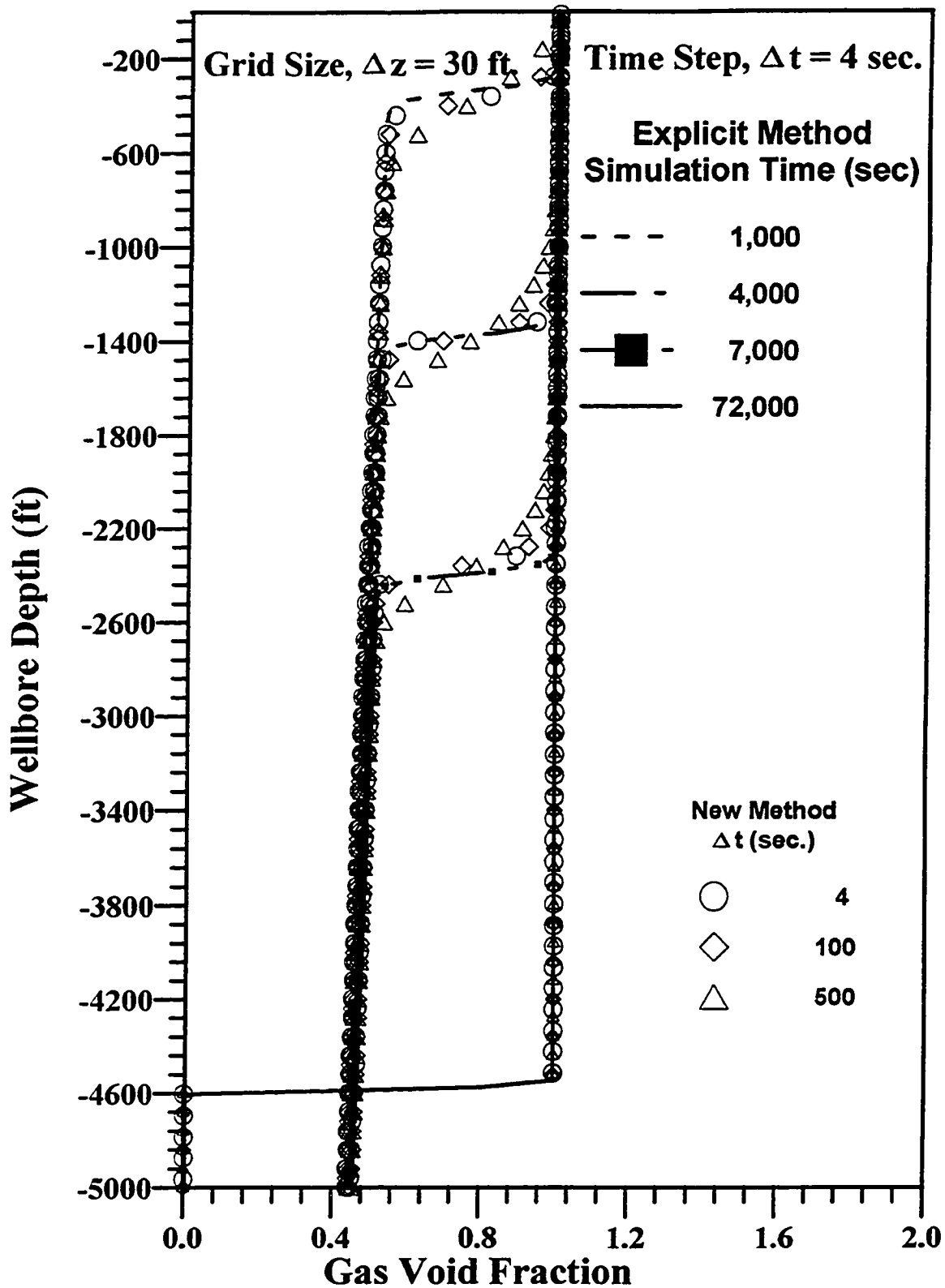**Fig. 4.15 - Change in Wellbore Storage Coeffient for Case C.**

Fig. 4.16 – Gas void fraction distribution for Case C.

Buildup data from both Case B and Case C are influenced by wellbore phase segregation. However, buildup data from Case B clearly show a decreasing wellbore storage effect while buildup data from Case C do not. Comparing the gas void fraction profiles for the two cases, Fig. 4.10 and Fig. 4.16, it can be concluded that the variation of wellbore storage coefficient is affected by both phase segregation and gas compression. If the magnitude of afterflow is small after the end of wellbore phase segregation, the phase segregation will be the dominating factor, and pressure buildup data will show an increasing wellbore storage coefficient. On the other hand, if the afterflow is still large after gas and liquid have completely segregated in the wellbore, the gas column will be compressed due to afterflow and the pressure buildup data will eventually show a decreasing wellbore storage coefficient.

To investigate the stability and accuracy performance of the implicit simulator, the time step was fixed to 100 seconds and several grid block sizes were used. The results presented in Fig. 4.17 indicate that all simulation results agree reasonably well. Again, there is considerable difference in the computational time required; from 60 minutes for the case of Δz equal to 30 ft. to 15 minutes for Δz equal to 1000 ft.

4.1.3 Validity of Fair and Hegeman Models.

Since our model was derived from mass, momentum and energy balances, it is appropriate consider whether buildup data obtained from our model can be analyzed by the Fair[1] or Hegeman et al.[2] models to obtain good estimates of permeability and skin factor. The nonlinear regression analysis package based on least absolute value method (LAV) implemented by Carvalho et al.[60] was used to analyze data from cases
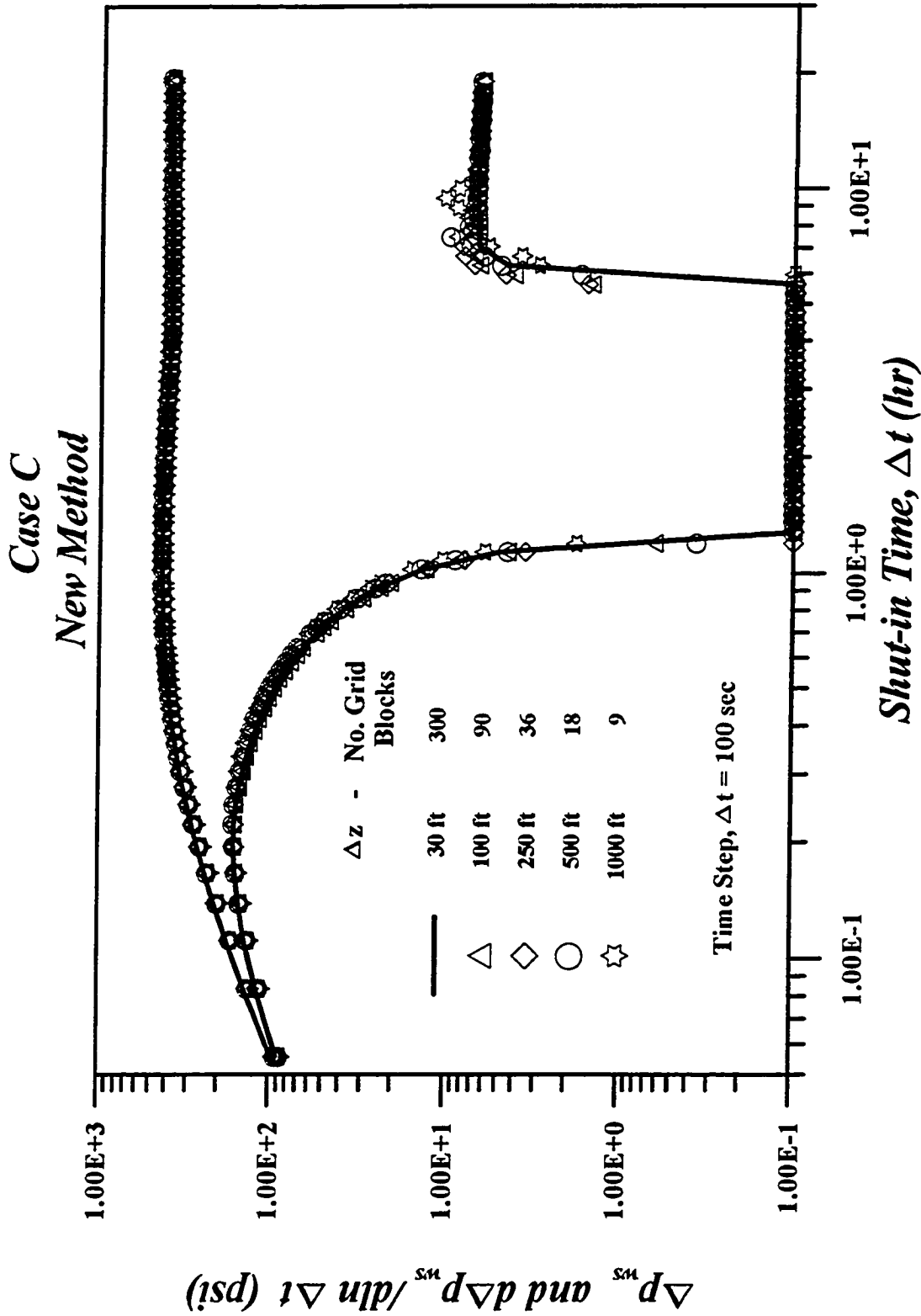
Fig. 4.17 – Log-Log Plot of Pressure and Pressure Derivative for Case C.

Case B-1 Fairs's Model					
Regression Parameters	Simul. Data	LAV No Outliers Detection	NLS Outliers Detection		
			Optimized Value	Minimum Value	Max. Value
k (md.)	25.00	3.9044E+02	3.4459E+02	0.0009E+00	4.3123E+03
C (bbl/psia)		1.5788E-03	1.5794E-03	0.0000E+00	9.541E-02
s	15.00	3.1948E+02	2.8124E+02	1.5670E+01	4.5340E+02
α (day)		3.7244E-02	7.70208E-02	-2.1675E+00	2.2491E+00
C_o/qB (psia/bbl/day)		1.7712E+01	-1.76866E+01	-2.4663E+03	-2.4309E+03

Table 4.5: Case B-1 Least Absolute Value and Least Squares Regression

B and C.

4.1.3.a   Case B-1

Case B-1 is exactly the same case B, discussed previously. Using the nonlinear regression package[60,61] an analysis of pressure buildup data was performed using the least absolute value (LAV) method, with outlier detection and no-imaging process[60,61]. Fair's Model and Hegeman's Model were both considered as the storage model for regression purposes. In all cases presented, regression was performed on the pressure data only. The regression analysis graphs are presented from Fig. 4.18 to Fig. 4.21. A table with a summary of results are presented in Tables 4.5 to 4.6.

We experienced extraordinary difficulty in matching this data and often got radically different answers depending on the initial guess. Since a major objective was to get the best possible fit of the data, we tried some special techniques using
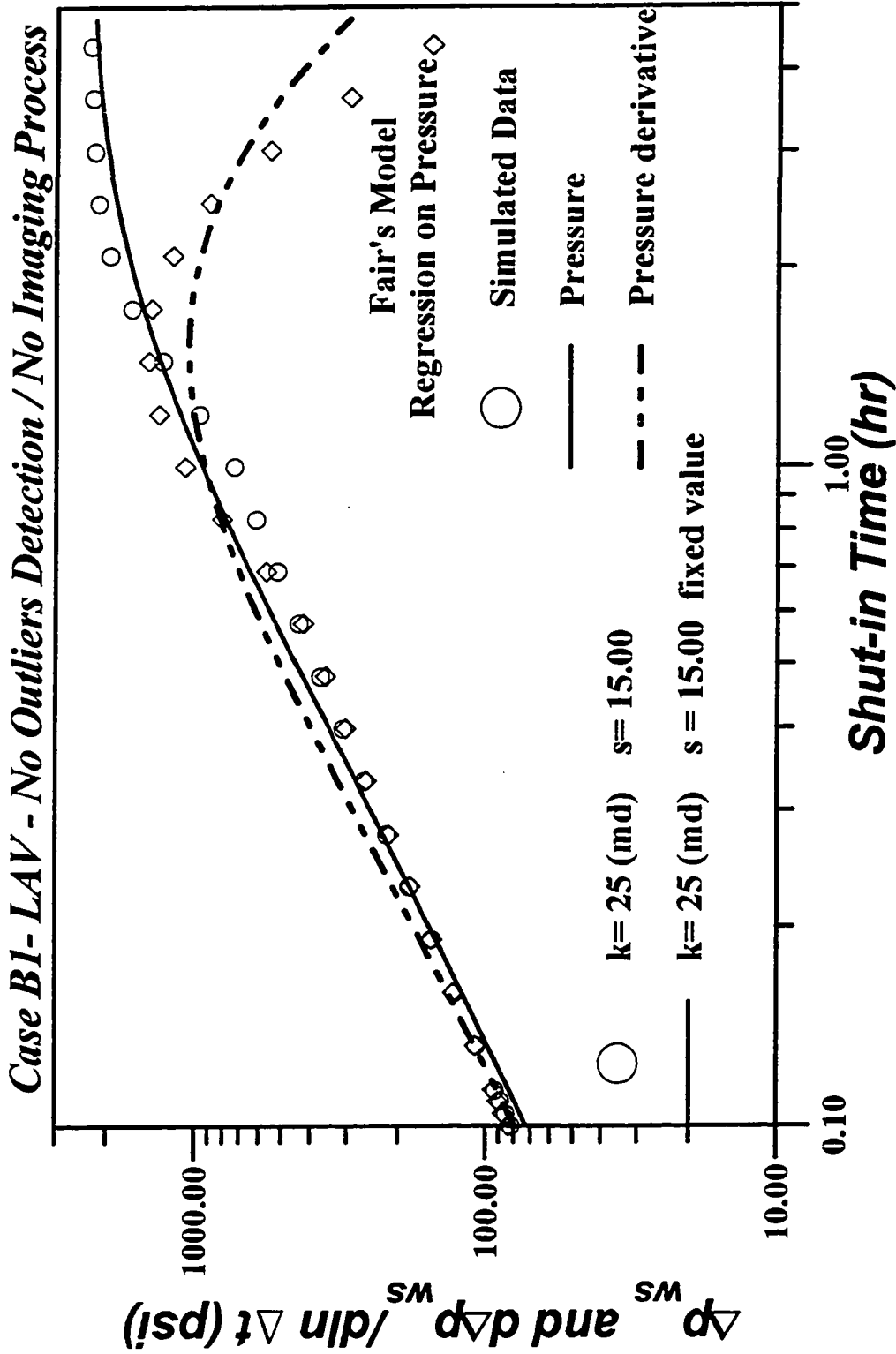
114

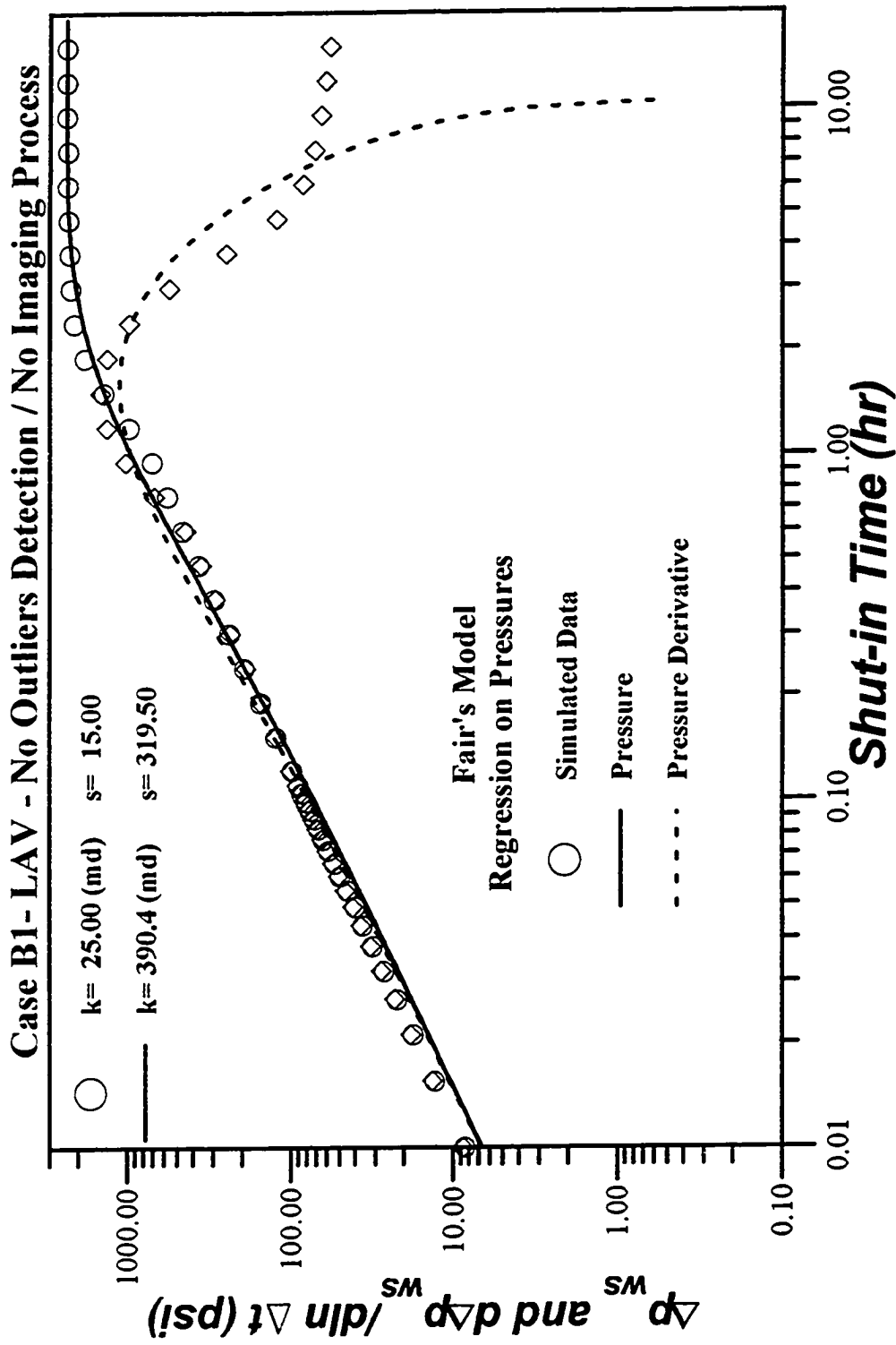Fig. 4.18 - Regression match of first five hours of data; k and s fixed; LAV with Fair's Model; Case B-1.

Fig. 4.19 - Regression of pressure buildup data; LAV with Fair's Model;
Case B-1.

		Case B-1 Hegeman's Model			
Regression Parameters	Simul. Data	LAV No Outliers Detection	NLS Outliers Detection		
			Optimized Value	Minimum Value	Max. Value
k (md.)	25.00	3.5615E+01	3.5615E+01	3.2796E+01	3.8435E+01
C (bbl/psia)		8.3165E-04	8.3165E-04	7.7588E-04	8.8743E-04
s	15.00	2.634E+01	2.3634E+01	2.1360E+01	2.598E+01
α (day)		5.1076E-02	5.1076E-02	5.0282E-02	5.1870E-02
C_o/qB (psia/bbl/day)		4.4452E+01	-4.4452E+01	-4.8583E+01	-4.0322E+01

Table 4.6: Case B-1 Least Absolute Value and Least Squares Regression

correct data. Specifically as a first matching process attempt, we consider only data for the first 5 hours. With this pressure data and k and s fixed at their correct values, we regressed on the three parameters, C, α and C_o/qB, where C_ϕ represents the maximum phase redistribution pressure change[1] and α represents the time at which about 63% of the total change has occurred[1]. The results are presented in Fig. 4.18, and as this figure shows, Fair's model fails to represent the early time data. The results from the early time regression were used as initial guesses for a regression using the complete twenty hours test. In this case, we obtained estimates of k, s, C, α and C_o/qB. Fig. 4.19 shows the results, indicating again a poor match, as is confirmed by the large confidence intervals in Table 4.5. These confidence intervals were obtained by applying least squares to the reduced data set obtained by using LAV to remove outliers. In all cases we applied LAV, removed outliers, and then applied least squares to generate confidence intervals. As shown in Table 4.5, our

estimates of permeability are $k = 390.4$ md and $s = 319.48$ as opposed to the correct

values of $k = 25$ md. and $s = 15$. The results of Fig. 4.19, although poor, is the

best overall pressure match we could obtain. In order to get values of k and s close

to the correct ones, we had to ignore all early time data. In effect, this is equivalent

to performing semilog analysis. However regression analysis of data corresponding to

$\Delta t > 6$ hours gave $k = 22.4$ md. and $s = 12.4$.

In the case of Hegeman's Model (Figs. 4.20 and 4.21), the early time data

match with k and s fixed at the true values presents a reasonable agreement with the

simulated data. In this case, when we match the complete test as shown in Fig. 4.21,

we obtain a reasonable match of pressure and rough estimates of k and s. Note the

confidence intervals (Table 4.6) are narrow for all the parameters even though the

true values of k and s are not within their confidence intervals. Note the derivatives

data do not match well the derivatives computed form the model at late times.

4.1.3.b   Case B-2

Case B-2 is a similar case to Case B-1 but in this case the value of permeability

was increased to 50.0 md and skin reduced to 5.0 . For the analysis of this case, the

data obtained from the simulator were cut to 2 hours in order to emphasize the

wellbore storage dominated data and the effect of phase redistribution. The non-

linear regression package was executed again to obtain the results shown in Figs.

4.22 to 4.23 and Tables 4.7 and 4.8.

For this case the answer for k and s are good for all the regression options and

storage model considered. However, the parameter estimates obtained by regression
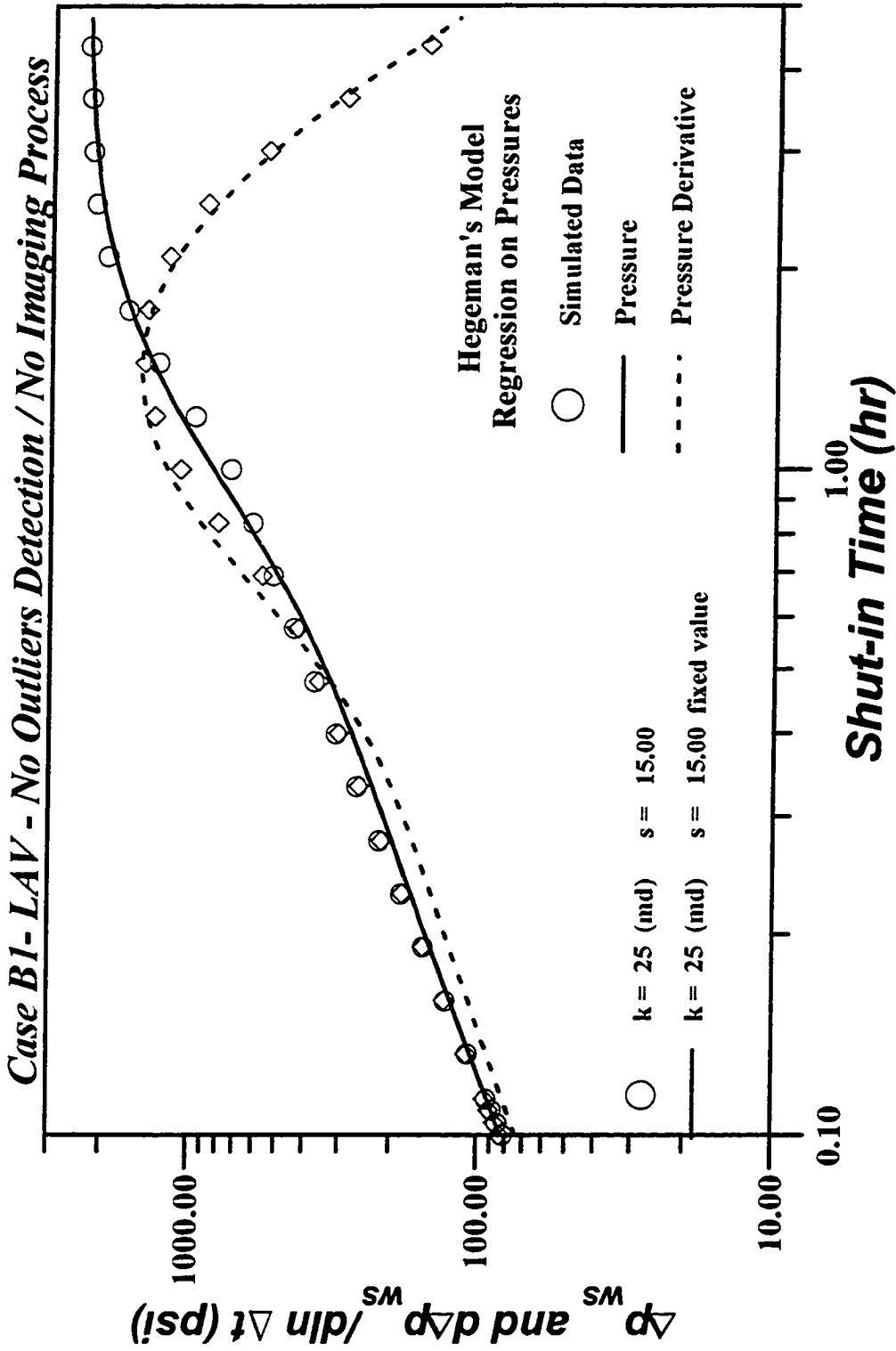
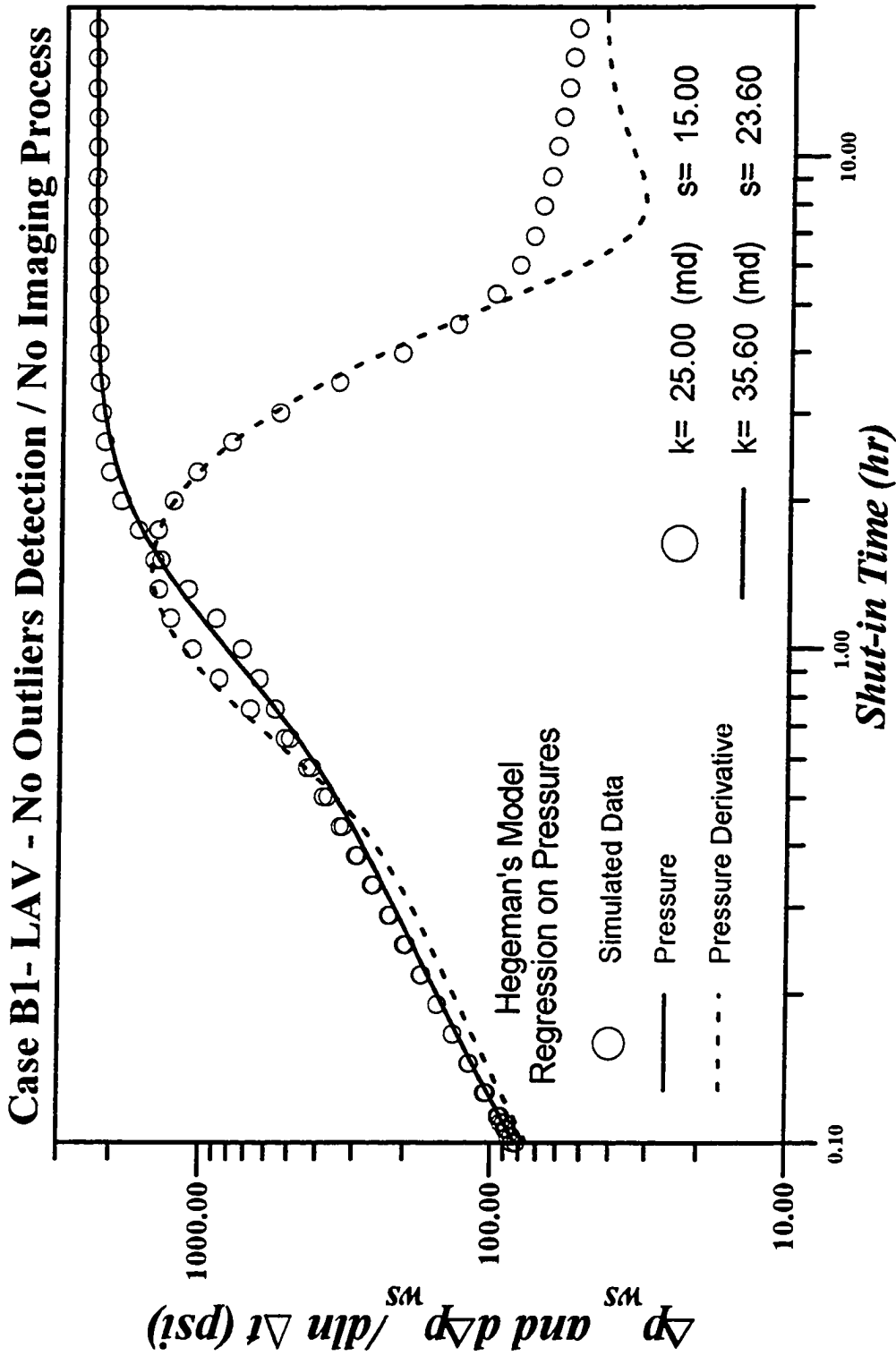Fig. 4.20 – Regression match of first five hours of data; k and s fixed; LAV with Hegeman's Model; Case B-1.

Fig. 4.21- Regression of pressure buildup data; LAV with Hegeman's Model; Case B-1.

Case B-2 Fairs's Model					
Regression Parameters	Simul. Data	LAV No Outliers Detection	NLS Outliers Detection		
			Optimized Value	Minimum Value	Max. Value
k (md.)	50.00	5.0144E+01	5.0144E+01	5.0009E+01	5.0279E+01
C (bbl/psia)		2.7054E-04	2.7054E-04	2.5933E-04	2.8175E-04
s	5.00	4.9597E+00	4.9597E+00	4.9320E+00	4.9842E+00
α (day)		1.4468E-03	1.4468E-03	1.3945E-03	1.4991E-03
C_ϕ/qB (psia/bbl/day)		6.7586E+00	-6.75586E+00	-7.2359E+00	-6.2814E+00

Table 4.7: Case B-2 Least Absolute Value and Least Squares Regression

with Fair's model (Fig. 4.22) is good only because it fits data corresponding to the semilog straight line. Fair's Model fails to represent the storage dominated period. Again the small confidence intervals obtained for Fair's model are meaningless because our LAV procedures identified all data prior to 0.7 hours as outliers.

Hegeman's model in this case shows a excellent performance for all the parameters (k, s, C, α and C_ϕ/qB). Although the nonlinear least squares results shown in Table 4.8 were obtained by matching data with outliers removed, the effect of outliers is not significant for this case as should be expected from the results shown in Fig. 4.23. In fact, when we regressed on all data using least squares, we obtained the following estimates $k = 48$ md, $s = 4.53$ with confidence intervals (47.7, 48.3 md) for k and (4.47,4.60) for s.
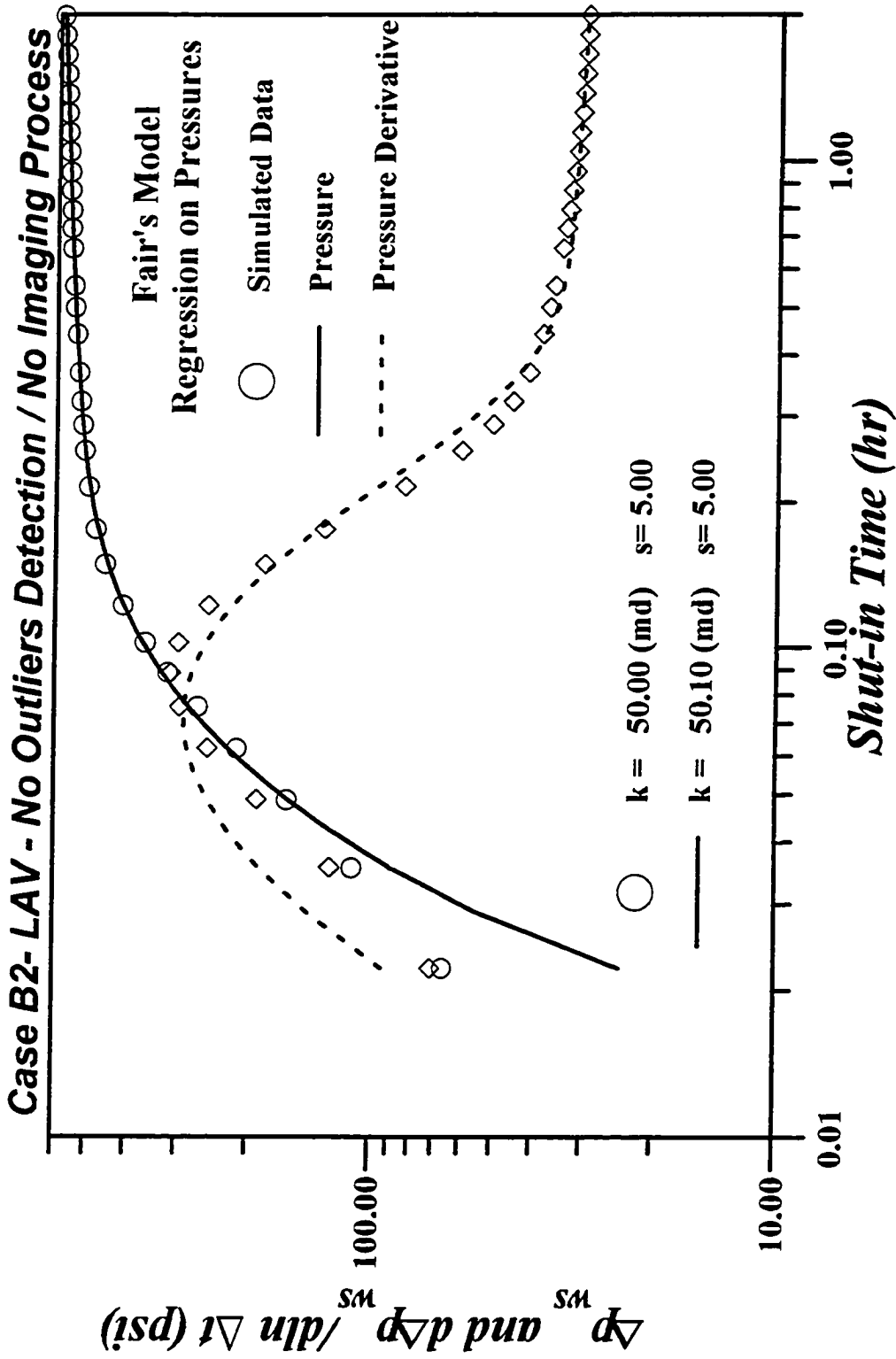
Fig. 4.22 - Regression match of first two hours of buildup data;
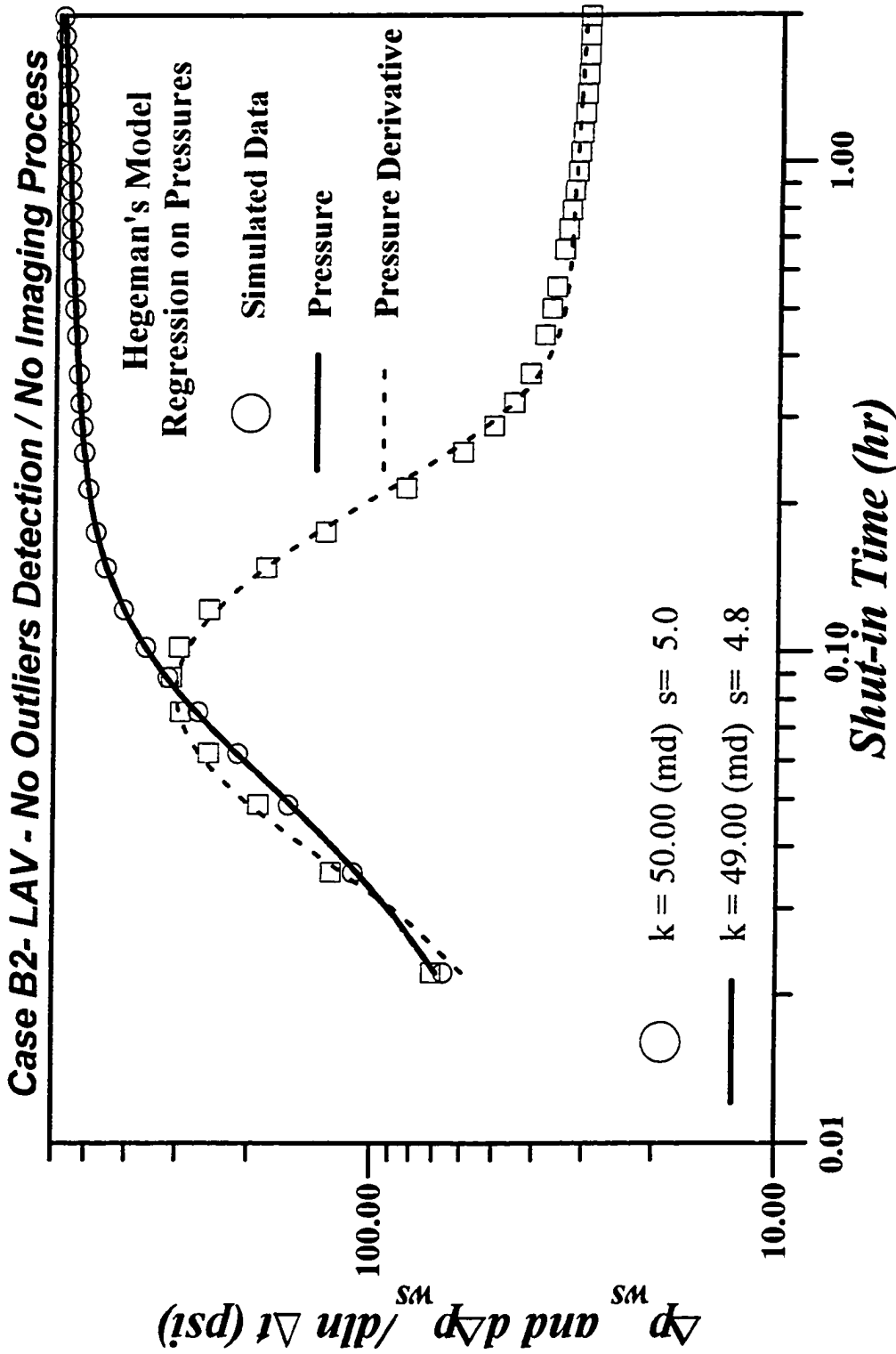LAV with Fair's Model; Case B-2.

Fig. 4.23 - Regression match of first two hours of buildup data; LAV with Hegeman's Model; Case B-2.

Case B-2 Hegeman's Model					
Regression Parameters	Simul. Data	LAV No Outliers Detection	NLS Outliers Detection		
			Optimized Value	Minimum Value	Max. Value
k (md.)	50.00	4.9094E+01	4.9028E+01	4.8878E+01	4.9178E+01
C (bbl/psia)		2.3599E-04	2.4129E-04	2.3637E-04	2.4621E-04
s	5.00	4.7527E+00	4.7264E+00	4.8276E+00	4.7699E+00
α (day)		2.7334E-03	2.6993E-03	2.6746E-03	2.7240E-03
C_o/qB (psia/bbl/day)		7.8161E+00	-7.5347E+00	-7.7739E+00	-7.2955E+00

Table 4.8: Case B-2 Least Absolute Value and Least Squares Regression

4.1.3.c   Case B-3

For Case B-3 the permeability was increased to 100 md and the skin factor was again set equal to 5. For this case, both storage models show a excellent agrement with the simulated data, when the match was done considering only the first two hours of the twenty hours test. However, as before, the regression match quality was strongly dependent of the values of the initial guesses for the parameters. This shows that we may have multiple local minima, or an improper solution for the analytical phase distribution model. The results are presented in Figs. 4.24 to 4.25 and Tables 4.9 and 4.10. Both phase redistribution models give a reasonably good match of data and good estimates of k and s. Also in this case the effect of outliers is small. When we applied non-linear least squares using the pressure data for $\Delta t \leq 2$ hours, the estimates obtained were $k = 100.9\ md$ and $s = 4.85$ for Fair's model (Fig. 4.24) and $k = 100\ md$ and $s = 4.79$ for Hegeman's model (Fig. 4.25).
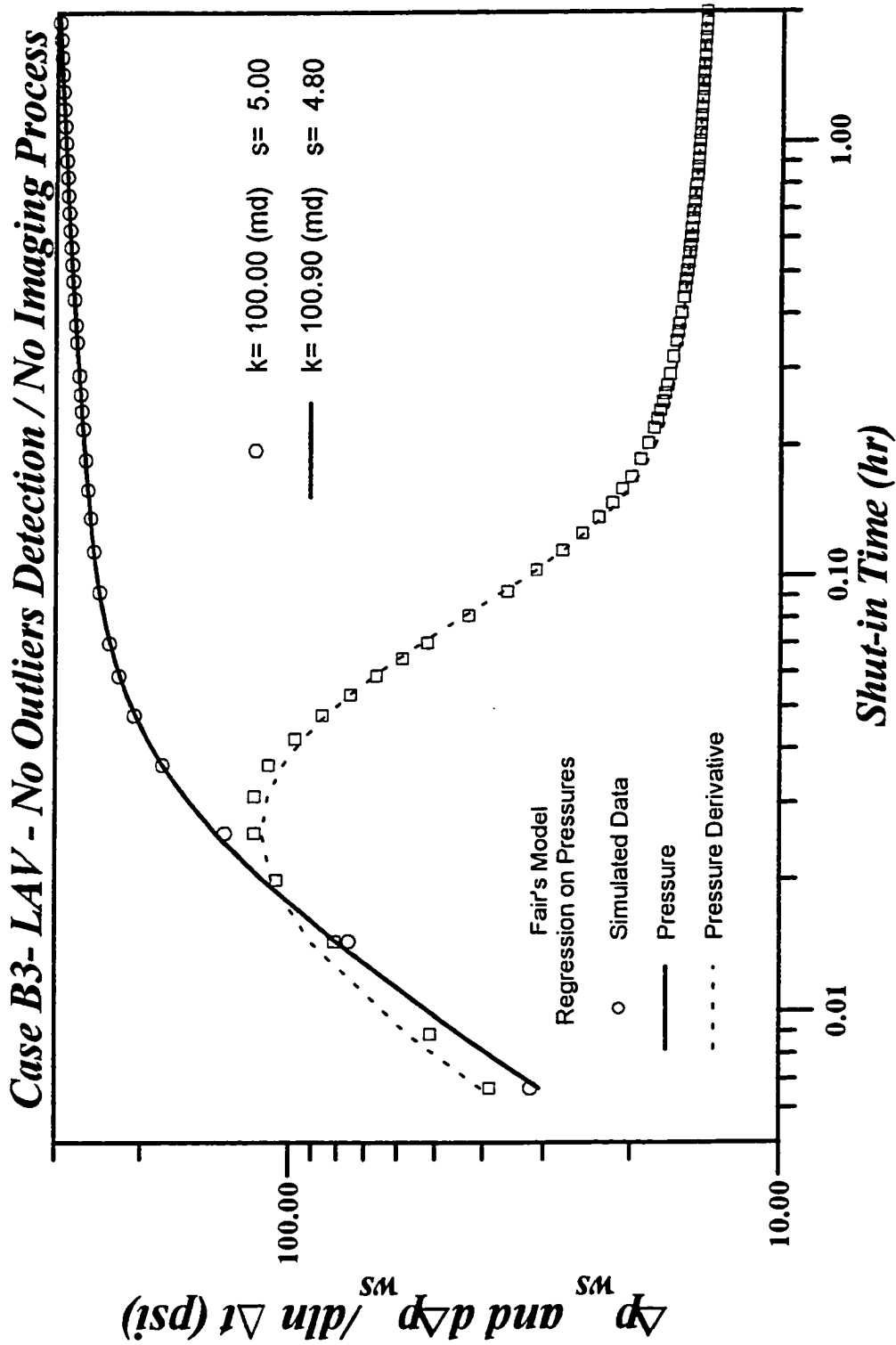
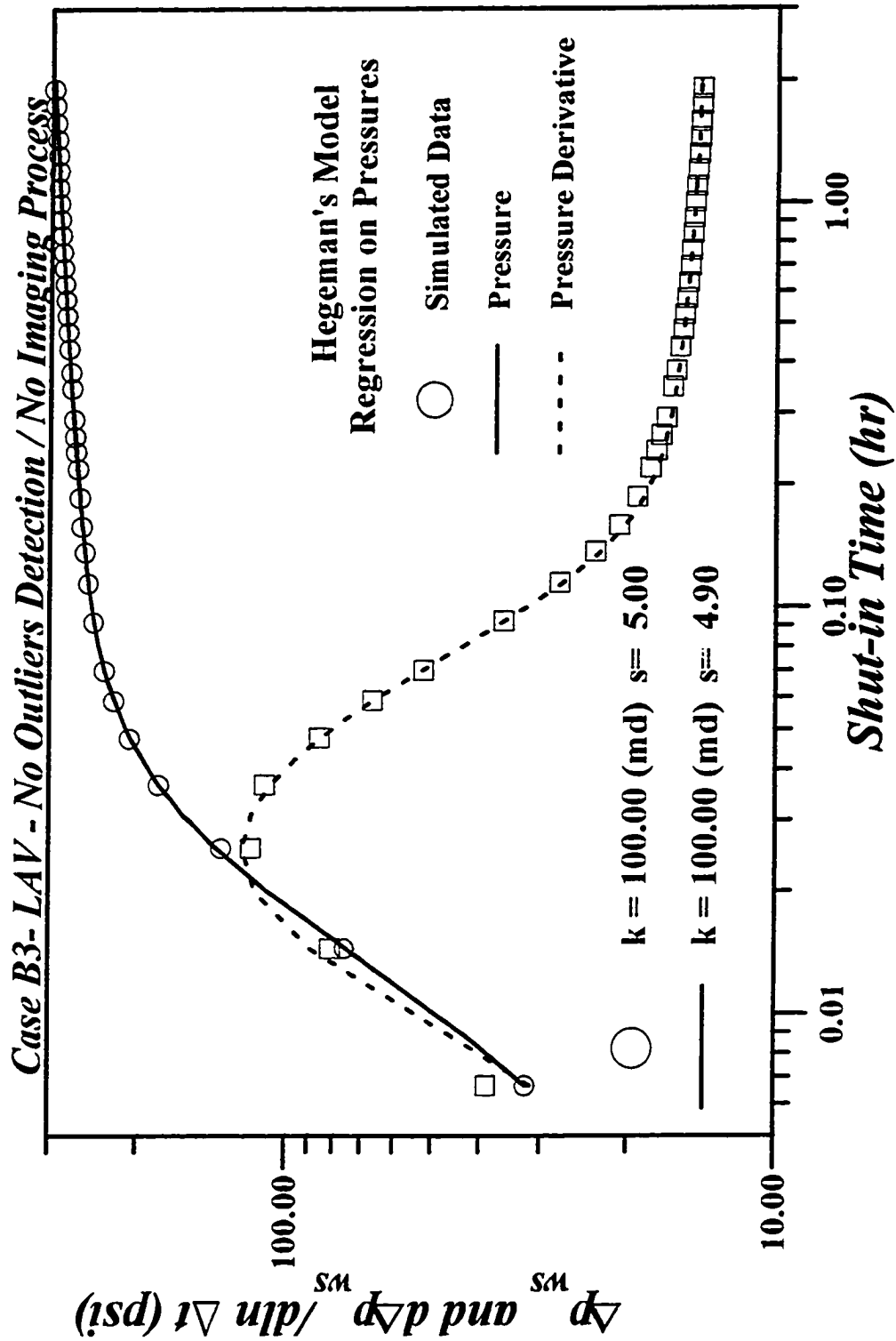**Fig. 4.24 – Regression match of first two hours of buildup data; LAV with Fair's Model; Case B-3.**

Fig. 4.25 - Regression match of first two hours of buildup data; LAV with Hegeman's Model; Case B-3.

Case B-3 Fairs's Model					
Regression Parameters	Simul. Data	LAV No Outliers Detection	NLS Outliers Detection		
			Optimized Value	Minimum Value	Max. Value
k ($md.$)	100.00	1.0092E+02	1.0104E+01	1.0100E+01	1.0107E+01
C ($bbl/psia$)		2.9043E-04	2.9500E-04	2.3637E-04	2.4621E-04
s	5.00	4.8508E+00	4.8590E+00	4.8590E+00	4.8656E+00
α (day)		4.1006E-04	3.9772E-04	3.9388E-03	4.0155E-04
C_ϕ/qB ($psia/bbl/day$)		1.1870E+00	-1.1354E+00	-1.1501E+00	-1.1207E+00

Table 4.9: Case B-3 Least Absolute Value and Least Squares Regression

Case B-3 Hegeman's Model					
Regression Parameters	Simul. Data	LAV No Outliers Detection	NLS Outliers Detection		
			Optimized Value	Minimum Value	Max. Value
k ($md.$)	100.00	1.0103E+02	1.0110+02	1.0107E+02	1.0112E+02
C ($bbl/psia$)		2.9940E-04	3.0028E-04	2.9961E-04	3.0096E-04
s	5.00	4.8619E+00	4.8677E+00	4.8663E+00	4.8712E+00
α (day)		6.1021E-04	6.0784E-04	6.0555E-04	6.1013E-04
C_ϕ/qB ($psia/bbl/day$)		1.1012E+00	-1.0922E+00	-1.0996E+00	-1.0848E+00

Table 4.10: Case B-3 Least Absolute Value and Least Squares Regression

Case B-4 Fairs's Model					
Regression Parameters	Simul. Data	LAV No Outliers Detection	NLS Outliers Detection		
			Optimized Value	Minimum Value	Max. Value
k $(md.)$	10.00	1.1506E+01	1.1511E+01	1.0633E+01	1.2388E+01
C $(bbl/psia)$		1.1377E-03	1.3786E-03	2.9009E-04	2.4672E-03
s	2.00	3.0211E+00	3.0236E+00	2.4034E+00	3.7067E+00
α (day)		3.0074E-02	3.0206E-02	1.2886E-02	4.7526E-02
C_o/qB $(psia/bbl/day)$		1.7010E+01	-1.6941E+01	-4.4027E+01	1.10144E+01

Table 4.11: Case B-4 Least Absolute Value and Least Squares Regression

4.1.3.d   Case B-4

Case B-4 is similar to Case B-1, but in this case the value of permeability was increased to 10.0 md and skin factor reduced to 2.0 . The non-linear regression package was executed again, in this case LAV and NLS with and without outliers detection were considered. Unlike case B-1, we had little difficulty in obtaining a reasonable match regardless of the initial guess, especially for Hegeman's model which again gives the best results: compare Figs. 4.26 and 4.27 and Tables 4.11 and 4.12.

For this case, the regression estimate of k and s are good for all the regression options. The regression with Fair's model show us that the storage dominated period is again not well matched, see Fig.4.26. Hegeman's model regression (Fig. 4.27) shows an excellent match through the time span of data and we obtain small confidence intervals for all parameters; see Table 4.12.
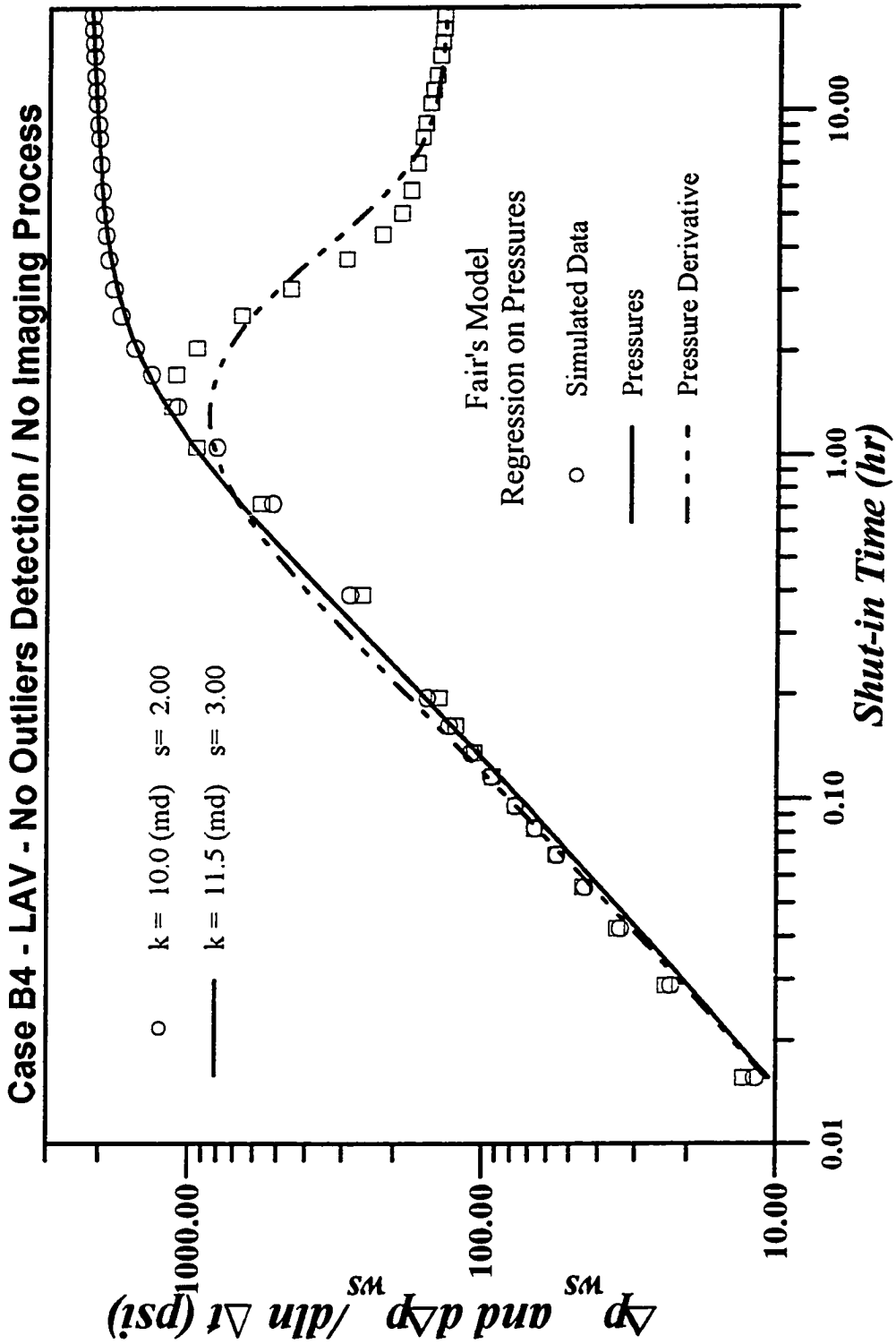
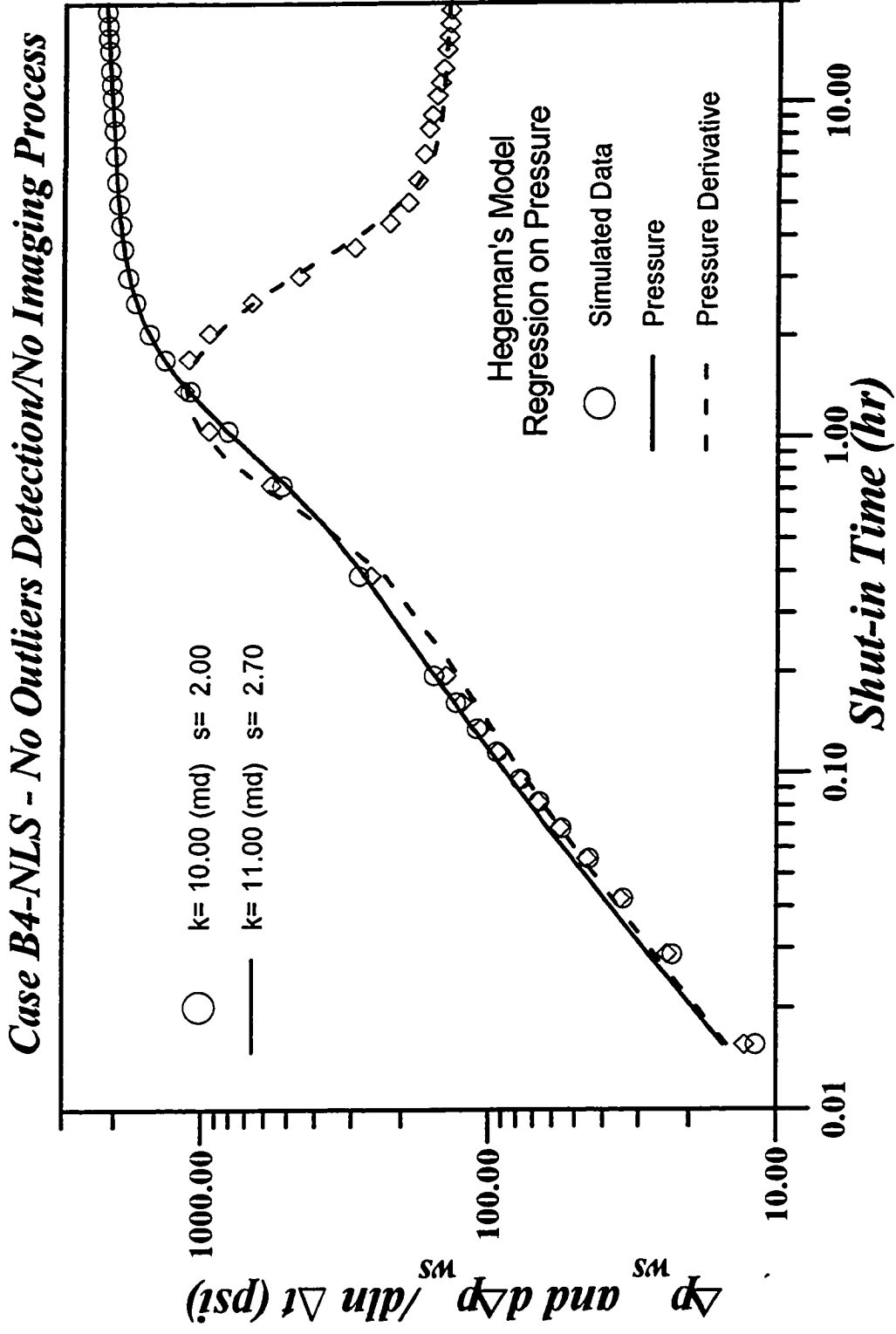Fig. 4.26 – LAV regression with Fair's Model; Case B-4.

Fig. 4.27 – Least squares regression with Hegeman's Model; Case B-4.

Case B-4 Hegeman's Model				
Regression Parameters	Simul. Data	NLS Outliers Detection		
		Optimized Value	Minimum Value	Max. Value
k (md.)	10.00	1.1080+01	1.0871E+01	1.1288E+01
C (bbl/psia)		9.2940E-04	8.6243E-04	9.9636E-04
s	2.00	2.6913E+00	2.5599E+00	2.8538E+00
α (day)		4.6716E-02	4.5888E-02	4.7543E-02
C_ϕ/qB (psia/bbl/day)		-3.4508E+01	-3.8032E+01	-3.0985E+01

Table 4.12: Case B-4 Least Squares Regression

4.1.3.e   Case C.

Although a additional pressure rise will result whenever phase segregation occurs in the wellbore. not all phase segregation can produce a hump in wellbore pressure. With Case C, we show that our simulator can also used to simulate pressure buildup tests in gas-lift wells. Moreover, unlike Case B, buildup data in Case C shows a substantial pressure hump.

Our regression results for Case C buildup data are presented from Fig. 4.28 to 4.29. In this case, we found a excellent agreement between the simulated data and the storage models of Fair and Hegeman. However, the number of outliers points detected using Fair's model are less than the number detected when we use the Hegeman's model and as shown in Table 4.13 and 4.14, we obtain better estimates of k and s with the Fair's model that with the Hegeman's model.
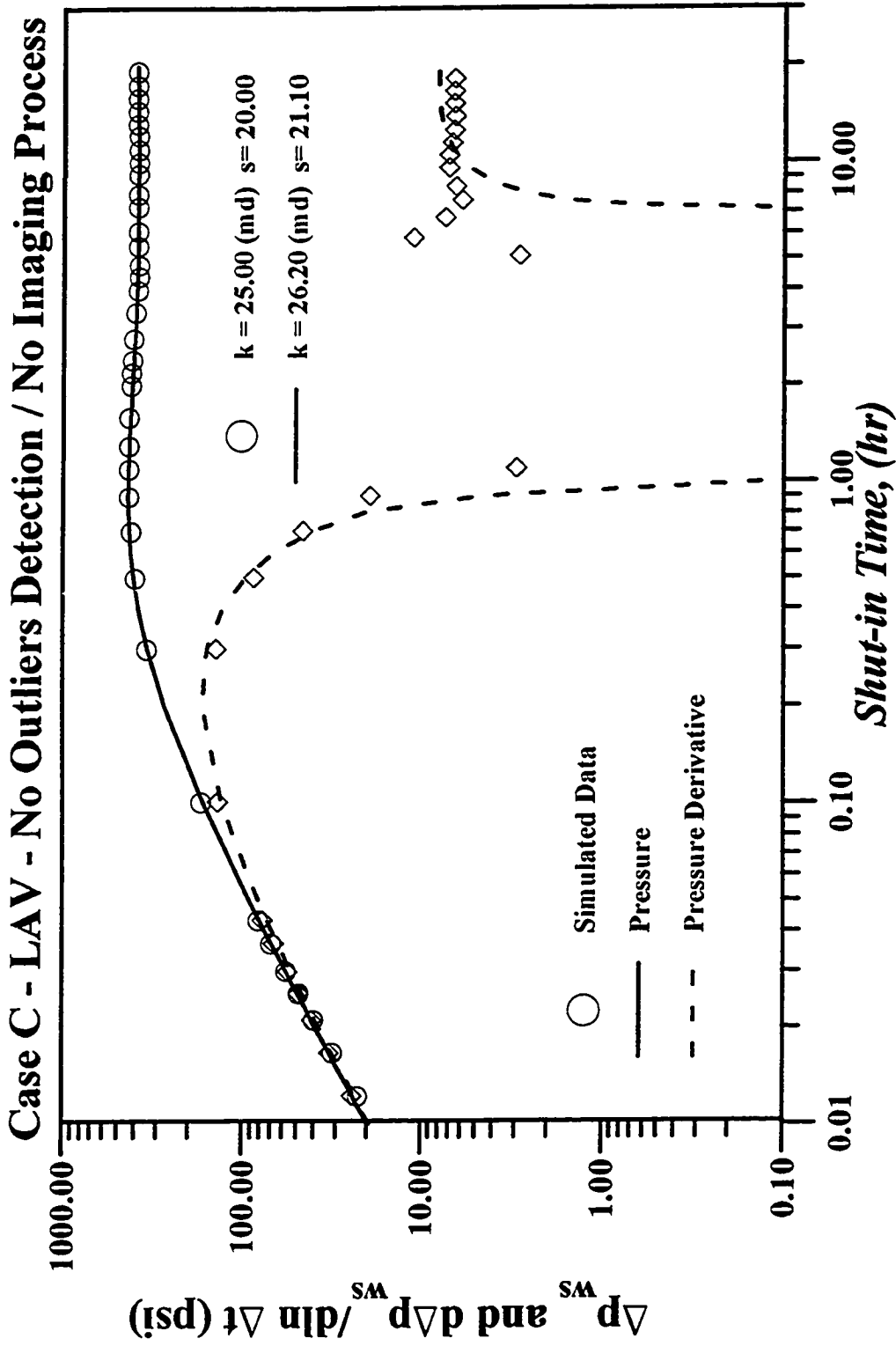
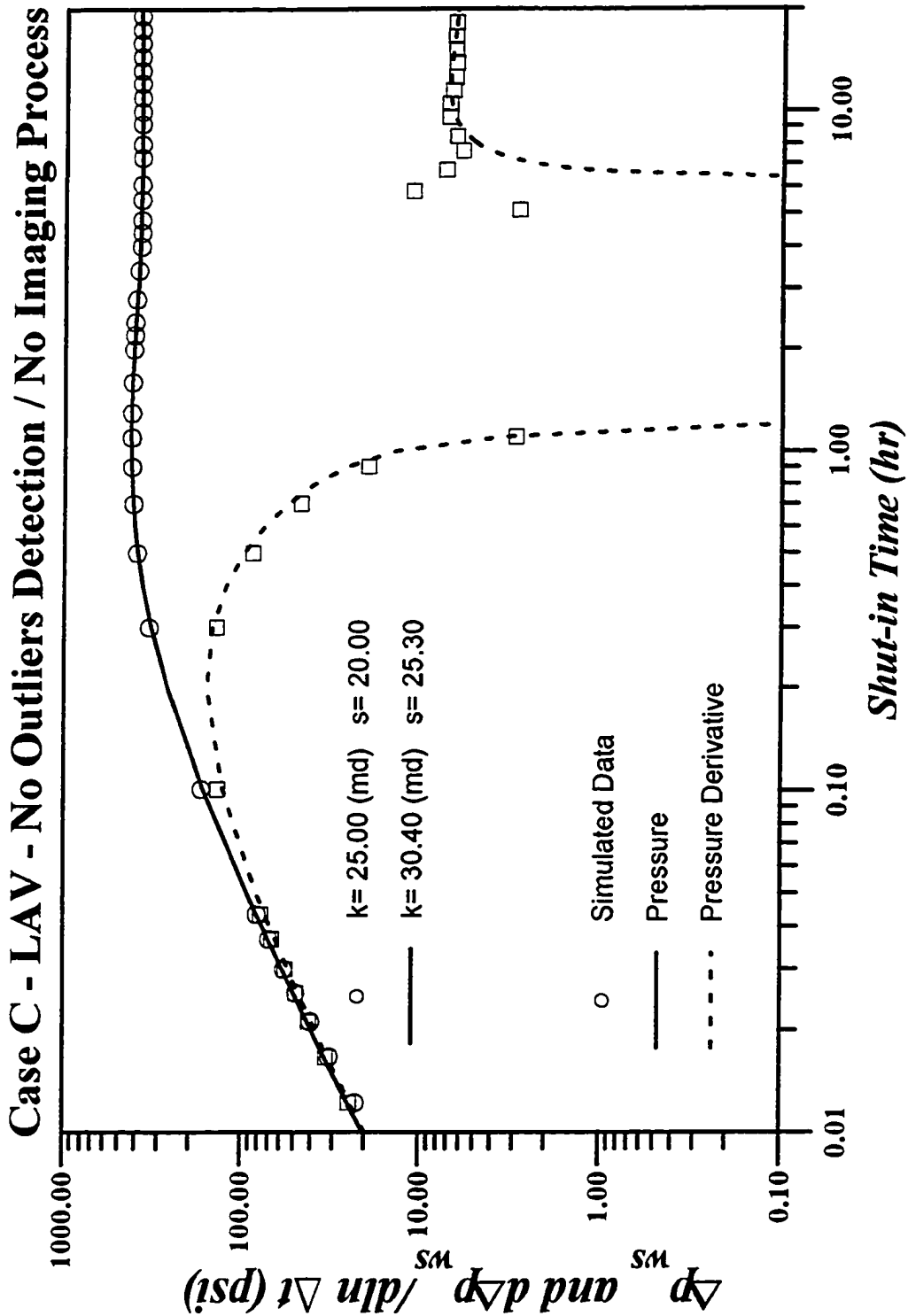Fig. 4.28 - LAV regression with Fair's Model; Case C.

Case C - LAV - No Outliers Detection / No Imaging Process

k= 25.00 (md)   s= 20.00
k= 30.40 (md)   s= 25.30

○   Simulated Data
———   Pressure
- - - - -   Pressure Derivative

Fig. 4.29 - LAV regression with Hegeman's Model; Case C.

Δp_{ws} and $d\Delta p_{ws}/dln\ \Delta t$ (psi)

Shut-in Time (hr)

Case C Fairs's Model					
Regression Parameters	Simul. Data	LAV No Outliers Detection	NLS Outliers Detection		
			Optimized Value	Minimum Value	Max. Value
k (md)	25.00	2.6260E+01	2.6464E+01	2.4926E+01	2.8003E+01
C ($bbl/psia$)		1.9497E-02	1.8707E-02	1.7775E-02	1.9638E-02
s	20.00	2.1415E+01	2.1348E+01	1.9980E+01	2.2929E+01
α (day)		9.9489E-03	1.0013E-02	9.9223E-03	1.0104E-02
C_ϕ/qB ($psia/bbl/day$)		4.3740E+00	4.3644E+00	4.3644E+00	4.3919E+00

Table 4.13: Case C Least Absolute Value and Least Squares Regression

Case C Hegeman's Model					
Regression Parameters	Simul. Data	LAV No Outliers Detection	NLS Outliers Detection		
			Optimized Value	Minimum Value	Max. Value
k (md)	100.00	1.0103E+02	1.0110+02	1.0107E+02	1.0112E+02
C (bbl/psi)		2.9940E-04	3.0028E-04	2.9961E-04	3.0096E-04
s	5.00	4.8619E+00	4.8677E+00	4.8663E+00	4.8712E+00
α (day)		6.1021E-04	6.0784E-04	6.0555E-04	6.1013E-04
C_ϕ/qB ($psi/bbl/day$)		1.1012E+00	-1.0922E+00	-1.0996E+00	-1.0848E+00

Table 4.14: Case C Least Absolute Value and Least Squares Regression

4.2   Temperature Influence on Pressure Response

The objective is to simulate an isothermal and a non-isothermal transient process of wellbore phase segregation, and to examine its effect on pressure buildup data analysis. In this section, pressure responses generated with our numerical simulator for a pressure buildup test is presented and analyzed. The Case B data described in previously is used. Case B is a pressure build-up test in a well that was flowed at a constant sandface rate for 120 hours prior to conducting a 20-hour pressure buildup test.

Fig. 4.30 presents a log-log plot of buildup data generated for Case B using our simulator for isothermal and non-isothermal cases. For the isothermal case the average reservoir temperature of $190°F$ is used as the average wellbore temperature. Toward the end of the buildup test, the derivative is still decreasing and fitting a semilog straight line through the last data points will yield a low estimate of kh. At early times, wellbore segregation is taking place. For the isothermal case, buildup data shows the classical appearance of the wellbore storage and skin solution.

For the nonisothermal case, the heat transfer causes a rate of decrease of the pressure response that causes the derivative to fall below the Δp plot at very early times; i.e., the rate of increase in pressure is less that for the isothermal case. Effectively, the wellbore storage coefficient decreases slightly during early times. Note in Fig. 4.30, we have included both the case where heat transfer in the annulus is by conduction and by natural convection. Since, we have found little difference between these two cases, at least for the cases analyzed here, we will simply refer to them both
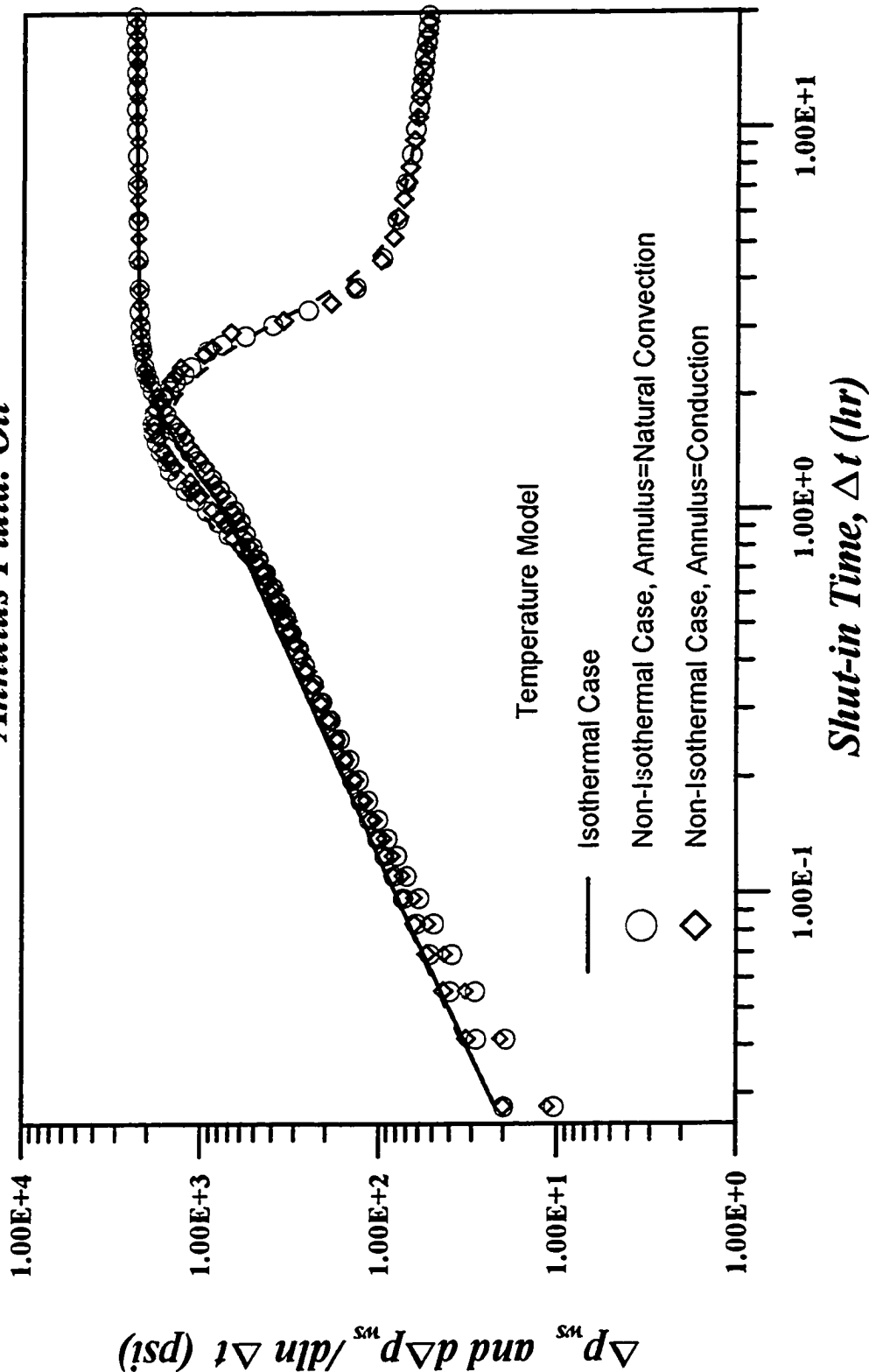
Fig. 4.30 – Log-Log Plot of Pressure and Pressure Derivative for Case B.

as the non-isothermal case.

During the buildup period, the apparent wellbore storage coefficient is computed from

$$C_a = \frac{q_{sf}(\Delta t)/24}{d\,p_{ws}/d\,\Delta t}, \tag{4.5}$$

where $q_{sf}(\Delta t)$ is the rate (afterflow) in RB/D. For a the case of a rising liquid level, it is well known that the wellbore storage coefficient is given by

$$C_L = \frac{144\pi r_p^2}{5.615\rho(g/g_c)}. \tag{4.6}$$

Here, ρ denotes the liquid density and r_p denotes the radius of the pipe in which the liquid is rising, i.e., for our problem, the radius of the tubing. Eq. 4.6 assumes single-phase liquid flow. For the case of a gas well, compressive storage exists during buildup and the wellbore storage coefficient is given by

$$C_G = V_w c_g, \tag{4.7}$$

where V_w is the volume of the wellbore and c_g is the gas compressibility. Eqs. 4.7 pertains to single-phase gas flow. Xiao and Reynolds[56] considered wellbore storage during a closed chamber test. They assumed negligible liquid compressibility and an ideal gas. Also in a closed chamber test, the two phases are completely segregated. For this problem, they showed that the effective wellbore storage coefficient is given by

$$C_a = \frac{C_G C_L}{C_G + C_L}. \tag{4.8}$$

Very early in the test, the wellbore pressure is low so c_g and hence C_g are large so

$$C_G \gg C_L. \tag{4.9}$$

When Eq. 4.9 applies, Eq. 4.8 can be approximated by

$$C_a \approx C_L. \qquad (4.10)$$

Thus at early times, the effective wellbore storage coefficient is approximately equal to one due to a rising liquid level. As pressure increases, gas compressibility decreases and C_a begins to decrease, and at late-times approximately stabilizes at a constant value less than C_L.

Our problem is more complex than any of those discussed above since at the instant of shut-in, a two phase mixture exists in most of the wellbore. Figs. 4.31 and 4.32, respectively, show the gas-void fractions in the top two-thousand feet of the wellbore for the isothermal and non-isothermal cases. The times shown are shut-in times. Note at the instant of shut-in the phases are not segregated; i.e., the gas void fraction is approximately 0.6 at the top of the well and gradually decreases as we go down the well, until we reach a point where we are at bubble-point pressure.

For the nonisothermal case, the wellbore fluid loses heat to the surrounding rock during pressure buildup. As noted by Miller[62], this causes a decrease in enthalpy, an increase in density and an increase in compressibility. Compared to the isothermal case, in the part of the wellbore where two phases exist, the fluids are at a lower temperature than in the isothermal, and hence the gas is more soluble in oil. The additional increase in R_s causes the system compressibility to be higher for the non-isothermal case. Thus, if the effective wellbore storage coefficient is dominated by compressibility effects, we expect to obtain a higher wellbore storage coefficient for the non-isothermal case. This also means that for a given pressure change, the afterflow
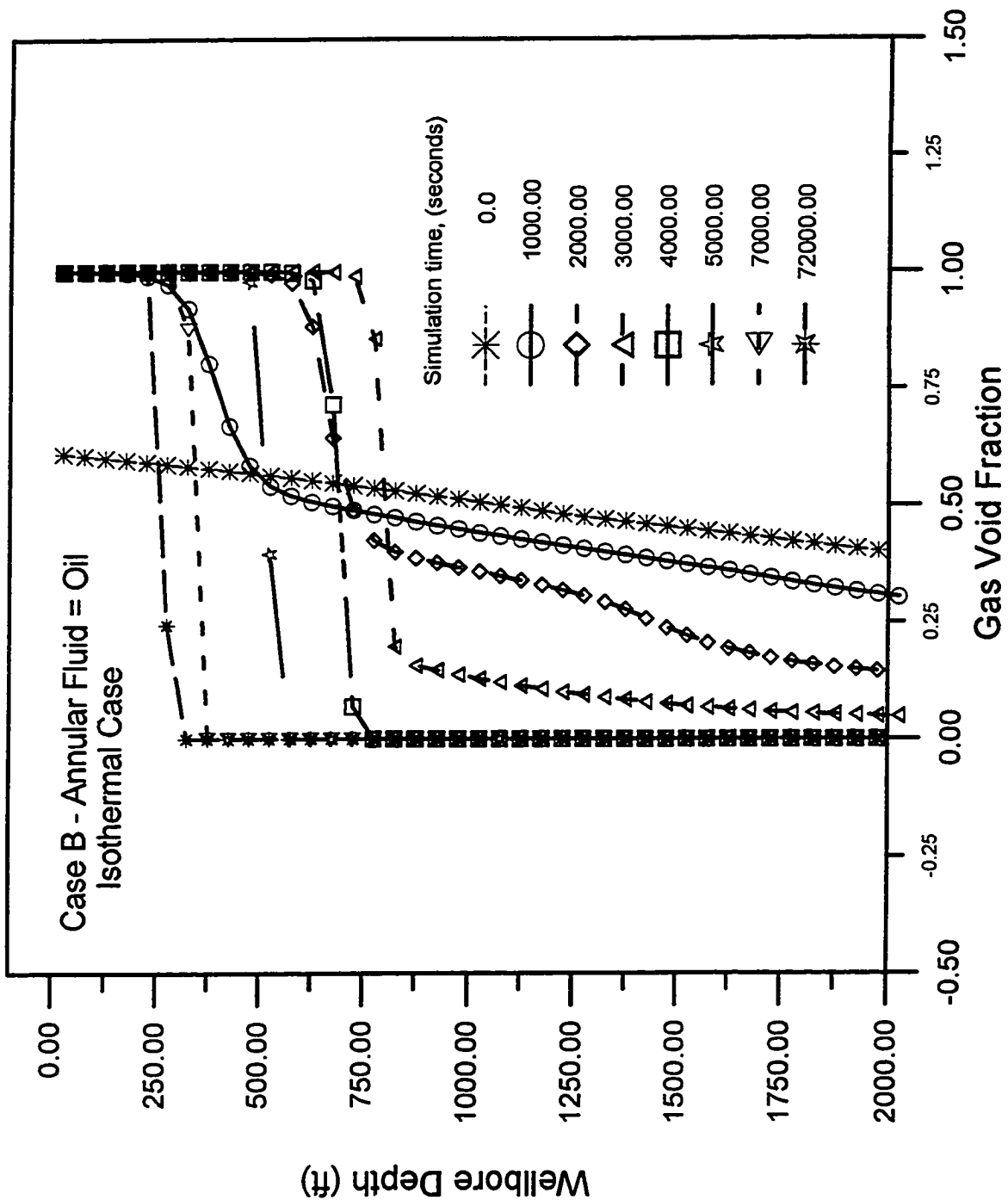
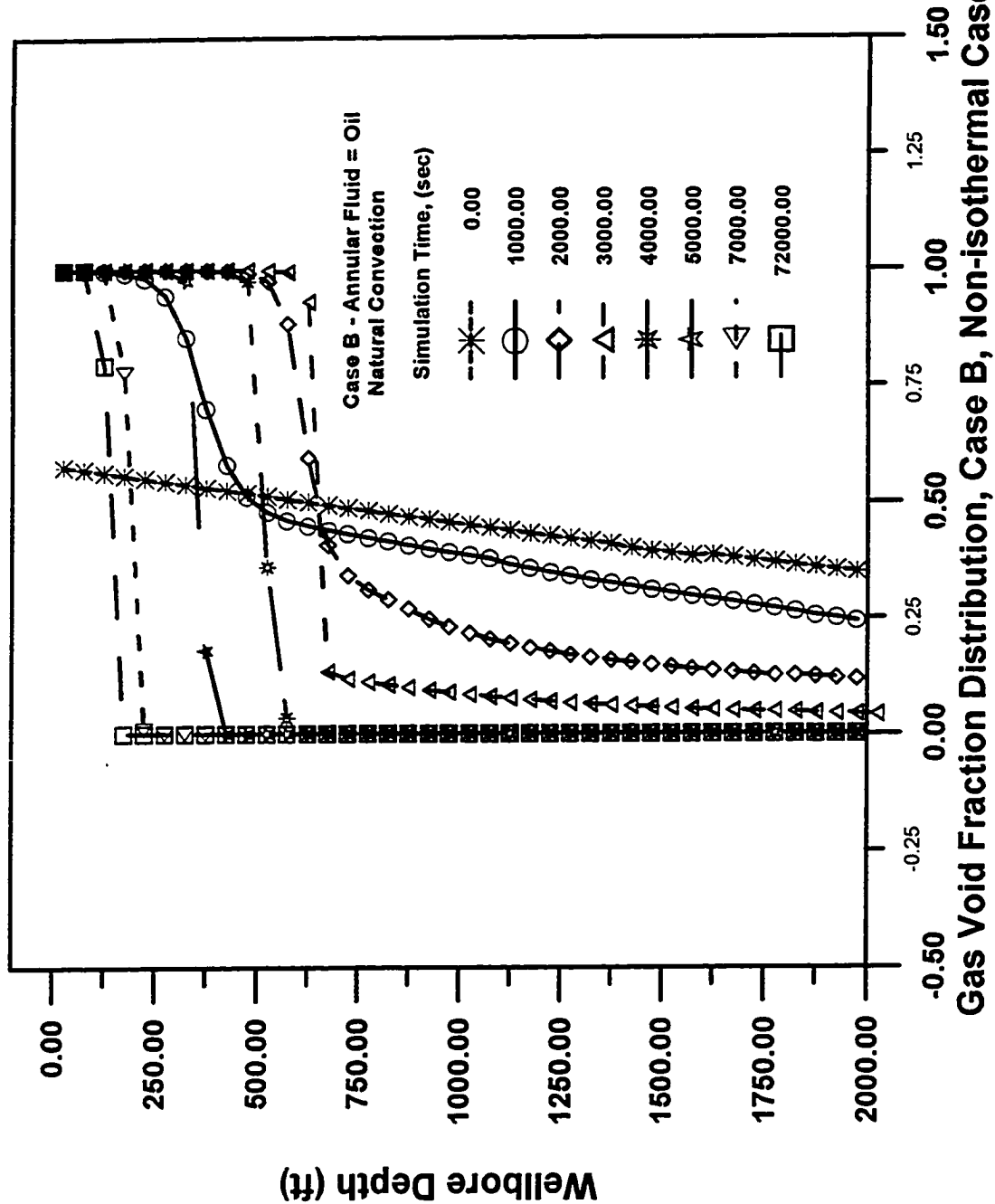Fig. 4.31 – Gas Void Fraction Distribution for Case B, Isothermal Case

Fig. 4.32 – Gas Void Fraction Distribution for Case B, Non Isothermal Case

will be greater for the nonisothermal case. Because of this, and the fact that more gas is dissolved in oil for the non-isothermal case, we expect to also obtain a higher liquid column in the wellbore once the phases segregate. On the other hand, since density is greater in the non-isothermal case, if the effective wellbore storage coefficient were dominated by a rising liquid level, we would expect the wellbore storage coefficient to be smaller for the non-isothermal case; see Eq. 4.6.

Fig. 4.33 shows a plot of the normalized sandface flow rate during buildup. Fig. 4.34 shows the same results during the first two hours of buildup. Note Fig. 4.34 shows the afterflow is greater for the non-isothermal case during the first two hours of buildup as postulated in our previous discussion. Since the total amount of afterflow is greater for the non-isothermal case and more gas can be dissolved in the oil, the phase-interface should be located higher in the wellbore for the non-isothermal case. This is verified by a comparison of the results of Figs. 4.31 and 4.32; compare for example the two sets of results at 4,000 seconds (1.11 hours). Note in both cases, the fluids are essentially completely segregated after 4,000 seconds of shut-in. Once the fluids have become segregated, the behavior becomes similar to a closed chamber test with subsequent afterflow compressing the gas column and resulting in a decreasing wellbore storage coefficient. The decreasing wellbore storage coefficient results in the pressure derivative curve rising above the pressure curve in Fig. 4.30. Note this occurs at approximately one hour (3,600 seconds) which is about the time when the fluids become completely segregated.

A plot of the effective wellbore coefficient computed from Eq. 4.5 is shown in Fig. 4.35. Note this plot also shows that the wellbore storage coefficient begins

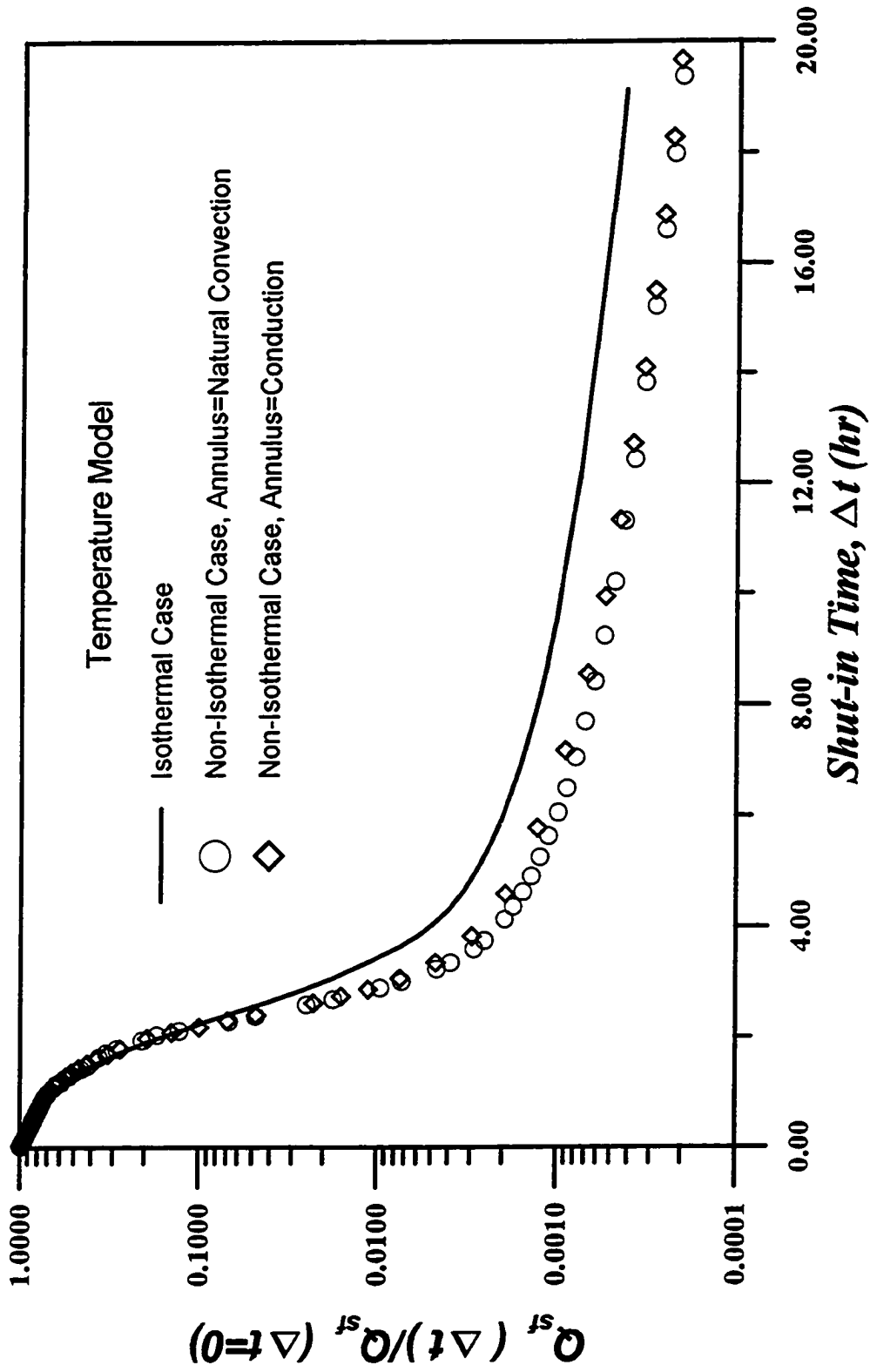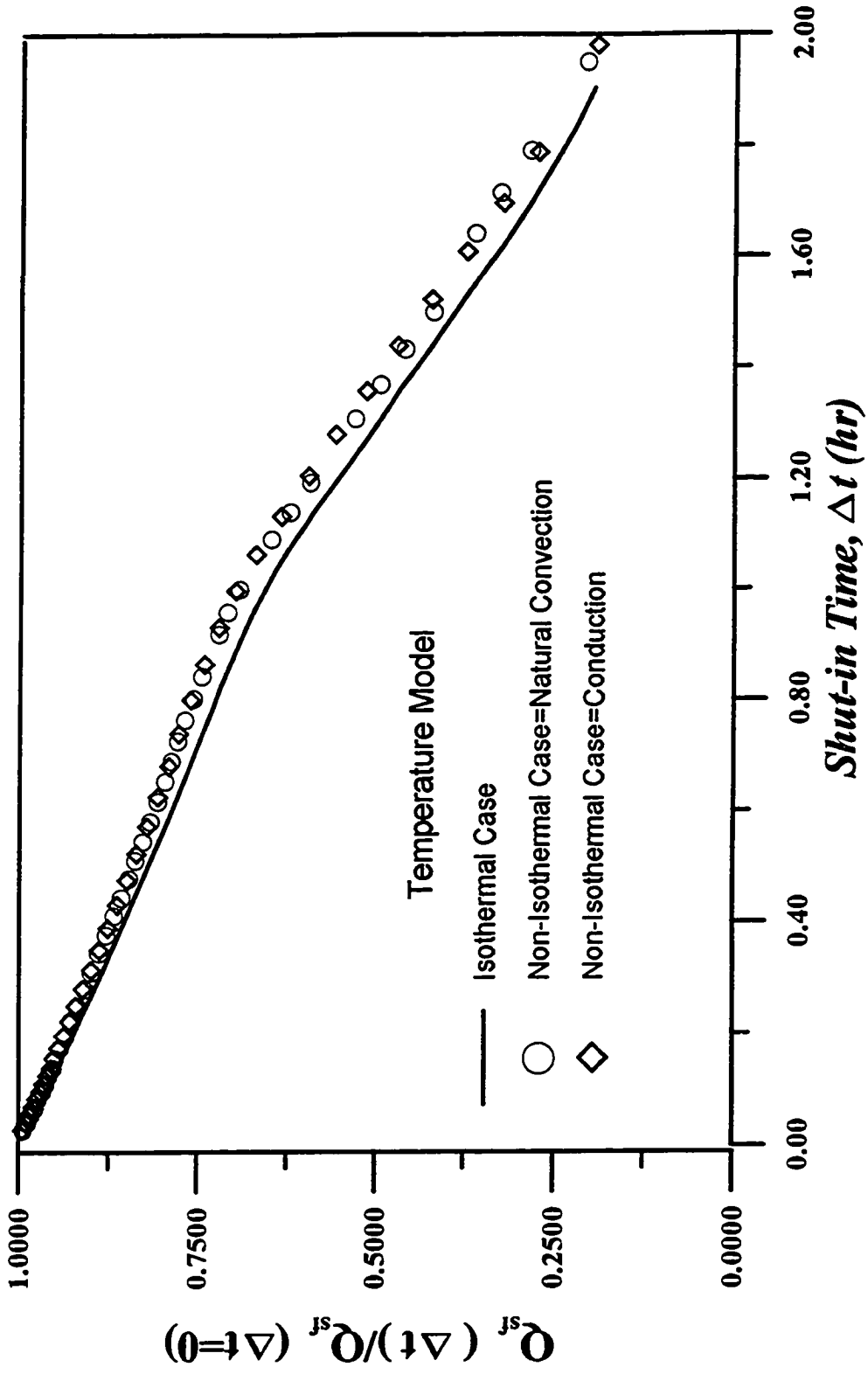Fig. 4.33 – Normalized Sandface Flow Rate as a Function of Shut-in Time for Case B.

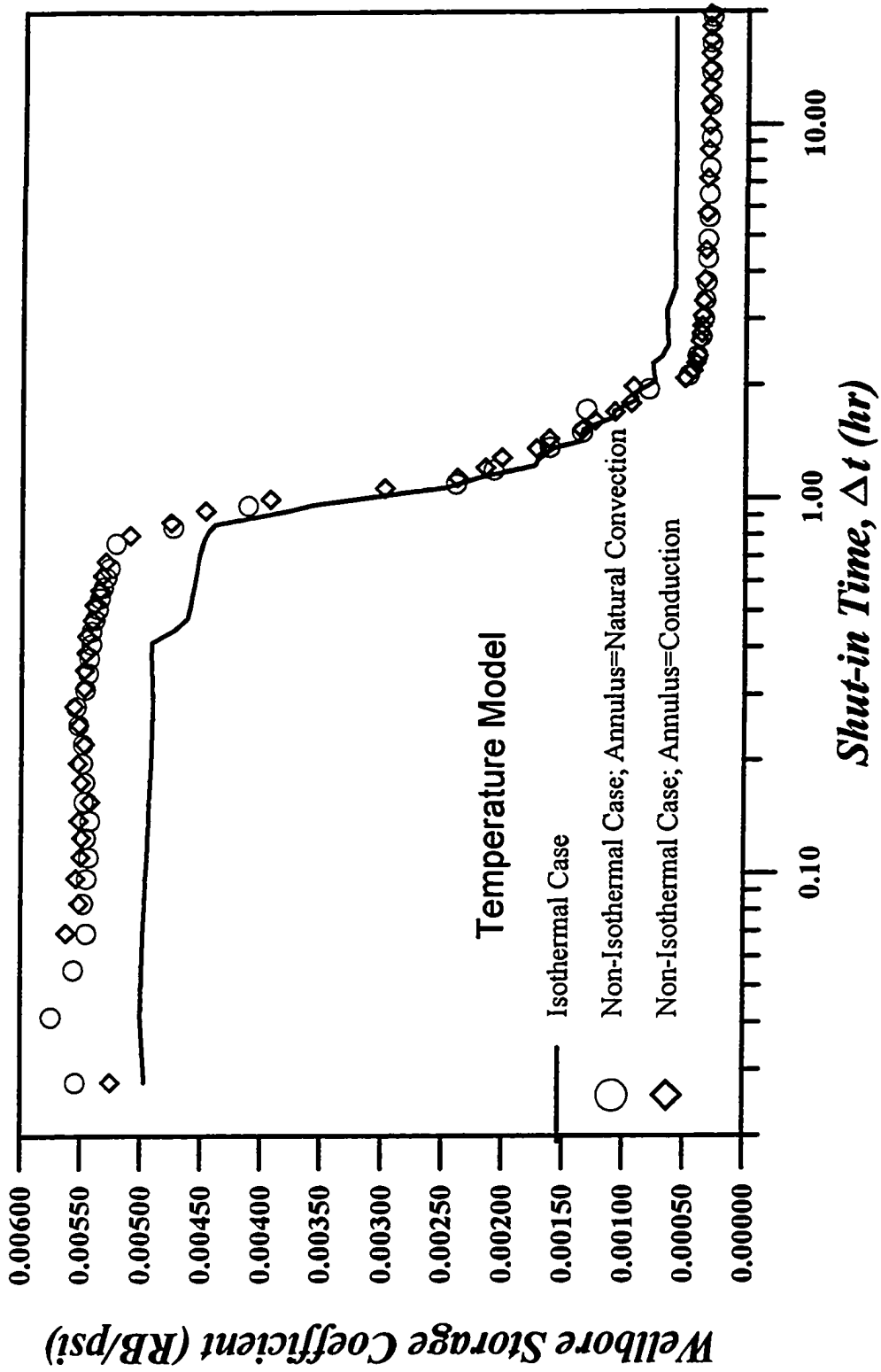**Fig. 4.34- Normalized Sandface Flow Rate as a Function of Shut-in Time for Case B.**

143

Fig. 4.35 – Change in Wellbore Storage Coefficient for Case B.

to decrease rapidly at about one hour. Also for $\Delta t < 1$ hour, the effective wellbore storage coefficient is higher for the non-isothermal case as expected based on our earlier discussion. This is also consistent with the greater afterflow rate which occurs for the non-isothermal case for $\Delta t < 2$ hours; see Fig. 4.34. If, as in a closed chamber test, the effective storage coefficient were dominated by the compression of the gas column due to a rising liquid level, then based on our earlier discussion (see Eqs. 4.8-4.10), Eq. 4.6 would give an approximation of the effective wellbore storage coefficient. Using the average wellbore density at 0.1 hours (using the value any other time between 0.1 and 1 hours has a negligible influence on the results), Eq. 4.6 gives $C_L = 0.0135$ RB/STB for the isothermal case and 0.0130 for the non-isothermal case. Note that C_L is larger for the isothermal case, whereas the results of Fig. 4.35 show the effective wellbore storage coefficient is greater for the non-isothermal case. Also the value of these liquid wellbore storage coefficients are more than twice as large as the effective wellbore storage coefficients obtained in Fig. 4.35 at early shut-in times.

At a shut-in time of $\Delta t \approx 2$ hours, the effective wellbore storage coefficient for the non-isothermal case falls below the effective wellbore storage coefficient obtained for the isothermal case and correspondingly, the rate of afterflow for the non-isothermal case becomes less than the flow rate for the isothermal case; see Fig. 4.33. The cumulative afterflow (Fig. 4.36) is always greater for the non-isothermal case.

Once the fluids have become completely segregated, the effects of mass transfer between the phases becomes negligible. At this time, the pressure profiles in the wellbore are not significantly different. Since the amount of free gas in the wellbore is less for the non-isothermal case, the total compressibility is less than for the
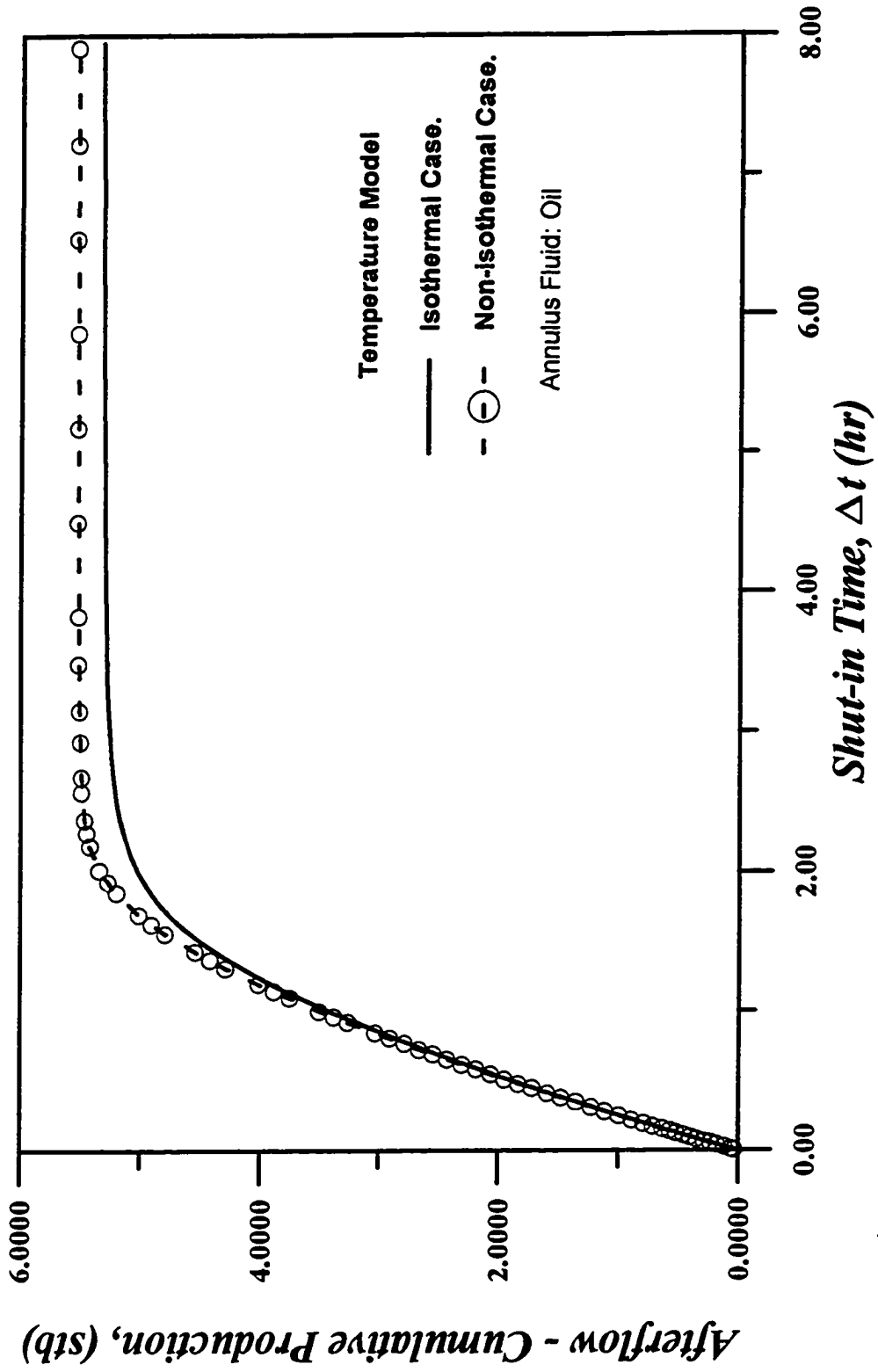
Fig. 4.36 - Cumulative Afterflow for Case B.

isothermal case. Thus, wellbore storage due to compressibility effects is less in the non-isothermal case. Also since the density is greater in the non-isothermal case, any wellbore storage effects due to a rising liquid level would be less. It follows that after the phases have become completely segregated, the effective wellbore storage coefficient for the nonisothermal case should be less than the wellbore storage coefficient for the isothermal case.

Fig. 4.37 shows the temperature profile in the top 2,000 feet of the well at shut-in times of 5,000 sec., 7,000 sec. and 72,000 sec. At a shut-in time of 20 hours (72,000 sec.), the temperature profile has returned to the one predicted by the geothermal gradient.

Fig. 4.39 shows the mixture density profile in the top 2,000 feet of the well. At the instant of shut-in a two phase mixture exists throughout this 2,000 feet. As a single-phase gas column is formed at the top, the density decreases in this region. Once the gas begins to cool, its density increases. Also the pressure at the wellhead is increasing which causes the density to increase. From a depth of 1,000 ft. to 2,000 ft., gas is both flowing to the top and being redissolved so the relative volume of liquid increases which causes the mixture density to increase. The fluids are also cooling in this part of the wellbore due to heat loss to the surrounding rock. Cooling also tends to increase the density. Note from 7,000 seconds to the end of the buildup test, the density in the liquid column increases as we go up the wellbore. This is due to the fact that the liquid is cooler at the top. We believe that during this time period natural convection is occurring with hot liquid continuing to rise to the top, cooling off and then falling back towards the bottom.
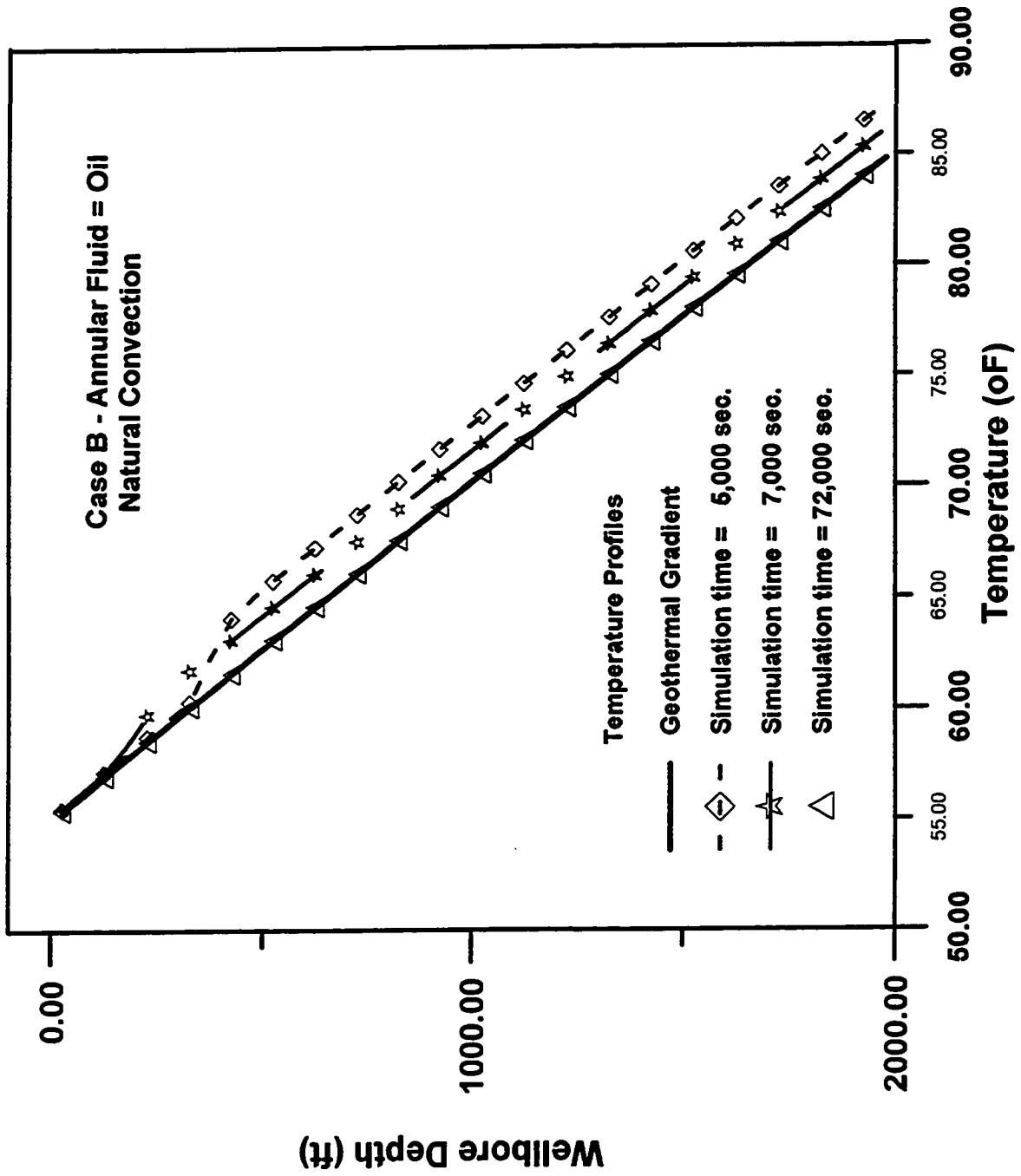
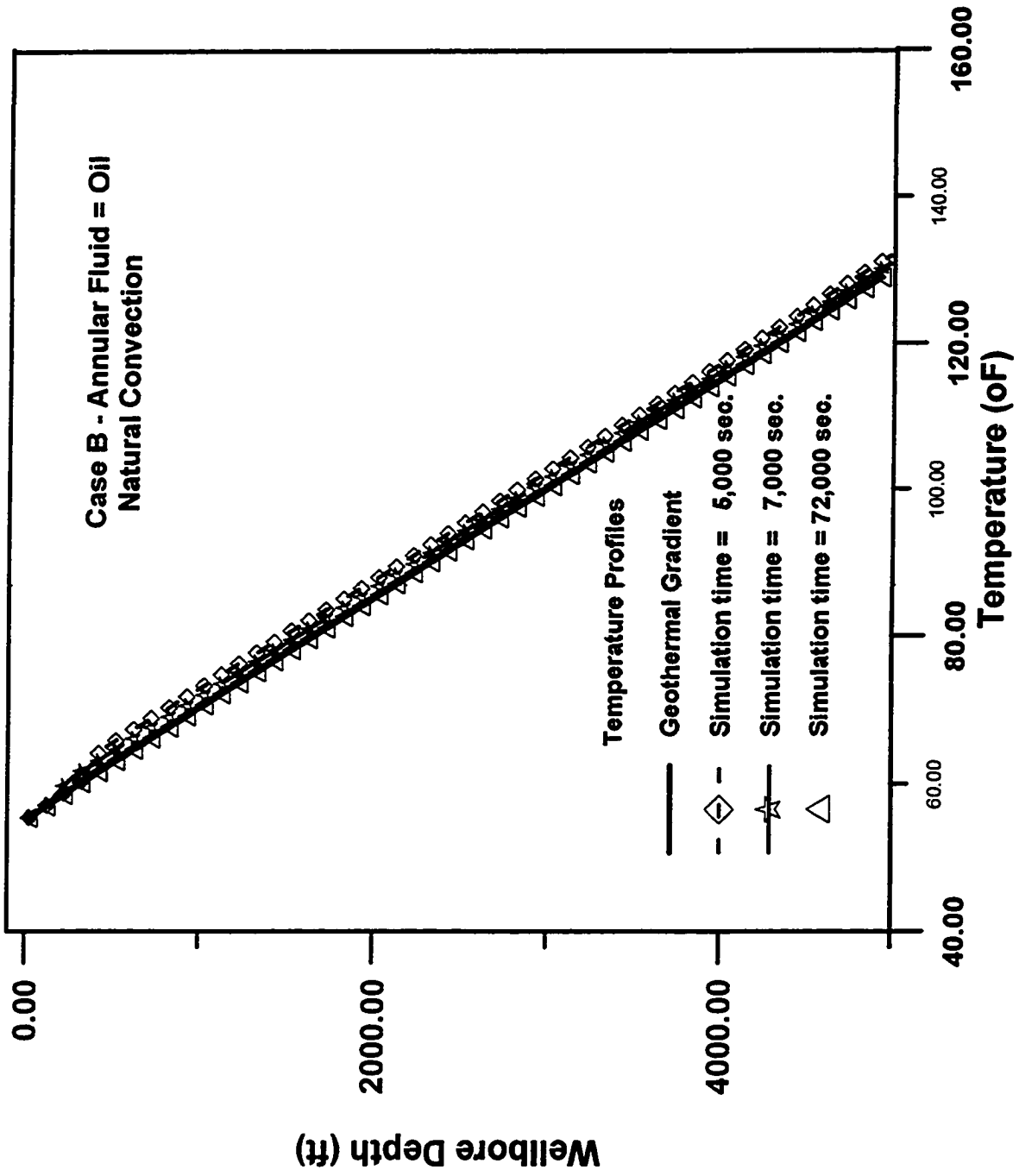**Fig. 4.37 – Temperature Distribution in the Wellbore for Case B.**

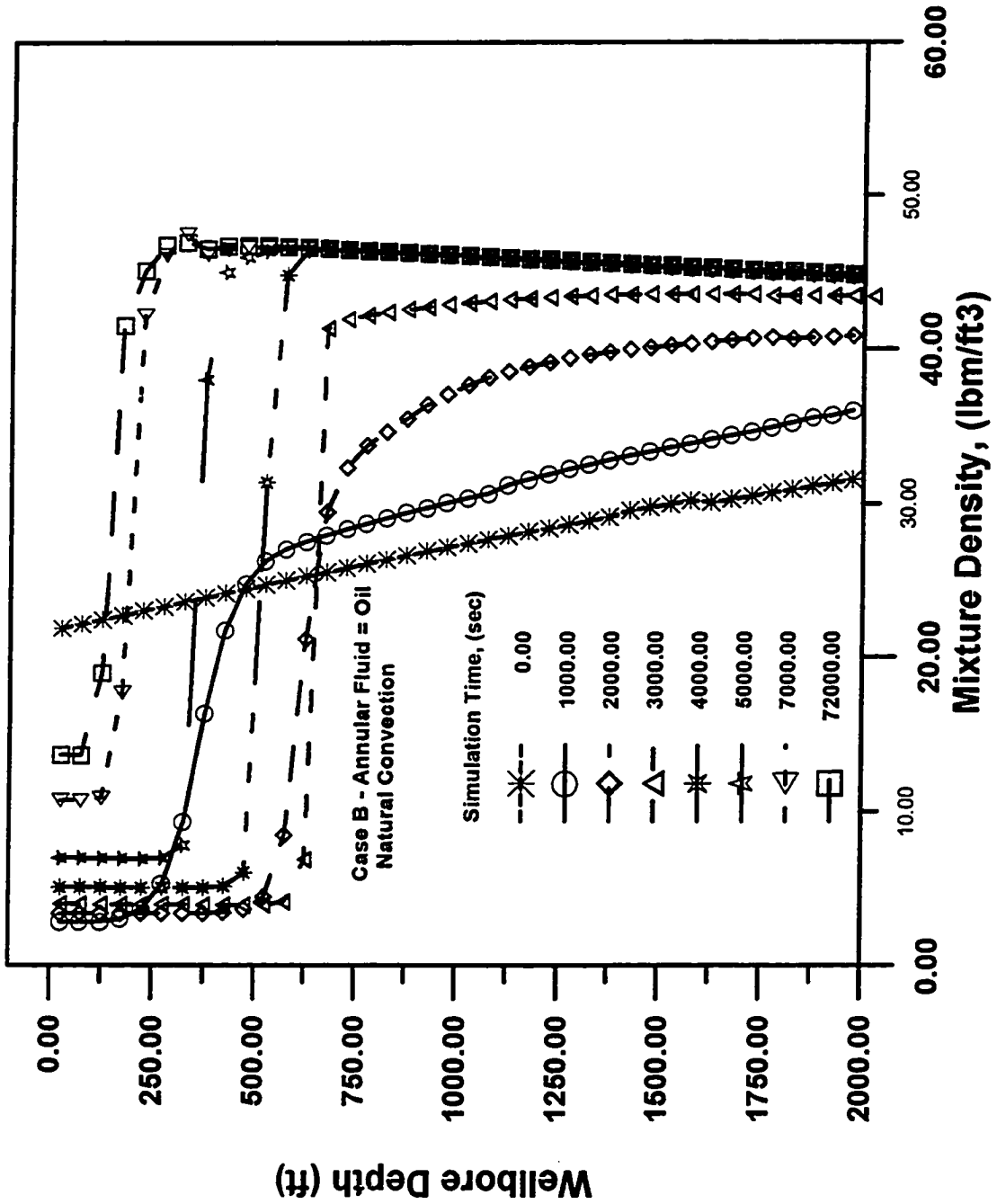Fig. 4.38 – Temperature Distribution in the Wellbore for Case B.

Fig. 4.39 - Mixture Density Distribution for Case B.

4.3   Matching Wellhead Responses.

In this section, the results of several simulations are presented. From these simulations wellhead and bottomhole data are recorded; this allows us to have synthetic "measured" data. Those wellhead data are used to invert the wellhead pressure and rate response to obtain pressure and rate at bottomhole conditions. The data obtained from the inverse problem are compared with the bottomhole data generated from the simulator, in order to verify the feasibility of using it as a practical method to compute bottomhole data from the wellhead pressure and rate responses.

A direct method of optimization (see Appendix B) was selected as a method to invert the wellhead recorded data to bottomhole conditions. This selection arose because our implementation of Newton's method did not converge to the current bottomhole values of pressure and rate. The method applied does not require derivatives which must be computed numerically if Newton's method is used.

The Rowan's subplex[75] method was selected as the optimization procedure because the method performs well with noisy or discontinuous objective functions and derivatives of the objective function are not required. The subplex method, which is based on the simplex method, was designed by Rowan to improve the performance of the standard simplex method. The subplex method decomposes the problem solution space into smaller regions that the simplex method itself can search efficiently. A more detailed discussion is presented in Appendix B and in Ref. 75.

4.3.1 Calculation Algorithm.

The method requires input data on well parameters, simulator control data and fluid property data including ρ_{os} and ρ_{gs}, gas-oil surface tension. Other required properties, such as R_s, B_o and B_g are computed by using empirical correlations (see chapter 2 of Ref. 30).

To determine the bottomhole values of pressure and velocity, we use the procedure discussed below. The matching procedure is done time step by time step, starting with the drawdown data, however, we match both drawdown and buildup data . Buildup data can be matched independently provided the distributions of v_m and p can be computed at the instant of shut-in, i.e., using wellbore model assuming steady-state conditions. In the matching procedure we use the wellbore model itself. There is no need to couple the wellbore model with a reservoir simulator. The following relationships are used to compute the wellhead oil rate or total mixture rate from the wellhead mixture velocity, this relations allow us to match a combination of either wellhead oil rate and pressure, or, wellhead total mixture rate and pressure, i.e.,

$$v_{sl,wellhead} = \frac{1}{E_l}(v_m - \frac{E_g\rho_g v_r}{\rho_m}), \tag{4.11}$$

$$(q_o)_{wellhead} = v_{sl,wellhead}\, A, \tag{4.12}$$

$$(q_{o,sc})_{wellhead} = \left(\frac{86400}{5.615}\right)\left(\frac{q_o}{B_o}\right)_{wellhead}, \tag{4.13}$$

$$(q_{g,sc})_{wellhead} = R\ (q_{o,sc})_{wellhead}, \tag{4.14}$$

and

$$(q_t)_{wellhead} = \frac{(q_{g,sc})_{wellhead}}{5.615} + (q_{o,sc})_{wellhead},$$ (4.15)

where $(q_{o,sc})_{wellhead}$ is the oil volumetric flow rate in $[STB/day]$, $(q_{g,sc})_{wellhead}$ is the gas volumetric flow rate in $[scf/day]$, $(q_t)_{wellhead}$ is the total volumetric flow rate in $[STB/day]$, $v_{w,wellhead}$ is the wellhead mixture velocity in $[ft/sec]$, $v_{sl,wellhead}$ is the liquid superficial velocity in $[ft/sec]$, v_r is the relative velocity between gas and liquid phasein$[ft/sec]$, A is the pipe cross sectional area in $[ft^2]$, and B_o is the oil volume factor in $[RB/STB]$.

In case of recorded wellhead oil volumetric rate, the following set of equation can be used to calculate the wellhead mixture velocity, i.e.,

$$q_l = (\frac{5.615}{86400}) (q_{o,sc})_{wellhead} B_o,$$ (4.16)

$$q_g = (\frac{5.615}{86400}) (q_{o,sc})_{wellhead} (R - R_s) B_g,$$ (4.17)

From the mixture velocity definition, i.e.,

$$v_{m,wellhead} = \frac{v_{sg} \rho_l + v_{sl} \rho_g}{\rho_m},$$ (4.18)

$$v_{m,wellhead} = \frac{1}{A} \left(\frac{q_g \rho_l + q_l \rho_g}{\rho_m} \right),$$ (4.19)

where q_l and q_g are the oil and gas phase volumetric flow rates in $[ft^3/sec]$, B_g is the gas volume factor $[RB/scf]$, R is total gas-oil ratio in $[scf/STB]$, R_s is the solution gas-oil ratio in $[scf/STB]$, and ρ_l and ρ_g are the oil and gas densities in $[lb_m/ft^3]$.

4.3.1.a   Matching Procedure.

1. Initially (at $t = 0$), we assume the well is closed so that gravity equilibrium exists in the wellbore. We assume that the temperature profile in the wellbore follows the geothermal gradient and the velocity profile is zero along the wellbore.

2. Bottomhole pressure is equal to the initial reservoir pressure.

3. The procedure described in section 3.3.1.b is used for each wellbore gridblock position to compute the pressure and dependent variables distribution along the wellbore, at $t = 0$.

4. For $t > 0$ at each time step, from the recorded data, we read the values of wellhead pressure, total production rate and wellhead temperature.

5. Guess the values for $(p_{1/2})^{n+1}$ and $(v_{m,1/2})^{n+1}$ at bottomhole. This guess can be obtained by simply using the value at the old time step. For the first time step, we can guess $(p_{1/2})^{n+1} = p_i$ and $(v_{m,1/2})^{n+1} = 0$.

6. Using these guesses, the subplex method is called (see section B.2.2 in Appendix B). The subplex method uses a modified version of the procedure described in section 3.3.1a when matching drawdown data. A modified version of the procedure described in section 3.3.2.a is used when matching buildup data. The only difference between the procedures of 3.3.1a and 3.3.2.a is that we assume a linear temperature gradient between the recorded wellhead temperature and the bottomhole temperature. The bottomhole temperature is assumed to be constant and computed using the geothermal gradient. The objective function

that the subplex method minimizes is

$$\phi = \quad \left(p_{wh,recorded} - p_{wh,wellbore\,model}\right)^2 / \sigma_p^2$$

$$+\left(v_{m,wh,recorded} - v_{m,wh,wellbore\,model}\right)^2 / \sigma_v^2$$

$$+\left(v_{m,1/2,subxplex} - v_{m,1/2,mass\,balance}\right)^2 / \sigma_v^2, \tag{4.20}$$

while the σ terms should be based on the resolution of the measurement instrument, in this work we used σ_p=0.5 $[psia]$, $\sigma_v = 0.01[ft/sec]$. These values of σ were selected by trial and error and give us a good combination of speed and accuracy in the matching procedure. The last term in Eq. 4.20 was added to help ensure the conservation of mass, see sections 3.1 and 3.3. In Eq. 4.20,

$$(v_m)_{1/2,mass\,balance} = \left(\frac{\Delta z}{\Delta t}\right)\frac{\sum_{i=1}^{N}[(\rho_m)_i^{n+1} - (\rho_m)_i^{n}]}{(\rho_m)_{1/2}^{n+1}} + \frac{(\rho_m)_{N+1/2}^{n+1}}{(\rho_m)_{1/2}^{n+1}}(v_m)_{N+1/2}^{n+1}. \tag{4.21}$$

If the difference in the estimated value of bottomhole velocity from the subplex method and the one computed with Eq. 4.21 is large, this difference is going to be reflected in the value of the objective function and causes that the subplex method to reject the estimated value of bottomhole velocity.

Another form of the objective function that we tried is

$$\phi = \quad \left(p_{wh,recorded} - p_{wh,wellbore\,model}\right)^2 / p_i^2$$

$$+\left(v_{m,wh,recorded} - v_{m,wh,wellbore\,model}\right)^2 / (v_m)_{N+1/2,tp}^2$$

$$+\left(v_{m,1/2,subxplex} - v_{m,1/2,mass\,balance}\right)^2 / (v_m)_{N+1/2,tp}^2, \tag{4.22}$$

where p_i is the initial reservoir pressure and $(v_m)_{N+1/2,tp}$ is the recorded wellhead mixture velocity at the end of the drawdown. This form of the objec-

tive function normalizes the differences in pressures and velocities to a relative nondimensional scale. We did not find significant differences between the results obtained from Eq. 4.20 and Eq. 4.22.

7. Repeat step 5-7 for all the time steps.

In the present study, as recommended in Ref. 75, the following parameters were used: $\alpha = 1$, $\beta = 0.5$, $\gamma = 2$, $\delta = 0.5$, $\psi = 0.25$ and $\omega = .1$, where α is the reflection coefficient, β is the contraction coefficient, γ is the expansion coefficient, δ is the massive contraction coefficient, ψ is the simplex reduction coefficient and ω is the step reduction coefficient (see Appendix B).

For all cases presented here, the drawdown was matched first, then the buildup period was matched. The matching of buildup data is done separately starting at $\Delta t = 0$ with the wellbore profiles of variables computed at the end of the drawdown period by matching the drawdown values of wellhead pressures and rates. In all cases presented, the data were generated using the wellbore model coupled with the RDRBOS (r-z) reservoir simulator[50].

4.3.1.b   Case M-1

Case M-1 pertains to a well which flowed for a period of 120 hours prior to conducting a 20 hour pressure buildup test. The main objective is to simulate a transient drawdown and buildup period using the wellbore model coupled with the (r-z) simulator. Table 4.15 gives a list of input parameters used in Case M-1. Input parameters for Case M-1 are chosen such that the bottomhole pressure is only a few

Parameter	Value	Unit
Drawdown oil production rate	65.00	STB/D
Total production time	120.00	hours
Inital reservoir pressure	5215.00	psia
Initial bubble point pressure	2710.00	psia
Oil compressibility ($p > p_b$)	1.0e-5	1/psia
Oil component API gravity at s.c.	45.00	API
Gas component specific gravity at s.c.	0.70	-
Oil-gas surface tension	4.50	dynes/cm
Wellbore pipe inside diameter	1.80	inch
Formation absolute permeability	25.00	md.
Formation thickness	10.00	ft.
Formation porosity	0.20	-
Wellbore radius	0.364	ft.
System isothermal compressibility	2e-5	1/psia
Average oil viscosity	2.00	cp.
Skin factor	15.00	-
Wellbore depth	9000.00	ft.
Spatial Increment	200.00	ft.
Buildup simulation time	20.00	hours

Table 4.15: Input Parameters for Case M-1

psia higher that the initial reservoir bubble-point pressure, and consequently, only single-phase flow occurs in the reservoir, but two phase flow develops in the wellbore. Case M-1 considers nonisothermal conditions for the wellbore but isothermal conditions for the reservoir. During the drawdown period the well produces at a constant wellhead oil rate.

A log-log plot of the drawdown bottomhole data ($\Delta p = p_i - p_{wf}$) for Case M-1 is shown in Fig. 4.40. As Fig. 4.40 shows, for the first eight hours of the test, we have excellent agreement between the measured data and wellhead pressure estimated from the subplex method, an agreement that is further illustrated by the pressure derivative curves. At late times, the matched pressure goes slightly below the measured pressure, and the derivatives of the matched pressure drop below the
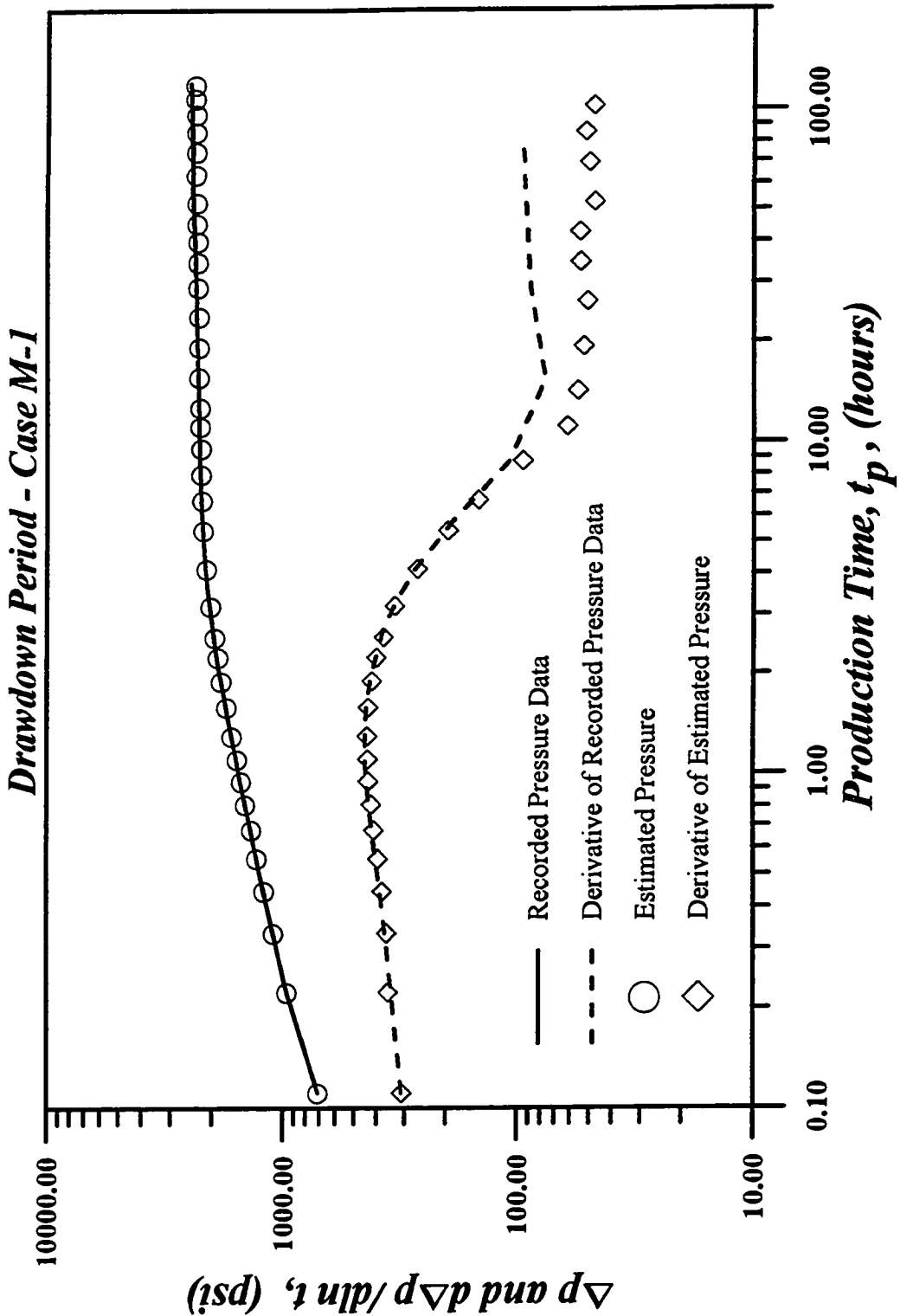
Fig. 4.40 – Log-Log Plot of Pressure and Pressure Derivative for Case M-1.

derivatives of the measured data. The results of bottomhole pressure and bottomhole rates are graphically displayed in Figs. 4.41 and 4.42 respectively. The bottomhole pressure match shows excellent agreement with the true bottomhole values for the first eight hours of production, after which the estimated pressure is higher than true bottomhole pressure. The normalized sandface total production rate plot (Fig. 4.42) shows that the estimated rate does not match the measured data extremely well but follows the right trend.

Another important comparison between recorded data and data generated by our optimization procedure pertains to the wellhead pressure and wellhead production rate; the results are presented in Fig. 4.43 and Fig. 4.44, respectively. Note that the optimization procedure has generated an excellent match of the "true" wellhead values. Based on these results, we can claim that the optimization procedure was quite successful in minimizing the objective function, even though the estimated values of bottomhole pressure and bottomhole rate are not as accurate as might be expected.

There are several reasons that could explain the discrepancy in the results. For example, the discrepancy may be due to nonuniqueness and/or influenced by the approximate approach used to compute the temperature profile. The assumption of a linear temperature gradient from the wellhead temperature effectively remove temperature as a variable at each timestep. By assuming a linear temperature gradient, the temperature at each wellbore gridblock position is fixed at each time step during the drawdown and buildup test matching procedure. However, when we kept temperature as a variable, the matching procedure become extremely time consuming and often did not converge.
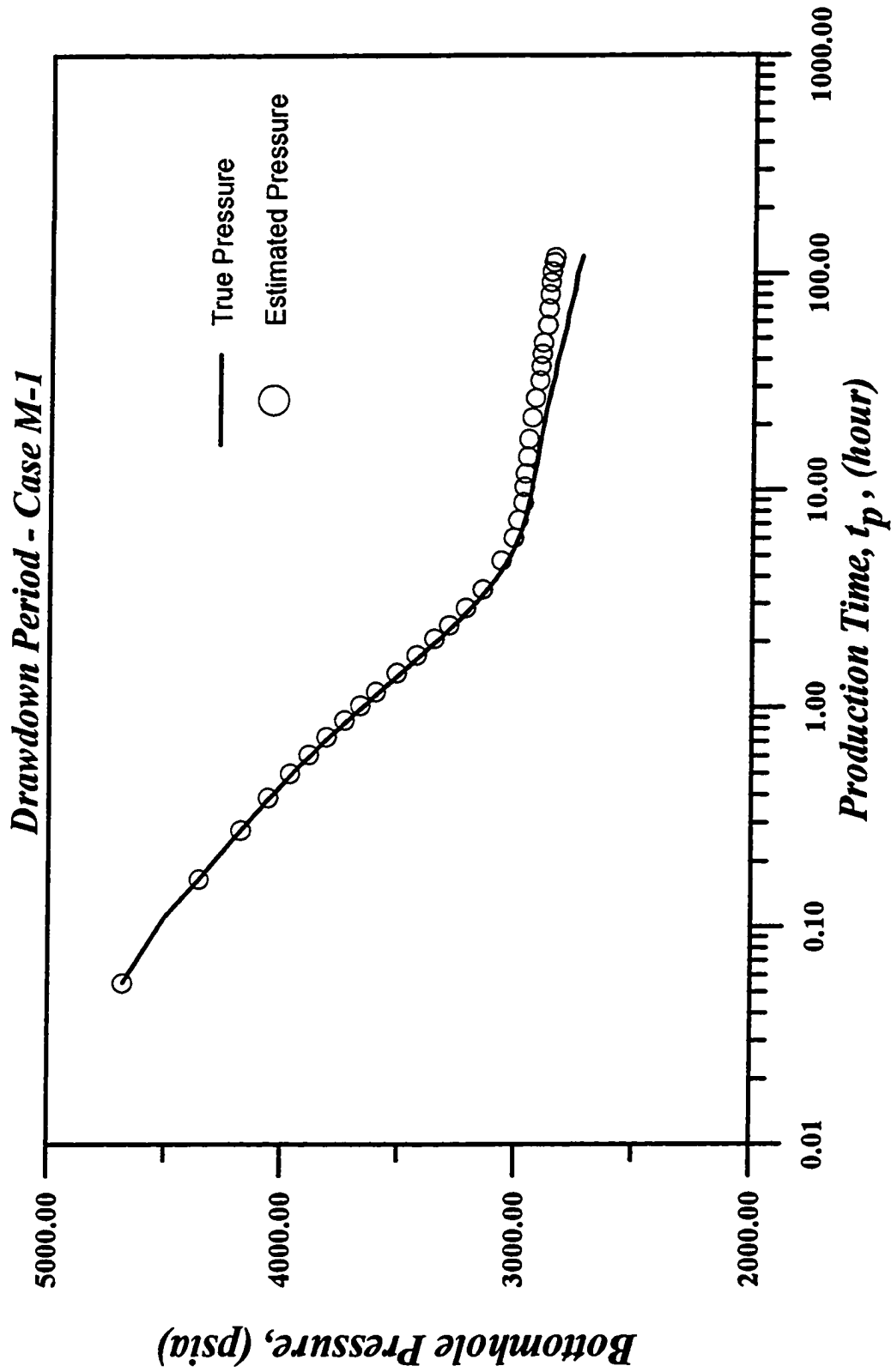
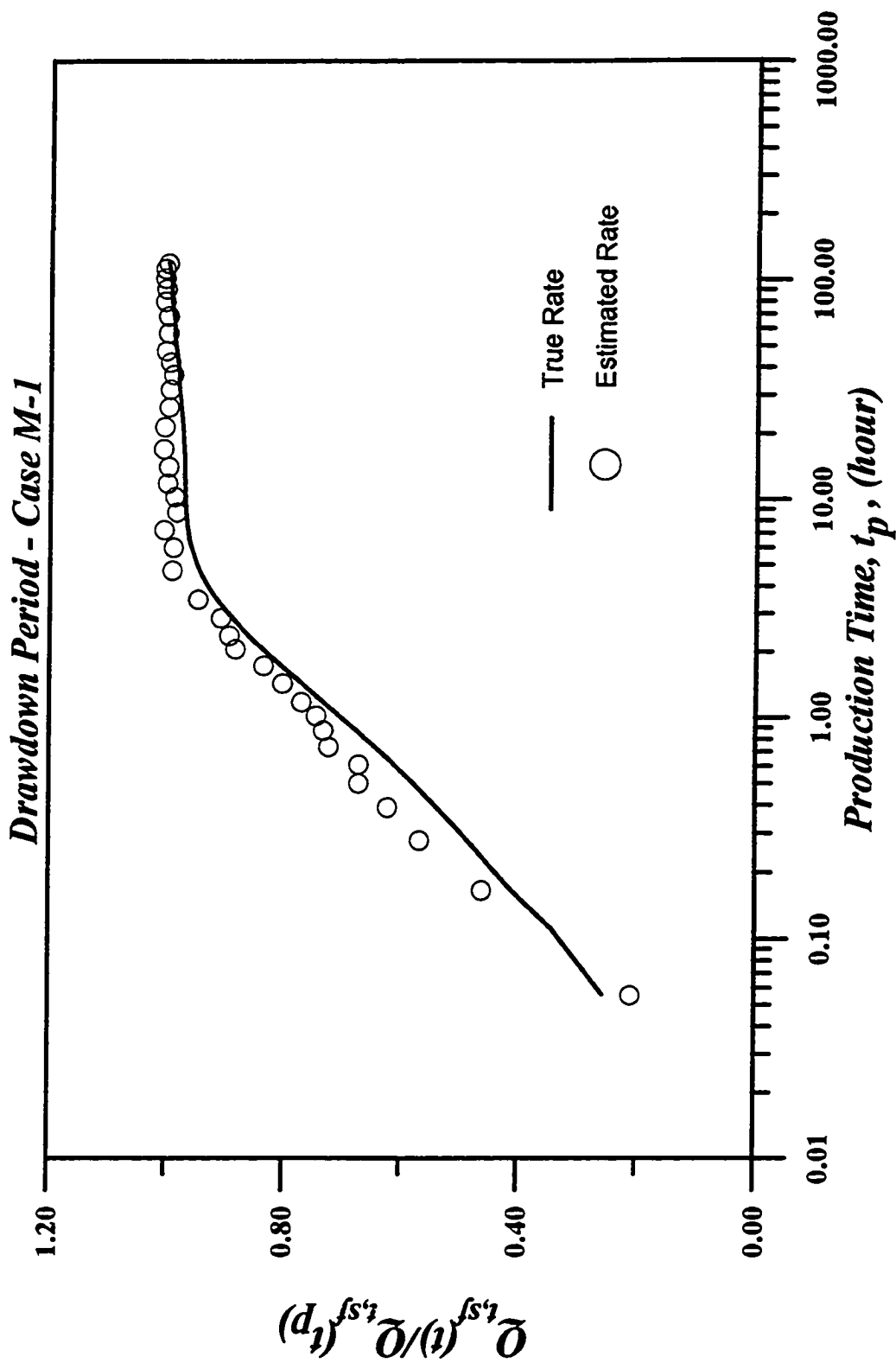**Fig. 4.41 – Bottomhole Pressure as Function of Production Time for Case M-1.**

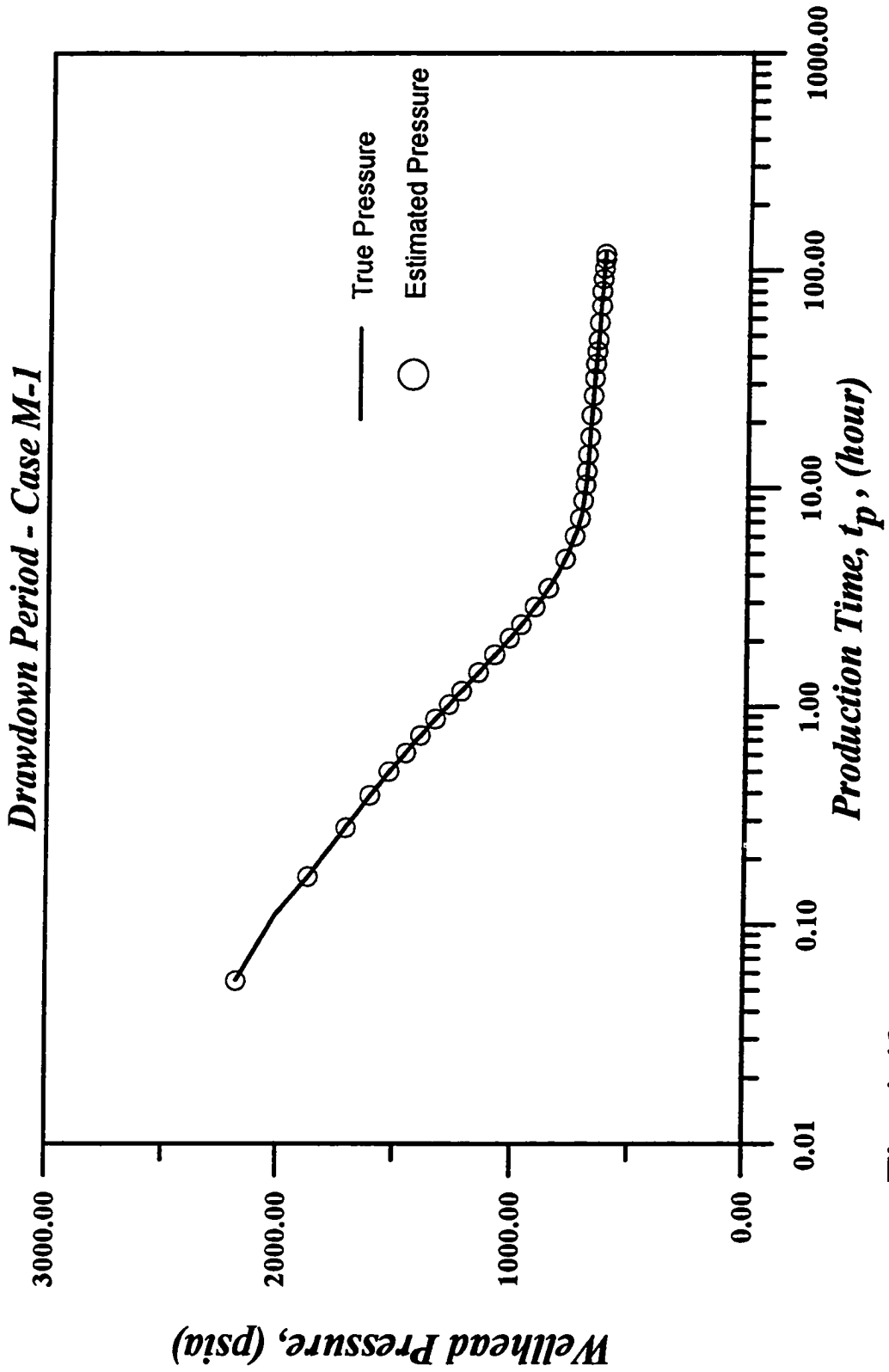**Fig. 4.42 – Normalized Sandface Flow Rate as a Function of Production Time for Case M-1.**

Fig. 4.43 – Wellhead Pressure as Function of Production Time for Case M-1.
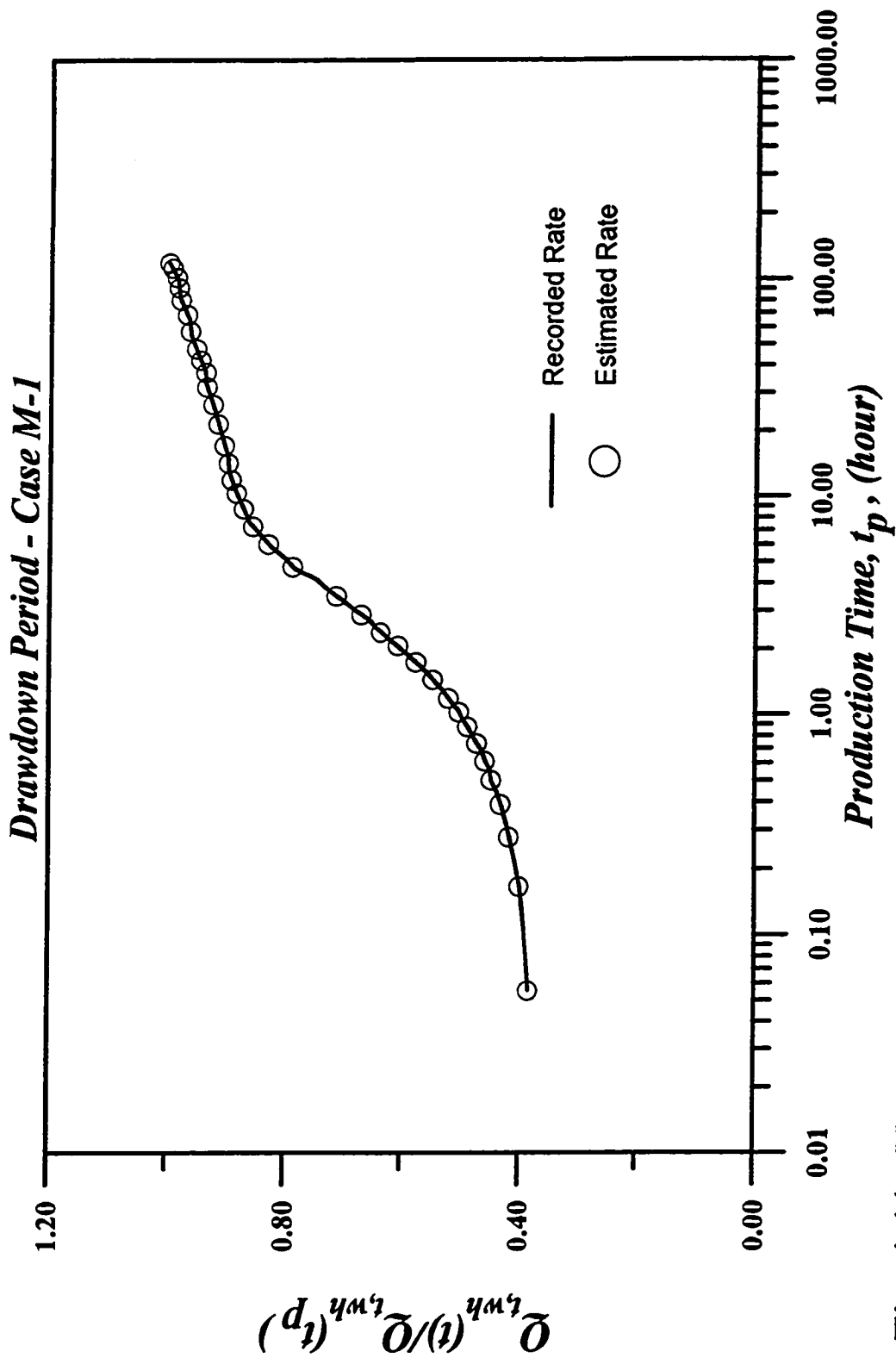
Drawdown Period - Case M-1

Legend:
— Recorded Rate
○ Estimated Rate

Production Time, t_p, (hour)

$Q_{twh}(t)/Q_{twh}(t_p)$

Fig. 4.44 - Normalized Wellhead Flow Rate as a Function of Production Time for Case M-1.

Fig. 4.45 shows the temperature profile in the well at production times of 2.90 hours, 15.60 hours and 120 hours. For the simulated data, the assumed linear temperature profiles result in a wellbore temperature that is lower than the correct value from the bottomhole (9,000 ft.) of the well to a depth of approximately 4,000 ft. From a depth of approximately 4,000 ft. to the surface, the linear temperature profiles result in wellbore temperatures which are higher than the correct values. When the fluids are at a lower temperature, the gas is more soluble in oil. This increases the value of R_s and causes the system compressibility to be higher. If we consider the fact that more gas is dissolved in oil at lower temperature, we expect to obtain more liquid in a gridblock at a given gridblock value of pressure.

The estimated and recorded gas void fraction profiles are presented in Fig. 4.46. At 2.90 hours, the recorded void fraction goes from zero (liquid only) at 8,500 ft. to approximately 0.6 at the wellhead. By the end of the drawdown (t_p =120 hours), the gas void fraction at bottomhole is approximately .07 and 0.73 at the wellhead. This means that at the instant of shut-in, the phases are not segregated. The recorded and simulated void fraction match well at 2.90 hours, after that the estimated void fraction profile appears displaced to the left. This behavior is a direct influence of the difference between the bottomhole pressures (see Fig. 4.41). Because the estimated pressures are higher than the true ones and the estimated temperatures are lower than the true ones near the bottom of the well, the solubility of the gas is higher using the estimated profiles. Thus, less gas is evolved from the oil phase so there is less free gas in the wellbore. This results in gas void fractions that are less than the true ones. The mixture density profile (see Fig. 4.47) shows a good agreement between
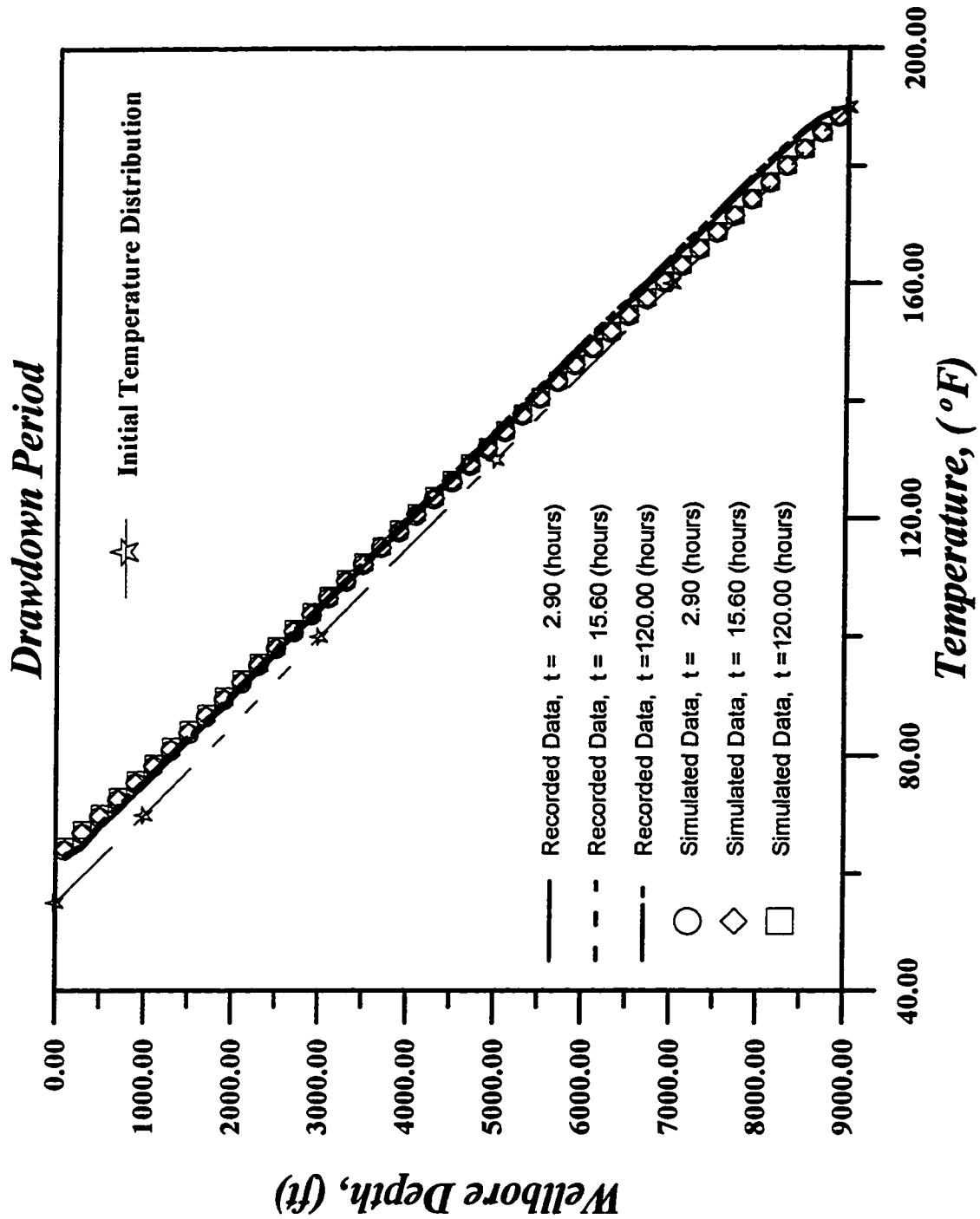
Fig. 4.45 - Temperature Distribution in the Wellbore for Case M-1.
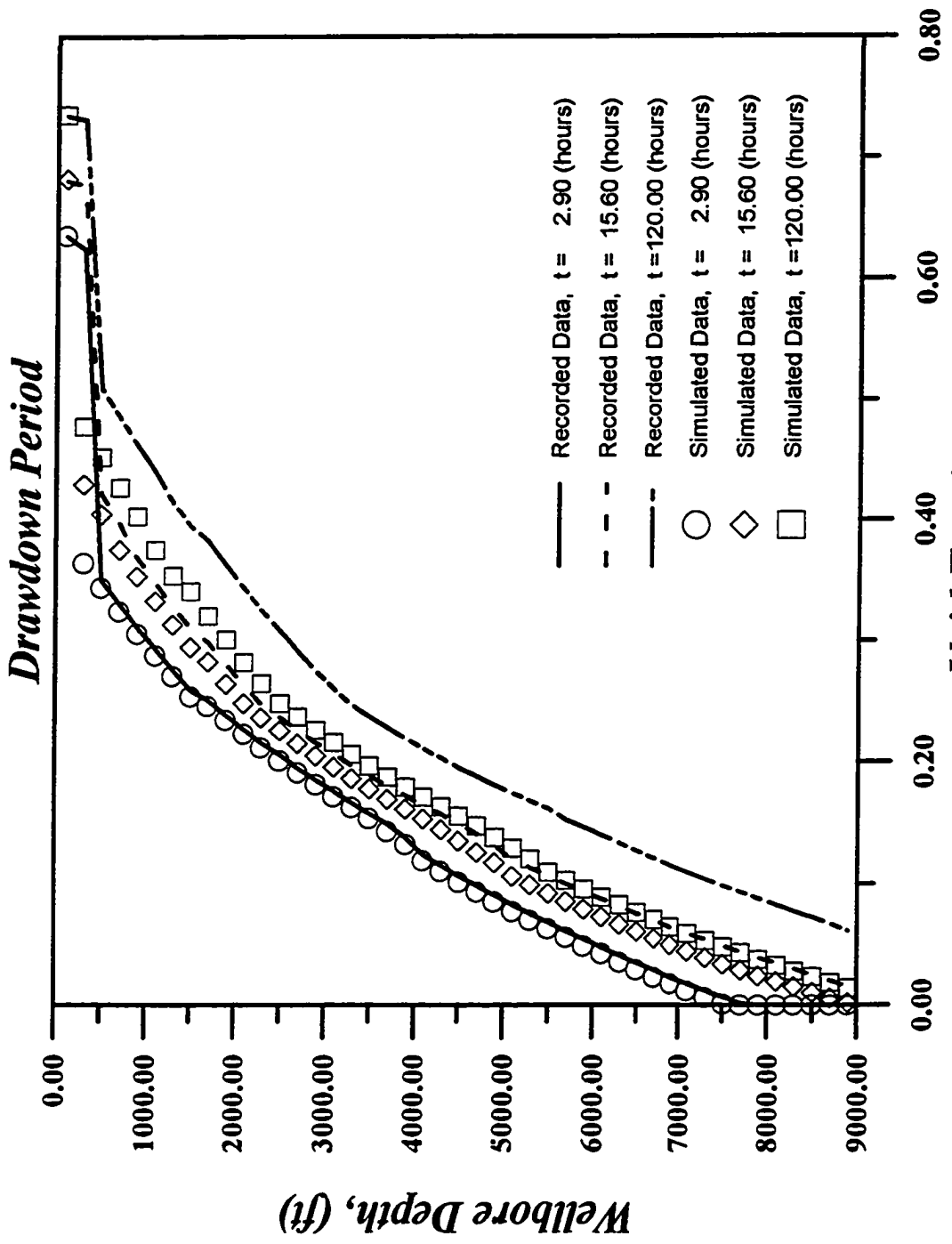
Fig.4.46 - Void Fraction Distribution in the Wellbore for Case M-1.

the recorded and estimated data at early times (2.90 hours), but by the end of the test, the recorded data is displaced to the right showing higher values of density. This results mainly from the fact that the estimated pressure profile is higher than the true pressure profile but is also influenced by the fact that the estimated temperatures are higher than the true ones near the bottom of the well.

Using the buildup period wellhead data, the matching procedure was executed again to obtain the log-log plot shown in Fig. 4.48. Although, the match is reasonably good, as shown in Fig. 4.49, the bottomhole pressure obtained from the match is higher than the measured data. This result is a direct influence of the pressure match obtained at late times for the drawdown period. The estimated pressure are in good agreement with the measured data at late times. A similar quality of agreement at early and late times is observed with the normalized total flow rate (see Fig. 4.50).

During the buildup period, the wellbore fluids lose heat to the surrounding rock. This causes an increase in density and an increase in compressibility. By the end of the buildup period, the wellbore fluid temperature profile is approximately the same as the geothermal gradient (see Fig. 4.51) and hence our procedure in which we assume a linear temperature profile in the wellbore becomes correct. The gas void fraction and mixture density profiles are shown in Fig. 4.52 and 4.53, respectively. At early times, the recorded and estimated values of void fraction and mixture density disagree, which again is a direct influence of the pressure and temperature differences during the drawdown period. At late times, when the temperature profile is almost identical to the geothermal gradient, the difference between the recorded and simulated temperature is minimal and the estimated and recorded void fraction
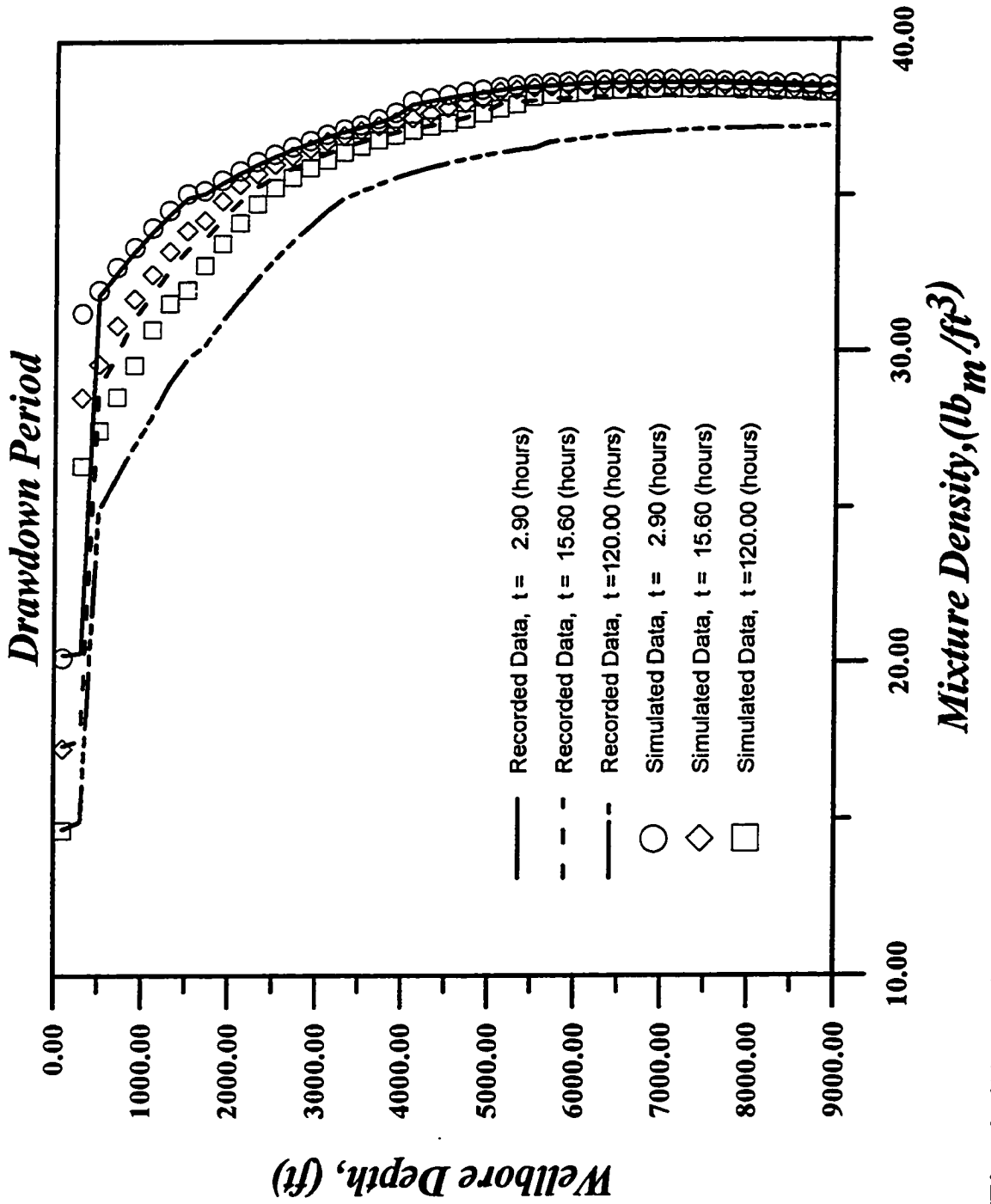
167

Fig.4.47 - Mixture Density Distribution in the Wellbore for Case M-1.
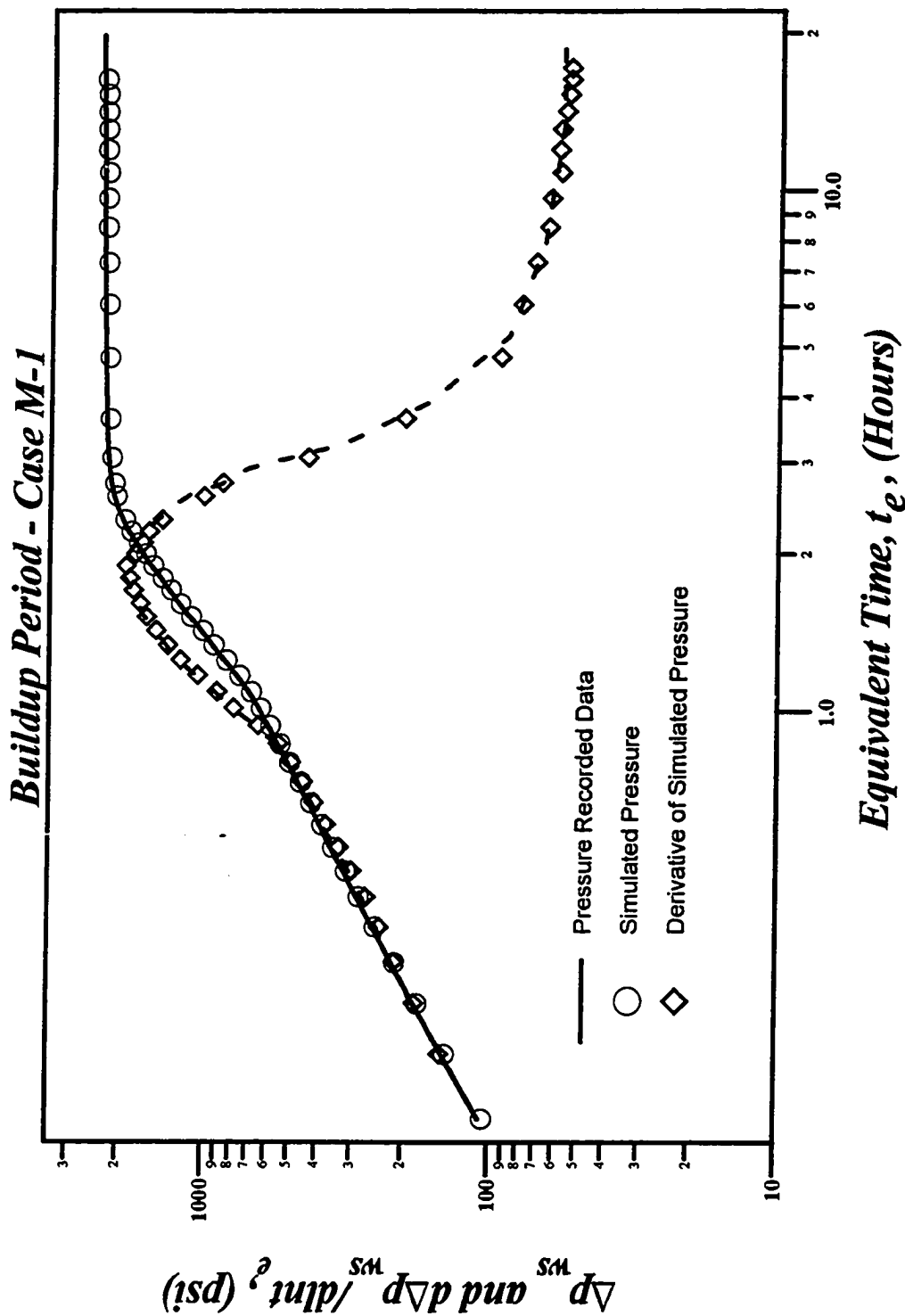
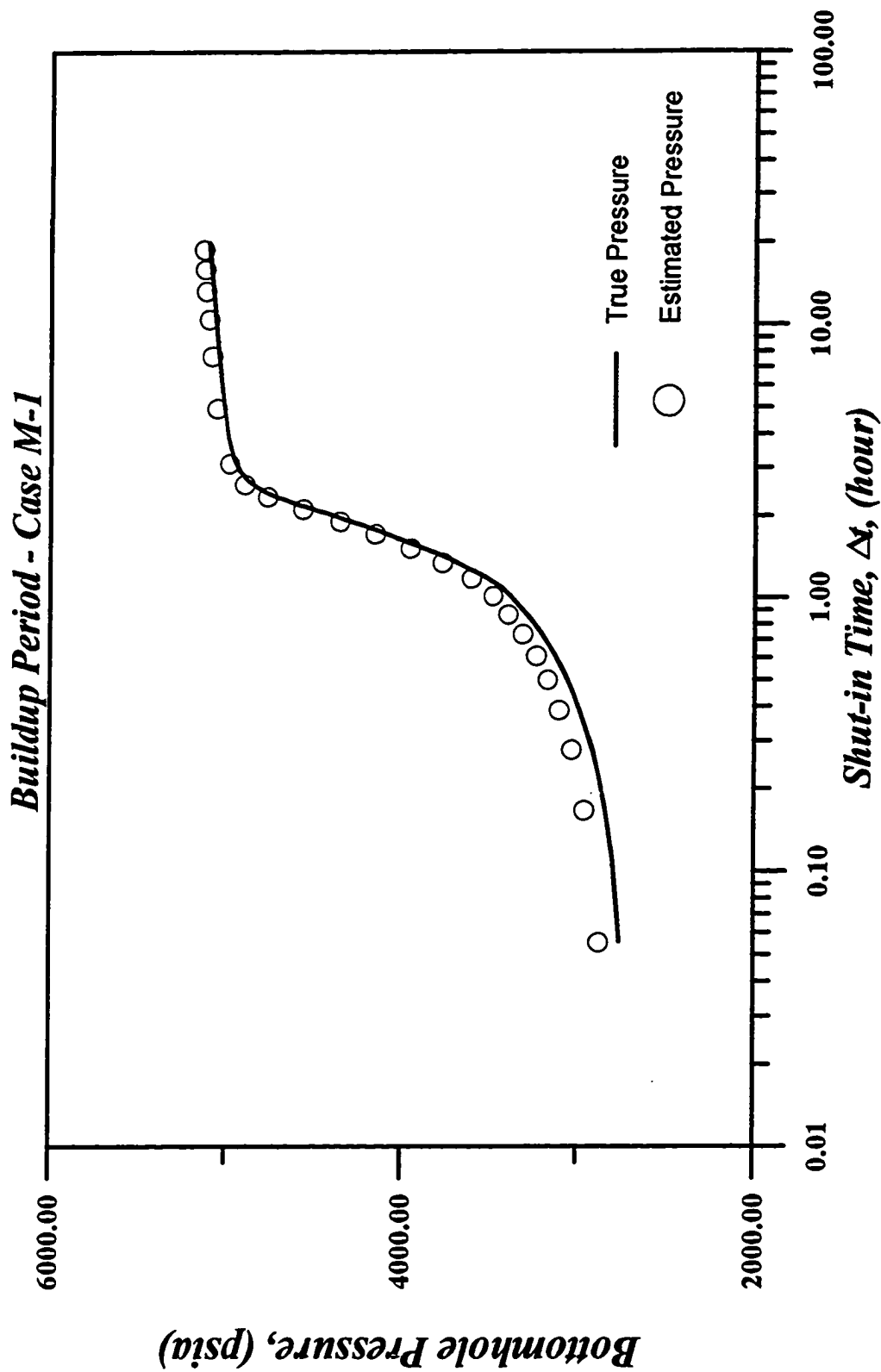**Fig. 4.48 – Log-log Plot of Pressure and Pressure Derivative for Case M-1**

169

Fig. 4.49 - Bottomhole Pressure as a Function of Shut-in Time for Case M-1.
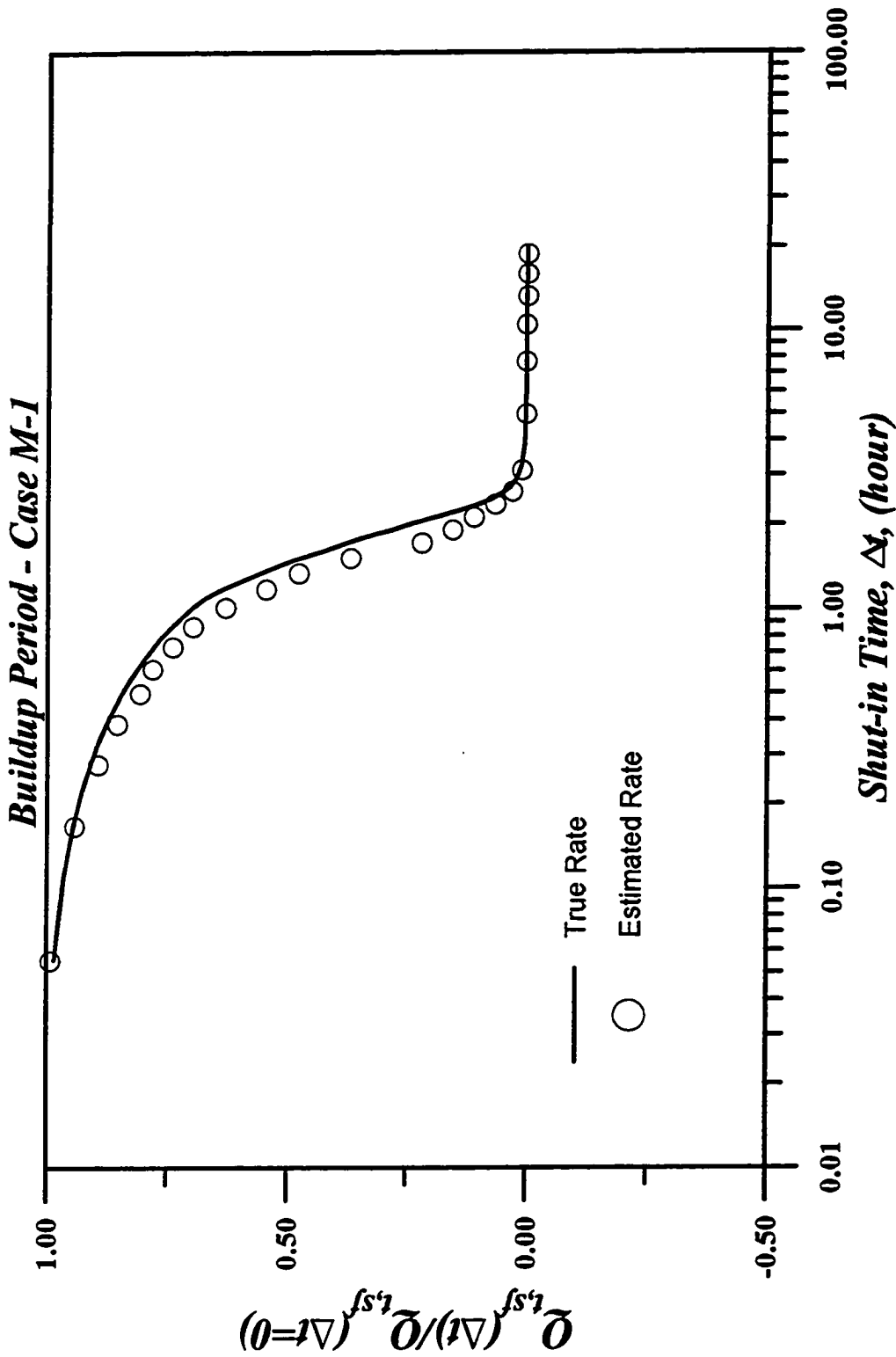
Buildup Period - Case M-1

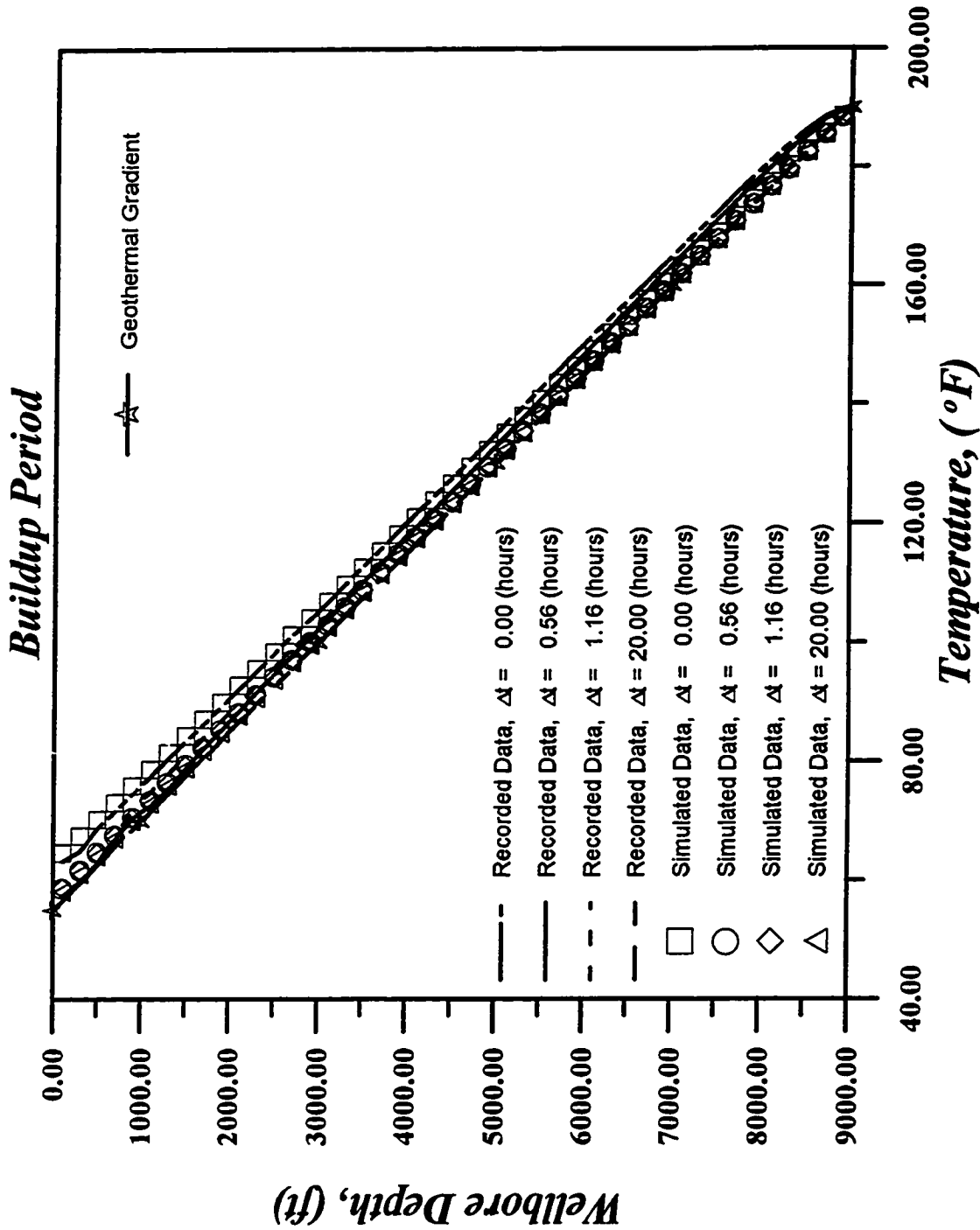Fig. 4.50 – Normalized Sandface Flow Rate as a Function of Shut-in Time for Case M-1.

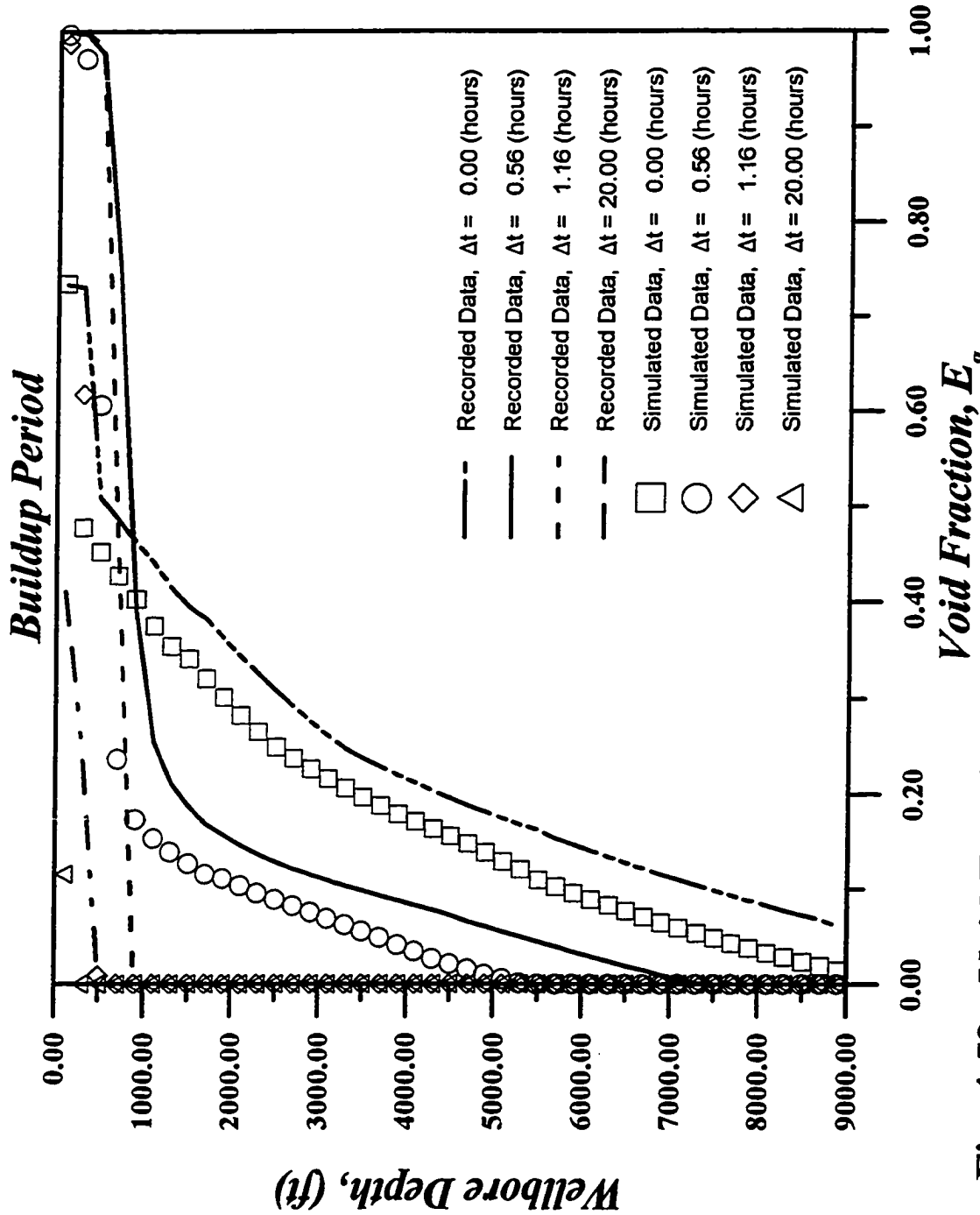**Fig. 4.51 - Temperature Distribution in the Wellbore for Case M-1.**

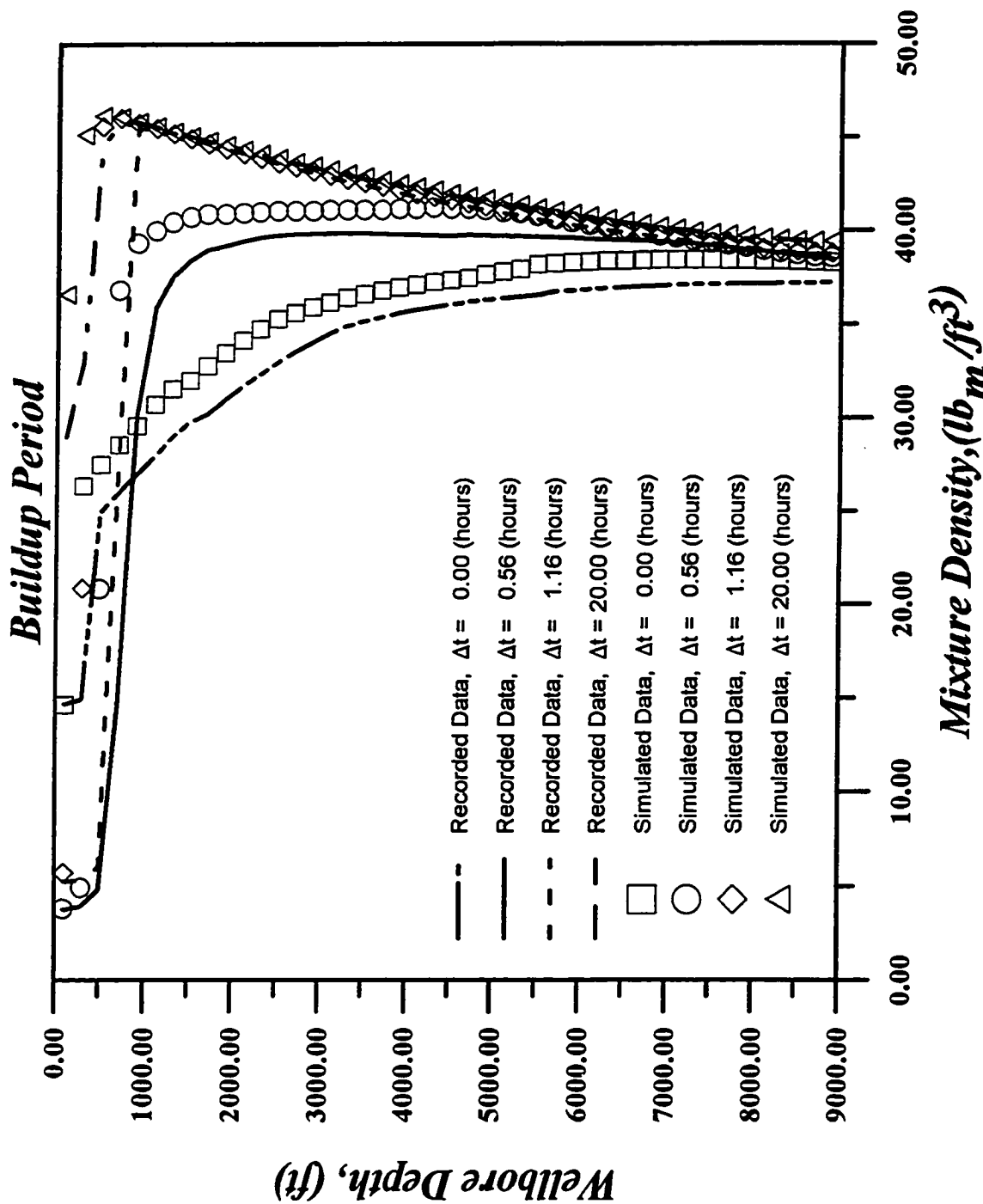Fig. 4.52 - Void Fraction Distribution in the Wellbore for Case M-1.

Fig. 4.53 - Mixture Density Distribution in the Wellbore for Case M-1.

and mixture density profile show a good agreement.

Matching of drawdown and buildup wellhead data required 8 hours on a PC-Pentium 90MHz.

4.3.1.c   Case M-2

Case M-2 represents a drawdown and a buildup test conducted in a well completed in solution-gas drive reservoir. The wellbore simulator was coupled with the RDRBOS (r-z) reservoir simulator to handle the two-phase flow reservoir condition. As in Case M-1, a drawdown test followed by a buildup test are conducted in a naturally flowing well. The initial reservoir pressure is higher than the initial bubble-point pressure, but the well is produced long enough so that the bottomhole pressure falls below the reservoir initial bubble-point pressure and two-phase flow appears in the reservoir as well as in the wellbore during the production period. The final bottomhole flowing pressure in Case M-2 is equal to $p_{wf,s} = 2529.7$ *psia* as compared to the reservoir initial bubble-point pressure of $p_b = 2710\,psia$. All the pertinent reservoir/wellbore parameters are listed in Table 4.16. We consider a 50-hours drawdown test followed by a 20-hour buildup test with nonisothermal conditions in the wellbore but isothermal conditions in the reservoir.

Using the data obtained using the wellbore simulator coupled with the (r-z) reservoir simulator, the wellbore matching program was used to estimate bottomhole rates and pressures. A log-log plot of bottomhole pressure drop and its derivative is shown in Fig. 4.54. At early times, the pressure and pressure derivative data exhibit the effects of wellbore storage and skin. At late times, the true bottomhole pressure

Parameter	Value	Unit
Drawdown surface oil production rate	40.00	STB/D
Total production time	50.00	hours
Inital reservoir pressure	4500.00	psia
Initial bubble point pressure	2710.00	psia
Oil compressibility $(p>p_b)$	1.0e-5	1/psia
Oil component API gravity at s.c.	45.00	API
Gas component specific gravity at s.c.	0.70	-
Oil-gas surface tension	4.50	dynes/cm
Wellbore pipe inside diameter	1.80	inch
Formation absolute permeability	40.00	md.
Formation thickness	10.00	ft.
Well Complety Penetrates Reservoir		
Formation porosity	0.20	-
Wellbore radius	0.364	ft.
System isothermal compressibility	2e-5	1/psia
Skin factor	10.00	-
Wellbore depth	9000.00	ft.
Spatial Increment	200.00	ft.
Buildup simulation time	20.00	hours

Table 4.16: Input Parameters for Case M-2

approximately exhibits a semilog straight line indicative of pseudoradial flow.

As in Case M-1, at early times the pressure match shows a good agreement with the measured data and the pressure derivative is in good agreement also. After 20 hours of production, the estimated bottomhole pressure drop falls slightly below the true data. This small difference results in a significant difference between the two sets of pressure derivative data. Fig. 4.55 shows a semilog plot of the two sets of pressure data and again shows a disagreement at late times.

The wellhead pressure match is presented in Fig. 4.56; this plots clearly shows an excellent match. This means that the subplex method was able to satisfy the objective function with respect to the measured wellhead pressure. This is ratified by the excellent match of the total wellhead rate showed in Fig. 4.57. On the other
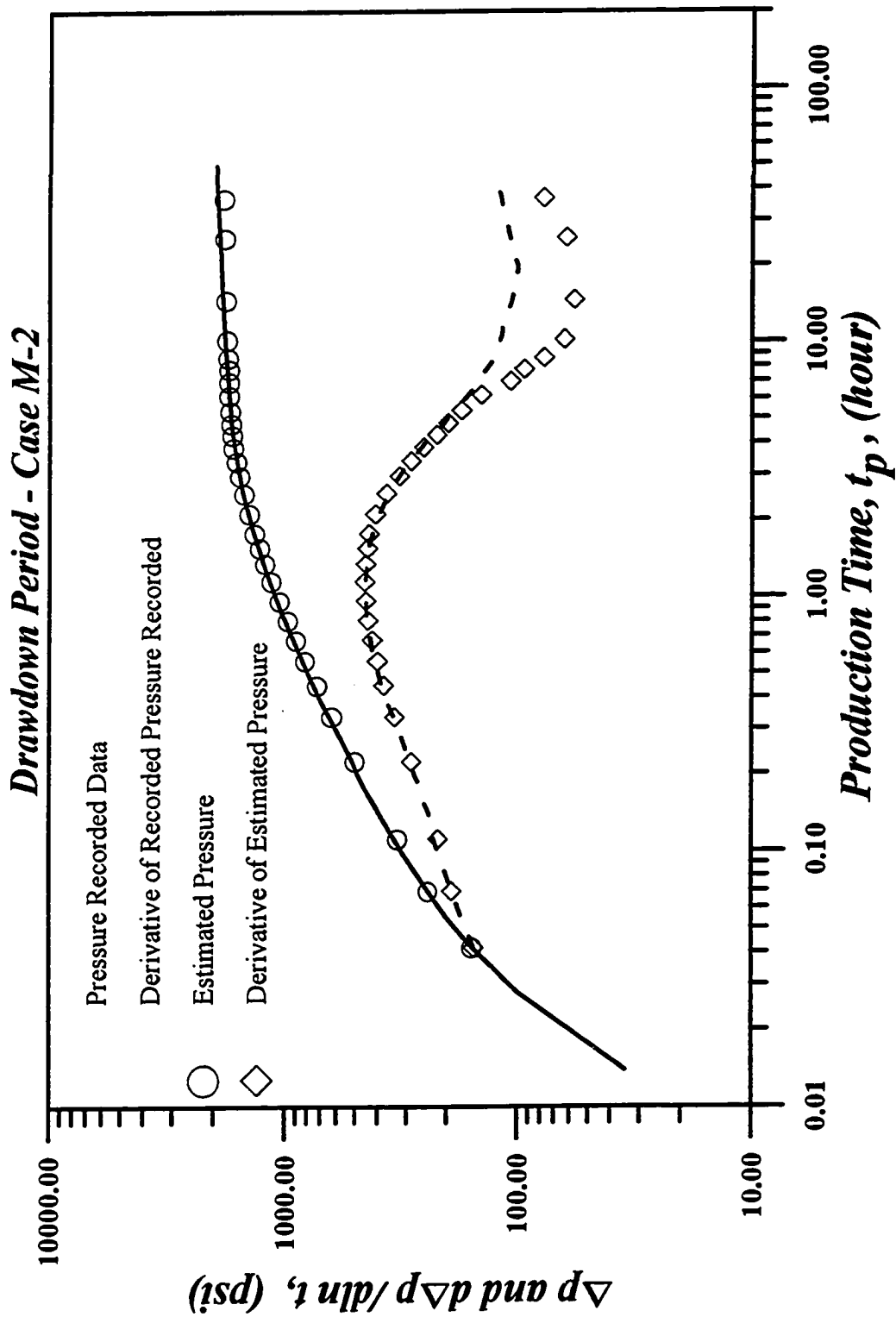
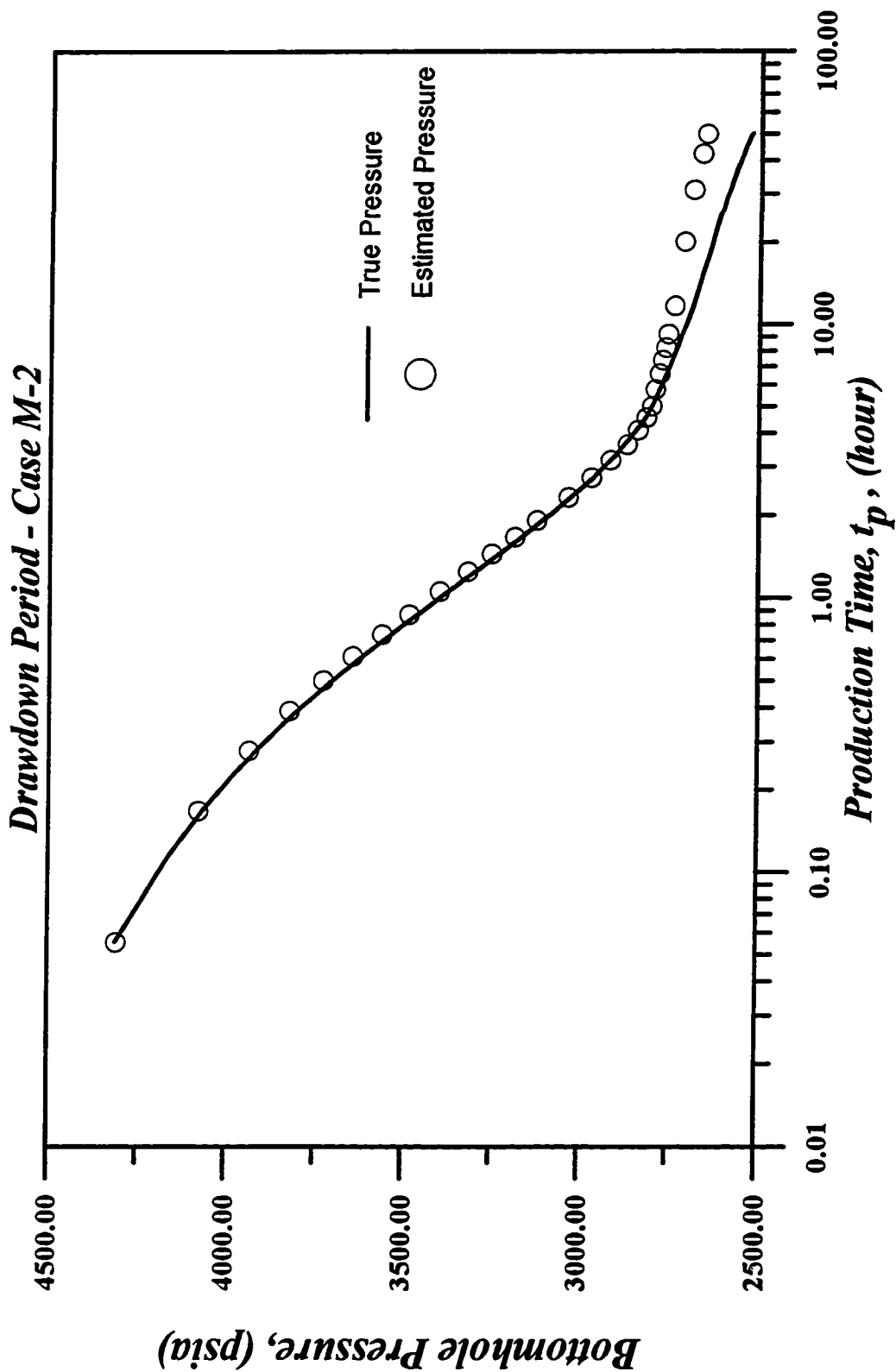Fig. 4.54 – Log-Log Plot of Pressure and Pressure Derivative for Case M-2.

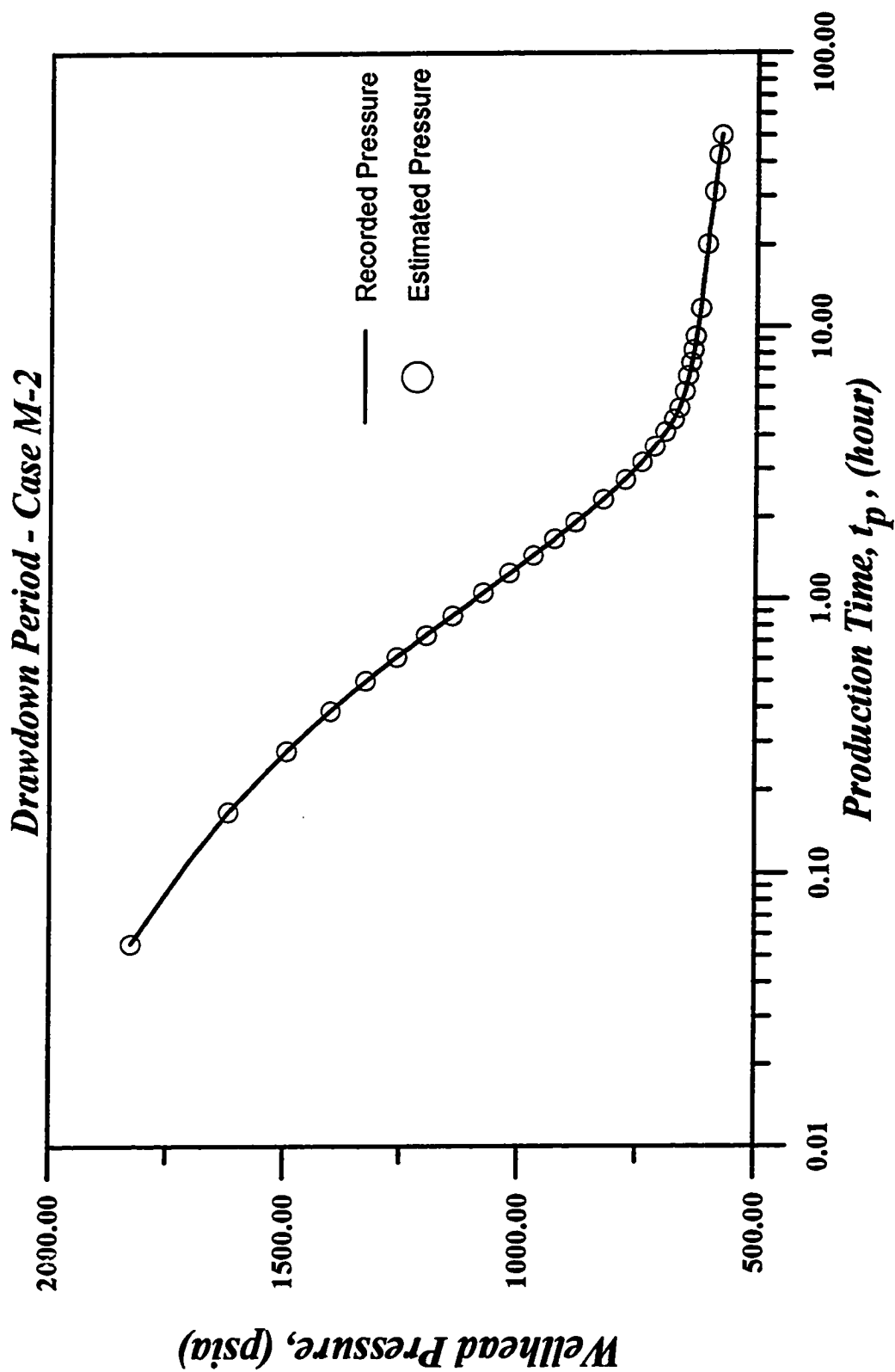Fig. 4.55 - Bottomhole Pressure as a Function of Production Time for Case M-2.

Fig. 4.56 – Wellhead Pressure as a Function of Production Time for Case M-2.

hand, the total bottomhole rate match is not good but gives the right trend, as shown in Fig. 4.58.

The temperature profile in the well at production times of 3.0 hours, 15.80 hours, 30.50 hours and 50 hours is presented in Fig. 4.59. As in Case M-1, the estimated temperature profiles gives lower temperature values than the true values from the bottomhole (9,000 ft.) of the well to a depth approximately of 3,000 ft. From that depth to surface, the temperature obtained by assuming a linear temperature profile is higher than the recorded temperature.

Fig. 4.60 shows the estimated and recorded gas void fraction profile. At $t =$ 3.0 hours, the recorded gas void fraction varies from approximately 0.01 at bottomhole to approximately 0.7 at the wellhead, indicating that two-phases exist at bottomhole. By the end of the drawdown (50 hours), the void at bottomhole is approximately 0.12 and 0.78 at the wellhead. As in case M-1, all the estimated void fraction profiles appear displaced to the left of the correct ones which is a direct result of the difference in the bottomhole pressures (see Fig. 4.55). The mixture density profile is depicted in Fig. 4.61, the estimated data are displaced to the right of the correct density profiles, due to the fact that in the lower part of the wells, the estimated pressures and temperatures are higher than the true values.

Using the profiles obtained from the drawdown match at the instant of shut-in, the build-up test match was performed. A log-log plot of the results generated is presented at Fig. 4.62 and a semilog plot is shown in Fig. 4.63. As Figs. 4.62 and 4.63 show, the true and estimated bottomhole pressure match reasonably well throughout the buildup period. At early times, the estimated pressure data are slightly above
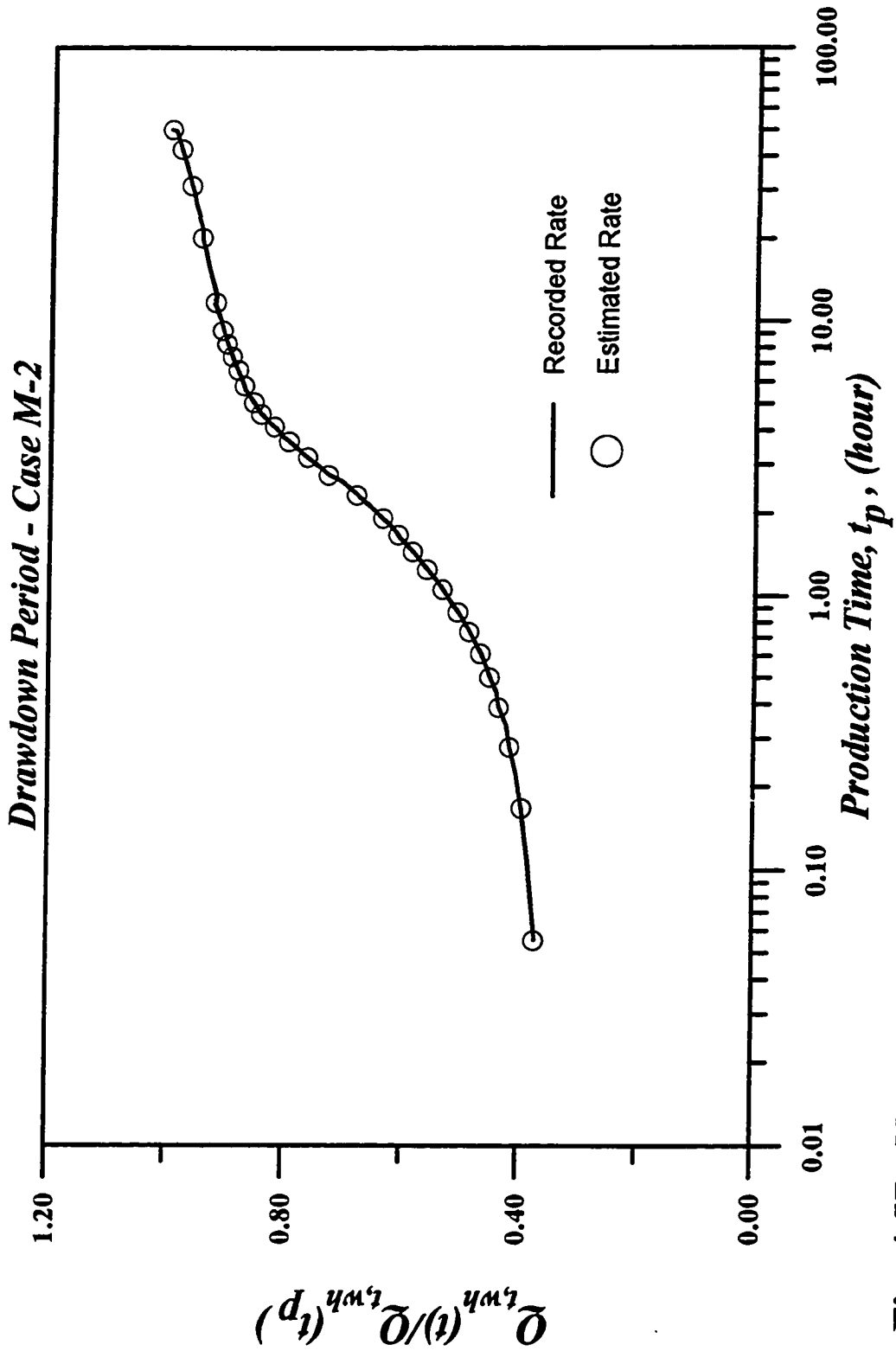
Fig. 4.57 – Normalized Wellhead Flow Rate as a Function of Production Time for Case M-2.

Fig. 4.58 – Normalized Sandface Flow Rate as a Function of Production Time for Case M-2

Fig. 4.59 - Temperature Distribution in the Wellbore for Case M-2.

Fig. 4.60 - Void Fraction Distribution in the Wellbore for Case M-2.

Fig. 4.61 – Mixture Density Distribution in the Wellbore for Case M-2.

Fig. 4.62 - Log-log Plot of Pressure and Pressure Derivative, Case M-2
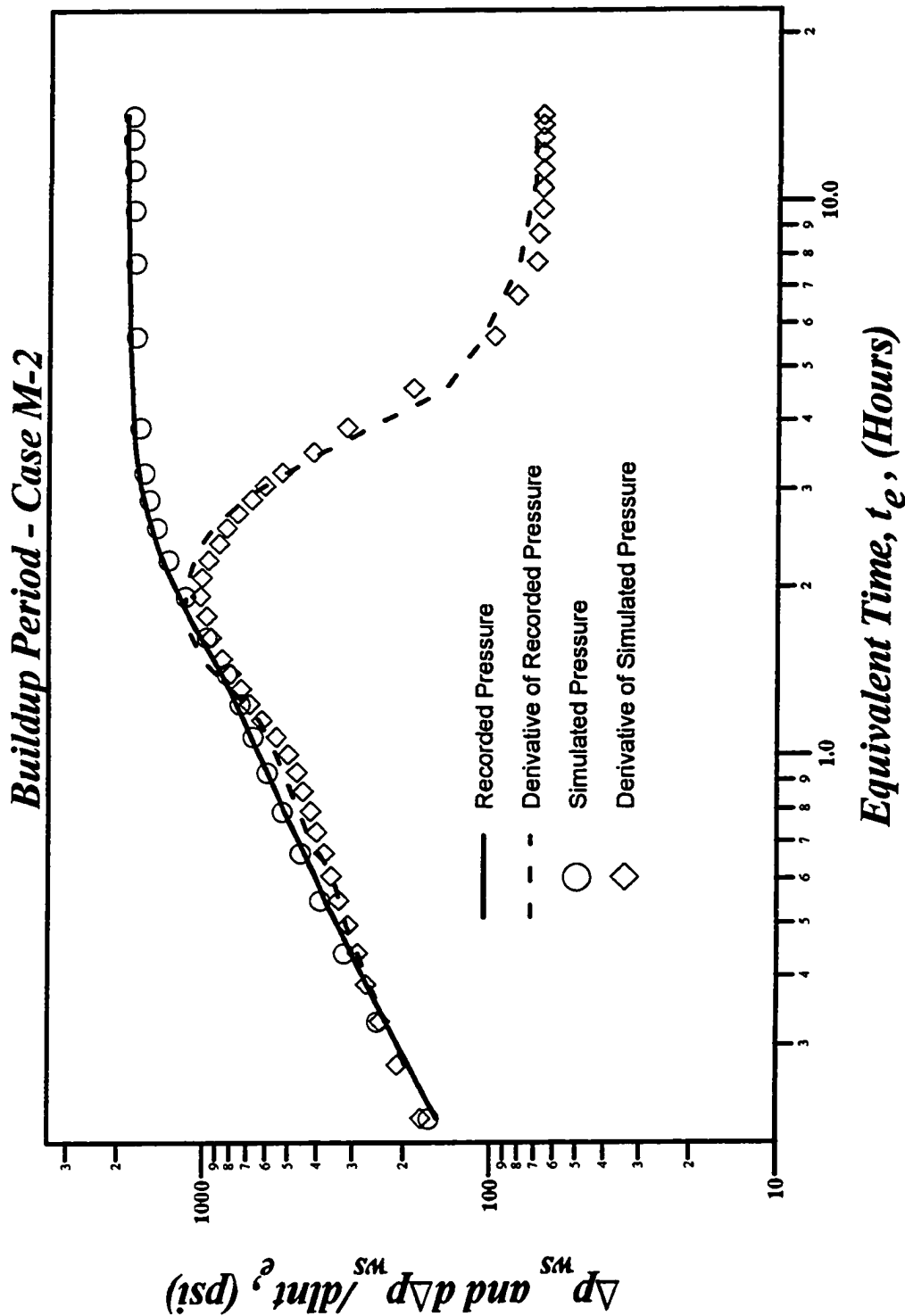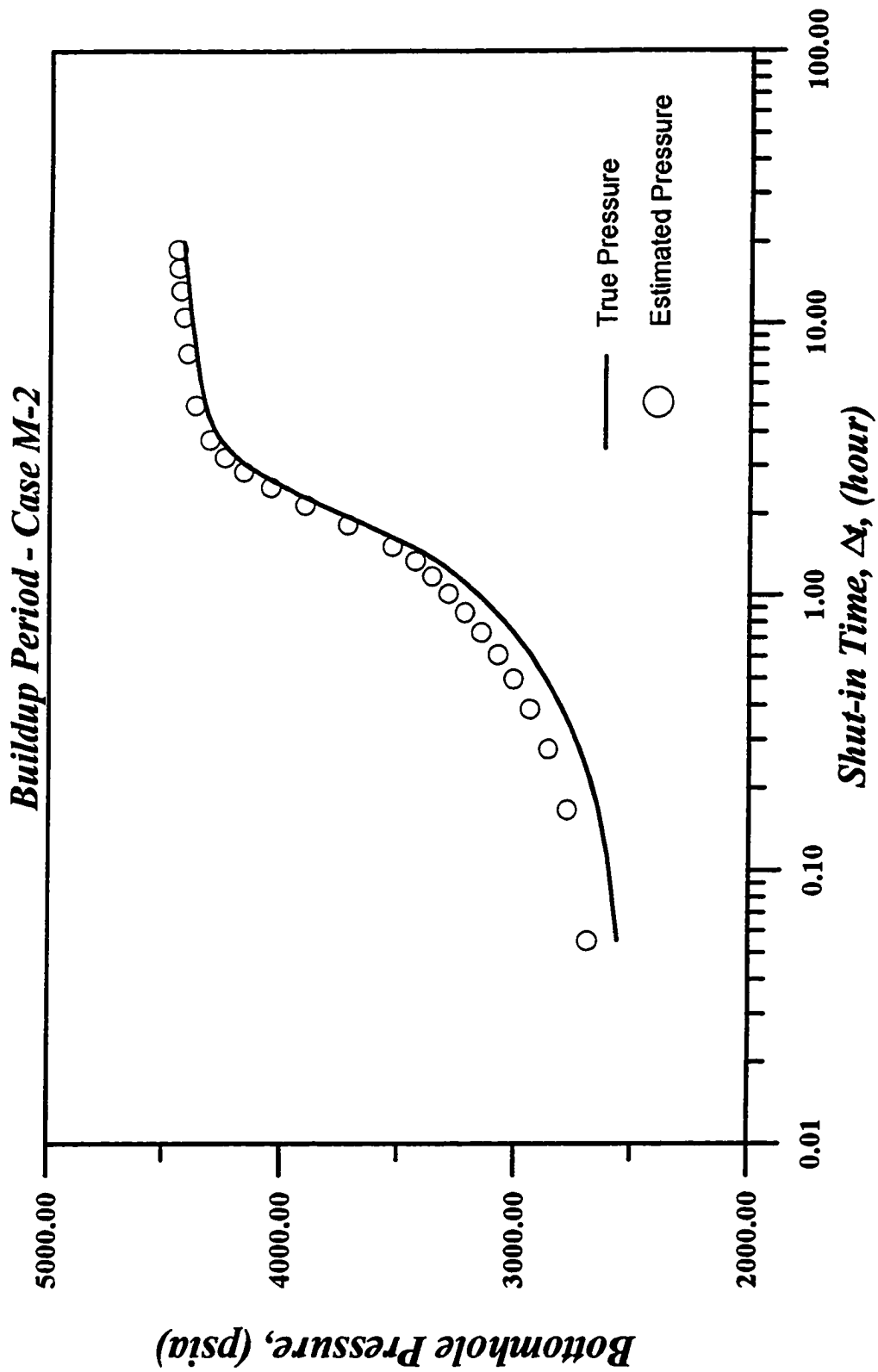
Fig. 4.63 - Bottomhole Pressure as a Function of Shut-in Time for Case M-2.

the measured pressure and at the end of the test, the estimated pressure data fall slightly below the measured data. The difference that appears at early times (first 1.5 hours) in the log-log plot is a direct influence of the lack of agreement between estimated and recorded data at end of the drawdown (see Fig. 4.55). At the end of the test, the two sets of data match well with the estimated pressure change lying slightly above the measured data but showing approximately the same slope.

The estimated total bottomhole rate generated from the optimization procedure is shown in Fig. 4.64. As in the drawdown period, the match shows the right trend, but the estimated rate is correct only at late times. Despite this difference, the optimization procedure yields an excellent match of recorded wellhead pressures and rates (see Fig. 4.65 and 4.66).

The wellbore fluids continuously loose heat to the surrounding rock during the buildup test. By the end of the buildup period, the wellbore fluid temperature profile is approximately equal to the geothermal gradient (see Fig. 4.67). Figs. 4.68 and 4.69 respectively, present the gas void fraction and mixture density profiles. At early times, the recorded and estimated values of void fraction and mixture density disagree due to the pressure and temperature differences during the drawdown period. At late times, we have a small difference between the recorded and simulated temperature and the estimated and recorded gas void fraction and mixture density profiles are in good agreement.

Matching of drawdown and buildup wellhead data required 15 hours on a PC-Pentium 90MHz.
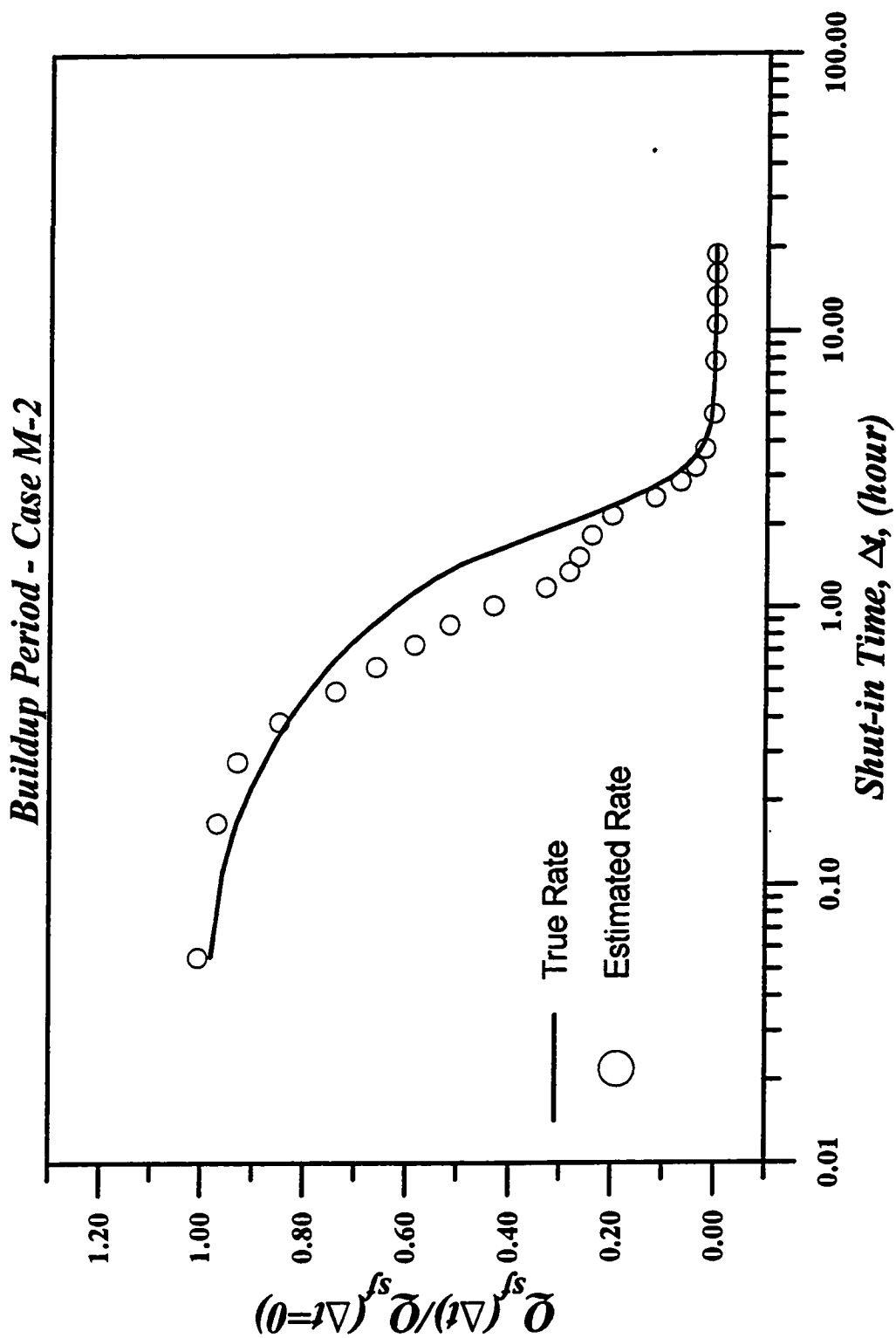
Fig. 4.64 – Normalized Sandface Flow Rate as a Function of Shut-in Time for Case M-2.

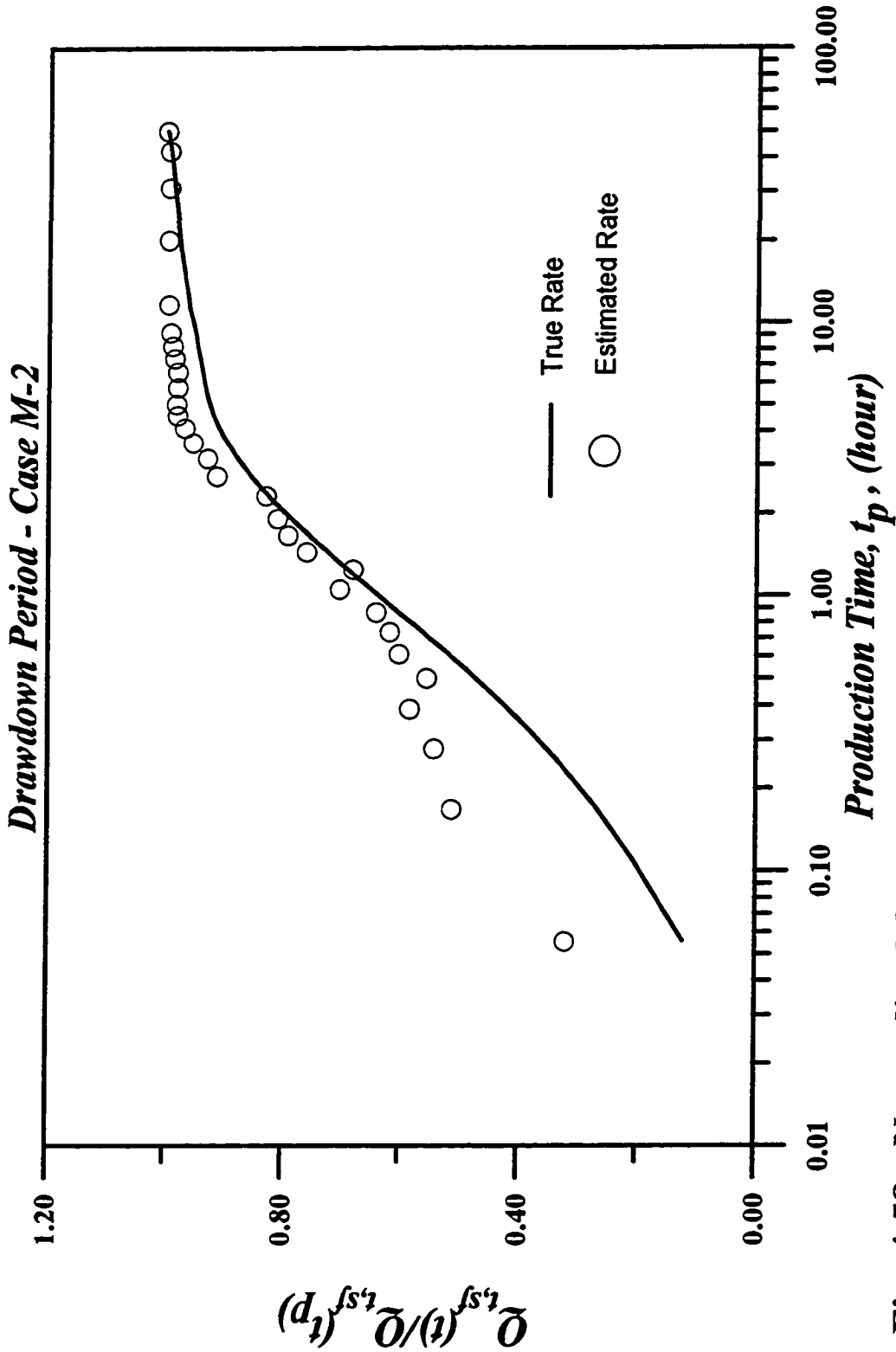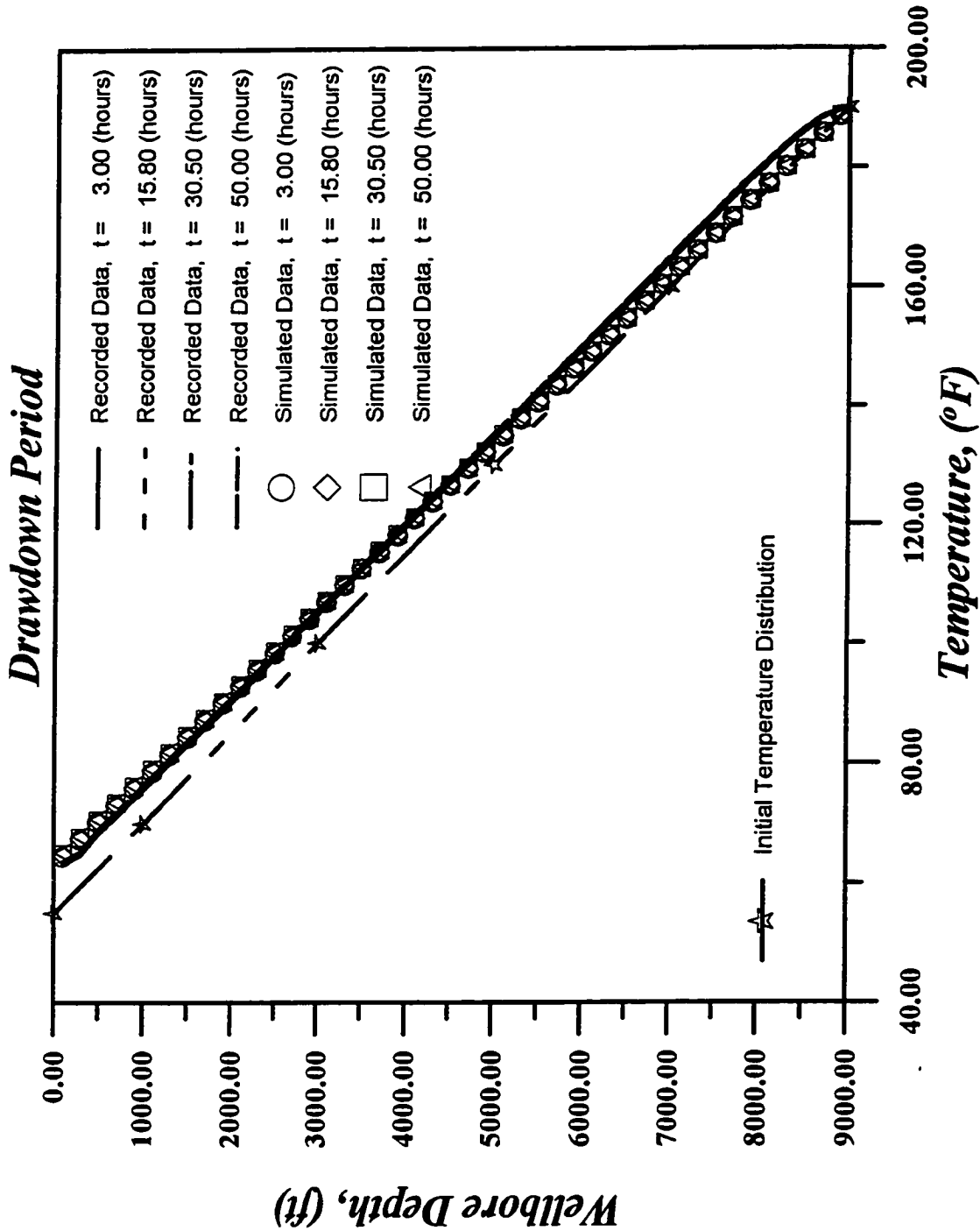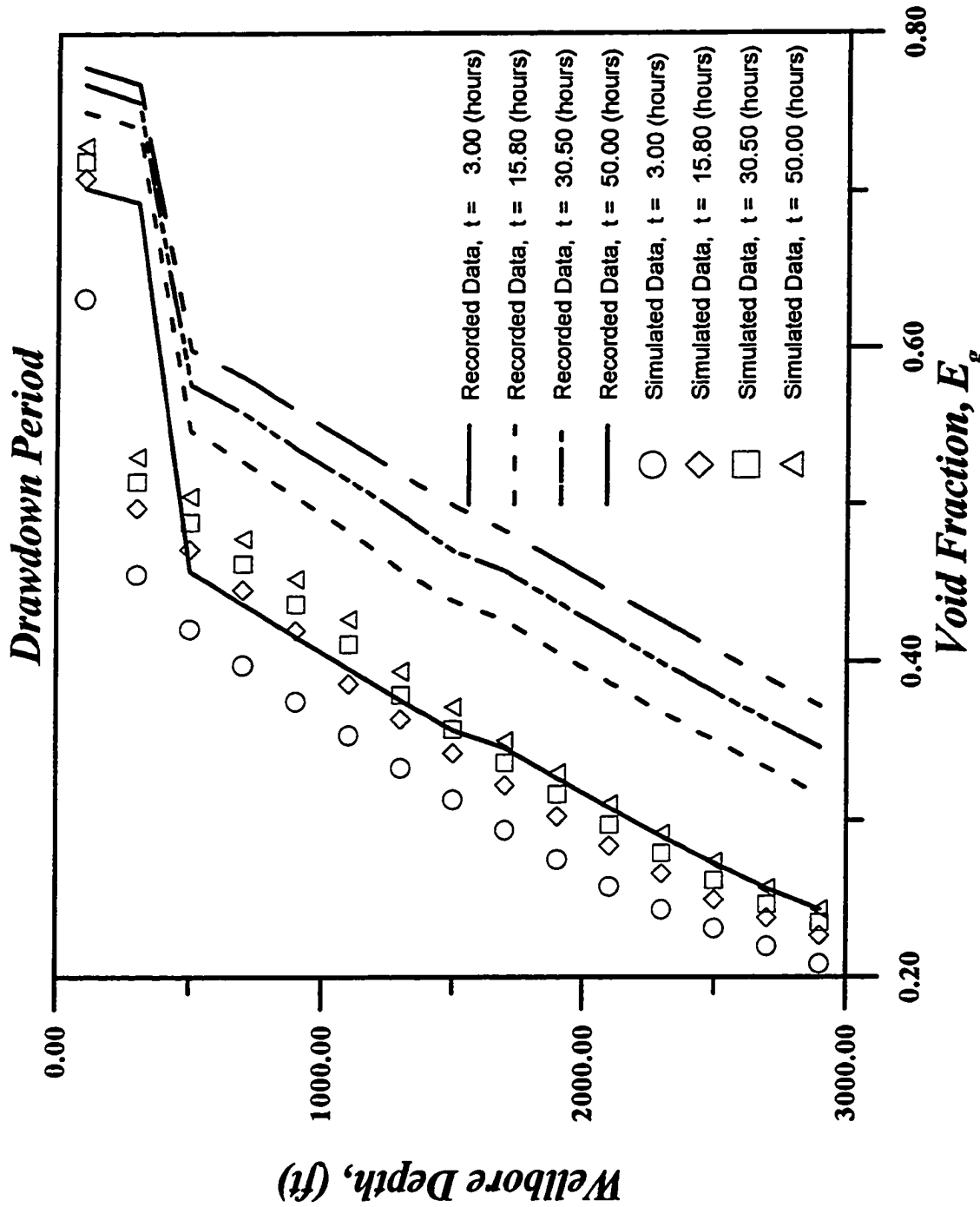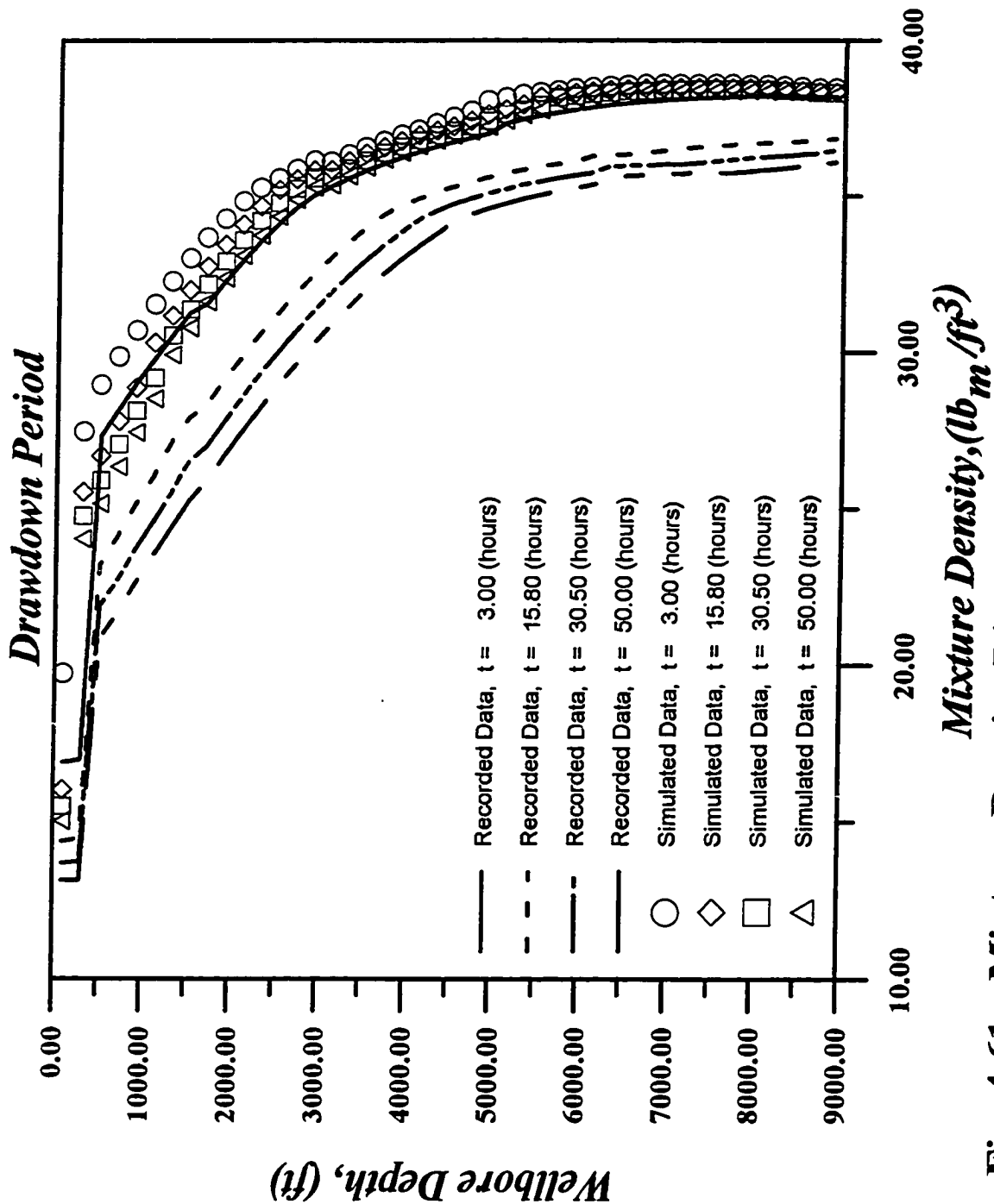Fig. 4.65 – Wellhead Pressure as a Function of Shut-in Time for Case M-2.

Fig. 4.66 – Normalized Wellhead Flow Rate as a Function of Shut-in Time for Case M-2.
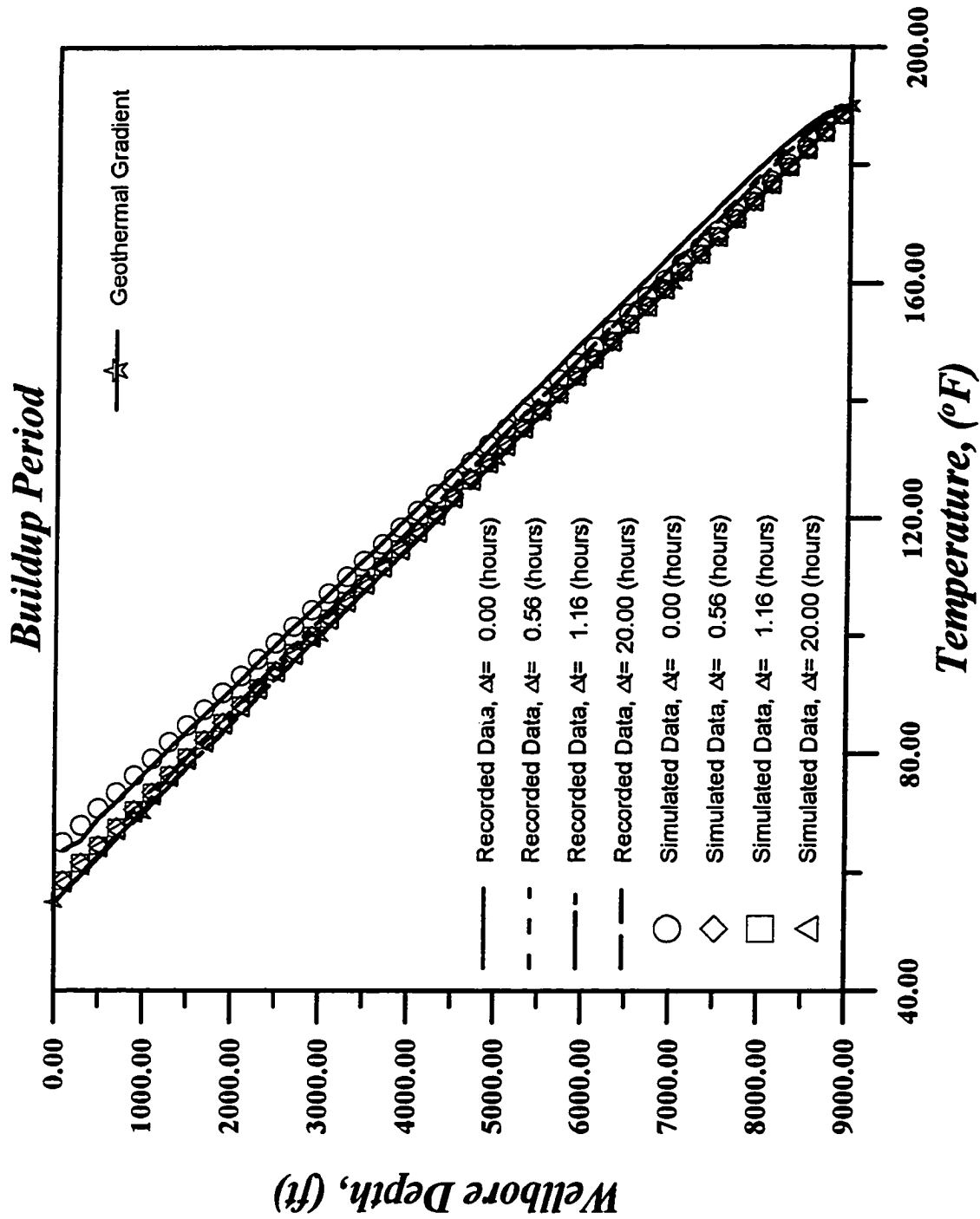
Fig. 4.67 – Temperature Distribution in the Wellbore for Case M-2.
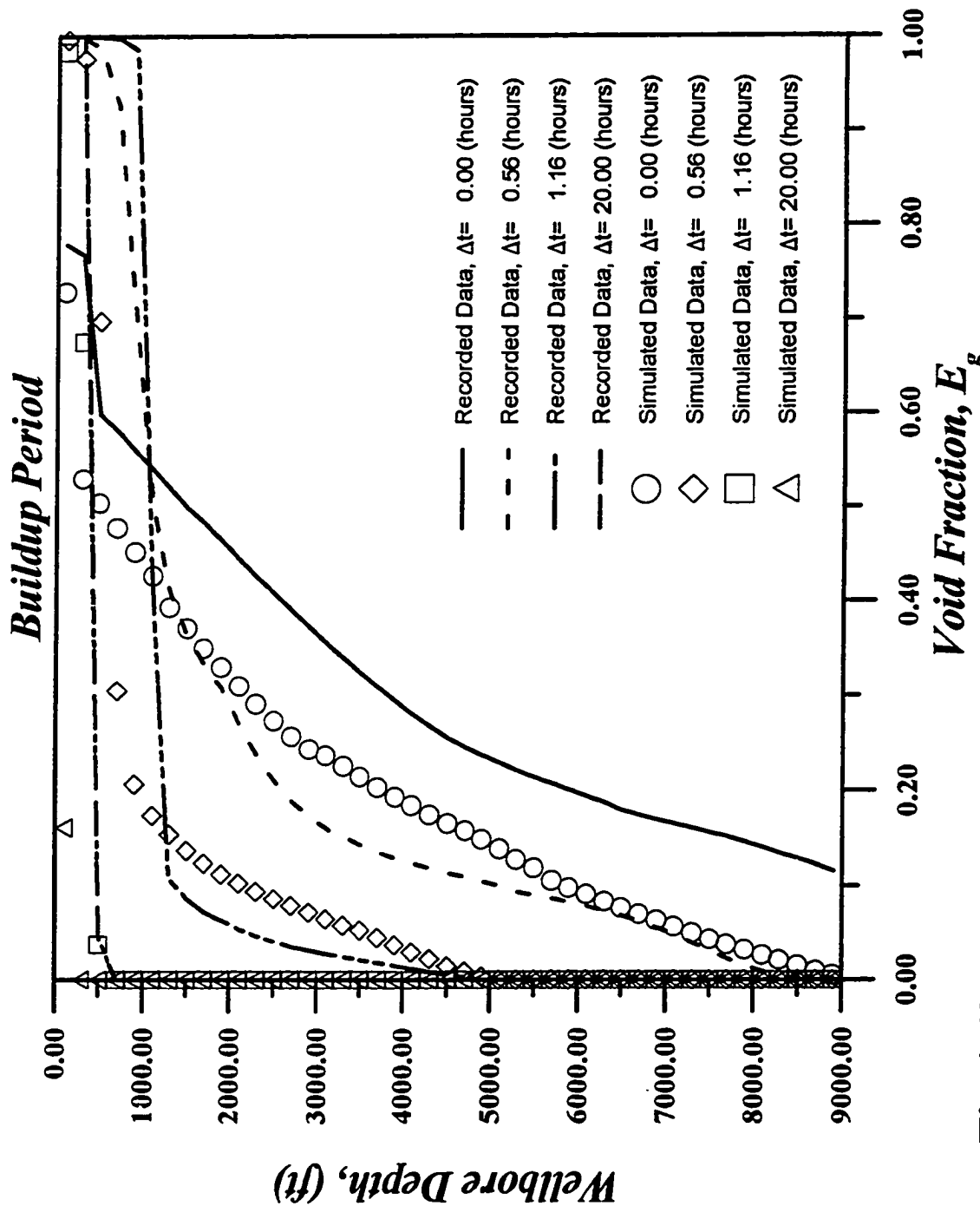
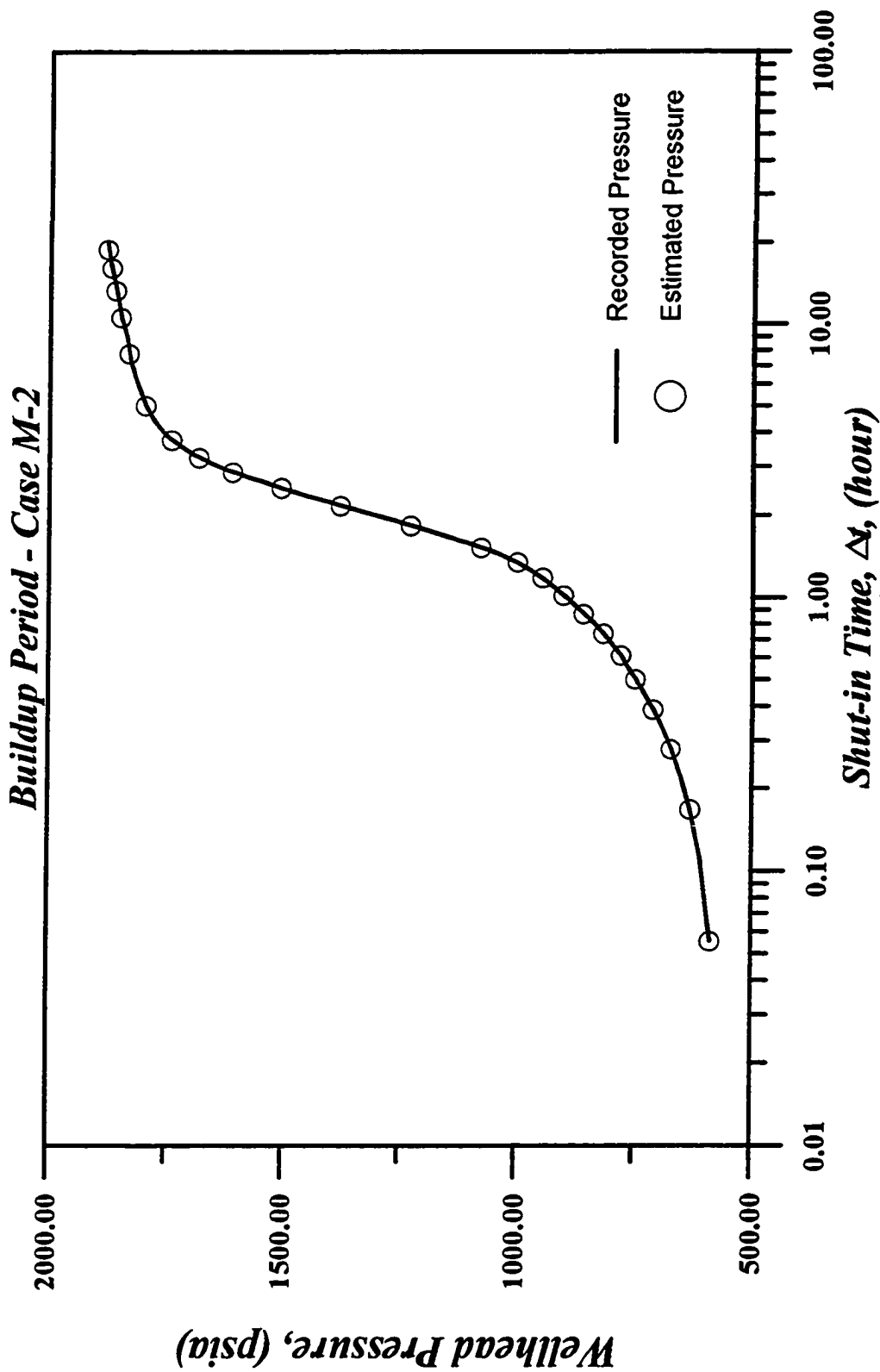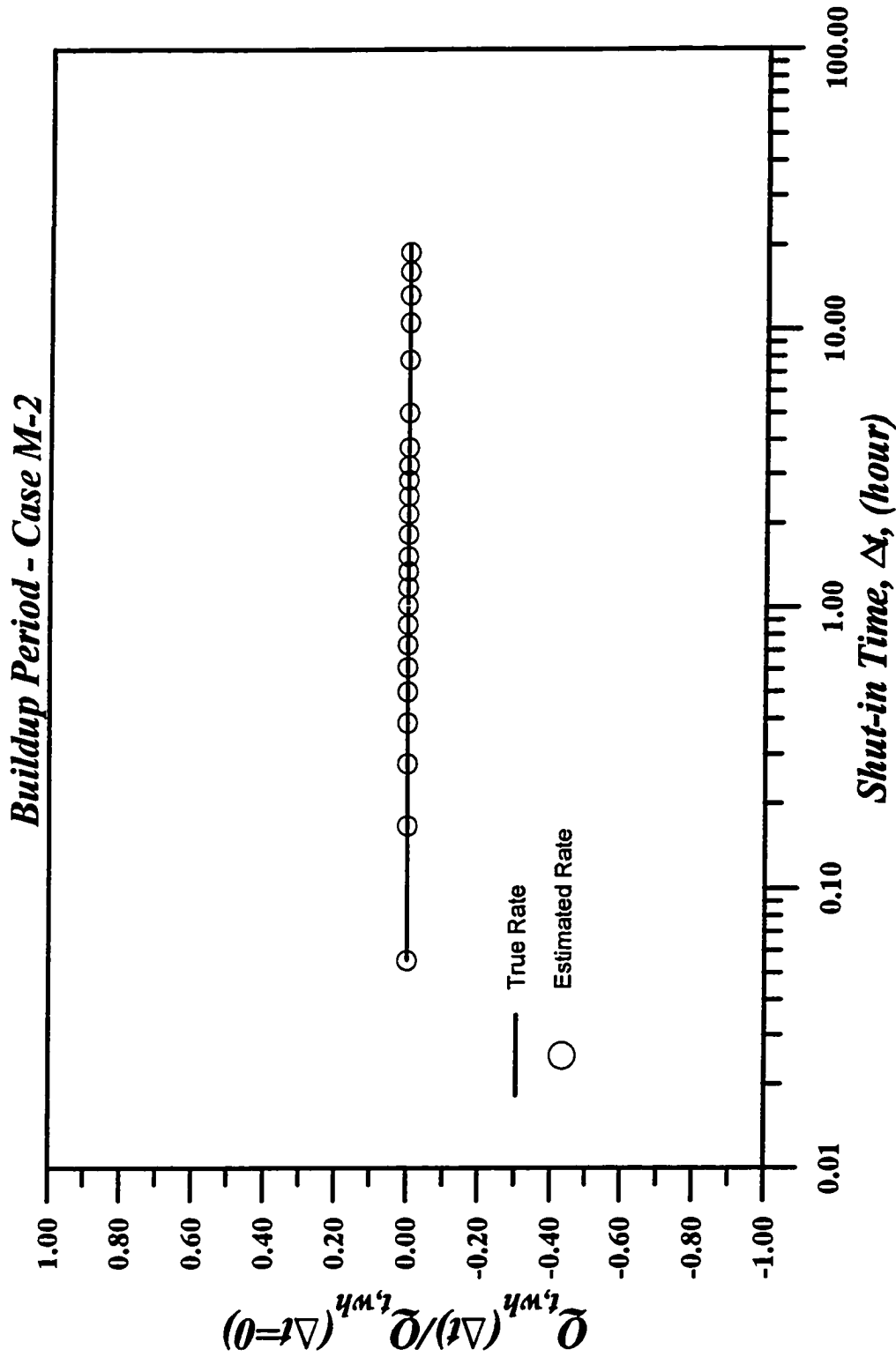Fig.4.68 - Void Fraction Distribution in the Wellbore for Case M-2.
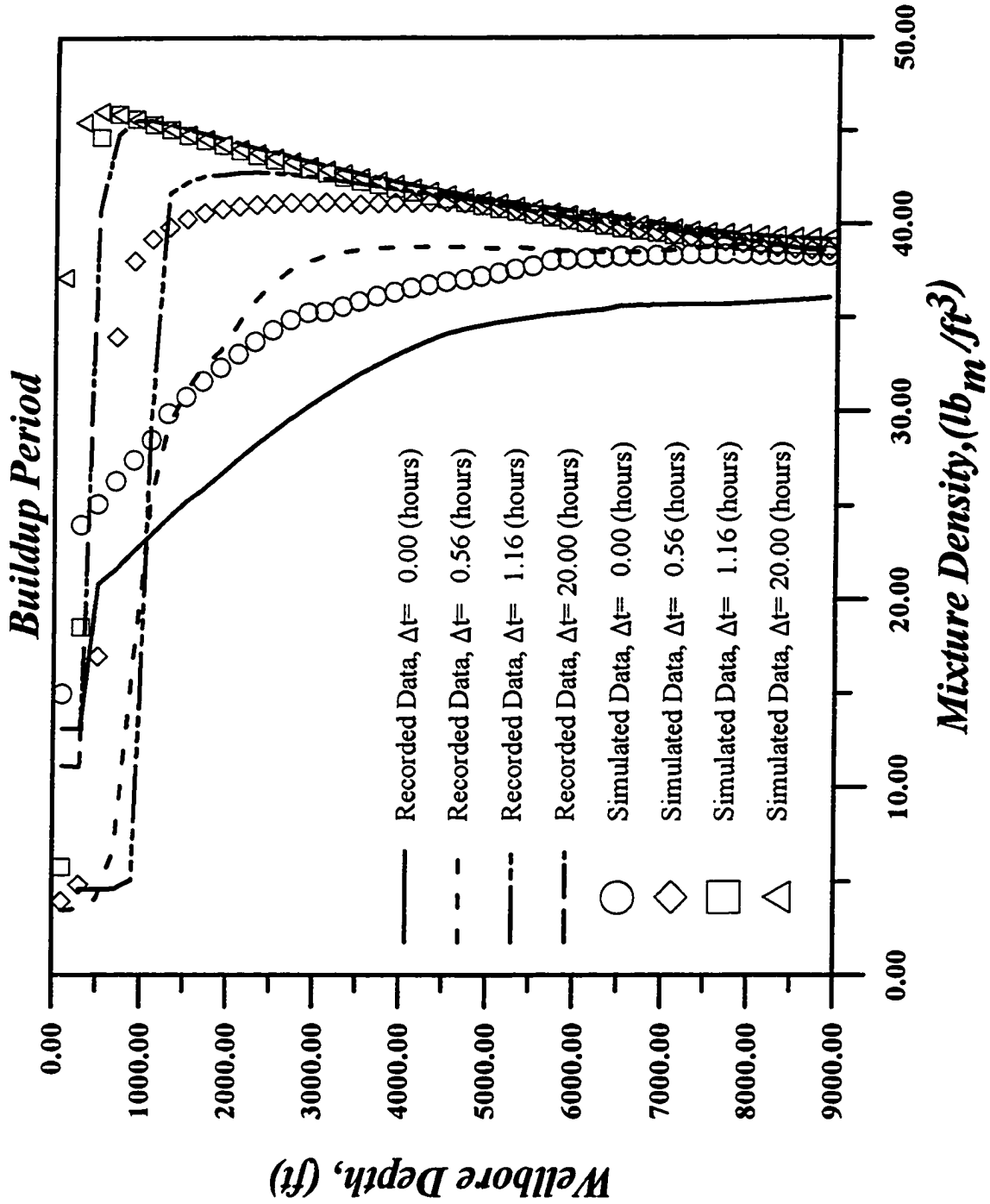
Fig. 4.69 – Mixture Density Distribution in the Wellbore for Case M-2.

4.3.1.d   Case M-3.

Case M-3 is a case that considers a restricted entry well. A simulation of a drawdown period followed by a buildup period was performed. The initial reservoir pressure is higher than the initial reservoir bubble-point pressure. The production period is run long enough so that the bottomhole pressure goes below the initial bubble point pressure and two-phase flow of oil and gas occurs in the reservoir. The reservoir is producing under solution gas drive. As in the two previous cases, the wellbore simulator is coupled with the RDRBOS (r-z) reservoir simulator to produce the "measured" data. Wellbore and reservoir parameters used for this case are given in Table 4.17.

Figure 4.70 is a log-log plot of two sets of drawdown bottomhole pressure drops and their derivatives. At early times, the pressure derivative shows the effects of wellbore storage and skin. At late times, we obtain approximate pseudoradial flow although the derivative is not exactly constant and the derivative of the true pressure drop is actually slightly declining. On the other hand, the two sets of pressure match well at early times. Fig. 4.71 shows a semilog plot of bottomhole pressure versus time. As in the log-log plot, good agreement between the recorded and estimated pressure is obtained during the first three hours of production, but at late times, the two sets of pressure are not in good agreement. However, as in the two previous cases, the optimization procedure successfully generates a match of the wellhead pressure (Fig. 4.72) and total rate (Fig. 4.73). However, the estimated bottomhole rate is only in rough agreement with the true bottomhole rate; see Fig. 4.74.

Parameter	Value	Unit
Drawdown surface oil production rate	70.00	STB/D
Total production time	100.00	hours
Inital reservoir pressure	4000.00	psia
Initial bubble point pressure	2710.00	psia
Oil compressibility (p>p_b)	1.0e-5	1/psia
Oil component API gravity at s.c.	45.00	API
Gas component specific gravity at s.c.	0.70	-
Oil-gas surface tension	4.50	dynes/cm.
Wellbore pipe inside diameter	1.80	inch
Formation permeability in r-direction	45.00	md.
Formation permeabilty in z-direction	5.00	md
Formation thickness	20.00	ft.
Layer 1 Thickness- not open to flow	5 (0-5)	ft.
Layer 2 Thickness- open to flow	5 (5-10)	ft.
Layer 3 Thickness- open to flow	5 (10-15)	ft.
Layer 4 Thickness-not open to flow	5 (15-20)	ft.
Formation porosity	0.20	-
Wellbore radius	0.364	ft.
System isothermal compressibility	2e-5	1/psia
Skin factor	10.00	-
Wellbore depth	9000.00	ft.
Spatial Increment	200.00	ft.
Buildup simulation time	20.00	hours

Table 4.17: Input Parameters for Case M-3

Fig. 4.70 – Log-Log Plot of Pressure and Pressure Derivative for Case M-3.

Fig. 4.71 – Bottomhole Pressure as Function of Production Time for Case M-3.

Fig. 4.72 – Wellhead Pressure as Function of Production Time for Case M-3.
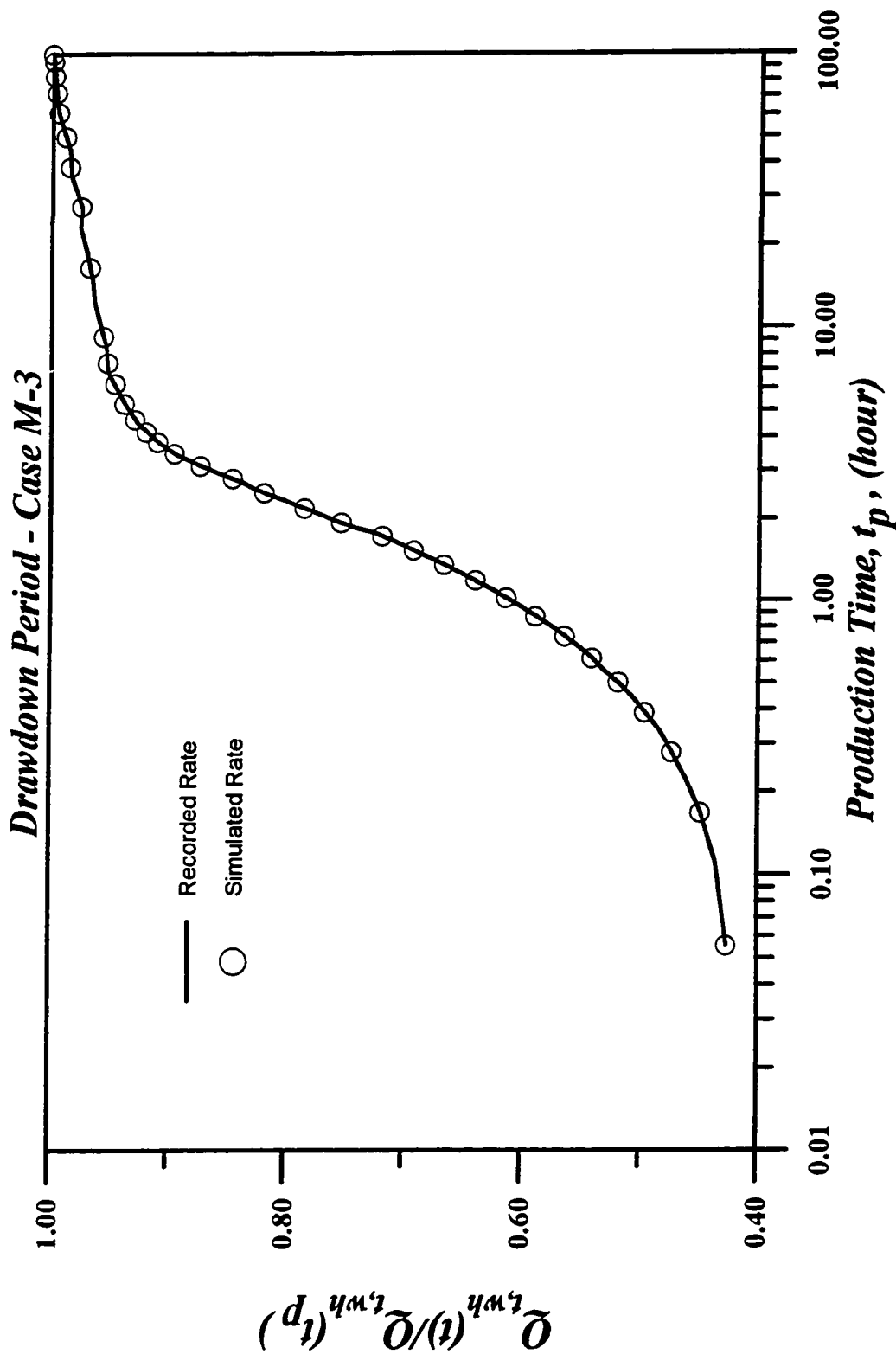
Fig. 4.73 – Normalized Wellhead Flow Rate as a Function of Production Time for Case M-3.
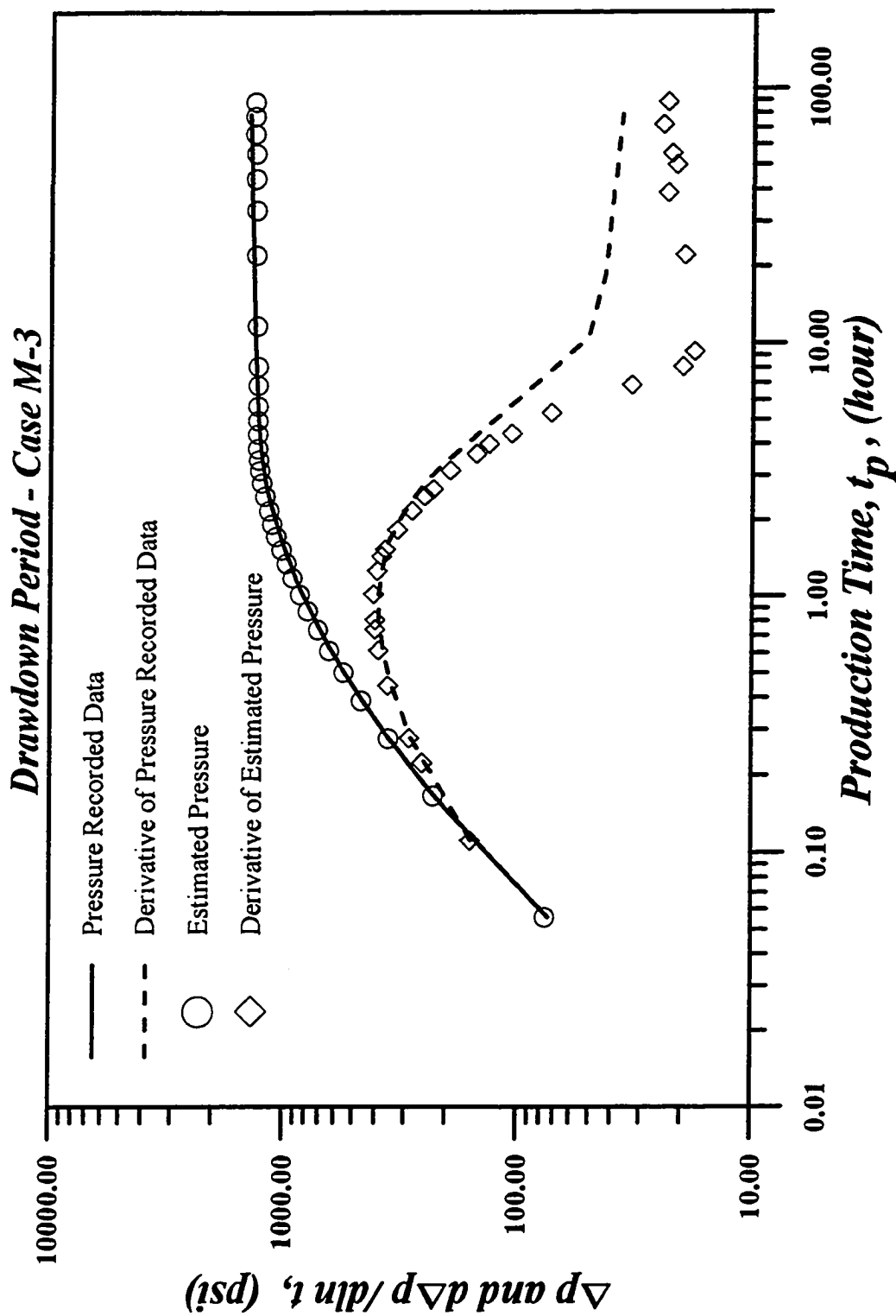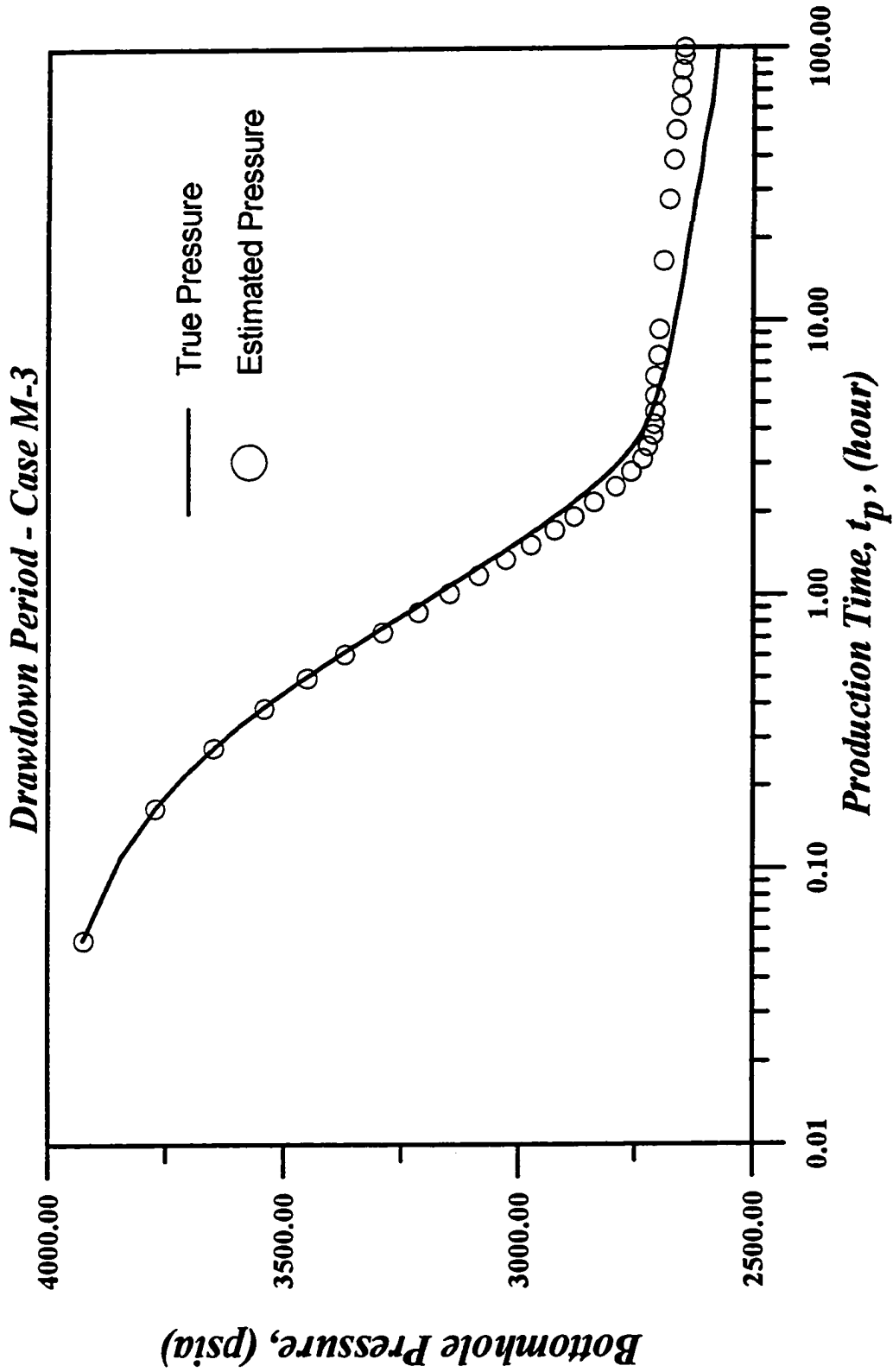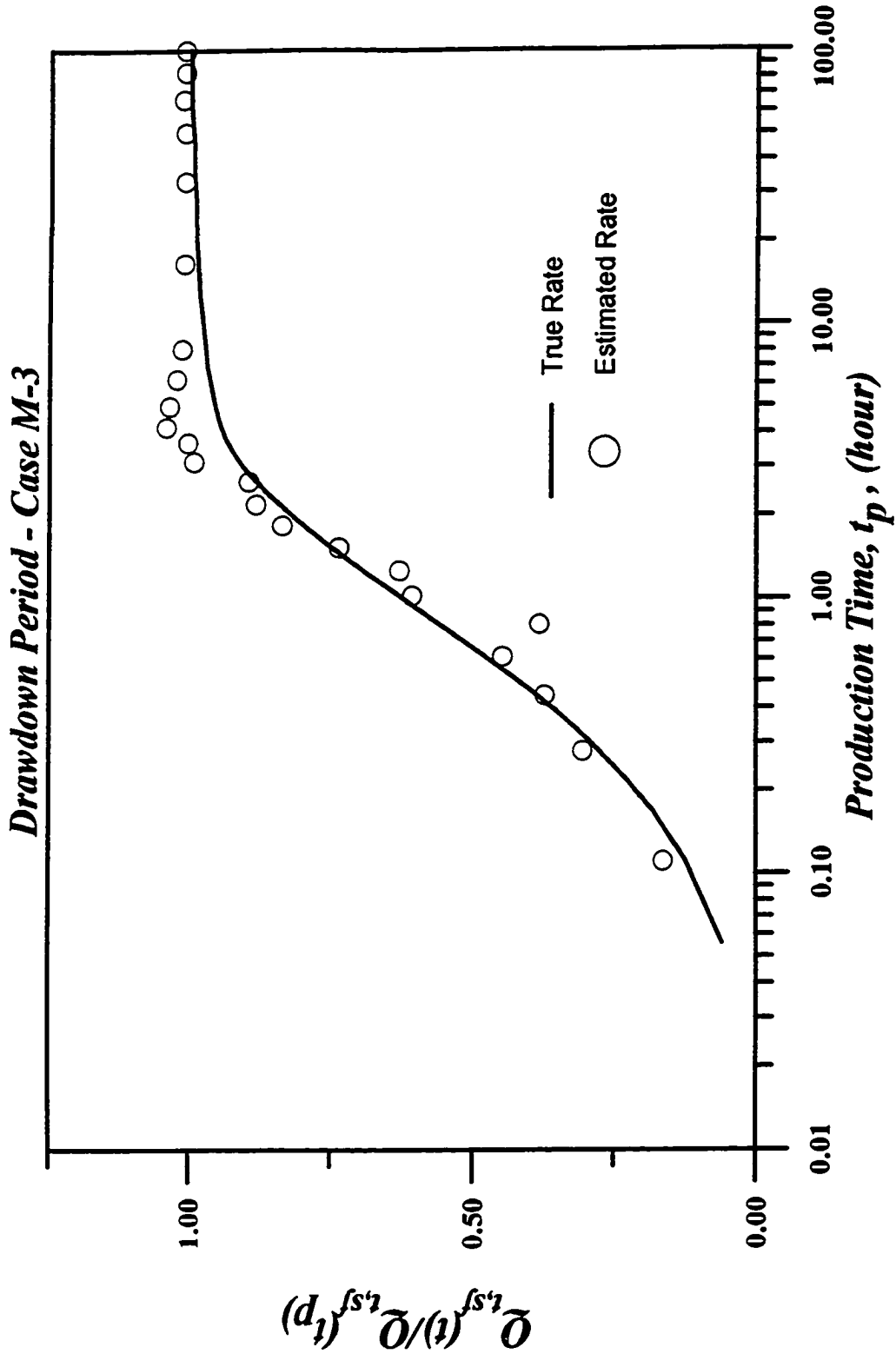
Fig. 4.74 – Normalized Sandface Flow Rate as a Function of Production Time for Case M-3

As in the two previous cases, the estimated temperature profiles give lower temperatures than the true temperature from the bottomhole (9,000 ft.) of the well to a depth of approximately 3,000 ft., see Fig. 4.75. From that depth to surface, the estimated temperature is higher than the true temperature.

Fig. 4.76 shows estimated and recorded gas void fraction profiles. At $\Delta t = 2.87$ hours,the recorded void fraction varies from approximately 0.05 at bottomhole to approximately 0.7 at the wellhead. By the end of the drawdown ($t_p = 100$ hours), the gas void fraction at bottomhole is approximately 0.10 and equal to 0.76 at the wellhead. All the estimated void fraction profile appear displaced to the left of the true ones, which is a direct influence of the discrepancy between true and estimated pressures (see Fig. 4.71) and temperatures near the bottom of the well. The estimated mixture density profiles (see Fig. 4.77) are displaced to the right of the true ones giving higher values of density due to the higher values of pressure and temperature in the bottom section of the well.

The optimization procedure was run to generate estimated bottomhole buildup pressures and rates from wellhead measurements recorded during buildup. Fig. 4.78 shows a log-log plot of the true and estimated bottomhole buildup pressure change ($\Delta p = p_{ws} - p_{wf,s}$) versus equivalent time and its derivative. Note the estimated results are in good agreement with the "true" results. A semilog plot of estimated and true bottomhole pressures is shown in Fig. 4.79. The two bottomhole pressures differs slightly. At late times, both pressure curves are approximately parallel, i.e., exhibit approximately the same semilog slope. As previous cases, the optimization procedure yields a good match of wellhead pressure (Fig. 4.80) and rates (Fig. 4.81). The

Drawdown Period

Legend:
- Recorded Data, t = 2.87 (hours)
- Recorded Data, t = 34.70 (hours)
- Recorded Data, t = 62.50 (hours)
- Recorded Data, t = 100.00 (hours)
- Simulated Data, t = 2.87 (hours)
- Simulated Data, t = 34.70 (hours)
- Simulated Data, t = 62.50 (hours)
- Simulated Data, t = 100.00 (hours)
- Initial Temperature Distribution

Temperature, (°F)

Wellbore Depth, (ft)

Fig. 4.75 – Temperature Distribution in the Wellbore for Case M-3.

203

Fig. 4.76 - Void Fraction Distribution in the Wellbore for Case M-3.

Fig. 4.77 - Mixture Density Distribution in the Wellbore for Case M-3.
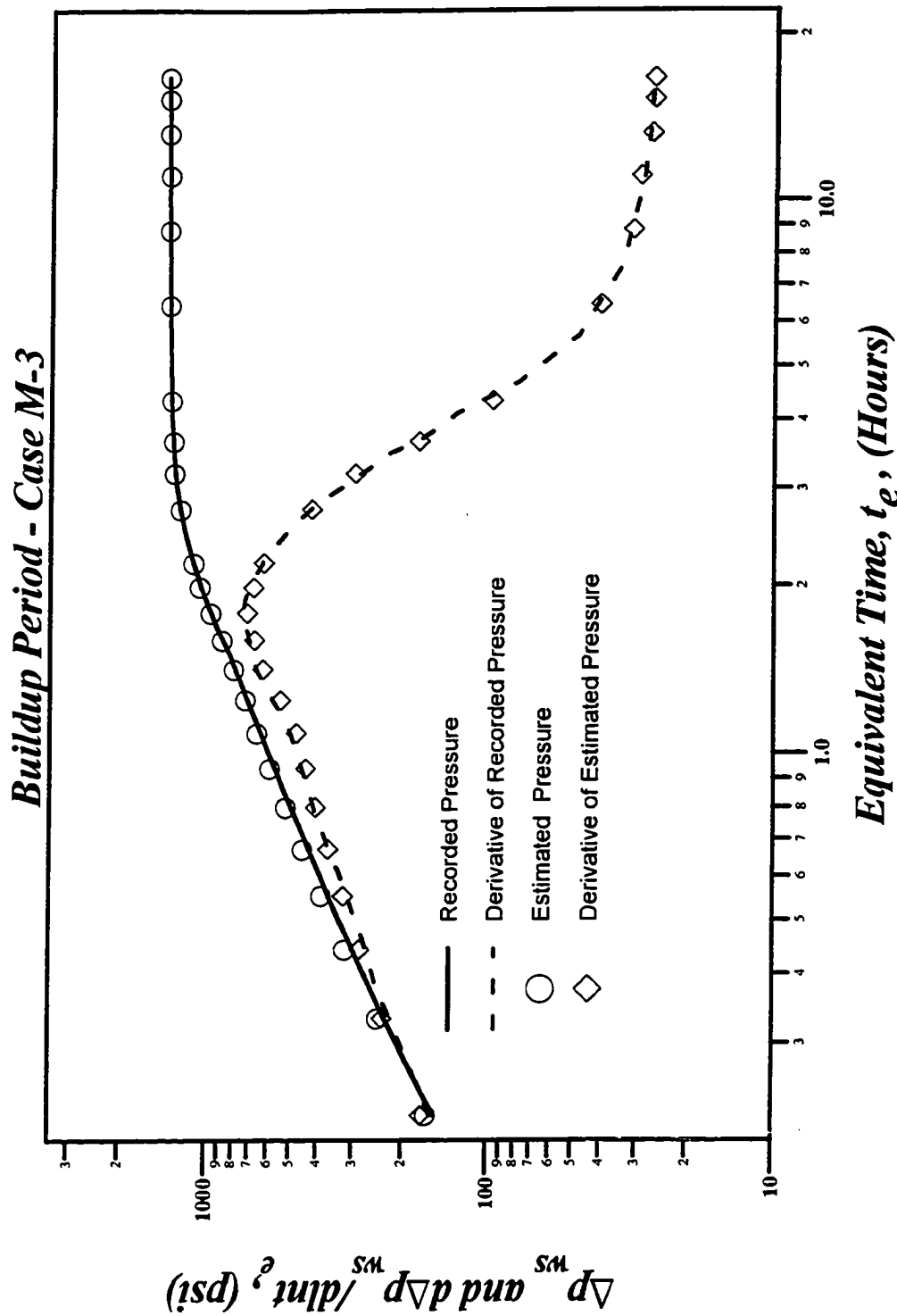
Fig. 4.78 – Log-log Plot of Pressure and Pressure Derivative for Case M-3.
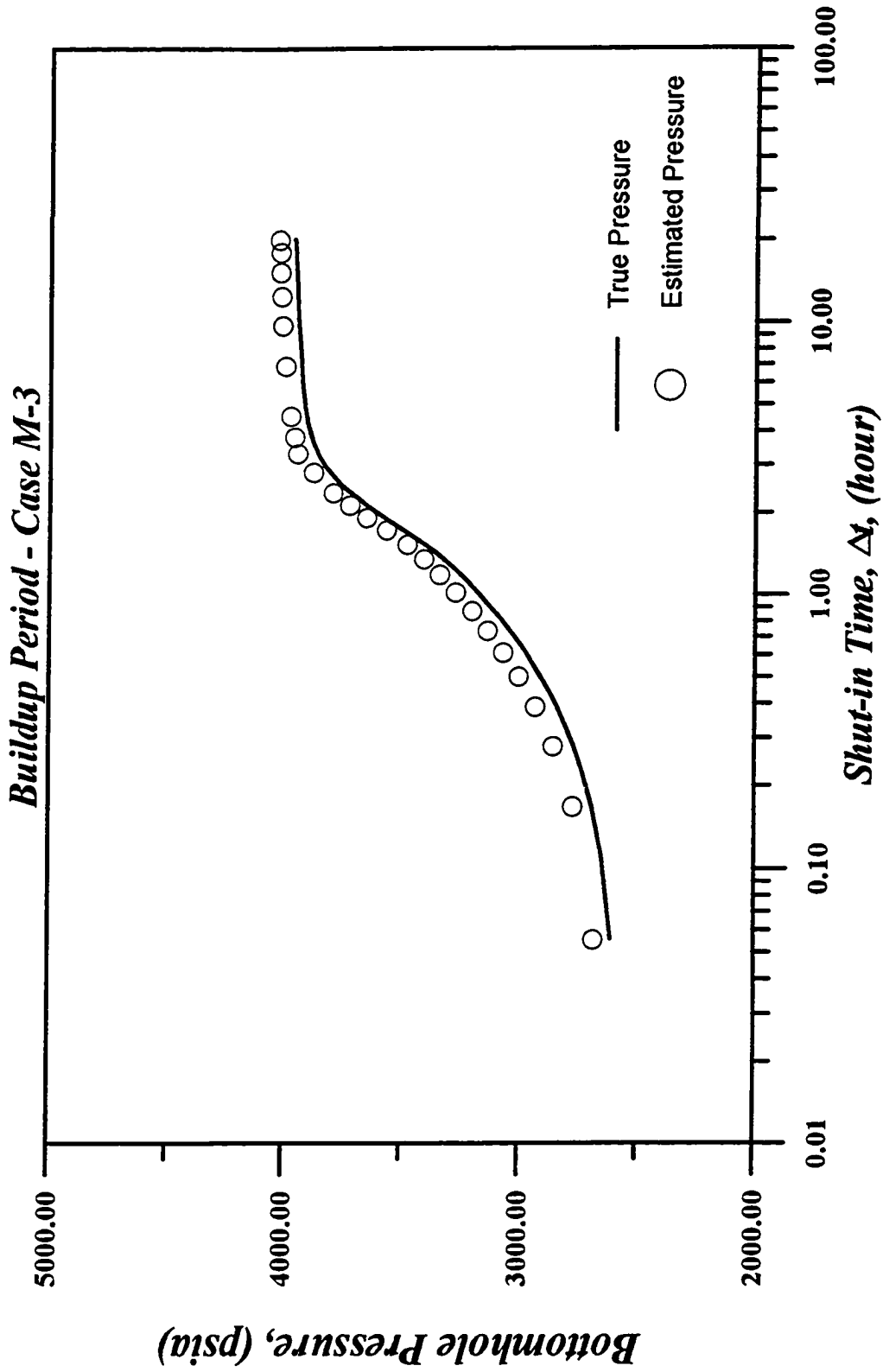
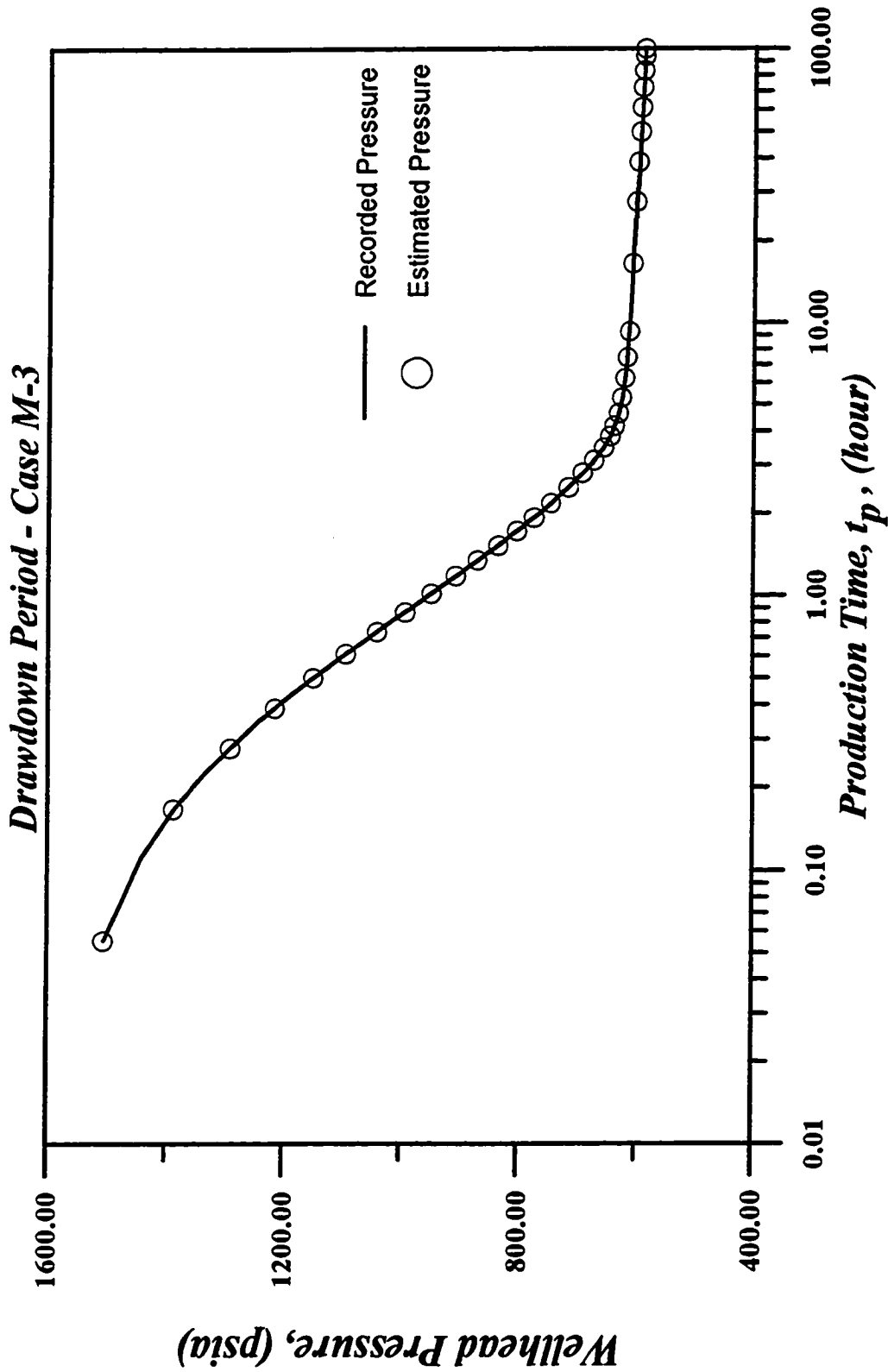**Fig. 4.79 – Bottomhole Pressure as a Function of Shut-in Time for Case M-3.**
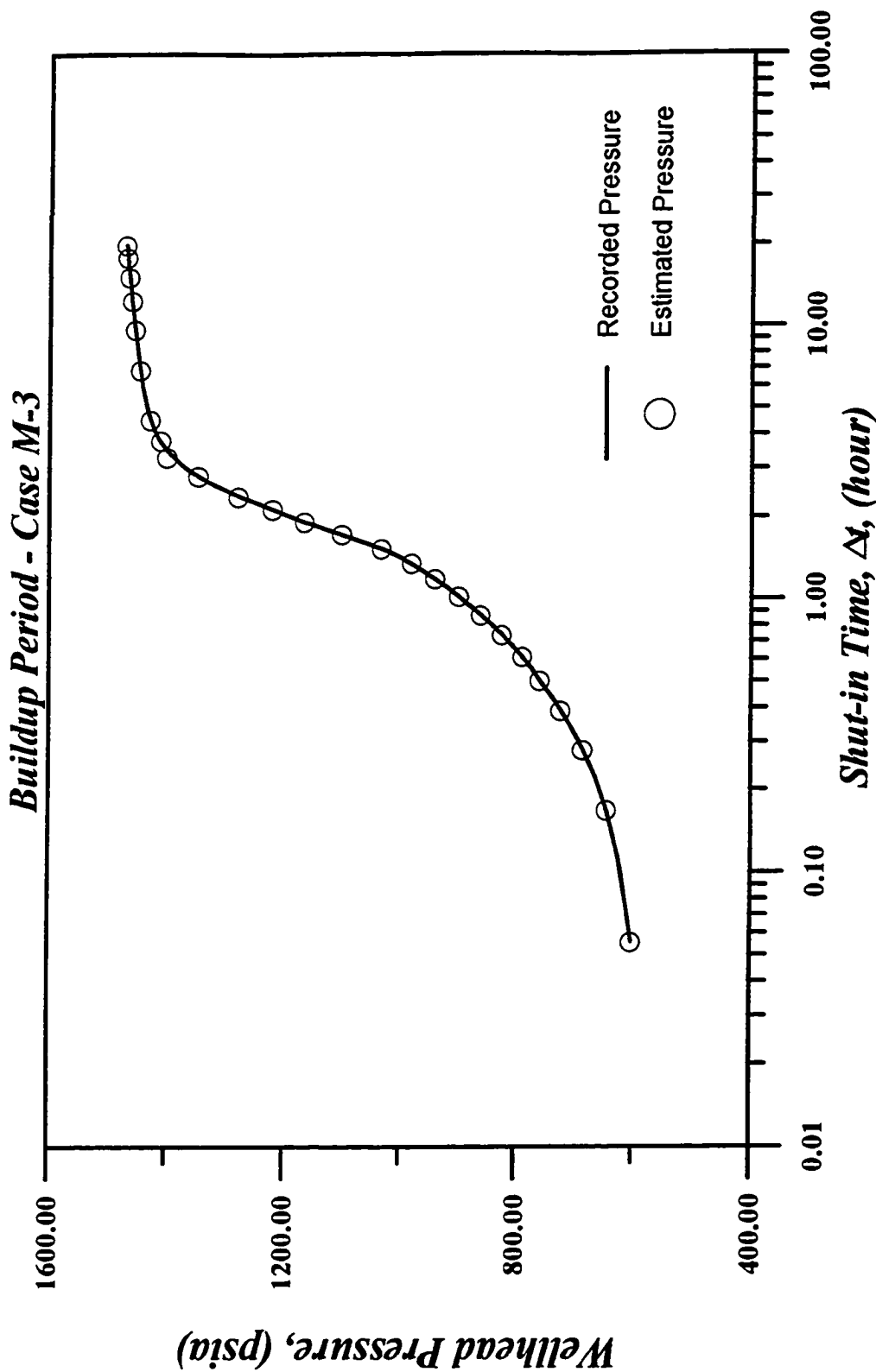
**Fig. 4.80 – Wellhead Pressure as a Function of Shut-in Time for Case M-3.**
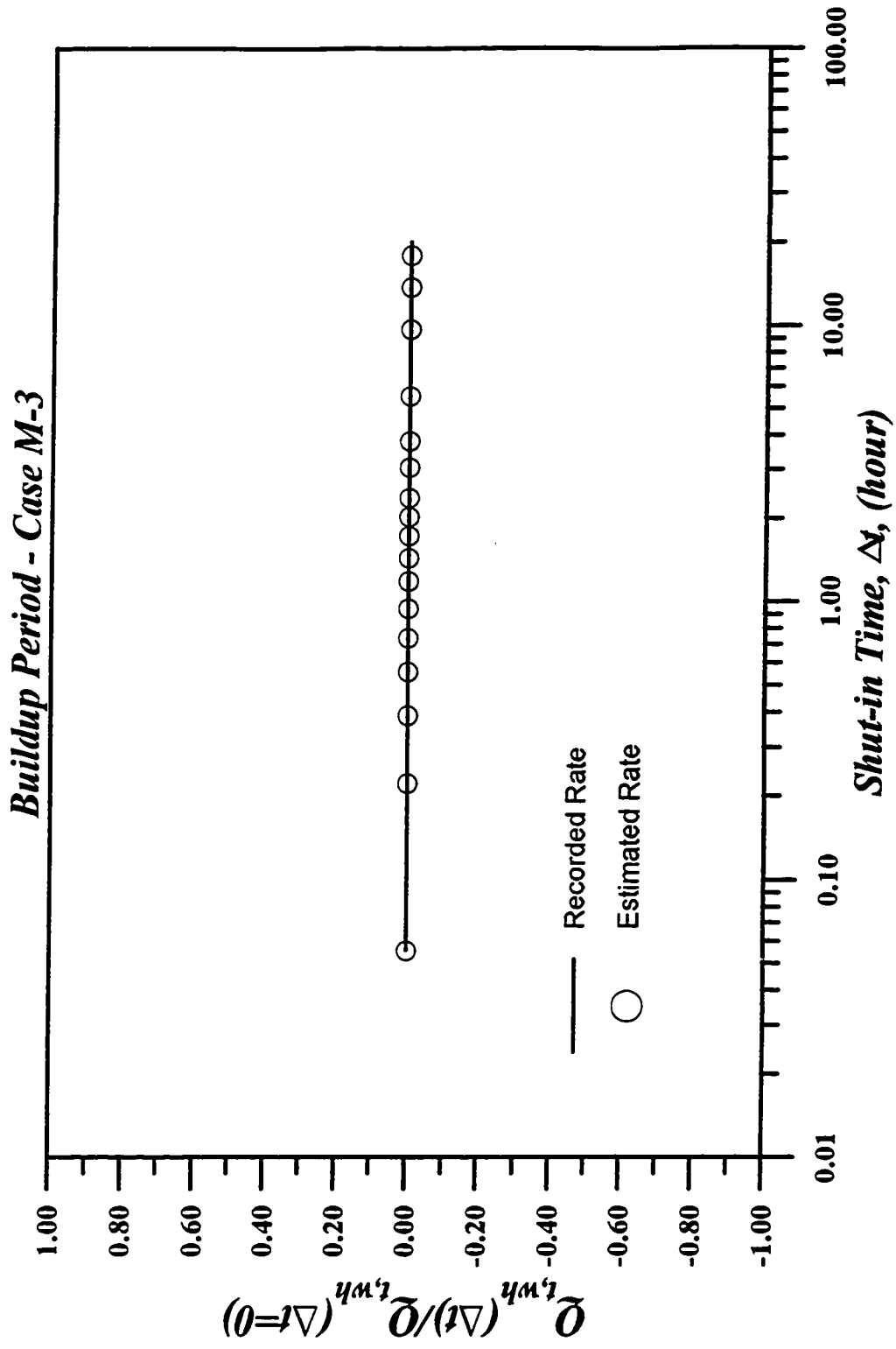
Fig. 4.81 – Wellhead Flow Rate as a Function of Shut-in Time, Case M-3

estimated bottomhole rate again exhibits the same trend as the true rate and at late times both rates are zero, see Fig. 4.82.

At the end of the buildup period, the wellbore fluid temperature profile is approximately the same as geothermal gradient, see Fig. 4.83. Figs. 4.84 and 4.85 graphically displayed the gas void fraction and mixture density profiles, respectively. As in our previous examples, at late times, the estimated profiles are in good agreement with the true ones

Matching of drawdown and buildup wellhead data required 20 hours on a PC-Pentium 90MHz.
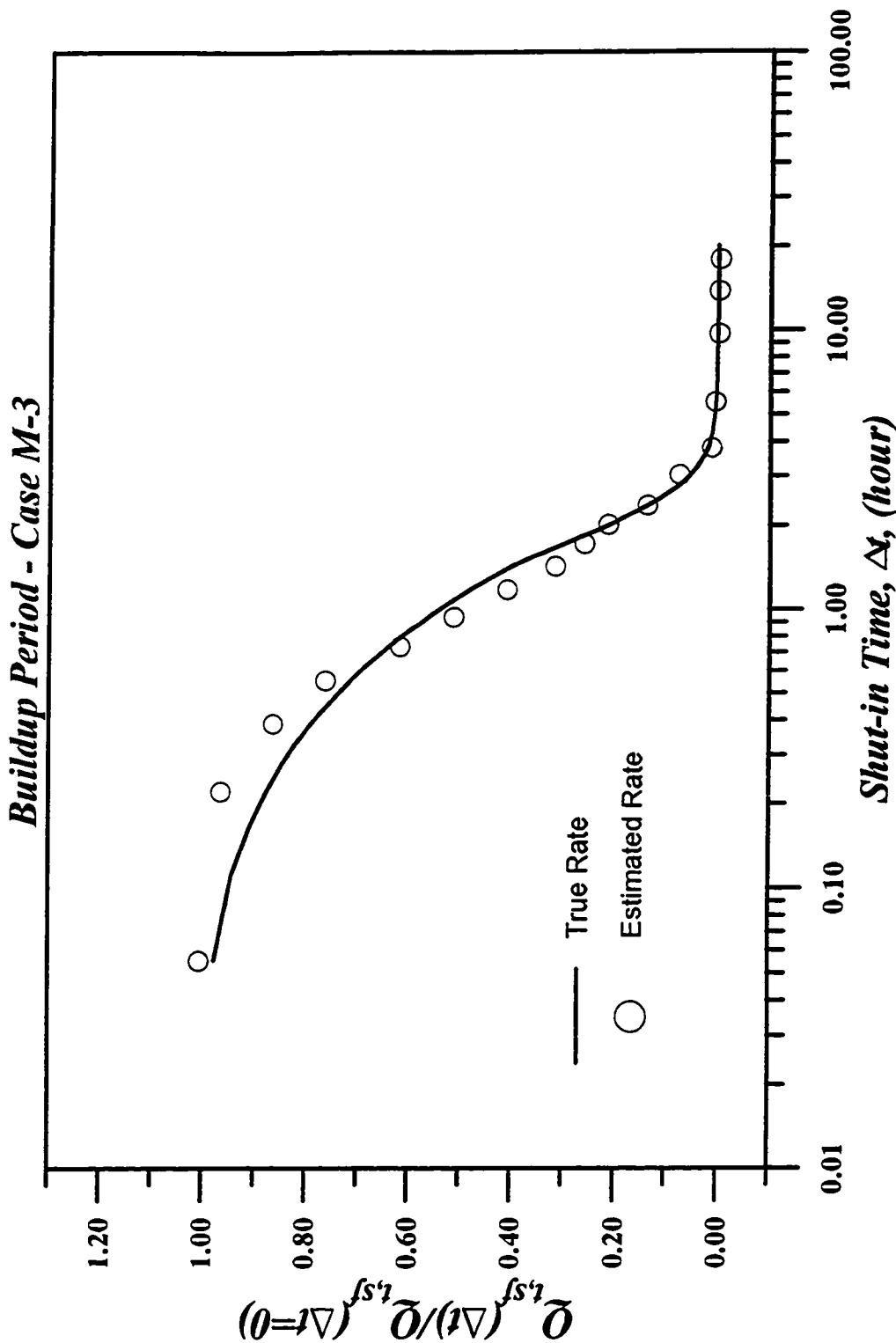
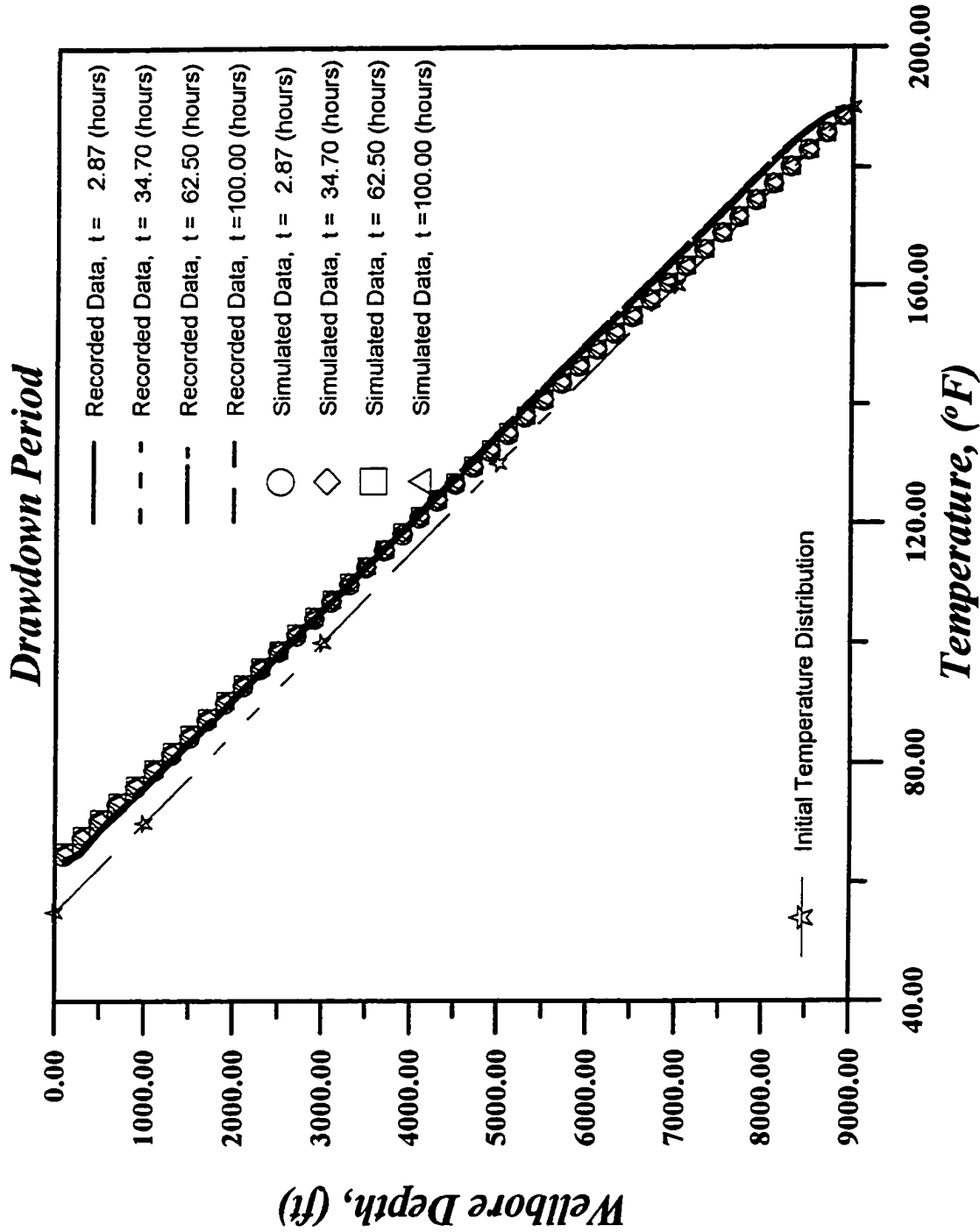**Fig. 4.82 – Normalized Sandface Flow Rate as a Function of Shut-in Time for Case M-3.**
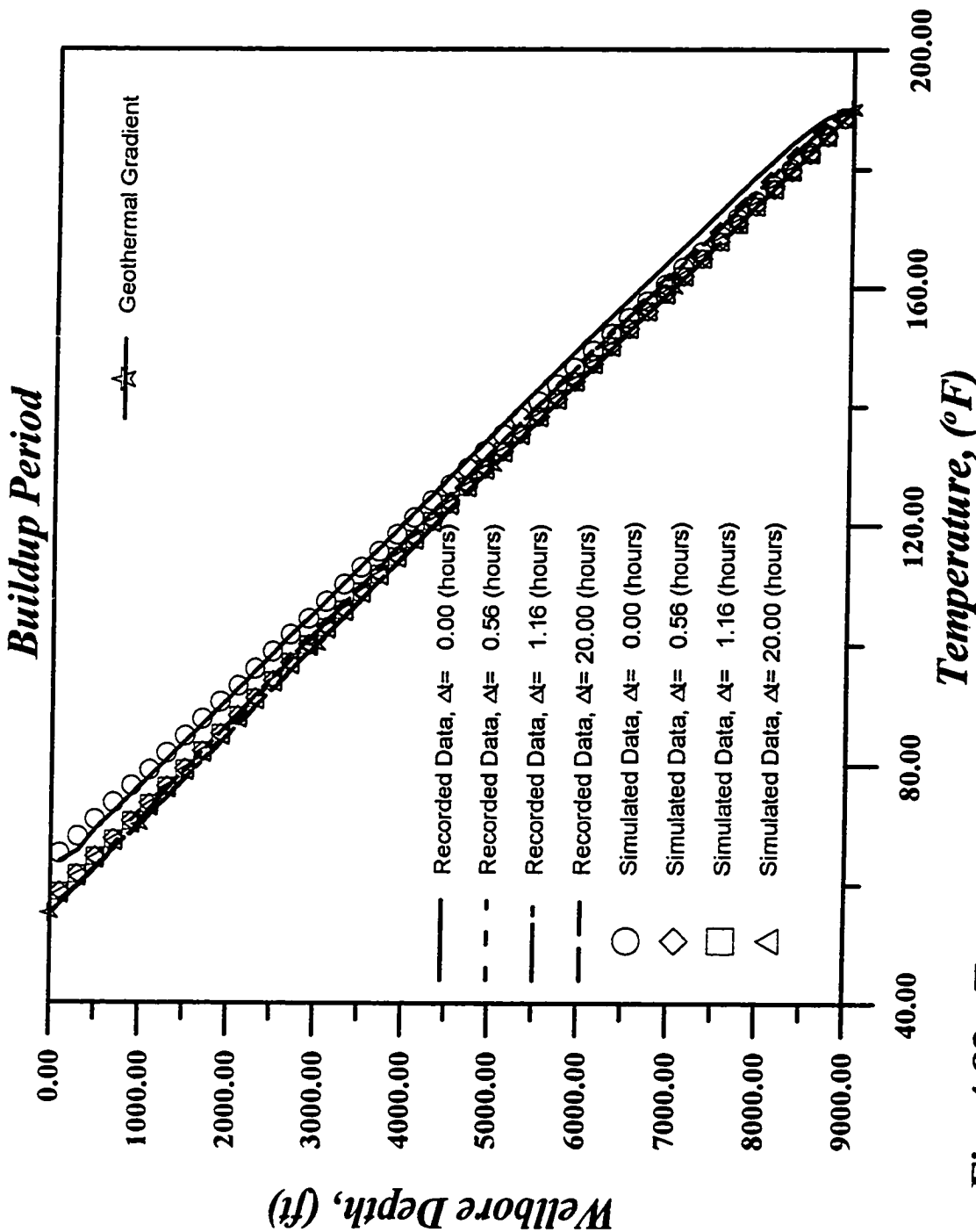
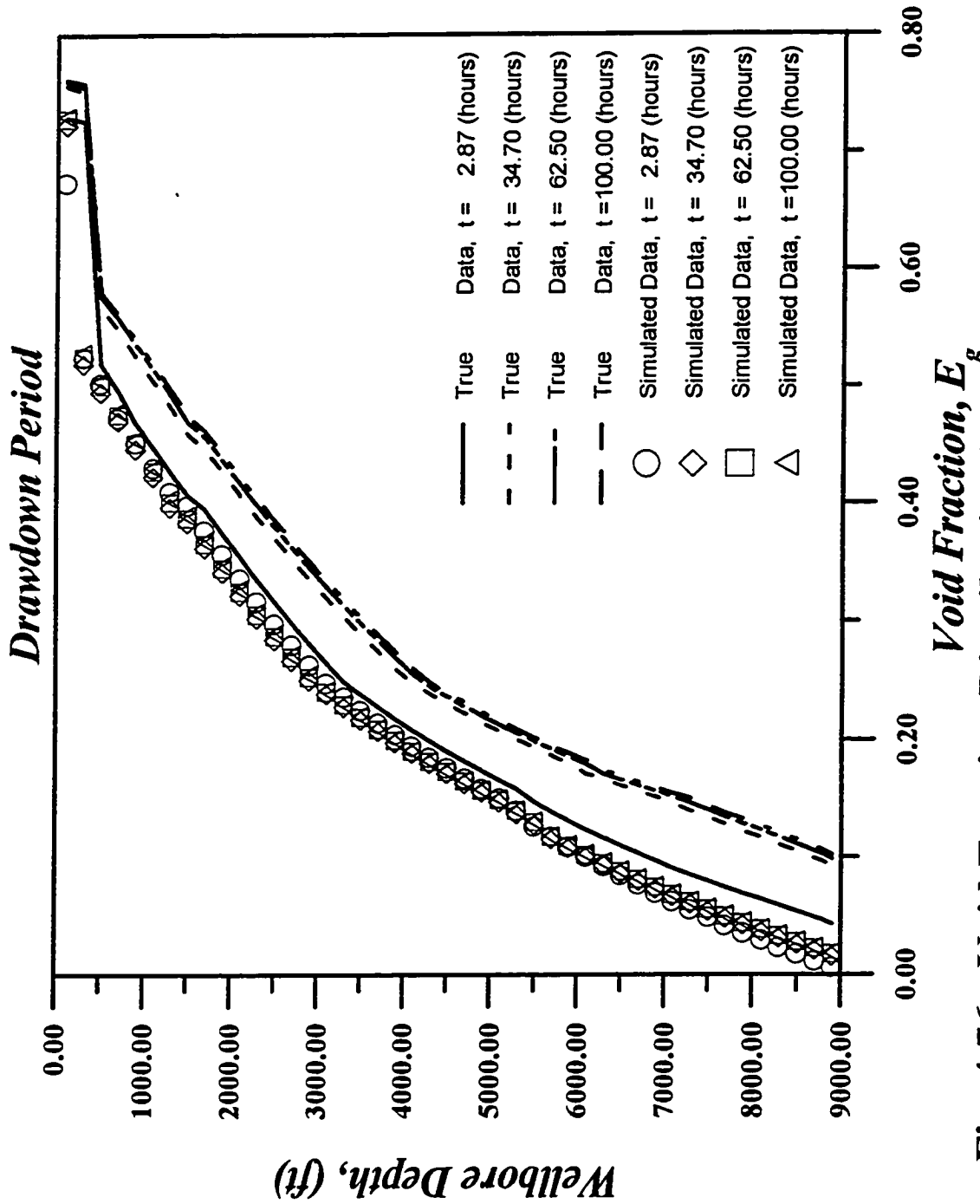**Fig. 4.83 – Temperature Distribution in the Wellbore for Case M-3.**
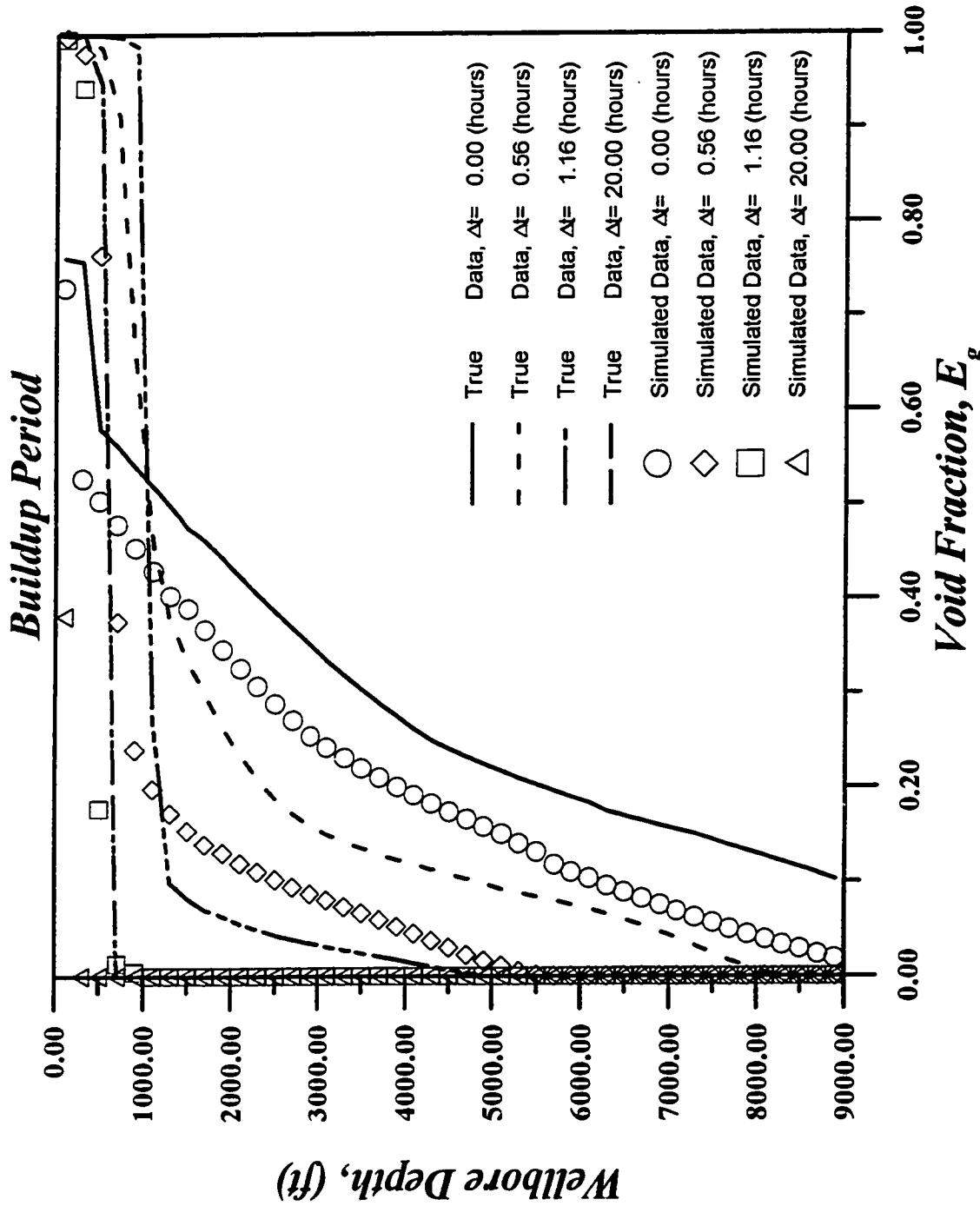
Fig. 4.84 - Void Fraction Distribution in the Wellbore for Case M-3.

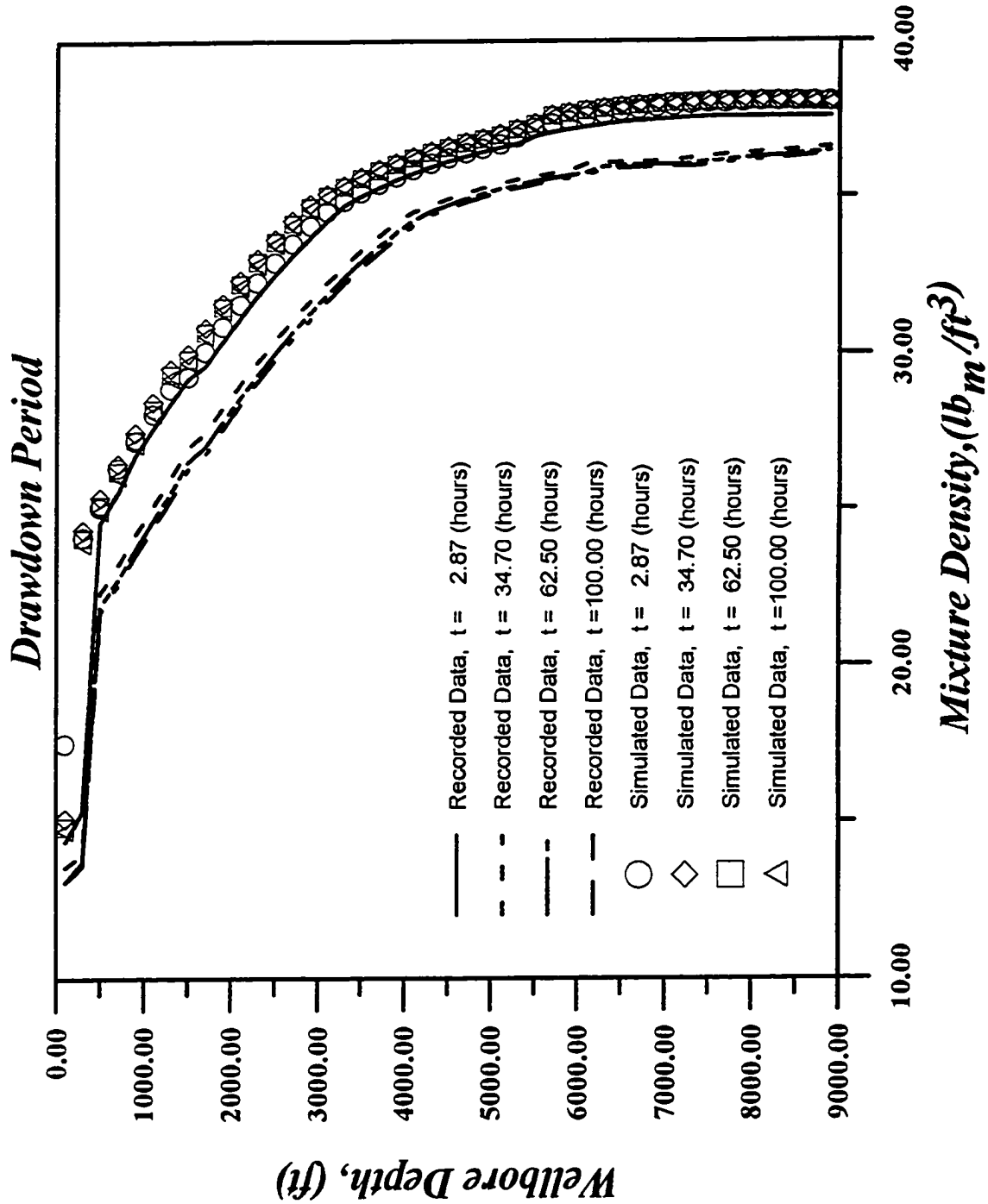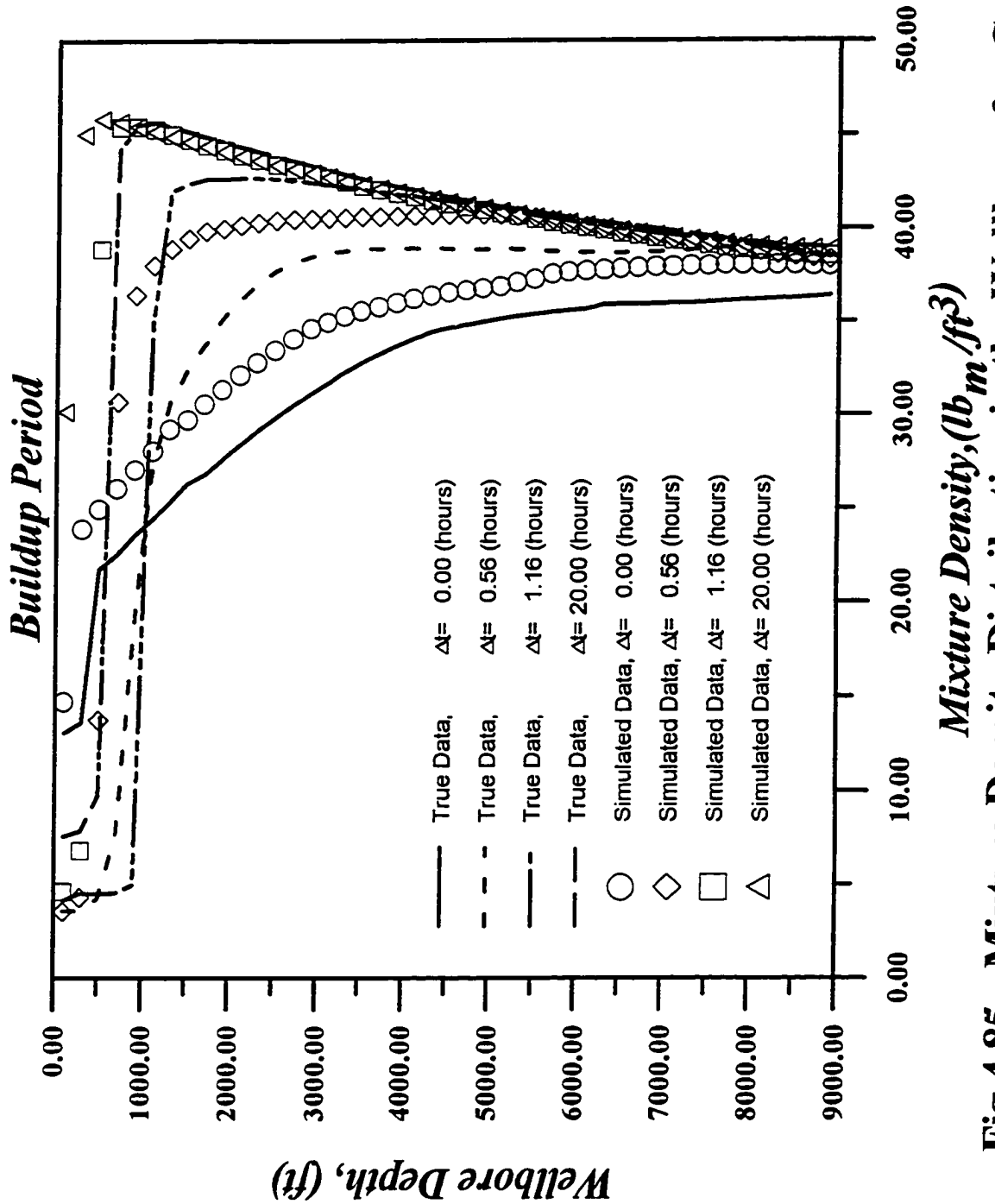Fig.4.85 - Mixture Density Distribution in the Wellbore for Case M-3.

CHAPTER V

CONCLUSIONS.

Although the classical analyses of transient well test pressure data are based on theories that assume a constant wellbore storage coefficient, it is widely recognized that in reality, wellbore storage is variable. Despite this, there are relatively few papers that considers the effect of wellbore phase segregation, variable wellbore storage or the complete wellbore dynamics.

In the present study, a mechanistic model has been developed to predict the effect that transient two-phase gas-oil flow in the wellbore has on pressure drawdown and buildup behavior. A one-dimensional drift-flux model is used to derive partial differential equations governing the two-phase flow in the wellbore. The black-oil approach, which accounts for a variable bubble-point pressure, is used to account for the effect of interphase mass transfer. After obtaining the corresponding finite-difference equations, solutions are computed with a sequential, iterative calculation procedure.

A computer simulator has been developed to implement the proposed model and the finite-difference solution procedure. For the purpose of verification, the simulator was first used to generate pressure responses from a buildup test in a well where single phase flow exits in the wellbore before shut-in. The analysis of generated pressure buildup data was carried out by type-curve matching with the classical wellbore

214

storage and skin type curves and also by using Horner analysis. These analyses gave virtually exact values of permeability, skin factor, initial reservoir pressure and also the wellbore storage coefficient.

After verification, the simulator was applied to simulate the phase redistribution process occurring in the wellbore during pressure buildup tests in wells shut-in at the surface. Two cases were considered: a buildup test in a naturally flowing well and a buildup test in a gas-lift well. The investigation confirmed that the wellbore storage coefficient can either increase or decrease, as reported in the literature. The variation in the wellbore storage coefficient is dominated by the relative effects of phase segregation and gas compression.

The preceding cases were used to considers numerical accuracy and stability of the model, and to investigate the validity of the Fair[1] and Hegeman[2] models for wellbore phase redistribution. Additionally, both an isothermal and a non-isothermal transient process were simulated to investigate the effect of temperature variation on the pressure response.

Finally, several simulations were done and synthetic wellhead and bottomhole data were recorded. The wellhead data were used to compute the bottomhole pressure and rate from the measured wellhead pressures and rates. The data obtained from the inverse problem were compared with the true bottomhole data generated from the forward simulation, in order to investigate the accuaracy of the procedure.

As results of this study, the following conclusions are warranted:

1. A mechanistic model has been developed to simulate the variable wellbore storage process in general, and phase segregation in particular. The wellbore and

reservoir flow interaction has been treated through the use of Duhamel's principle or by using a (r-z) numerical reservoir simulator. A variable bubble-point pressure methodology has been integrated to correctly model the interphase mass in the black oil model formulation.

2. The results presented indicate that when two-phase flow exits in the wellbore, a variable wellbore storage coefficient should be expected and the effective wellbore storage coefficient can be either increasing or decreasing. As first shown by Xiao[18] and Xiao et al.[19], the variation in the wellbore storage coefficient is a direct result of the effects of phase segregation and gas compression. If the magnitude of afterflow is small after the end of wellbore phase segregation, phase segregation will be the dominating factor, and pressure buildup data will show an increasing wellbore storage coefficient at the end. On the other hand, if the afterflow is still large after liquid and gas have completely segregated in the wellbore, the gas column will be compressed due to afterflow and the pressure buildup data will show a decreasing wellbore storage coefficient.

3. For the decreasing wellbore storage case, regression analysis based on the Hegeman et al.[2] model often gives reasonable estimates of permeability and skin factor, but Fair's model[1] usually yields highly erroneous estimates of these parameters and may not fit the pressure data well. For the decreasing wellbore storage cases, Fair's model does not give a good match of the pressure response.

4. For the increasing wellbore storage case, limited cases shows Fair's model fits the pressure data better and gives better estimates of permeability and skin

factor than the Hegeman et al. model. However, in the cases we have considered, the estimate of C_ϕ obtained from regression is unreasonable from a physical viewpoint. In essence, the Fair's model and the Hegeman et al. model contain sufficient parameters to give the right qualitative behavior of the pressure response when the wellbore storage is variable, but do not capture the true physics of the problem.

5. The addition of temperature gradient affects the buildup data pressure response and causes a small deviation from the unit slope line on a log-log plot. The temperature effects result in a higher value of the wellbore storage coefficient at early times and a lower value at late times in comparison to the response that we obtain for the isothermal case.

6. We have presented a subplex procedure to estimate bottomhole pressure and flow rates from measurements of these variables at the wellhead. The method yields good results during the late buildup period when the temperature gradient in the wellbore becomes approximately equal to the geothermal gradient. Estimated bottomhole values during the drawdown may not be sufficiently accurate for practical applications. The subplex method was able to obtain a match of wellhead data, but is extremely time consuming. The minimization process for difficult problems may take as long as 20 hours on a PC-Pentium 90 MHz. From this point of view, a search for a more efficient optimization method is highly recommended.

NOMENCLATURE

Variable		Definition
a	=	matrix coefficient
A	=	pipe across sectional area, ft^2
b, b', b''	=	matrix coefficient
B_g	=	gas formation volume factor, RB/scf
B_o	=	oil formation volume factor, RB/STB
B_{ob}	=	oil formation volume factor at p_b, RB/STB
c	=	matrix coefficient
c_o	=	oil compressibility for $p > p_b$, 1/psia
c_t	=	system compressibility, 1/psia
C_g	=	gas component mass concentration
C_{gl}	=	gas component mass concentration in liquid phase
C_l	=	oil component mass concentration
C_{ol}	=	oil component mass concentration in liquid phase
C_ϕ	=	max. phase redistribution pressure change, psia
d, d', d''	=	matrix coefficient
D	=	pipe diameter, ft
D_r	=	diffusion term
E_g	=	gas void fraction
E_l	=	liquid holdup

218

e = internal energy per unit of mass

g = acceleration of gravity, ft/sec^2

g_c = unit conversion factor, 32.17 lbm ft/(lb$_f$ sec^2)

g_e = geothermal gradient, °F/100ft

h = formation thickness, ft

h = convective heat transfer coefficient, BTU/hr-ft^2-°F

k = formation permeability, md

k = thermal conductivity, BTU/hr-ft^2-°F

K_1 = modified Bessel function of the second kind of order one

K_o = modified Bessel function of the second kind of order zero

L = well vertical depth, 100 ft

n = time step

N_{gr} = Grashof Number

N_{pr} = Prandtl Number

N_{re} = Reynolds Number

p = pressure, psia

p_b = bubble point pressure, psia

p_i = initial reservoir pressure, psia

p_{cD} = dimensionless wellbore pressure for constant sandface rate

production with $s = 0$

$\bar{p}_{cD}$ = Laplace transform of p_{cD}

p_{sc} = pressure at standard conditions 14.7 psia

p_{wcD} = dimensionless wellbore pressure for constant sandface rate production

p_{wf} = wellbore flowing pressure, psia

$p_{wf,s}$ = wellbore pressure at the instant of shut-in, psia

p_{wh} = wellhead pressure, psia

p_{ws} = wellbore buildup pressure, psia

p_{wsD} = dimensionless buildup pressure

q = sandface production rate, RB/D

q = heat flow, BTU/hr

$\hat{q}$ = heat flux, BTU/hr-ft^2

q_g = in-situ gas flow rate, ft^3/sec

q_{ginj} = gas injection rate, scf/D

q_{gs} = gas component production rate at standard conditions, scf/D

q_{os} = oil component production rate at standard conditions, STB/D

q_l = liquid in-situ flow rate, ft^3/sec

q_{sf} = sandface production rate after shut-in, RB/D

r_w = wellbore radius, ft

R = total gas-oil ratio, scf/STB

R_s = solution gas-oil ratio, scf/STB

s = skin factor

t = time, hours

t_p = producing time, hours

t_{pD} = dimensionless producing time

t_D = dimensionless time

T = total simulation time

T = temperature, °F

T_D = dimensionless temperature

T_{sc} = temperature at standard conditions, 60°F

T_w = wellbore temperature, °R

u = Laplace transform variable

U = combined heat transfer coefficient, BTU/hr-°F

U_o = overall heat transfer coefficient, BTU/hr-ft-°F

v_g = gas true velocity, ft/sec

v_l = liquid true velocity, ft/sec

v_m = density averaged mixture velocity, ft/sec

v_r = relative velocity

v_{sg} = superficial gas velocity, ft/sec

v_{sl} = superficial liquid velocity, ft/sec

W = mass flow rate, $lbm/$ sec

z = coordination or gas compressibility

α = earth thermal diffusivity, ft/hr

α = changing storage time parameter, day

μ = oil viscosity at reservoir condition, cp

ϕ = formation porosity

ρ_g = density of gas, lbm/ft^3

ρ_{gl} = partial density of gas component in the liquid phase, lbm/ft^3

ρ_{gs} = gas component density at standard conditions, lbm/ft^3

ρ_l = density of liquid, lbm/ft^3

ρ_m = mixture density, lbm/ft^3

ρ_{ol} = partial density of oil component in the liquid phase, lbm/ft^3

ρ_{os} = oil component density at standard conditions, lbm/ft^3

τ_w = wall shear stress

Δt = shut-in time, hours

Δt_D = dimensionless shut-in time

ΔT = time step size, sec.

Δz = length of each control volume, ft.

ϵ = convergence tolerance

Θ = relaxation factor

σ = gas-oil surface tension, dynes/cm

σ = Stefan-Boltzmann constant

Subscripts.

cem = cement

ci = inside casing

co = outside casing

D = dimensionless

e = earth

g = gas

i	=	initial or index
ins	=	insulation
l	=	liquid
o	=	oil
p	=	production
s	=	steel
ti	=	inside tubing
to	=	outside tubing
wh	=	wellhead
wf	=	wellbore

REFERENCES

1. Fair, W. B.: "Pressure Buildup Analysis with Wellbore Phase Redistribution," Society of Petroleum Engineers Journal, 259-270, (April 1981); Trans., AIME, Vol. 271.

2. Hegeman, P. S., Hallford, D. L. and Joseph, J. A.: "Well Test Analysis with Changing Wellbore Storage," SPE Formation Evaluation, 201-207, (Sept. 1993).

3. Van Everdingen, A.F. and Hurt, W.:"The Application of Laplace Transform to Flow Problems," Trans., AIME, Vol. 186, 305-324, (1949).

4. Chatas, Angelos T:"A Practical Treatment of Non-Steady State Flow Problems in Reservoir Systems," Pet. Eng., Part 1 (May 1953), Part 2 (June 1953), Part 3 (August 1953).

5. Gladfelter, R.E., Tracy, G.W., and Wilsey, L.E.:"Selecting Wells Which Will Respond to Production Stimulation Treatment," Drill. and Prod. Prac., API 117-129. (1955).

6. Stegemeier, G. L. and Matthews, C. S.: "A Study of Anomalous Pressure Build-up Behavior," Trans., AIME, Vol. 213, 44-50, (1958).

7. Pitzer, S. C., Rice, J. D. and Thomas, C. E.: "A Comparison of Theoretical Pressure Build-up Curves with Field Curves Obtained From Bottom-Hole Shut-in Tests," Trans., AIME, Vol. 216, 416-419, (1959).

8. Thompson, L. G., Jones, J. R. and Reynolds, A. C.: "Analysis of Pressure Buildup Data Influenced by Wellbore Phase Redistribution," SPE Formation Evaluation, 435-452, (Oct. 1986).

9. Fuentes-Nucamendi, F. A. and Reynolds, A. C.: "Phase Redistribution in Pressure Buildup Tests," TUPREP Research Report 10, Vol. I, 147-190, (Nov. 1993).

10. Rushing, J.A. and Lee, W.J.:"Use of an Automatic Hystory-Matching Technique to Analyse Pressure Buildup Data Affected by Wellbore Phase Segregation: Case Histories," paper SPE 18837, SPE Production Operation Sympoium, Oklahoma City, OK., (March 13-14, 1989).

11. Olarewaju, J. S., Holditch, S. A. and Lee, W. J.: "Effects of Phase Segregation on Buildup Test Data from Gas Wells," paper SPE 19100 presented at the SPE Gas Technology Symposium, Dallas, TX., (June 7-9, 1989).

12. Olarewaju, J. S.: "Detection and Interpretation of Well Test Data Distorted by Phase Segregation," Journal of Petroleum Science and Engineering, 5, 210-212, (1990).

13. Winterfeld, P. H.: "Simulation of Pressure Buildup in a Multiphase Wellbore Reservoir System," SPE Formation Evaluation, 247-252, (June 1989).

14. Almehaideb, R. A., Aziz, K. and Pedrosa, O. A.: "A Reservoir/Wellbore Model for Multiphase Injection and Pressure Transient Analysis," paper SPE 17941 presented at the SPE middle East Oil Technical Conference and Exhibition, March 11-14, 1989, Manama, Bahrain.

15. Hasan, A. R. and Kabir, C. S.: "Modeling Changing Storage During a Shut-in Test," paper SPE 24717 presented at the 1992 Annual Technical Conference and Exhibition of the Society of Petroleum Engineers, Washington, D.C., (Oct. 4-7, 1992).

16. Hasan, A. R. and Kabir, C. S.: "A Mechanistic Approach to Understanding Wellbore Phase Redistribution," paper SPE 26483 presented at the 1993 Annual Technical Conference and Exhibition of the Society of Petroleum Engineers, Houston, Texas, (Oct. 3-6, 1993).

17. Fuentes-Nucamendi, F. A. and Reynolds, A. C.: "A Transient Wellbore Model for Simulating Pressure Buildup Data Affected by Phase Redistribution in the Wellbore," TUPREP Research Report 11, Vol. I, 154-213, (Sept. 1994).

18. Xiao, J. J. : *Wellbore Effects on Pressure Transient Analysis*, Ph.D. Dissertation, The University of Tulsa, (1993).

19. Xiao, J. J., Fuentes-N, F. A, Alhanati, F., and Reynolds, A. C.: "Modeling and Analyzing Pressure Buildup Data Affected by Phase Redistribution in the Wellbore," SPE 26965, presented at the III Latin American/Caribbean Petroleum Engineering Conference, Buenos Aires, (April 27-29, 1994).

20. Wallis, G. B.: *One-Dimensional Two-Phase Flow*, McGraw-Hill, Inc., (1969).

21. Ishii, M.: *Thermo-Fluid Dynamic Theory of Two-Phase Flow*, Eyrolles, (1975).

22. Liles, D. R. and Reed, W. H.: "A Semi-Implicit Method for Two-Phase Fluid Dynamics," Journal of Computational Physics, 26, 390-407, (1978).

23. Gokdemir, O. M.: *Transient Drift Flux Model for Wellbore*, M.S. Thesis, The University of Tulsa, (1992).

24. Scoggins, M. W. Jr.: *A Numerical Simulation Model for Transient Two-Phase Flow in a Pipeline*, Ph.D. Dissertation, The University of Tulsa, (1977).

25. Sarica, C.: *Two-Phase Flow in Low Velocity Hilly Terrain Pipelines*, Ph.D. Dissertation, The University of Tulsa, (1990).

26. Peaceman, D. W.: *Fundamentals of Numerical Reservoir Simulation*, Elsevier Scientific Publishing Company, New York, (1977).

27. Yadigaraglu, G. and Lahey, R. T. Jr.: "On the various forms of the Conservation Equations in Two- Phase Flow," Int. J. Multiphase Flow, Vol. 2, 477-494, (1976).

28. Allison, C. M., and Johnson, E. C. : "SCDAP/RELAP5/MOD2 Code Manual," NUREG/CR-5273, U.S. Nuclear Regulatory Commission, Washington, D.C.

29. Lockhart, R. W., and Martinelli, R. C.: "Proposed Correlation of Data for Isothermal Two-Phase Two- Component Flow in Pipes," ASME J. Energy Resources Tech., vol. 109, 206-213, (1987).

30. Brill, J. P. and Beggs, H. D. : *Two-Phase Flow in Pipes*, The University of Tulsa, (1991).

31. Zigrang, D. and Sylvester, N. D.: "Explicit Approximation to the Solution of Colebrook's Friction Factor Equation," AICHE J., Vol. 28, 514, (1982).

32. Ramey, H.J., Jr.:"Wellbore Heat Transmission," Journal of Petroleum Technology, 427-435, (April 1962); Trans., AIME, Vol. 225.

33. Alves, I.N., Alhanati, F.J.S., Shoham, O.:"A Unified Model for Predicting Flowing Temperature Distribution in Wellbores and Pipelines," SPE Production Engineering, 363-367, (November 1992).

34. Brodkey, R.S. and Hershey, H. C.:*Transport Phenomena, A Unified Approach*, McGraw-Hill Book Company, (1988).

35. Sleicher, C. A. and Rouse, M. W. : "A Convenient Correlation for Heat Transfer to Constant and Variable Property Fluid in Turbulent Pipe Flow," Int. J. Heat and Mass Transfer, Vol. 18, 677, (1975).

36. Roshsenow, W. M., Hartnett, J. P., Ganic, E. N.:*Hadbook of Heat Transfer Fundamentals*, MacGraw-Hill Book Company, (1985).

37. Jakob, M.:*Heat Transfer*, Vol I, John Wiley & Sons, Inc., New York, (1949).

38. Sieder, E.N. and Tate, G.E.:"Heat Transfer and Pressure Drop of Liquids in Tubes," Ind. Eng. Chem., Vol. 28, 1429-1435, (1936).

39. Sellars, J. R., Tribus, M. and Klein, J. S. :"Heat Transfer to Laminar Flow in a Round Tube or a Flat Conduit-The Graetz Problem Extended," Trans. ASME, Vol. 78, 441, (1956).

40. Hausen, H. :"Darstellung des Warmenberganges in Rohren durch verallgemeinerte Potenzbeziehungen," Zeit. V.D.I. Beihefte Verfahrenstechnik, Vol. 4, 91, (1943).

41. Withaker, Stephen: *Fundamentals Principles of Heat Transfer*, Pergamon Press Inc, New York, (1977).

42. Dropkin, D. and Sommerscales, E.:"Heat Transfer by Natural Convection in Liquids Confines by Two Parallel Plates Inclined at Various Angles with Respect to the Horizontal," J. of Heat Transfer; Trans. ASME, Series C, Vol. 87, 77-84, (Feb. 1965).

43. Willhite, G. P.:"Over-all Heat Transfer Coefficients in Steam and Hot Water Injection Wells," J. of Petroleum Technology, 607-615, (May 1967).

44. Globe, S. and Dropkin, D. :"Natural Convection Heat Transfer in Liquids Confined by Two Horizontal Plates and Heated from Below," Trans. ASME, Vol 81, 24-28, (1959).

45. Evans, L.B. and Stefany, N.E.:"An Experimental Study of Transient Heat Transfer to Liquids in Cylindrical Enclosures," AIChE Heat Transfer Conference, Los Angeles, (August 1965).

46. Kreith, Frank: *Principles of Heat Transfer*, Intext Educational Publishers, New York, (1973).

47. Ansari, A. M.: *A Comprehensive Mechanistic Model for Upward Two-Phase Flow*, MS Thesis, The University of Tulsa, (1988).

48. Hsu, Y.Y.:"Codes and Two-Phase Flow Transfer Calculations," in *Thermohydraulics of Two Phase Flow Systems for Industrial Design and Nuclear Engineering*, edited by Delhaye, J. M., Giot, M. and Reithmuller, M. L., McGraw-Hill, (1981).

49. Capucci, E. C. and Serra, K. V.: "Transient Aspects of Unloading Oil Wells Through Gas-lift Valves," SPE 22791 presented at the 1991 SPE Annual Technical Conference and Exhibition, Dallas, TX, (Oct. 6-9, 1991).

50. Roadifer, Randahl D.: Analysis of Well Test Data From a Restricted-Entry Well Under Mulphase Flow Conditions, Ph.D. Dissertation, The University of Tulsa, Tulsa, OK. (1995).

51. Patankar, S. V.: *Numerical Heat Transfer and Fluid Flow*, Hemisphere Publishing Corporation, (1980).

52. Alhanati, F.: *Bottomhole Gas Separation Efficiency in Electrical Submergible Pump Installation*, Ph.D. Dissertation, The University of Tulsa, (1993).

53. Carver, M. B.: "A Method of Limiting Intermediate Values of Volume Fraction in Iterative Two-Fluid Computations," *J. Mechanical Engineering Science*, Vol. 24, 4, 221-224, (1982).

54. Mahaffy, J. H.: "A Stability Enhancing Two-Step Method for Fluid Flow Calculations," F. Computational Physics, 46, 329-341, (1982).

55. Burden, R.L., Faires, J.D. and Reynolds, A.C.:*Numerical Analysis*, Prindle, Weber and Schmidt, (1978).

56. Xiao, J. J. and Reynolds, A. C.: "New Methods for the Analysis of Closed Chamber Tests," SPE 24059 presented at 1992 Western Regional Meeting, Bakersfield, California, (March 30-April 1, 1992).

57. Agarwal, R. G., Al-Hussainy, R. and Ramey, H. J.:"An Investigation of Wellbore Storage and Skin Effects in Unsteady Liquid Flow," SPEJ, 278-290, (Sept. 1970).

58. Mattar, L. "Critical Evaluation and Processing of Data Prior to Pressure Transient Analysis," SPE 24729 presented at the 1992 SPE Annual Technical Conference and Exhibition, Washington, (Oct. 4-7, 1992).

59. Kazemi, H. et al.:"Complexities of the Analysis of Surface Shut-in Drillstem Tests in an Offshore Volatile Oil Reservoir," J. of Petroleum Technology, 173-177, (January 1983).

60. Carvalho, R. and Thompson, L.:"TUPREP Nonlinear Regression Program for Analysis of Well Test Data," TUPREP Research Report 12, 380-390, (May. 1995).

61. Carvalho, R.: *Nonlinear Regression: Application to Well Test Analysis*, Ph.D. Dissertation, The University of Tulsa, (1993).

62. Miller, C. W.:"Wellbore Storage Effects in Geothermal Wells," SPEJ, 555-566, (Dec. 1980.)

63. Perrine, R.L.:"Analysis of Pressure Buildup Curves," Drill. and Prod. Prac., API, 482-509, (1956).

64. Martin, J.C.:"Simplified Equations of Flow in Gas Drive Reservoirs and the Theoretical Foundation of Multiphase Pressure Buildup Analysis," J. Pet. Tech., 321-323, (Oct. 1959).

65. Chu, W.C, Reynolds, A.C. and Raghavan, R.:"Pressure Transient Well-Test Analysis of Two-Phase Flow Problems," SPE Form. Eval., 151-164, (April 1986).

66. Chu, W.C. *Well Test Analysis for Two-Phase Flow,* Ph.D. dissertation, U. of Tulsa, Tulsa, OK (1981).

67. Milne-Thompson, L. M. : *Theoretical Hydrodynamics,* Chapter II, The Macmillan Company, New York, 1960.

68. Pauchon, C. and S. Banerjee: "Interphase Momentum Interaction Effects in the Averaged Multifield Model," Int. J. Multiphase Flow, vol. 12, No. 4, 559-573, 1986.

69. Hetsroni, Gad: *Handbook of Multiphase Systems,* Hemisphere Publishing Corporation, 1982.

70. Bird, R.B., Stewart, W.E. and Lightfoot, E.N: *Transport Phenomena,* Wiley, New York, 1960.

71. Delhaye, J. M.: "Jump Conditions and Entropy Sources in Two-Phase Systems," Int. J. Multiphase Flow, vol. I, 395-409, 1974.

72. Delhaye, J. M. and Achard, J.L.: "On the Averaging Operations introduced in Two-Phase Flow Modelling," Proc. 1st OECD/NEA Specialists Meeting on Transient Two-Phase Flow, Toronto, vol. I, 5-84, 1976.

73. Davidson, G.W., Seaton M.A. and Simpson, J.: *The Wordsworth Concise English Dictionary,* Wordsworth Editions Ltd., London, U.K., 1994.

74. Shoup, T. E. and Mistree, F.: *Optimization Methods with Applications for Personal Computers,* Prentice-Hall Inc, New Jersey, 1987.

75. Rowan, Thomas Harvey: Functional Stability Analysis of Numerical Algorithms, Ph.D. Dissertation, Department of Computer Sciences, University of Texas at Austin, Austin, Texas, 1990.

76. Fletcher, R.: *Optimization,* Academic Press, London, 1987.

77. Spendley, W., Hest, G. R. and Himsworth, F. R.: "Sequential Applications of Simplex Designs in Optimization and Evolutionary Operations," Technometrics, vol. 4, 441-461, 1962

78. Nelder, J. A. and Mead, R.: "An Simplex Method for Function Minimization," Computer Journal, vol. 7, 308-313, 1964.

79. Box, M. J.: "A New Method for Constrained Optimization and a Comparison with other Methods," Computer Journal, vol. 8, 42-52, 1965.

80. Ward, L., Nag, A. and Dixon, L. C. W.:"Hill-Climbing Techniques as a Method of Calculating the Optical Constants and Thickness of a Thin Metallic Film," Brit. J. Appl. Phys., Ser. 2, vol 2, 301-304, 1969.

81. Dambrauskas, A. P.: "The Simplex Optimization Method with Variable Step," Eng. Cybern., vol. 8, 28-36, 1970.

82. Dambrauskas, A. P.:"Investigation of the Efficiency of the Simplex Method of Optimization with Variable Step in a Noise Function," Eng. Cybern., vol. 10, 590-599, 1972.

83. Box, M. J.:"A Comparison of Several Current Optimization Methods, and the use of Transformations in Constrained Problems," Computer Journal, vol. 9, 67-77, 1966.

APPENDIX A

AVERAGED AND LOCAL INSTANTANEOUS FORMULATIONS.

Consider a fixed tube with axis Oz (unit vector $\mathbf{n}_z$) in which a volume, V_k^*, of a certain phase k, is cut by two cross-sectional planes separated by a distance Z (Z can be arbitrarily small), see Fig. A.1. Let V_k be the volume limited by A_{k1}, A_{k2}, that define the two cross-sectional planes, and the portions A_i and A_{kw}, that define the phase-k surface interface and the wall enclosed between the two cross-sectional planes. Consider the unit vector normal to the interface and directed away from phase-k,where this normal vector is denoted by $\mathbf{n}_k$. The cross-sectional planes limiting the volume V_k are not necessarily fixed and their speeds of displacement are denoted by $(-v_{Ak1} \cdot \mathbf{n}_z)$ and $(-v_{Ak2} \cdot \mathbf{n}_z)$. To derive the volume averaged form of the conservation equations, we will use Gauss' theorem (divergence theorem) and Leibnitz's rule (Reynolds transport theorem). The distance Z shown in Fig. A.1 can be as small as desired, so we essentially average over a slice.

Consider a control volume $V(t)$, moving in space (Fig. A.2) and bounded by a closed surface $A(t)$. At a certain point in this surface, $\mathbf{n}$ represents a unit outward normal vector; the speed of the surface at that point is $\mathbf{v}_A \cdot \mathbf{n}$. Leibnitz's rule applied to on function f on volume $V(t)$ gives

$$\frac{\partial}{\partial t} \int_{V(t)} f(x,y,z,t) \, dV = \int_{V(t)} \frac{\partial f}{\partial t} \, dV + \oint_{A(t)} f \, \mathbf{v}_A \cdot \mathbf{n} \, dA, \qquad (A.1)$$

235
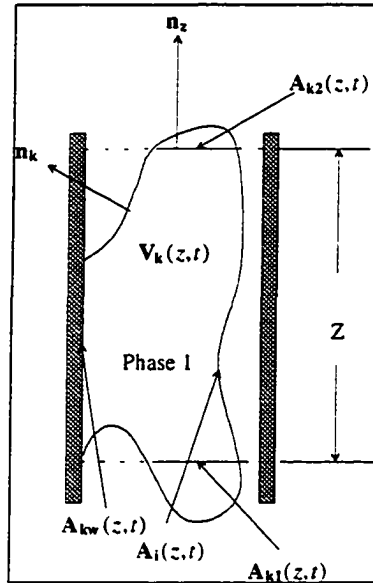
Figure A.1: Control Volume

where v_A represents the speed of the surface A.

Assuming that our control volume V_k (Fig. A.2) moves only in the z-direction, Eq. A.1 becomes

$$\frac{\partial}{\partial t} \int_{V_k(z,t)} f(x,y,z,t) \, dV \quad = \quad \int_{V_k(z,t)} \frac{\partial f}{\partial t} \, dV + \int_{A_i(z,t)} f \, \mathbf{v}_i \cdot \mathbf{n}_k \, dA \qquad (A.2)$$

$$+ \quad \int_{A_{k_1}(z,t)} f \, \mathbf{v}_{Ak1} \cdot \mathbf{n}_z \, dA + \int_{A_{k_2}(z,t)} f \, \mathbf{v}_{Ak2} \cdot \mathbf{n}_z \, dA,$$

where $\mathbf{v}_i$ is the velocity of the interface, $\mathbf{v}_{Ak1}$ is the velocity of the lower cross-sectional area, $\mathbf{v}_{Ak2}$ is the velocity of the upper cross-sectional area.

If the cross-sectional planes are fixed,

$$\frac{\partial}{\partial t} \int_{V_k(z,t)} f(x,y,z,t) \, dV = \int_{V_k(z,t)} \frac{\partial f}{\partial t} \, dV + \int_{A_i(z,t)} f \, \mathbf{v}_i \cdot \mathbf{n}_k \, dA. \qquad (A.3)$$

Gauss' theorem applied to volume V_k leads to

$$\int_{V_k(z,t)} \nabla \cdot \mathbf{C}\, dV = \int_{A_i(z,t)} \mathbf{C} \cdot \mathbf{n}_k\, dA + \int_{A_{kw}(z,t)} \mathbf{C} \cdot \mathbf{n}_k\, dA \qquad (A.4)$$

$$- \int_{A_{k1}(z,t)} \mathbf{C} \cdot \mathbf{n}_z\, dA + \int_{A_{k2}(z,t)} \mathbf{C} \cdot \mathbf{n}_z\, dA,$$

considering the definition of volume integral (see Milne-Thompson[67], Pauchon and Banerjee[68])

$$\frac{\partial}{\partial z} \int_{V_k(z,t)} C_z\, dV = \frac{\partial}{\partial z} \int_{z-Z/2}^{z+Z/2} \left(\int_{A_k(\tilde{z})} C_z\, dS \right) d\tilde{z} \qquad (A.5)$$

where $C_z = \mathbf{C} \cdot \mathbf{n}_z$. Noting that

$$\frac{d}{d\sigma} \int_{a(\sigma)}^{b(\sigma)} f(r)\, dr = b'(\sigma)\, f[b(\sigma)] - a'(\sigma)\, f[a(\sigma)], \qquad (A.6)$$

we have

$$\frac{\partial}{\partial z} \int_{V_k(z,t)} \mathbf{C} \cdot \mathbf{n}_z\, dV = \int_{A_{k2}(z,t)} \mathbf{C} \cdot \mathbf{n}_z\, dA - \int_{A_{k1}(z,t)} \mathbf{C} \cdot \mathbf{n}_z\, dA, \qquad (A.7)$$

Using Eq. A.7 in Eq. A.4, it follows that

$$\int_{V_k(z,t)} \nabla \cdot \mathbf{C}\, dV = \frac{\partial}{\partial z} \int_{V_k(z,t)} \mathbf{C} \cdot \mathbf{n}_z\, dV + \int_{A_i(z,t)} \mathbf{C} \cdot \mathbf{n}_k\, dA + \int_{A_{kw}(z,t)} \mathbf{C} \cdot \mathbf{n}_k\, dA.$$

or

$$\int_{V_k(z,t)} \nabla \cdot \mathbf{C}\, dV = \frac{\partial}{\partial z} \int_{V_k(z,t)} \mathbf{C} \cdot \mathbf{n}_z\, dV + \int_{A_i(z,t)+A_{kw}(z,t)} \mathbf{C} \cdot \mathbf{n}_k\, dA, \qquad (A.8)$$

which is equivalent to

$$\int_{V_k(z,t)} \nabla \cdot \mathbf{C}\, dV = \frac{\partial}{\partial z} \int_{V_k(z,t)} C_z\, dV + \int_{A_i(z,t)+A_{kw}(z,t)} \mathbf{C} \cdot \mathbf{n}_k\, dA, \qquad (A.9)$$
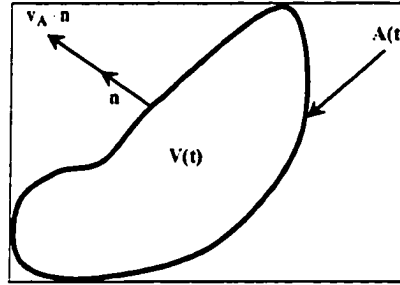
Figure A.2: Control volume moving in space.

where C_z is the z-direction component of $\mathbf{C}$.

For a tensor field, we have (Hetsroni[69])

$$\int_{V_k(z,t)} \nabla \cdot \bar{\bar{\mathbf{C}}}\, dV = \frac{\partial}{\partial z} \int_{V_k(z,t)} \mathbf{n}_z \cdot \bar{\bar{\mathbf{C}}}\, dV + \int_{A_i(z,t)+A_{kw}(z,t)} \mathbf{n}_k \cdot \bar{\bar{\mathbf{C}}}\, dA. \qquad (A.10)$$

We define averages as in Pauchon and Barnerjee[68], i.e.,

$$< f_k > = \frac{1}{V_k} \int_{V_k} f_k\, dV, \qquad (A.11)$$

and

$$< f_k >_i = \frac{1}{V} \int_{A_i} f_k\, dA, \qquad (A.12)$$

where $V = \sum V_k$.

A.1   General Conservation Equation.

Consider $\rho_k \psi_k$ as the quantity that is conserved in the k-th phase, with $\mathbf{j}_k$ and $\hat{S}_k$ respectively, representing the flux and source terms of ψ_k. In our control volume V_k, it is possible to write a general conservation equation as

$$\left\{ \begin{array}{c} \text{Rate of Accumulation} \\ \text{of Quantity} \end{array} \right\} = \left\{ \begin{array}{c} \text{Rate of} \\ \text{Quantity in} \end{array} \right\} - \left\{ \begin{array}{c} \text{Rate of} \\ \text{Quantity out} \end{array} \right\}$$

$$+ \left\{ \begin{array}{c} \text{Rate of} \\ \text{Quantity Generated} \end{array} \right\} \quad (A.13)$$

which gives

$$\frac{\partial \rho_k \psi_k}{\partial t} + \nabla \cdot \rho_k \psi_k \mathbf{v}_k + \nabla \cdot \mathbf{j}_k - \rho_k \hat{S}_k = 0. \quad (A.14)$$

Each term of the general conservation equation can be volume averaged. Using Eqs. A.3 and A.9 on each term of Eq. A.14 , it follows that

$$\int_{V_k} \frac{\partial \rho_k \psi_k}{\partial t} \, dV = \frac{\partial}{\partial t} \int_{V_k} \rho_k \psi_k \, dV - \int_{A_i} \rho_k \psi_k (\mathbf{v}_i \cdot \mathbf{n}_k) \, dA, \quad (A.15)$$

and

$$\int_{V_k} \nabla \cdot (\rho_k \psi_k \mathbf{v}_k + \mathbf{j}_k) \, dV = \frac{\partial}{\partial z} \int_{V_k} \mathbf{n}_z \cdot (\rho_k \psi_k \mathbf{v}_k + \mathbf{j}_k) \, dV$$

$$+ \int_{A_i + A_{kw}} \mathbf{n}_k \cdot (\rho_k \psi_k \mathbf{v}_k + \mathbf{j}_k) \, dA. \quad (A.16)$$

Integrating Eq. A.14 over V_k and using Eqs. A.15 and A.16 in the resulting equation gives

$$\frac{\partial}{\partial t} \int_{V_k} \rho_k \psi_k \, dV - \int_{A_i} \rho_k \psi_k (\mathbf{v}_i \cdot \mathbf{n}_k) \, dA + \frac{\partial}{\partial z} \int_{V_k} \mathbf{n}_z \cdot (\rho_k \psi_k \mathbf{v}_k + \mathbf{j}_k) \, dV$$

$$+ \int_{A_i + A_{kw}} \mathbf{n}_k \cdot (\rho_k \psi_k \mathbf{v}_k + \mathbf{j}_k) \, dA - \int_{V_k} \rho_k \hat{S}_k \, dV = 0 \quad (A.17)$$

At the pipe wall (A_{kw}) $v_k = 0$ (see Bird et al.[70]). By collecting terms, we can rewrite Eq. A.17 as

$$\frac{\partial}{\partial t} \int_{V_k} \rho_k \psi_k \, dV + \frac{\partial}{\partial z} \int_{V_k} \mathbf{n}_z \cdot (\rho_k \psi_k \mathbf{v}_k + \mathbf{j}_k) \, dV - \int_{V_k} \rho_k \hat{S}_k \, dV =$$
$$- \int_{A_i} [\rho_k \psi_k \mathbf{n}_k \cdot (\mathbf{v}_k - \mathbf{v}_i) + \mathbf{n}_k \cdot \mathbf{j}_k] \, dA - \int_{A_{kw}} \mathbf{n}_{kw} \cdot \mathbf{j}_k \, dA. \qquad (A.18)$$

The void fraction, E_k, is defined as

$$E_k = \frac{1}{V} \int_{V_k} dV. \qquad (A.19)$$

Using Eqs. A.11 and A.12 and A.19 in Eq. A.18, we have

$$\frac{\partial}{\partial t} E_k \; < \; \rho_k \psi_k > + \frac{\partial}{\partial z} E_k < \mathbf{n}_z \cdot (\rho_k \psi_k \mathbf{v}_k + \mathbf{j}_k) > -E_k < \rho_k \hat{S}_k >$$
$$= \; -\frac{1}{V} \int_{A_i} (\dot{m}_k \psi_k + \mathbf{j}_k \cdot \mathbf{n}_k) \, dA - \frac{1}{V} \int_{A_{kw}} \mathbf{n}_{kw} \cdot \mathbf{j}_k \, dA, \qquad (A.20)$$

where the interphase mass transfer is defined as

$$\dot{m}_k = \rho_k \mathbf{n}_k \cdot (\mathbf{v}_k - \mathbf{v}_i). \qquad (A.21)$$

The general form of the conservation equation is represented by Eq. A.20, and can be used to derived continuity, momentum and energy equations for each phase.

A.3   Continuity Equation.

For our control volume V_k, we can establish our mass balance for a k-th phase as

$$\left\{ \begin{array}{c} Rate\ of \\ Accumulation\ of \\ k\text{-}th\ phase \end{array} \right\} = \left\{ \begin{array}{c} Rate\ of \\ k\text{-}th\ phase \\ in \end{array} \right\} - \left\{ \begin{array}{c} Rate\ of \\ k\text{-}th\ phase \\ out \end{array} \right\} \qquad (A.22)$$

$$+ \left\{ \begin{array}{c} Rate\ of \\ k\text{-}th\ phase \\ from\ intephase\ mass\ transfer \end{array} \right\}$$

For the continuity equation, we set $\psi_k = 1$, $j_k = 0$ and $\hat{S}_k = 0$, so Eq. A.20 becomes

$$\frac{\partial}{\partial t}(E_k < \rho_k >) + \frac{\partial}{\partial z}(E_k < \mathbf{n}_z \cdot (\rho_k \mathbf{v}_k) >) = -\frac{1}{V} \int_{A_i} \dot{m}_k\ dA. \qquad (A.23)$$

From Eq. A.12,

$$- < \dot{m}_k >_i = -\frac{1}{V} \int_{A_i} \dot{m}_k\ dA, \qquad (A.24)$$

hence, Eq. A.23 can be written as

$$\frac{\partial}{\partial t}(E_k < \rho_k >) + \frac{\partial}{\partial z}(E_k < \mathbf{n}_z \cdot (\rho_k \mathbf{v}_k) >) = - < \dot{m}_k >_i = \Gamma_{mk}, \qquad (A.25)$$

where Γ_{mk} represents the volume averaged interphase mass transfer rate and is defined by Eq. A.24. Thus, the final form of the continuity equation is

$$\frac{\partial}{\partial t}(E_k < \rho_k >) + \frac{\partial}{\partial z}(E_k < \rho_k v_k >) = \Gamma_{mk}. \qquad (A.26)$$

A.3   Momentum Equation.

For the control volume V_k, we write our momentum balance as

$$
\left\{ \begin{array}{c} Rate\ of \\ Accumulation\ of \\ Momentum \end{array} \right\} = \left\{ \begin{array}{c} Rate\ of \\ Momentum \\ in \end{array} \right\} - \left\{ \begin{array}{c} Rate\ of \\ Momentum \\ out \end{array} \right\} + \left\{ \begin{array}{c} Sum\ of \\ forces\ acting \\ on\ phase\ k \end{array} \right\}
$$

(A.27)

where the forces acting on phase k-th are defined as

$$
\left\{ \begin{array}{c} Sum\ of \\ forces\ acting \\ on\ phase\ k \end{array} \right\} = \left\{ \begin{array}{c} Surface \\ forces \end{array} \right\} + \left\{ \begin{array}{c} Body \\ Forces \end{array} \right\}.
$$

(A.28)

The body forces can be classified as gravitational, electrostatic and contact forces. If we denote the body force vector per unit mass as $\hat{S}_k = \mathbf{F}_k$, we can express the body forces acting on the body, relative to the last term on Eq. A.17, as

$$
\left\{ \begin{array}{c} Body \\ Forces \end{array} \right\} = \int_{V_k} \rho_k \hat{S}_k\ dV = \int_{V_k} \rho_k \mathbf{F}_k\ dV.
$$

(A.29)

In the case of surface forces, a stress vector is defined by

$$
\mathbf{j}_{(n_k)} = \frac{d\mathbf{F}}{d\mathbf{A}},
$$

(A.30)

The subscript n_k indicated that the stress vector depends on the unit outward normal vector n_k, in addition to being function of time and space[69]. The simplest form of

the stress tensor is founded in hydrostatics, where for a single phase $\mathbf{j}_{(n)}$ is defined as

$$\mathbf{j}_{(n)} = -p\,\mathbf{n} \quad \text{static fluids,} \tag{A.31}$$

Indicating that the pressure always acts normal to the surface and is opposite in direction to the unit normal vector. The stress vector can be represented in terms of the stress tensor by the following expression

$$\mathbf{j}_{(n_k)} = \bar{\bar{\mathbf{j}}}_{(n_k)} \cdot \mathbf{n}_k. \tag{A.32}$$

The stress vector represents the vector force per unit area exerted by the phase into which $\mathbf{n}_k$ points on the phase for which $\mathbf{n}_k$ is the outwardly directed unit normal vector. We have

$$\left\{ \begin{array}{c} Surface \\ \\ Forces \end{array} \right\} = + \int_{A_i + A_{kw}} \mathbf{n}_k \cdot \bar{\bar{\mathbf{j}}}_k \; dA. \tag{A.33}$$

In Eq. A.20, we now set $\psi_k = \mathbf{v}_k, \bar{\bar{\mathbf{j}}}_k = p_k\bar{\bar{\mathbf{I}}} - \bar{\bar{\tau}}_k$, and $\hat{S}_k = \mathbf{F}_k$. The pressure p_k is defined in terms of thermodynamics quantities, and for this reason, is referred as a thermodynamic stress. The tensor $\bar{\bar{\tau}}$ is referred as a stress tensor, or in our case as a viscous stress tensor. The unit stress tensor is designed as $\bar{\bar{\mathbf{I}}}$. With this notation, Eq. A.20 becomes

$$\frac{\partial}{\partial t}E_k < \rho_k\mathbf{v}_k > + \frac{\partial}{\partial z}E_k < \mathbf{n}_z \cdot (\rho_k\mathbf{v}_k\mathbf{v}_k) > \quad + \frac{\partial}{\partial z}E_k < \mathbf{n}_z \cdot p_k\bar{\bar{\mathbf{I}}} >$$

$$- \frac{\partial}{\partial z}E_k < \mathbf{n}_z \cdot \bar{\bar{\tau}}_k > - E_k < \rho_k\mathbf{F}_k >$$

$$= -\frac{1}{V} \int_{A_i} \left[\dot{m}_k\mathbf{v}_k + p_k\bar{\bar{\mathbf{I}}} \cdot \mathbf{n}_k - \bar{\bar{\tau}}_k \cdot \mathbf{n}_k \right] dA$$

$$-\frac{1}{V}\int_{A_{kw}} \mathbf{n}_{kw} \cdot (p_k\bar{\bar{\mathbf{I}}} - \bar{\bar{\tau}}_k)\, dA\,. \tag{A.34}$$

By taking the dot product in the general conservation equation, Eq. A.34, with the unit direction vector $\mathbf{n}_z$, we can obtain the equation for conservation of momentum in the z—direction.

Recalling that, when a tensor is dotted with a vector, we get a vector[70]. If $\bar{\bar{\mathbf{f}}}$ is a tensor and $\mathbf{g}$ is vector then $[\bar{\bar{\mathbf{f}}} \cdot \mathbf{g}]$ differs from $\mathbf{g}$ in both length and direction; that is, the tensor $\bar{\bar{\mathbf{f}}}$ "deflects" or "twists" the vector $\mathbf{g}$ to form a new vector pointing in a different direction. In this case the direction is controlled by the unit z direction vector $\mathbf{n}_z$. Additionally, we assume no area change, so $\mathbf{n}_{kw} \cdot \mathbf{n}_z p_k = 0$, since $\mathbf{n}_{kw} \cdot \mathbf{n}_z = 0$. The unit tensor $\bar{\bar{\mathbf{I}}}$ has the property that

$$\mathbf{g}\cdot\bar{\bar{\mathbf{I}}} = \bar{\bar{\mathbf{I}}}\cdot\mathbf{g} = \mathbf{g}, \tag{A.35}$$

and

$$\mathbf{n}_z \cdot \left[\mathbf{n}_z \cdot (p_k\bar{\bar{\mathbf{I}}} - \bar{\bar{\tau}}_k)\right] = p_k - \mathbf{n}_z \cdot (\mathbf{n}_z \cdot \bar{\bar{\tau}}_k)\,, \tag{A.36}$$

$$\mathbf{n}_z \cdot \mathbf{v}_k = v_k, \tag{A.37}$$

$$\mathbf{n}_z \cdot [\mathbf{n}_z \cdot (\rho_k\mathbf{v}_k\mathbf{v}_k)] = \rho_k v_k^2, \tag{A.38}$$

$$\mathbf{n}_z \cdot \rho_k\mathbf{F}_k = \rho_k F_{z,k}. \tag{A.39}$$

By substituting Eq. A.36 to A.39 into Eq. A.34, we find

$$\frac{\partial}{\partial t}E_k < \rho_k v_k > + \frac{\partial}{\partial z}E_k < \rho_k v_k^2 > + \frac{\partial}{\partial z}E_k < p_k >$$

$$+\frac{\partial}{\partial z} E_k < \mathbf{n}_z \cdot (\mathbf{n}_z \cdot \bar{\bar{\tau}}_k) > -E_k < \rho_k F_{z,k} >$$

$$= -\frac{1}{V} \int_{A_i} [\dot{m}_k v_k + \mathbf{n}_z \cdot \mathbf{n}_k p_k - \mathbf{n}_z \cdot (\mathbf{n}_k \cdot \bar{\bar{\tau}}_k)] \, dA$$

$$+\frac{1}{V} \int_{A_{kw}} \mathbf{n}_z \cdot (\mathbf{n}_{kw} \cdot \bar{\bar{\tau}}_k) \, dA. \tag{A.40}$$

If we let Δp_{ki} denote the difference between the average interfacial pressure and average phase pressure, i.e.,

$$\Delta p_{ki} = < p_{ki} > - < p_k >, \tag{A.41}$$

and let $\Delta p'_{ki}$ be the difference between the local and average interfacial pressure. i.e.,

$$\Delta p'_{ki} = p_k - < p_{ki} > . \tag{A.42}$$

Combining Eq. A.41 and A.42, solving for p_k, we have

$$p_k = \Delta p_{ki} + < p_k > + \Delta p'_{ki}, \tag{A.43}$$

and

$$\frac{1}{V} \int_{A_i} \mathbf{n}_k \cdot (\mathbf{n}_z \, p_k) \, dA = \frac{1}{V} \int_{A_i} \mathbf{n}_k \cdot [\mathbf{n}_z (< p_k > + \Delta p_{ki})] \, dA$$

$$+\frac{1}{V} \int_{A_i} \mathbf{n}_k \cdot (\mathbf{n}_z \, \Delta p'_{ki}) \, dA. \tag{A.44}$$

Using Gauss' theorem

$$\frac{1}{V} \int_{A_i} \mathbf{n}_k \cdot [\mathbf{n}_z (< p_k > + \Delta p_{ki})] \, dA = -\frac{1}{V} \frac{\partial}{\partial z} \int_{V_k} \mathbf{n}_z \cdot \mathbf{n}_z (< p_k > + \Delta p_{ki}) \, dV$$

$$+\frac{1}{V} \int_{V_k} \nabla \cdot \mathbf{n}_z (< p_k > + \Delta p_{ki}) \, dV$$

$$= -\frac{1}{V} \frac{\partial}{\partial z} \int_{V_k} \mathbf{n}_z \cdot \mathbf{n}_z (< p_k > + \Delta p_{ki}) \, dV$$

$$+\frac{1}{V}\int_{V_k}\nabla\cdot(\mathbf{n}_z<p_{ki}>)\,dV$$

$$=\quad-\frac{1}{V}\frac{\partial}{\partial z}\int_{V_k}\mathbf{n}_z\cdot\mathbf{n}_z(<p_k>+\Delta p_{ki})\,dV.\ (A.45)$$

By substituting Eq. A.45 in Eq. A.44, we find

$$\frac{1}{V}\int_{A_i}\mathbf{n}_k\cdot(\mathbf{n}_zp_k)\,dA\ =\ -(<p_k>+\Delta p_{ki})\left[\frac{1}{V}\frac{\partial}{\partial z}\int_{V_k}dV\right]$$

$$+\frac{1}{V}\int_{A_i}\mathbf{n}_k\cdot\left(\mathbf{n}_z\Delta p'_{ki}\right)\,dA$$

$$=\ -(<p_k>+\Delta p_{ki})\frac{\partial}{\partial z}\left[\frac{1}{V}\int_{V_k}dV\right]$$

$$+\frac{1}{V}\int_{A_i}\mathbf{n}_k\cdot\left(\mathbf{n}_z\Delta p'_{ki}\right)\,dA.\qquad(A.46)$$

By definition

$$E_k=\frac{1}{V}\int_{V_k}dV.\qquad(A.47)$$

Substituting Eq. A.47 in Eq. A.46, we have

$$\frac{1}{V}\int_{A_i}\mathbf{n}_k\cdot(\mathbf{n}_zp_k)\,dA=-(<p_k>+\Delta p_{ki})\frac{\partial E_k}{\partial z}+<\mathbf{n}_k\cdot\mathbf{n}_z\Delta p'_{ki}>_i,\qquad(A.48)$$

Note that

$$[\mathbf{n}_z\cdot(\mathbf{n}_{kw}\cdot\bar{\bar{\tau}}_k)]_{A_{k,w}}=-\mathbf{n}_{kw}\cdot\tau_{z,k,w},\qquad(A.49)$$

$$[\mathbf{n}_z\cdot(\mathbf{n}_k\cdot\bar{\bar{\tau}}_k)]_{A_i}=-\mathbf{n}_k\cdot\tau_{z,k,i}.\qquad(A.50)$$

Using Eqs. A.48, A.49, A.50, A.11 and A.12 our linear momentum equation (Eq. A.40) can be written as

$$\frac{\partial}{\partial t}E_k < \rho_k v_k > + \frac{\partial}{\partial z}E_k < \rho_k v_k^2 > + E_k \frac{\partial}{\partial z} < p_k >$$

$$+ \frac{\partial}{\partial z}E_k < \tau_{zz,k} > - \Delta p_{ki}\frac{\partial}{\partial z}E_k =$$

$$E_k < \rho_k F_{z,k} > - < \dot{m}_k v_k >_i - < \mathbf{n}_k \cdot \mathbf{n}_z \Delta p'_{ki} >_i$$

$$+ < \mathbf{n}_k \cdot \mathbf{\tau}_{z,k,i} > - < \mathbf{n}_k \cdot \mathbf{\tau}_{z,k,w} > . \tag{A.51}$$

As noted by Yadigaraglu[27], Delhaye et al.[71] and Ishii[21], $\frac{\partial}{\partial z}E_k < \tau_{zz,k} >$ and $\Delta p'_{ki}$ are generally negligible compared to the other terms, thus, we neglect them We also define

$$- < \dot{m}_k >_i = \Gamma_{mk}, \tag{A.52}$$

$$< \mathbf{n}_k \cdot \mathbf{\tau}_{z,k,i} > = \tau_{z,k,i} \, S_k^i, \tag{A.53}$$

$$< \mathbf{n}_{k,w} \cdot \mathbf{\tau}_{z,k,w} > = \tau_{z,k,w} \, S_k^w, \tag{A.54}$$

and

$$< F_{z,k} > = g \sin \beta. \tag{A.55}$$

Substituting Eqs. A.52 to A.55 into Eq. A.51, the final form of our momentum equation is given by

$$\frac{\partial}{\partial t}E_k < \rho_k v_k > + \frac{\partial}{\partial z}E_k < \rho_k v_k^2 > - \Gamma_{mk} < v_{k,i} > =$$

$$- E_k \frac{\partial}{\partial z} < p_k > + < \Delta p_{ki} > \frac{\partial}{\partial z}E_k$$

$$- E_k < \rho_k > g \sin \beta + \tau_{z,k,i} S_k^i - \tau_{z,k,w} S_k^w. \tag{A.56}$$

A.4 Energy Equation

The fundamental law of conservation of energy for the fluid contained within our control volume V_k, at any given time is

$$
\left\{ \begin{array}{c} Rate\,of \\ Accumulation \\ of\ internal\ and \\ kinetic\ energy \end{array} \right\} = \left\{ \begin{array}{c} Rate\ of \\ internal\ and \\ kinetic\ energy \\ in\ by\ convection \end{array} \right\} - \left\{ \begin{array}{c} Rate\ of \\ internal\ and \\ kinetic\ energy \\ out\ by\ convection \end{array} \right\}
$$

$$
+ \left\{ \begin{array}{c} Net\ Rate\ of \\ heat\ addition \\ by\ conduction \end{array} \right\} - \left\{ \begin{array}{c} Net\ rate\ of \\ work\ done\ by \\ system\ on\ surroundings \end{array} \right\}
$$

$$
+ \left\{ \begin{array}{c} Net\ rate\ of \\ heat\ generated\ by \\ the\ system \end{array} \right\}, \tag{A.57}
$$

where the work done on phase k is defined as

$$
\left\{ \begin{array}{c} Net\ rate\ of \\ work\ done\ on \\ phase\ k \end{array} \right\} = \left\{ \begin{array}{c} Work\ done \\ by\ Surface \\ forces \end{array} \right\} + \left\{ \begin{array}{c} Work\ done \\ by\ Body \\ Forces \end{array} \right\}. \tag{A.58}
$$

The work done by the body forces is mainly due to gravitational forces and the work done by the surface forces is mainly due by pressure forces and viscous forces. This means

$$\left\{ \begin{array}{c} Work\,done \\ by\,Body \\ Forces \end{array} \right\} = \int_{V_k} \rho_k \hat{S}_k \, dV = \int_{V_k} \rho_k \left(\mathbf{F}_k \cdot \mathbf{v}_k \right) dV, \qquad (A.59)$$

and

$$\left\{ \begin{array}{c} Work\,done\,by \\ Surface \\ Forces \end{array} \right\} = + \int_{A_\iota + A_{kw}} \mathbf{n}_k \cdot \bar{\bar{\mathbf{j}}}_k \, dA = + \int_{A_\iota + A_{kw}} \left(\mathbf{n}_k \cdot \left(p_k \bar{\bar{\mathbf{I}}} - \bar{\bar{\tau}}_k \right) \right) \cdot \mathbf{v}_k \, dA.$$

$$(A.60)$$

The rate of heat transfer to the body by conduction is represented by

$$\left\{ \begin{array}{c} Net\,Rate\,of \\ heat\,addition \\ by\,conduction \end{array} \right\} = \int_{A_\iota + A_{kw}} \mathbf{n}_k \cdot \mathbf{q} \, dA, \qquad (A.61)$$

where $\mathbf{q}$ is the heat transferred per unit of volume and time,

$$\left\{ \begin{array}{c} Net\,Rate\,of \\ heat\,generated\,by \\ the\,system \end{array} \right\} = \int_{V_k} Q_k \, dV. \qquad (A.62)$$

where Q_k is the heat generated per unit of volume and time.

For the energy equation, we set

$$\psi_k = U_k = \hat{u}_k + \frac{\mathbf{v}_k \cdot \mathbf{v}_k}{2}, \qquad (A.63)$$

$$\mathbf{j}_k = \mathbf{q}_k + \left(p_k \bar{\bar{\mathbf{I}}} - \bar{\bar{\tau}}_k \right) \cdot \mathbf{v}_k, \qquad (A.64)$$

$$\hat{S}_k = \mathbf{F}_k \cdot \mathbf{v}_k + Q_k, \tag{A.65}$$

where the pressure p_k is defined in terms of thermodynamics quantities, the tensor $\bar{\bar{\tau}}_k$ is defined as a viscous stress tensor and $\hat{u}_k$ is the specific internal energy. U_k is the total energy (internal plus kinetic). Substituting Eqs. A.63 and A.65 into Eq. A.20, we have

$$\frac{\partial}{\partial t} E_k < \rho_k U_k > + \frac{\partial}{\partial z} E_k < \rho_k U_k v_k > + \frac{\partial}{\partial z} E_k < q_{z,k} >$$
$$+ \frac{\partial}{\partial z} E_k < \mathbf{n}_z \cdot (p_k \bar{\bar{\mathbf{I}}} \cdot \mathbf{v}_k) > - \frac{\partial}{\partial z} E_k < \mathbf{n}_z \cdot (\bar{\bar{\tau}}_k \cdot \mathbf{v}_k) > - E_k < \rho_k (\mathbf{F}_k \cdot \mathbf{v}_k + Q_k >$$
$$= -\frac{1}{V} \int_{A_i} [\dot{m}_k U_k + \mathbf{q}_k \cdot \mathbf{n}_k + p_k \mathbf{v}_k \cdot \mathbf{n}_k - \bar{\bar{\tau}}_k \cdot \mathbf{n}_k] \, dA$$
$$-\frac{1}{V} \int_{A_{kw}} \mathbf{n}_{kw} \cdot \mathbf{q}_k \, dA, \tag{A.66}$$

where $q_{z,k}$ is the heat transferred by phase k in the z direction. From the definition of the interphase mass transfer, Eq. A.21

$$\dot{m}_k = \rho_k \mathbf{n}_k \cdot (\mathbf{v}_k - \mathbf{v}_i), \tag{A.21}$$

we find that

$$\mathbf{n}_k \cdot p_k \mathbf{v}_k = \frac{p_k}{\rho_k} \{\rho_k \mathbf{n}_k \cdot (\mathbf{v}_k - \mathbf{v}_i)\} + p_k \mathbf{n}_k \cdot \mathbf{v}_i$$
$$= \dot{m}_k \frac{p_k}{\rho_k} + p_k \mathbf{v}_i \cdot \mathbf{n}_k. \tag{A.67}$$

Using Eq. A.67, we can show that

$$\frac{1}{V} \int_{A_i} [\dot{m}_k U_k + p_k \mathbf{v}_k \cdot \mathbf{n}_k] \, dA = \frac{1}{V} \int_{A_i} \left[\dot{m}_k U_k + \dot{m}_k \frac{p_k}{\rho_k} + p_k \mathbf{v}_i \cdot \mathbf{n}_k\right] \, dA, \tag{A.68}$$

from Eq. A.43

$$p_k = \Delta p_{ki} + < p_k > + \Delta p'_{ki}, \tag{A.69}$$

so we can write the last term in Eq. A.68 as

$$\frac{1}{V}\int_{A_\imath} p_k \mathbf{v}_i \cdot \mathbf{n}_k \, dA = \frac{1}{V}\int_{A_\imath} \mathbf{n}_k \cdot [\mathbf{v}_i(<p_k> +\Delta p_{ki})] \, dA$$
$$+\frac{1}{V}\int_{A_\imath} \mathbf{n}_k \cdot \left(\mathbf{v}_i\Delta p'_{ki}\right) dA. \qquad (A.70)$$

Using Leibnitz's rule and definitions of average, we find

$$\frac{1}{V}\int_{A_\imath} p_k \mathbf{n}_k \cdot \mathbf{v}_i \, dA = (<p_k> +\Delta p_{ki})\left[\frac{1}{V}\frac{\partial}{\partial t}\int_{V_k} dV\right]$$
$$+\frac{1}{V}\int_{A_\imath} \mathbf{n}_k \cdot \left(\mathbf{v}_i\Delta p'_{ki}\right) dA, \qquad (A.71)$$

since

$$E_k = \frac{1}{V}\int_{V_k} dV, \qquad (A.72)$$

we can rewrite Eq. A.71 as

$$\frac{1}{V}\int_{A_\imath} p_k \mathbf{n}_k \cdot \mathbf{v}_i \, dA = (<p_k> +\Delta p_{ki})\frac{\partial E_k}{\partial t} + <\mathbf{n}_k \cdot \mathbf{v}_i\Delta p'_{ki}> . \qquad (A.73)$$

Substituting Eqs. A.68 and A.73 into Eq. A.66, and assuming that the flow is mainly in the z−direction, we have

$$\frac{\partial}{\partial t}E_k <\rho_k U_k> +\frac{\partial}{\partial z}E_k <\rho_k U_k v_k> +\frac{\partial}{\partial z}E_k <q_{z,k}>$$
$$+ \quad \frac{\partial}{\partial z}E_k <p_k v_k> + <p_k + \Delta p_{ki}> \frac{\partial}{\partial t}E_k - \frac{\partial}{\partial z}E_k <\mathbf{n}_z \cdot (\bar{\bar{\tau}}_k \cdot \mathbf{v}_k)> =$$
$$E_k <\rho_k(\mathbf{F}_k \cdot \mathbf{v}_k + Q_k)> - <\mathbf{n}_k \cdot \mathbf{q}_k>_w$$
$$-\left\langle\left[\left(\dot{m}_k(U_k + \frac{p_k}{\rho_k})\right)_i + \mathbf{n}_k \cdot \mathbf{v}_i\Delta p'_{ki} + (\mathbf{q}_k \cdot \mathbf{n}_k)_i - (\bar{\bar{\tau}}_k \cdot \mathbf{v}_k \cdot \mathbf{n}_k)_i\right]\right\rangle . \quad (A.74)$$

we recall that

$$- <\dot{m}_k>_i= \Gamma_{mk}, \qquad (A.75)$$

$$< \mathbf{n}_k \cdot \mathbf{v}_k \cdot \bar{\bar{\tau}}_k >_i = \tau_{k,i} \, S_k^i \, v_{k,i}, \tag{A.76}$$

$$< \mathbf{n}_k \cdot \mathbf{q}_k >_i = q_{k,i} \, S_k^i, \tag{A.77}$$

$$< \mathbf{n}_k \cdot \mathbf{q}_k >_w = q_{k,w} \, S_k^w, \tag{A.78}$$

$$\Delta p_{ki}' \approx 0, \tag{A.79}$$

$$Q_k = 0, \tag{A.80}$$

$$\frac{\partial}{\partial z} E_k < \mathbf{n}_z \cdot (\bar{\bar{\tau}}_k \cdot \mathbf{v}_k) > \approx 0, \tag{A.81}$$

and

$$< F_k > = -g \sin \beta. \tag{A.82}$$

Using Eqs. A.75 to A.82 in Eq. A.74, and collecting terms, we have

$$\frac{\partial}{\partial t}[E_k < \rho_k U_k >] + \frac{\partial}{\partial z}[E_k < \rho_k U_k v_k >] \quad -\Gamma_{mk} < \quad U_k > =$$

$$q_{k,w} \, S_k^w + q_{k,i} \, S_k^i - E_k < \rho_k \, v_k > g \sin \beta \quad -\tfrac{\partial}{\partial z}[E_k < \quad p_k v_k >]$$

$$+\tau_{k,i} \, S_k^i \, v_{k,i} \quad -\tfrac{\partial}{\partial z} E_k < \quad q_{z,k} >$$

$$-[< p_k > + < \Delta p_{ki} >]\frac{\partial E_k}{\partial t} \quad +\Gamma_{mk} < \quad \frac{p_k}{\rho_k} > . \tag{A.83}$$

Because the flow is dominant in the z direction, $\mathbf{v_k} \cdot \mathbf{v_k} \approx v_k^2$, and neglecting terms, we can write our energy equation as

$$\frac{\partial}{\partial t}[E_k < \rho_k \, \hat{u}_k > +E_k < \rho_k \frac{v_k^2}{2} >] \quad +\tfrac{\partial}{\partial z}[E_k < \quad \rho_k \hat{u}_k v_k > + < \rho_k v_k \frac{v_k^2}{2} >]$$

$$-\Gamma_{mk}(< \hat{u}_k \quad + \tfrac{v_k^2}{2} > \quad) \quad =$$

$$q_{k,w} \, S_k^w + q_{k,i} \, S_k^i - E_k < \rho_k \, v_k > g \sin \beta \quad -\tfrac{\partial}{\partial z}[E_k < \quad p_k v_k >] + \tau_{k,i} \, S_k^i \, v_{k,i}. \tag{A.84}$$

We use the following expansion:

$$\frac{\partial}{\partial t}\left[\rho_k E_k \frac{v_k^2}{2}\right] = \rho_k E_k v_k \frac{\partial v_k}{\partial t} + \frac{v_k^2}{2}\frac{\partial}{\partial t}\left(\rho_k E_k\right),$$ (A.85)

and

$$\frac{\partial}{\partial z}\left[\rho_k E_k v_k \frac{v_k^2}{2}\right] = \rho_k E_k v_k^2 \frac{\partial v_k}{\partial z} + v_k^2 \frac{\partial}{\partial z}\left(\rho_k E_k v_k\right).$$ (A.86)

Adding Eqs. A.85 and A.86, we have

$$\frac{\partial}{\partial t}\left[\rho_k E_k \frac{v_k^2}{2}\right] + \frac{\partial}{\partial z}\left[\rho_k E_k v_k \frac{v_k^2}{2}\right] = v_k\left\{\rho_k E_k \frac{\partial v_k}{\partial t} + \rho_k E_k v_k \frac{\partial v_k}{\partial z}\right\}$$
$$+ \frac{v_k^2}{2}\left\{\frac{\partial}{\partial t}\left(\rho_k E_k\right) + \frac{\partial}{\partial z}\left(\rho_k E_k v_k\right)\right\}.$$ (A.87)

By considering the momentum and continuity, we can rewrite Eq. A.87 as

$$\frac{\partial}{\partial t}\left[\rho_k E_k \frac{v_k^2}{2}\right] + \frac{\partial}{\partial z}\left[\rho_k E_k v_k \frac{v_k^2}{2}\right] =$$
$$+ v_k\left\{\Gamma_{m,k}\left(v_{k,i} - v_k\right) - \tau_{z,k,w}\frac{S_k^w}{A} + \tau_{z,k,i}\frac{S_k^i}{A} - \rho_k E_k \sin\beta + \Delta p_{k,i}\frac{\partial}{\partial z}E_k - E_k\frac{\partial}{\partial z}p_k\right\}$$
$$+ \frac{v_k^2}{2}\left(\Gamma_{m,k}\right).$$ (A.88)

Substituting Eq. A.88 into Eq. A.84, we have

$$\frac{\partial}{\partial t}[E_k\rho_k \hat{u}_k] + \frac{\partial}{\partial z}[E_k\rho_k \hat{u}_k v_k] - \Gamma_{m,k}(< \hat{u}_k + \frac{v_k^2}{2} >) + \frac{v_k^2}{2}\left(\Gamma_{m,k}\right)$$
$$+ \quad v_k\left\{\Gamma_{m,k}\left(v_{k,i} - v_k\right) - \tau_{z,k,w}\frac{S_k^w}{A} + \tau_{z,k,i}\frac{S_k^i}{A} - \rho_k E_k \sin\beta + \Delta p_{k,i}\frac{\partial}{\partial z}E_k - E_k\frac{\partial}{\partial z}p_k\right\} =$$
$$+ \quad q_{k,w}\,S_k^w + q_{k,i}\,S_k^i - E_k\rho_k v_k g \sin\beta - \frac{\partial}{\partial z}[E_k p_k v_k] + \tau_{z,k,i}\,S_k^i\,v_{k,i}.$$ (A.89)

Simplifying Eq. A.89, we obtain

$$
\frac{\partial}{\partial t}[E_k \rho_k \hat{u}_k] + \frac{\partial}{\partial z}[E_k \rho_k \hat{u}_k v_k] - \Gamma_{m,k} \hat{u}_k - \frac{1}{2}\Gamma_{m,k}\left(v_{k,i} - v_k\right)^2 =
$$

$$
+q_{k,w}\, S_k^w + q_{k,i}\, S_k^i + v_k \tau_{z,k,w}\frac{S_k^w}{A} + \tau_{z,k,i}\frac{S_k^i}{A}\left(v_{k,i} - v_k\right)
$$

$$
-\Delta p_{k,i} v_k \frac{\partial}{\partial z}E_k - p_k\frac{\partial}{\partial z}[E_k v_k]. \tag{A.90}
$$

From thermodynamics definitions we have that

$$
\hat{u}_k = h_k - \frac{p_k}{\rho_k}, \tag{A.91}
$$

and we assume

$$
\Gamma_{m,k} = 0, \tag{A.92}
$$

$$
v_{k,i} = v_k, \tag{A.93}
$$

$$
q_{k,i} = 0, \tag{A.94}
$$

and

$$
p_{k,i} = p_k \tag{A.95}
$$

Substituting Eqs. A.91 through A.95 into Eq. A.90, the final form of our energy equation is given by

$$
\frac{\partial}{\partial t}[E_k \rho_k h_k] + \frac{\partial}{\partial z}[E_k \rho_k v_k h_k] \;=\; +q_{k,w}\, S_k^w + v_k \tau_{z,k,w}\frac{S_k^w}{A}
$$

$$
+E_k v_k \frac{\partial}{\partial z}[p_k] + \frac{\partial}{\partial z}[E_k p_k]. \tag{A.96}
$$

APPENDIX B

NON-LINEAR OPTIMIZATION-SUBPLEX METHOD.

The word optimum means "that point at which any condition is most favorable"[73], under this condition, it is synonymous with "most" or "maximum" in case of a maximization process, and with "least" or "minimum" in case of a minimization process. Optimize is described as "make the most or best of"[73]. The optimization theory encompasses the quantitative study of optima and methods for finding them. Shout[74] considers: "from an engineering point of view, that although it is desirable to have the very best or optimum solution to a problem, the engineer usually must settle for improvement rather than perfection in designs". Optimization can be considered as the process of movement towards improvement rather than achievement of perfection.

The optimization problem can be expressed mathematically as

$$F(x) = F(x_1, x_2, ..., x_n), \qquad (B.1)$$

where the function F is defined as the quality, merit or objective function that we want to maximize or minimize. Mathematically speaking, it provides the quantitative way for evaluating and comparing the relative goodness of several options or proposal

255

"designs". The objective function depends on the n-independent variables

$$x = \begin{bmatrix} x_1 \\ x_2 \\ \vdots \\ x_n \end{bmatrix} = (x_1, x_2, \ldots, x_n)^T \qquad (B.2)$$

We can refers to the variables x as design variables which uniquely and completely define our objective function. The design variables may be function of other parameters. Note that as main results of our optimization process, the "optimum" values of these variables are found.

Whether a maximum or a minimum is sought, it is possible to define the following relationship

$$Min\{F(x)\} = -Max\{-F(x)\}, \qquad (B.3)$$

Eq. B.3 clearly establish that a maximization problem can be converted in a minimization problem by simply changing the sign of the objective function.

Another important point about optimization is the definition of static and dynamic optimization. Static optimization considers that the optimization process and the optimum itself are time independent, so once the location of the extremum has been found, the search is over. On the other hand, the dynamic optimization goal is to maintain an optimal condition in the face of varying conditions, in which case the search becomes a continuous process.

B.1   Optimization with and without constraints.

The objective function solution domain is defined by the set of all possible values x variables and is called the solution or design space. But when an optimization process is applied, several restrictions are used to prevent solutions that are physically impossible, illegal, unsafe or uneconomical. These restrictions are known as constraints, and collectively restrict the entire solution space to a restricted region called problem feasible region which is denoted by Γ.

In general, we can classify the constraints as functional and regional constraints. Functional constraints are set by a certain number of relationships of the design variables, x, that must be satisfied by the optimum solution in order to comply with certain restrictions imposed by nature, economics, safety, law, etc. These restrictions have the following form

$$C_1\left(x_1, x_2, \ldots, x_n\right) = 0$$

$$C_2\left(x_1, x_2, \ldots, x_n\right) = 0$$

$$\vdots$$

$$C_n\left(x_1, x_2, \ldots, x_n\right) = 0$$

(B.4)

The regional constraints that are a subset of the functional constraints, are set in the form of inequalities. These constraints have the following form

$$l_1 \leq R_1\left(x_1, x_2, \ldots, x_n\right) \leq L_1$$

$$l_2 \leq R_2\left(x_1, x_2, \ldots, x_n\right) \leq L_2$$

$$\vdots$$

$$l_n \leq R_1\left(x_1, x_2, \ldots, x_n\right) \leq L_n$$

(B.5)

B.2 Optimization Algorithms.

The methods of optimization are usually based on a model that is a convenient approximation to the objective function, which enables a prediction of the location of an optimum (minimum or maximum). The typical behavior of an algorithm that is considered acceptable is

1. With each iteration step, the estimation of the optimum, x^k, moves steadily towards the solution neighborhood of a local minimum x^*,

2. then converges rapidly to the point x^* itself,

3. and the process is completed when the user-supplied convergence criteria is satisfied.

Among the several models available the most successful have been the quadratic models and the prototype models. Since the optimization algorithm depends on the characteristics of the objective function, a complete information about the objective function is unavailable. Rowan[75] described some question about the characteristics of the objective function $F(x)$ that should be considered when selecting an optimization method:

- Is $F(x)$ a noisy function?. That means that we have a high variation of the objective function value with a small variation of the design variables x..

- Is $F(x)$ an extremely inaccurate functional approximation of the real process that we are trying to simulate?.

- Is $F(x)$ discontinuous or may have large jumps?

- Is the problem dimension large or small ?

- Is $F(x)$ expensive to evaluate?

- Is $F(x)$ have derivatives which can be easily computed?

- Is $F(x)$ undefined at some points? If so, the optimization may have to be constrained.

B.2.1 Quadratic Models.

The quadratic models define a quadratic approximation $Q(x)$ to the objective function $F(x)$,

$$F(x) \approx Q(x) = c^T x + \frac{1}{2} x^T G\, x \qquad \text{(B.6)}$$

so that

$$Q(x_k + p_k) = Q_k + g_k^T\, p_k + \frac{1}{2} p_k^T G_k p_k, \qquad \text{(B.7)}$$

where

$g \equiv \nabla Q(x)$ is the gradient n-vector of x, p is the vector of displacement from x and $G \equiv \nabla^2 Q(x)$ is the Hessian matrix of x.

$$\nabla Q(x) \equiv g \equiv \begin{bmatrix} \frac{\partial F}{\partial x_1} \\ \frac{\partial F}{\partial x_2} \\ \vdots \\ \frac{\partial F}{\partial x_n} \end{bmatrix} \tag{B.8}$$

$$p = \begin{bmatrix} \Delta x_1 \\ \Delta x_2 \\ \vdots \\ \Delta x_n \end{bmatrix} \tag{B.9}$$

$$\nabla^2 Q(x) \equiv G \equiv \begin{bmatrix} \partial^2 F/\partial x_1 \partial x_1 & \cdots & \partial^2 F/\partial x_1 \partial x_n \\ \vdots & & \vdots \\ \partial^2 F/\partial x_n \partial x_1 & \cdots & \partial^2 F/\partial x_n \partial x_n \end{bmatrix} \tag{B.10}$$

Some properties of a quadratic function are[76]

- A quadratic function is one of the simplest smooth functions with a well determined minimum or maximum,

- A general function expanded about a local minimizer x^* is well approximated by a quadratic function, so the method should have a rapid ultimate rate of convergence,

- Methods based on quadratic models can be made invariant under a linear transformation of variables.

B.2.1.a Failure of Classical Optimization Methods[75].

The classical methods are designed to locate local optima that are stationary points rather than points where the objective function reaches a threshold value. The objective function needs to be smooth in order to be well approximated, i.e., quadratic function approximations.

In case of quadratic function approximations, we need to estimate the objective function derivatives analytically or numerically. But, if we are working with discontinuous or noisy functions or with functions that are computationally expensive to evaluate, we can easily avoid to consider methods that require derivatives, because we are certain that the derivative estimation are going to be too inaccurate or costly to compute in order to be useful.

The nonsmooth optimization methods also called nondifferenciable optimization methods will generally fail in case of functions that are not piecewise smooth.

The main rule that we always need to have in main is that if the objective function characteristics violate the fundamental assumptions upon which the method is based, that method is not appropriate for the optimization of the function.

B.2.2 Direct Search Methods.

Direct search strategies work without constructing a model of the objective function, instead the directions of search and step lengths are fixed heuristically or by using a certain scheme rather than in mathematically optimal way. Thus, the risk is that it may not be possible to convergence. The "trial" character of their search strategies has earned the name of trial-and-error procedures. In contrast to

the classical methods, the direct search methods make few, if any, assumptions about the objective function. Because the direct search methods are based on "trials" of the function, they behave well for "noisy" or "discontinuous" functions, i.e., functions which are not smooth.

The main attraction of the direct search methods lie not in theoretical proofs and rates of convergence, but in their simplicity. Also, they have proved themselves useful in practice. The direct search methods are designed to locate local minimum.

B.2.2.a   Simplex Method.

There is a group of unconstrained direct search method called simplex strategies. The original idea comes from Stanley, Hest and Himsworth[77] with later modifications from Nelder and Mead[78], Box[79], Ward et al.[80] and Dambrauskas[81,82]. It is often recommended as the best alternative for optimizing "noisy" objective functions. The basic idea is that instead of defining a single starting point, a polyhedron of $n+1$ vertices is used (n is the number of design variables), and the objective function is evaluated at each vertex.

Algorithm Description.   A simplex in the n-space is a polyhedron of a set of $n+1$ points, this simplex moves through the n-dimensional domain space of the objective function, changing size and shape, and automatically shrinking when it envelopes the minimum. The algorithm proceeds a follows

1. A starting point, x_o, is selected as initial guess,

2. The initial simplex is formed by setting the simplex vertices as

$$x_i = x_o + scale_i \cdot e_i, \tag{B.11}$$

for $i = 1, 2, ..., n$, where $scale_i$ is the $i - th$ component of $scale$, $scale$ are the initial stepsized for the $n - coodinate$ directions and e_i is the $i - th$ column for the $n \times n$ identity matrix.

3. Once the simplex has been formed, the objective function is evaluated at each vertex point. The worst point, x_h (the one with the highest value of the objective function in case of minimization or with the lowest value in case of maximization) is computed so that

$$f(x_h) = \max_i f(x_i), \tag{B.12}$$

and the centroid of the remaining vertices, c, is calculated as

$$c = \frac{1}{n} \sum_{\substack{i=0 \\ i \neq h}}^{k} x_i, \tag{B.13}$$

the vertex with the minimum value of the objective function is denoted as x_l, so that

$$f(x_l) = \min_{i=h} f(x_i), \tag{B.14}$$

4. The worst vertex, x_h, is reflected through the centroid of the remaining vertices as follows

$$x_r = c + \alpha \left(c - x_h \right), \tag{B.15}$$

where α is a positive constant.

5. If x_r is the best point in the new simplex, i.e., $f(x_r) < f(x_l)$, a further expansion in the same direction is tried and we generate the point x_e, i.e.,

$$x_e = c + \gamma \left(x_r - c \right).$$

(B.16)

6. If x_r is neither the best nor the worst point of the new simplex, then

$$x_r = x_h.$$

(B.17)

7. If x_r has the worst objective function, x_r or x_h (whichever has the higher function values), a contracted point is located as follows

$$x_c = c + \beta \left(x_h - c \right), \quad \text{if } f(x_r) > f(x_h),$$

(B.18)

or

$$x_c = c + \beta \left(x_r - c \right), \quad \text{if } f(x_r) \leq f(x_h).$$

(B.19)

8. The objective function is now evaluated at the contracted point. If an improvement over the current points is achieved, the process is restarted. If improvement is not achieved and x_c is still the worst point, the simplex shrinks in a massive contraction movement by contracting each vertex towards the best point

$$x'_s = x_l + \delta \left(x_s - x_l \right),$$

(B.20)

$$x'_h = x_l + \delta \left(x_h - x_l \right).$$

(B.21)

9. The procedure is terminated when the convergence criterion is satisfied or a specified number of iterations are achieved.

A general description of the algorithm as given in Ref. 75 is presented in Fig. B.1.

Simplex Method Characteristics.[75] The main characteristics of the simplex method are

- Compared with other methods, the simplex method works well with noisy functions,

- The simplex method performs well when n is small ($n \leq 5$), but may be very inefficient when n is much larger as reported by Box[83] and Rowan[75].

- The simplex method does poorly when constraints are handled by rejecting infeasible points since the simplex may collapse into a subspace. When minimizing a function, the usual mechanism for rejecting a point is to assign it a large function value.

- The simplex method requires $O(n^2)$ storage because a simplex has $n+1$ vertices, and each vertex is an $n - vector$.

Algorithm:Nelder-Mead Simplex Method.
Notation:

$x_i \equiv i-$th vertex of simplex
$f_i \equiv f(x_i)$

Input:

n	:problem dimension
f	:function to be minimized
x	:initial approximation to minimum
$scale$	:initial stepsizes for the n coordinate directions
α	:reflection coefficient
β	:contraction coefficient
γ	:expansion coefficient
δ	:shrinkage (massive contraction) coefficient

$(\alpha > 0)$
$(0 < \alpha < 1)$
$(\gamma > 1)$
$(0 < \delta < 1)$

Output:

x :computed minimum

begin (*start of simplex method*)
generate initial simplex
while termination test not satisfied **do**
begin
determine h, s, l such that
$f(x_h) =\max_i f(x_i)$, $f(x_i) =\max_{i \neq h} f(x_i)$, $f(x_l) =\min_{i \neq h} f(x_i)$

$c \leftarrow \frac{1}{n} \sum_{\substack{i=0 \\ i \neq h}}^{n} x_i$ (*calculate centroid*)

$x_r \leftarrow c + \alpha (c - x_h)$ (*reflect*)
if $(f_r < f_l)$ **then**
begin
$x_e \leftarrow c + \gamma(x_r - c)$
if $(f_e < f_l)$ **then** $x_h \leftarrow x_e$ **else** $x_h \leftarrow x_r$
end
else if $(f_r < f_s)$ **then** $x_h \leftarrow x_r$ (*neither best nor worst point, accept*)
else
begin
if $(f_h < f_r)$ **then** $x_c \leftarrow c + \beta(x_h - c)$ **else** $x_c \leftarrow c + \beta(x_r - c)$
if $(f_c < \min(f_r, f_h))$ **then** $x_h \leftarrow x_c$ (*successful contraction*)
else
for $i \leftarrow 0$ **to** n **do if** $(i \neq l)$ **then** $x_i \leftarrow x_e + \delta(x_i - x_l)$
end
end
end (*end of simplex method*)

Figure B.1: Nelder-Mead Simplex Algorithm

B.2.2.b   The Subplex Method.

The subplex method was designed by Rowan[75] to remove the weaknesses of the simplex method retaining its positive features. The subplex method's approach is to decompose the problem solution space into low-dimensional subspaces that the simplex method itself can be able to search efficiently. This approach allows to avoid the difficulties of the simplex method with high-dimensional problems. The subplex method is designed as a general-purpose optimization method and is not restricted to any particular application and can be used to minimize or maximize the objective function under consideration.

Algorithm Description.   A simplify description of the method is presented here, for completeness some material from Rowan[75] is reproduced, for a full detailed description of the method the reader is referred to Ref. 75.

The subplex method, at each iteration, determines an improved set of search directions and performs a line search along those directions. The subplex method determines an improved set of subspaces and then uses the simplex method to search each subspace.

The subplex strategy consists of the values for α, β, γ, δ, ψ, ω, $nsmin$, and $nsmax$. The first four coefficients are exactly the ones that are used in the simplex method. The coefficient ψ allows to control the accuracy of the subspace searches within the simplex method. The coefficient ω controls the scale of the stepsizes. The

Algorithm:Rowan's SUBPLEX Method.
Input:

n	:problem dimension
f	:function to be minimized
x	:initial approximation to minimum
$scale$	:initial stepsizes for the n coordinate directions
α	:reflection coefficient $\qquad\qquad\qquad (\alpha > 0)$
β	:contraction coefficient $\qquad\qquad (0 < \alpha < 1)$
γ	:expansion coefficient $\qquad\qquad\quad (\gamma > 1)$
δ	:shrinkage (massive contraction) coefficient $\quad (0 < \delta < 1)$
ψ	:simplex reduction coefficient $\qquad (0 < \psi < 1)$
ω	:step reduction coefficient $\qquad\quad (0 < \omega > 1)$
$nsmin$	:minimum subspace dimension
$nsmax$	:maximum subspace dimension

$$(1 \leq nsmin \leq nsmax \leq n \text{ and } nsmin[n/nsmax] \leq n)$$

Output:

x	:computed minimum

begin   (*start of Complex method*)
    generate initial simplex
    while termination test not satisfied **do**
      begin
        set stepsizes
        set subspaces
        for each subspace do use Simplex Method to search subspace
        check termination
      end
end   (*end of Complex method*)

Figure B.2: Rowan - Subplex Method

range of the subspace dimensions are determined by the values of $nsmin$ and $nsmax$.

An outline of the method as given in Ref. 75 is presented in Fig. B.2.